Cellulose Nanocrystal Reinforcement of Nylon 6 Films and Fibres

by

Nicole Christine Jankovic

A thesis submitted in partial fulfillment of the requirements for the degree of

Doctor of Philosophy

Department of Chemistry
University of Alberta

© Nicole Christine Jankovic, 2022

Abstract

Cellulose Nanocrystals (CNC) are abundant, renewable, and highly crystalline by-products from the forestry industry. CNCs are known to have excellent thermal and mechanical properties which have been exploited in a variety of applications across numerous fields, such as drug delivery, photonics, and in films. With the focus of integrating CNC into functional materials, there have been a multitude of methods for the surface modification of CNC and for incorporation in polymer composites.

It is known that CNC can increase the mechanical strength of many polymers, however, Polyamides (including Nylon 6) have not yet been thoroughly investigated. This thesis describes the effects of CNC in Nylon 6 composites and the influence of CNC on the mechanical strength and characteristics of the polymer. Nanofibers were produced using solution electrospinning and freestanding thin films were produced using spin coating. Further, a comparison of the reinforcing impact of CNC in randomly distributed and aligned nanofibres, and the effect of each of the electrospinning processing parameters on fibre diameter and alignment is described. Furthermore, the influence of CNC on the crystallization of Nylon 6 in both thin films and electrospun fibres is also studied.

Further modification of CNC with diazonium salts and with an alkylamine group *via* diazonium-mediated surface functionalization was performed. Both the unmodified and modified CNC was incorporated into Nylon 6 solutions and spin coated into freestanding thin films. The modification of CNC with hydrophobic aryl and alkyl groups using diazonium chemistry provides a quick and facile route towards increased interactions with hydrophobic polymers.

Due to the wide range of applications that CNC has in functional materials, it is crucial to understand the factors attributed to changes in the mechanical strength of CNC-polymer composites, and to develop methods that effectively yield and control high quality nanocomposites. By detailing the effects of CNC in polymer composites, recommendations can be established for industry to use as guidelines when using CNC in Polyamides. The large reinforcing impact of a bio-renewable resource at low loadings is an exciting route for stronger materials and a stepping-stone towards more sustainable products.

Preface

This thesis is an original work by Nicole C. Jankovic under the supervision of Professor Mark T. McDermott and Professor Cagri Ayranci. Pieces of this research have been in collaboration with others and have been published. The details pertaining to each experimental chapter are below.

Part of Chapter 2 is published as Osorio, D.A.; Niinivaara, E.; Jankovic, N.C.; Demir, E.C; Benkaddour, A.; Jarvis, V.; Ayranci, C.; McDermott, M.T.; de Lannoy, C.-F.; and Cranston, E.D., Cellulose Nanocrystals Influence Polyamide 6 Crystal Structure, Spherulite Uniformity, and Mechanical Performance of Nanocomposite Films. *ACS Applied Polymer Materials* **2021**, *3*, 4673-4684. I was responsible for the experimental design, data analysis, and writing of the manuscript. I was responsible for all of the data collection, data analysis, and writing of this Chapter. The tensile tests were completed by Daniel Osorio from McMaster University. DSC was completed by Eyup C. Demir. TGA and FTIR was collected by the Analytical Instrumentation Laboratory in the Department of Chemistry at the University of Alberta. The samples for TEM imaging were prepared by and the images were collected by Dr. Kacie Norton from the Microscopy Unit in the Department of Biological Sciences at the University of Alberta. Critical inputs and suggestions for this Chapter was provided by Dr. McDermott and Dr. Ayranci.

I was responsible for all of the experimental design, data collection, data analysis, and writing of Chapter 3. Critical inputs and suggestions were provided by Dr. McDermott and Dr. Ayranci. I developed the plans for the humidity chamber presented in this Chapter and the building of the chamber was completed by the Machine Shop in the Department of Chemistry at the University of Alberta.

I was responsible for the experimental design, data collection, data analysis, and writing of Chapter 4. Critical inputs and suggestions were provided by Dr. McDermott and Dr. Ayranci. The tensile tests were performed by Eyup C. Demir and Jiawei Chen, PhD students in Dr. Ayranci's group. The samples for TEM imaging were prepared by and the images were collected by Dr. Kacie Norton from the Microscopy Unit in the Department of Biological Sciences at the University of Alberta. The FTIR spectra were collected by the Analytical Instrumentation Lab in the Department of Chemistry at the University of Alberta. The DSC and TGA data were collected with Eyup C. Demir at nanoFAB at the University of Alberta.

I was responsible for the experimental design, data collection, data analysis, and writing of Chapter 5. Critical inputs and suggestions were provided by Dr. McDermott. FTIR, CHNS, and TGA data was collected by the Analytical Instrumentation Laboratory in the Department of Chemistry at the University of Alberta. XPS data was collected by staff at nanoFAB at the University of Alberta. The contact angle measurements and XRD were collected by Dr. Rongbing Du.

I was responsible for the experimental design, data collection, data analysis, and writing of Chapter 6. Critical inputs and suggestions were provided by Dr. McDermott. FTIR, CHNS, and TGA data was collected by the Analytical Instrumentation Laboratory in the Department of Chemistry at the University of Alberta. XPS data was collected by staff at nanoFAB at the University of Alberta. The TEM images were prepared and collected by Dr. Arlene Oatway from the Microscopy Unit in the Department of Biological Sciences at the University of Alberta.

Dedication

This dissertation is firstly dedicated to my extraordinarily supportive friends and partner. Without all of your undying support, I would not have made it to the end of my program and become the loving and patient person I am today.

I would also like to dedicate this dissertation to my parents and siblings, all of whom have relentlessly pushed myself to strive for the best.

"Don't be afraid to be open-minded. Your brain isn't going to fall out." – Unknown

Acknowledgements

The work presented in this dissertation would not be possible without the support from everyone in the Department of Chemistry at the University of Alberta. I am extremely grateful for all of the support in my undergraduate studies leading up to the enrolment and completion of my graduate degree. I would like to specifically thank Dr. Michael Serpe and Dr. Jonathan Veinot, both of whom took me into their labs as a bright-eyed undergraduate student excited about starting her research journey. I learned valuable skills that propelled me into success during my PhD. Thank you to all of the past undergraduate and graduate students in both Dr. Serpe and Dr. Veinot's groups who helped along the way!

Most importantly, the completion of this dissertation and my program would not be possible without the unwavering of support from my supervisor, Dr. Mark McDermott. I am forever grateful to work with a supervisor that encourages both scientific exploration and to still have fun along the way. Another thanks to Dr. Cagri Ayranci and his group members, specifically, Eyup Demir, Muhammad Alyaan Ahmed Khan, Jiawei Chen, Yu Chen, and Irina Garces Arguello.

A warm thank you to past and current McDermott Group members who have always worked together to support one another, even when times got tough (*e.g.*, thefts, fires, floods, and a global pandemic!). Thank you to Dr. Casey Rusin, Dr. Sunil Rajput, Taylor Lynk, Dr. Thuy Nyugen, Dr. Ahmed Mahmoud, Huijun Mao, Dr. Abdelhaq Benkaddour, Dr. Rongbing Du, Khandaker Akib Shahriar, and Ola Mabrouk.

Thank you to all of the staff from the Department of Chemistry Analytical Services and Chem Stores, NRC-Nano, the Department of Biological Sciences' Microscopy Unit, and nanoFAB facilities and staff who have helped progress my research. I am also grateful to all of the teaching

staff in the Department of Chemistry – all of whom have taught me valuable soft skills that I can apply to my future careers. Thank you to Dr. Norman Gee, Dr. Yoram Apelblat, Dr. Vladimir Michaelis, Dr. Jason Cooke, and Dr. Gregory Kiema for all of your guidance as I served as a Teaching Assistant for your courses. I would like to especially thank Dr. Charles Lucy for providing me with the incredible opportunity of being a Chemistry Education Teaching Assistant with Michael Sorochan Armstrong. It was an extraordinary experience creating, filming, and editing educational videos for the next generation of chemists.

Finally, I would like to acknowledge all of the incredible people I have met in my University of Alberta journey during both my undergraduate and graduate degrees. I would like to especially thank everyone that I have met as part of the following student groups, associations, and organizations: Let's Talk Science, Chemistry Graduate Students' Society, Chemistry Students' Association, University of Alberta Nanotechnology Group, Friends of Glenrose Association, University of Alberta Canadian Red Cross Club, Canadian Red Cross Alberta Branch, Faculty of Science's Science Mentors, WISEST, Chemical Institute of Canada Edmonton Branch, CSC 75th Lectureship Fund Committee, HIV Edmonton, TELUS World of Science Edmonton, Covenant Health & the Misericordia Hospital, and the Heart of the City Piano Program. A special thank you to Elizabeth Freiter, longtime friend and past piano teacher.

It is bittersweet bidding farewell to the University of Alberta, where I have spent the last 9 years of my early adulthood pursuing higher education. Thank you all!

Table of Contents

ABSTRACT ..... **II**

PREFACE ..... **IV**

DEDICATION ..... **VI**

ACKNOWLEDGEMENTS ..... **VII**

LIST OF TABLES ..... **XII**

LISTS OF FIGURES ..... **XIII**

LIST OF SYMBOLS ..... **XVII**

LIST OF ABBREVIATIONS ..... **XX**

CHAPTER 1. INTRODUCTION **1**

1.1 Research Scope & Objectives 1
1.2 Cellulose Nanocrystals 3
1.2.1 The Structure of Cellulose Nanocrystals *3*
1.2.2 Production of Cellulose Nanocrystals *7*
1.3 Cellulose Nanocrystals as Polymer Additives 9
1.3.1 Surface Modification of Cellulose Nanocrystals *9*
1.3.2 The Reinforcing Mechanism of Unmodified Cellulose Nanocrystals in Polymers *13*
1.3.3 Cellulose Nanocrystal Composite Processing Techniques *14*
1.3.4 Electrospun Nanofibres *16*
1.4 Reinforced Nylon 6 Composites 19
1.4.1 Nylon 6 Properties and Characteristics *19*
1.4.2 Fillers for the Mechanical Reinforcement of Nylon 6 ..... *21*
1.5 Thesis Outline 23
1.6 References 25

CHAPTER 2. SPIN COATED CELLULOSE NANOCRYSTAL-NYLON 6 THIN FILMS **31**

2.1. Introduction 31
2.2 Experimental 34
2.2.1 Chemicals and Materials *34*
2.2.2 Preparation of Cellulose Nanocrystal and Nylon 6 Solutions *34*
2.2.3 Preparation of Spin Coated Films *35*
2.2.4 Characterization *35*
2.3 Results and Discussion 38
2.4 Conclusion 54
2.5 References 54

CHAPTER 3. EFFECT OF ELECTROSPINNING PARAMETERS ON FIBRE DIAMETER AND ALIGNMENT OF NYLON 6 FIBRES 58

3.1 INTRODUCTION 58
3.2 EXPERIMENTAL 60
3.2.1 Chemicals and Materials 60
3.2.2 Preparation of Nylon 6 Solutions 61
3.2.3 Electrospinning 61
3.2.4 Characterization 62
3.3 RESULTS AND DISCUSSION 63
3.4 CONCLUSION 74
3.5 REFERENCES 75

CHAPTER 4. INFLUENCE OF CELLULOSE NANOCRYSTALS ON THE MECHANICAL PROPERTIES AND CRYSTALLIZATION OF ALIGNED NYLON 6 ELECTROSPUN FIBRE MATS 77

4.1 INTRODUCTION 77
4.2 EXPERIMENTAL 79
4.2.1 Chemicals and Materials 79
4.2.2 Preparation of Cellulose Nanocrystal and Nylon 6 Solutions 79
4.2.3 Production of Randomly Distributed Electrospun Fibre Mats 80
4.2.4 Production of Aligned Electrospun Fibre Mats 80
4.2.5 Characterization 81
4.3 RESULTS AND DISCUSSION 83
4.4 CONCLUSION 102
4.5 REFERENCES 103

CHAPTER 5. SURFACE MODIFICATION OF CELLULOSE NANOCRYSTALS WITH DIAZONIUM SALTS 107

5.1 INTRODUCTION 107
5.2 EXPERIMENTAL 112
5.2.1 Chemicals and Materials 112
5.2.2 Purification of 4-Nitrobenzenediazonium Tetrafluoroborate (4-dNB) 113
5.2.3 Ex-Situ Diazonium Salt Synthesis and Cellulose Nanocrystal Modification 113
5.2.4 In-Situ Diazonium Salt Synthesis and Cellulose Nanocrystal Modification 114
5.2.5 Characterization 114
5.3 RESULTS AND DISCUSSION 116
5.3.1 Surface Modification of CNC Using the Ex-Situ Method 116
5.3.2 Surface Modification of CNC Using the In-Situ Method 123
5.3.3 Proposed Mechanism 126
5.3.4 Diazonium Modified CNC and Nylon 6 Thin Films 127
5.4 CONCLUSION 129

5.5 References 129

CHAPTER 6. DIAZONIUM RADICAL MEDIATED SURFACE MODIFICATION OF CELLULOSE NANOCRYSTALS WITH AN ALKYLAMINE 135

6.1 Introduction 135
6.2 Experimental 137
6.2.1 Chemicals and Materials 137
6.2.2 Surface Modification of Cellulose Nanocrystals with Propylamine 138
6.2.3 Characterization 138
6.3 Results and Discussion 140
6.4 Conclusion 151
6.5 References 152

CHAPTER 7. CONCLUSIONS AND FUTURE DIRECTIONS 154

7.1 Chapter Summaries 154
7.2 Future Directions 158
7.2.1 Post-Functionalization of Diazonium or Propylamine Modified CNC 158
7.2.2 Incorporation of Modified CNC in Nylon 6 Electrospun Fibres 158
7.2.3 CNC-Polymer Electrospun Yarns 159
7.3 References 160

BIBLIOGRAPHY (ALPHABETICAL BY FIRST AUTHOR) 162

List of Tables

Table 1-1. Examples of modifications of CNC (M-CNC) in polymer composites with respective percent increase in elastic modulus (EM) results compared to the neat polymer (NP) and unmodified CNC (UM-CNC) at the optimal modified CNC loading..... 12
Table 1-2. Previously reported CNC-Nylon 6 composite preparation and manufacturing methods. 22
Table 2-1. Summary of mechanical properties of the CNC-Nylon 6 spin coated films. 45
Table 2-2. FTIR band assignments for the CNC-Nylon 6 spin-coated films..... 49
Table 2-3. Summarized DSC and TGA results for the CNC-Nylon 6 films..... 53
Table 3-1. Electrospinning parameters and the corresponding rotation speeds investigated in this chapter..... 62
Table 4-1. Calculated effective eross-sectional areas of the randomly distributed and aligned fibre mats. 85
Table 4-2. Summarized mechanical results for the random and aligned fibre mats. 91
Table 4-3. FTIR band assignments for the CNC-Nylon 6 spin-coated films..... 94
Table 4-4. Summarized DSC and TGA data for the aligned CNC-Nylon 6 fibres..... 102
Table 5-1. CHNS analysis of cellulose nanocrystals (CNC) and the material resulting from the reaction of 4-dNB and CNC (4-dNB+CNC). 120
Table 6-1. CHNS analysis of CNC and PA-CNC..... 143
Table 6-2. Summarized HR-XPS data in the C1s regions for CNC and PA-CNC..... 146
Table 6-3. Summarized XPS survey scan data for CNC and PA-CNC. 147

Lists of Figures

Figure 1-1. The hierarchal structure of cellulose from a tree: a) a pine tree, b) a cross-section of the tree trunk, c) SEM image of the tissue structure, d) TEM image of the layered cell wall, e) illustration of the lignocellulosic region, and f) illustration of extracted lignin and cellulose fibrils coated with hemicellulose. Reprinted with permission from Zhu, H.; Luo, W.; Ciesielski, P. N.; Fang, Z.; Zhu, J. Y.; Henriksson, G.; Himmel, M. E.; Hu, L., Wood-Derived Materials for Green Electronics, Biological Devices, and Energy Applications. *Chemical Reviews* 2016, 116 (16), 9305-9374. Copyright 2022 American Chemical Society. 3
Figure 1-2. A) The chemical structure of cellulose with each carbon number labelled, B) the arrangement of amorphous and crystalline regions in untreated cellulose, and C) TEM image of CNCs. 4
Figure 1-3. A) The packing of the Iβ polymorph of cellulose with black arrows showing the unit cell *a* and *c* edges and B) a cross-section of a CNC depicting the unit cell and lattice planes. Fig. 1-3B is adapted from S. Eyley and W. Thielemans, *Nanoscale*, 2014, 6, 7764 DOI: 10.1039/C4NR01756K with permission from the Royal Society of Chemistry, used under CC BY 3.0 6
Figure 1-4. General procedure for the production of CNC. 7
Figure 1-5. Visualization of the Taylor cone and bending instabilities of a polymer jet during electrospinning: A) The formation of the Taylor cone at the needle tip after a voltage is applied (*U*) and B) the trajectory of the jet going through a series of instabilities. Figure 1-5b is adapted with permission from Xue, J.; Wu, T.; Dai, Y.; Xia, Y., Electrospinning and Electrospun Nanofibers: Methods, Materials, and Applications. *Chemical Reviews* 2019, 119 (8), 5298-5415. Copyright 2022 American Chemical Society. 17
Figure 1-6. Summarized reaction for the synthesis of Nylon 6 from caprolactam. 19
Figure 1-7. Crystal structure of the two dominant allomorphs of Nylon 6. A) Hydrogen bonding (left) and 3D packing (right) of α allomorph and B) hydrogen bonding (left) and 3D packing (right) of the γ allomorph. Adapted from Dasgupta, S.; Hammond, W. B.; Goddard, W. A., Crystal Structures and Properties of Nylon Polymers from Theory. Journal of the American Chemical Society 1996, 118 (49), 12291-12301. Copyright 2022 American Chemical Society. 20
Figure 2-1. Schematic of the solution preparation, final CNC-Nylon 6 solutions, spin coating procedure and instrument, and an example of the final thin film after removal from the glass substrate. The red box indicates where the test strip was cut for tensile testing. 38
Figure 2-2. (A) Photographs of the thin films produced at CNC loadings of 0-5 wt% and (B) the corresponding thickness of the films at each CNC loading. The film thickness measurements were collected by Daniel Osorio. 39

Figure 2-3. TEM images of (A) neat Nylon 6 film and (B) 5 wt% CNC film, and SEM images of (C) neat Nylon 6 film and (D) 5 wt% CNC film. The TEM images in Fig. 2-3A,B were provided by Abdelhaq Benkaddour and Akib Shahriar. 41
Figure 2-4. Schematic illustrating tensile testing of the spin coated films. A) Specimen (blue) loaded into the grips (grey) at the original length (L_0), B) specimen after displacement ($L-L_0$), and C) specimen after break. The black arrow indicates top grip displacement direction. 42
Figure 2-5. An example of a stress-strain curve for a 1 wt% CNC-Nylon 6 film. The points labelled on the curve are the (a) Young's modulus, (b) ultimate tensile strength, and (c) strain at break. 43
Figure 2-6. Young's modulus (blue) and ultimate tensile strength (red) results for the CNC-Nylon 6 films at 0-5 wt% loadings. The mechanical results were obtained by Daniel Osorio. 44
Figure 2-7. FTIR analysis of the spin-coated CNC-Nylon 6 films at 0 wt% CNC (blue), 1 wt% CNC (green), 2.5 wt% CNC (purple), and 5 wt% CNC (red). 47
Figure 2-8. DSC analysis of the CNC-Nylon 6 films at 0 wt% CNC (blue), 1 wt% CNC (green), 2.5 wt% CNC (purple), and 5 wt% CNC (red). A comparison to the as-received Nylon 6 pellet is also included (orange). 50
Figure 2-9. (A) TGA and (DTG) curves for the CNC-N6 films at 0 wt% (blue), 1 wt% (green), 2.5 wt% (purple), and 5 wt% (red). 52
Figure 3-1. Photograph of the rotating drum electrospinner set-up inside the plexiglass chamber. Each of the components are labelled as follows: a) air inlet, b) air outlet, c) air disperser, d) sliding door, e) cord connected to power supply, f) grounding wire, g) rotating drum, h) drum control box, i) arm that holds syringe(s), and j) syringe pump. 63
Figure 3-2. SEM images of electrospun mats collected at increasing drum rotation speeds: A) 0 rpm, B) 100 rpm, C) 500 rpm, D) 1000 rpm, E) 2000 rpm, F) 3000 rpm, G) 4000 rpm, H) a jitter plot of the angles of deviance for the fibres in each mat, and I) a plot of the fibre diameters for each fibre mat. The white arrows indicate drum rotation direction. 65
Figure 3-3. Photographs of the copper wire ring placed onto the syringe needle for jet focusing. 67
Figure 3-4. Effect of jet focusing on the alignment of fibres. SEM images of focusing done at A) 2500 rpm, C) 3000 rpm, and D) 4000 rpm. Distribution frequency for the angle of alignment of fibres collected at B) 2500 rpm, D) 3000 rpm, and F) 4000 rpm, and G) a jitter plot of the angles of deviance for each of the fibre mats. The white arrows indicate drum rotation direction. 68
Figure 3-5. Effect of varying voltage on fibres collected at 3000 rpm on A) fibre diameters and B) alignment, and at 4000 rpm on C) fibre diameters and D) alignment. 69
Figure 3-6. Effect of varying flow rate on fibres collected at 3000 rpm on A) fibre diameters and B) alignment, and at 4000 rpm on C) fibre diameters and D) alignment. 71
Figure 3-7. Effect of varying needle-to-collector distance on fibres collected at 3000 rpm on A) fibre diameters and B) alignment, and at 4000 rpm on C) fibre diameters and D) alignment. 73
Figure 4-1. Electrospinning set-up for (A) the randomly distributed fibre mats and (B) the aligned fibre mats. 84

Figure 4-2. SEM images of randomly distributed electrospun fibre mats at A) 0 wt% CNC, B) 1 wt% CNC, C) 2.5 wt% CNC, and D) 5 wt% CNC. The inset images are average shifted histogram (ASH) plots for each sample. 86
Figure 4-3. Close-up SEM images of the spider-web structures for the 5% CNC randomly distributed fibre mats (A) and aligned fibre mats (B). 87
Figure 4-4. SEM images of aligned electrospun fibre mats at A) 0 wt% CNC, B) 1 wt% CNC, C) 2.5 wt% CNC, and D) 5 wt% CNC. The white arrows indicate drum rotation direction, and the inset images are average shifted histogram (ASH) plots for each sample. 88
Figure 4-5. TEM images of neat Nylon 6 along the fibre axis (A) and of the cross section (C), and of 5 wt% CNC along the fibre axis (B) and of the cross section (D). The red circles indicate a cross-section of a fibre, and the white arrows point to CNCs. 89
Figure 4-6. Mechanical results comparing randomly distributed (blue) and aligned (pink) fibre mats at increasing CNC loadings (0, 1, 2.5, and 5 wt%): A) Elastic Modulus, B) Tensile Strength, and C) Strain at Break. 91
Figure 4-7. FTIR analysis of aligned CNC-Nylon 6 electrospun mats at 0 wt% CNC (blue), 1 wt% CNC (green), 2.5 wt% CNC (purple), and 5 wt% CNC (red). 94
Figure 4-8. DSC analysis of aligned CNC-Nylon 6 electrospun mats at 0 wt% CNC (blue), 1 wt% CNC (green), 2.5 wt% CNC (purple), and 5 wt% CNC (red). 97
Figure 4-9. XRD patterns for the aligned CNC-Nylon 6 electrospun mats at 0 wt% (blue), 1 wt% (green), 2.5 wt% (purple), and 5 wt% (red) CNC. The theoretical peak positions for the α and γ allomorphs are denoted with the vertical dotted lines. 99
Figure 4-10. TGA (A) and DTG (B) analysis of aligned CNC-Nylon 6 electrospun mats at 0 wt% CNC (blue), 1 wt% CNC (green), 2.5 wt% CNC (purple), and 5 wt% CNC (red). The black arrows denote the trend with increasing CNC loading. 101
Figure 5-1. Proposed monolayer and multilayer bonding of diazonium molecules on a surface. 110
Figure 5-2. Structures of diazonium cations used for surface modification of CNC. From left to right: 4-nitrobenzenediazonium, 4-aminobenzyldiazonium, and p-aminobenzenediazonium. .. 111
Figure 5-3. Summarized reaction scheme for the synthesis of diazonium salts. HBF_4 is used for the *ex-situ* method and HCl is used for the *in-situ* method. R = NO_2, NH_2, or CH_2NH_2. 116
Figure 5-4. Contact angle measurements and photographs of CNCs. (A) Photographs of unmodified CNC dried powder and (B) unmodified CNC spin coated film, (C) contact angle measurement of unmodified CNC spin coated film, (D) photographs of 4-dNB+CNC freeze dried material and (E) 4-dNB+CNC spin coated film, and (F) contact angle measurement of 4-dNB+CNC spin coated film. 117
Figure 5-5. FTIR spectra of 4-nitrobenzenediazonium tetrafluoroborate (4-dNB), cellulose nanocrystals (CNC), and the material resulting from the reaction of 4-dNB and CNC (4-dNB+CNC). 118
Figure 5-6. HR-XPS spectra in the N1s region for cellulose nanocrystals (CNC) and the material resulting from the reaction of 4-dNB and CNC (4-dNB+CNC). 119

Figure 5-7. XRD analysis of cellulose nanocrystals (CNC) and the material resulting from the reaction of 4-dNB and CNC (4-dNB+CNC). 121
Figure 5-8. Thermogravimetric analysis (TGA) and the first derivative thermograms (DTG) of CNC (blue) and 4-dNB+CNC (red). The Weight Loss (%) axis on the left is for the TGA spectra (solid lines) and the dW/dT axis on the left is for the DTG spectra (dashed lines). 122
Figure 5-9. FTIR spectra of 4-dABA+CNC and CNC. (A) FTIR spectra of cellulose nanocrystals (CNC) and the materials resulting from the reaction of 4-dABA and CNC (4-dABA+CNC), and (B) enlarged FTIR spectra of CNC and 4-dABA+CNC in the 2400-800 cm^{-1} region. The absorbance intensity of the 4-dABA+CNC spectrum in (B) is increased by a factor of 4 to better show the peaks. 124
Figure 5-10. FTIR spectra of p-dAB+CNC and CNC. (A) FTIR spectra of cellulose nanocrystals (CNC) and the materials resulting from the reaction of p-dAB and CNC (p-dAB+CNC), and (B) Enlarged FTIR spectra of CNC and p-dAB+CNC in the 2500-600 cm^{-1} region. 125
Figure 5-11. Proposed mechanism for the formation of aryl radicals from diazonium cations (A) and the attachment of the aryl molecules onto CNC (B). 126
Figure 5-12. Elastic modulus results for the diazonium modified CNC and Nylon 6 thin films at CNC loadings of 0, 0.5, 1, and 2 wt%**.** The blue line is unmodified CNC, the red line is 4-dNB+CNC, the green line is 4-dABA+CNC, and the purple line is p-dAB+CNC. 127
Figure 6-1. A) In-situ diazotization of 2,6-dimethylaniline and subsequent radical formation of 3-bromopropylamine and B) proposed mechanism for the surface modification of CNC with the propylamine radical. 140
Figure 6-2. Photographs of (left) water, 5 wt% CNC and 5 wt% PA-CNC dispersed in water, and (right) the same solutions after they were left to stand for 7 hours. 141
Figure 6-3. TEM images of A) unmodified CNC and B) PA-CNC. The inset photographs are of the dried powders corresponding to each CNC sample. 142
Figure 6-4. FT-IR spectra of unmodified CNC and PA-CNC. The blue line is unmodified CNC and the orange line is PA-CNC. 142
Figure 6-5. HR-XPS of A) the C1s region for unmodified CNC, B) the C1s region for PA-CNC, and C) the N1s region for PA-CNC. 145
Figure 6-6. XPS survey spectra of CNC and PA-CNC. The blue line is unmodified CNC and the orange line is PA-CNC. 147
Figure 6-7. A) TGA and B) DTG thermograms of CNC and PA-CNC. 148
Figure 6-8. Elastic moduli for the CNC or PA-CNC and Nylon 6 composite films. The blue line is for unmodified CNC and the orange line is for PA-CNC. 150
Figure 7-1. Photographs depicting the yarn spinning of Nylon 6 solutions: A) yarn spinning setup with the two syringe pumps, cone collector, and drum collector, B) side-view of cone collector and motor powering the rotation of the cone, and C) collection of the polyer yarn onto the rotating drum collector. 159
Figure 7-2. SEM images of electrospun Nylene yarns. 160

List of Symbols

α	Alpha
Iα	Alpha allomorph of cellulose I
ω	Angular velocity
U	Applied voltage
β	Beta
Iβ	Beta allomorph of cellulose I
$1 \longrightarrow 4$	Carbon 1 to carbon 4 bonding
cm	Centimeter
V_c	Critical voltage
I	Current
$^\circ$	Degree
$^\circ$C	Degree Celsius
$^\circ$C/min	Degree Celsius per minute
χ_c	Degree of crystallinity
ρ	Density
d	Diameter
ε	Dielectric constant
d	Distance
E	Electric field strength
eV	Electron volt
ε	Engineering strain
σ	Engineering stress
h	Film thickness
Q	Flow rate
γ	Gamma
GPa	Gigapascal
g	Gram
g/mL	Gram per milliliter
ΔH_f	Heat of fusion

ΔH_f^{100}	Heat of fusion of the fully crystalline polymer
hr	Hour
in	Inch
A_0	Initial cross-sectional area
L_0	Initial length
η_0	Initial solution viscosity
cm^{-1}	Inverse centimeter
J/g	Joule per gram
kV	Kilovolt
μ	Kinematic viscosity
l or L	Length of sample
P	Load
m	Mass
∅	Mass fraction
L	Measured length
MΩ•cm	Megaohm centimeter
MPa	Megapascal
μL/min	Microliter per minute
μm	Micron or micrometer
mg	Milligram
mg/mL	Milligram per milliliter
mL	Milliliter
mm	Millimeter
mm/mm•min	Millimeter per millimeter minute
mM	Millimole per liter
min	Minute
M	Mole per liter
nm	Nanometer
H or z	Needle-to-collector distance
N	Newton
n	Number of measurements or samples
Ω	Ohm

%	Percent
1˚	Primary
h	Radius of the jet
R	Radius of the needle
s	Second(s)
2˚	Secondary
χ	Slope of the jet's surface
γ	Surface tension
θ	Theta
U	Voltage
V	Volume fraction
W	Watt

List of Abbreviations

TEMPO	2,2,6,6-Tetramethylpiperidine-1-oxyl
2,6-dDM	2,6-Dimethyldiazonium
4-ABA	4-Aminobenzylamine
4-dABA	4-Aminobenzyldiazonium
4-dABA+CNC	4-Aminobenzyldiazonium modified cellulose nanocrystals
4-dNB	4-Nitrobenzenediazonium
4-dNB+CNC	4-Nitrobenzenediazonium modified cellulose nanocrystals
ACN	Acetonitrile
ABS	Acrylonitrile butadiene styrene
ALPAC	Alberta-Pacific Forest Industries Inc.
ACS	American Chemical Society
$-NH_2$	Amine
APS	Aminopropyltriethoxysilane
AGU(s)	Anhydroglucose unit(s)
AFM	Atomic force microscopy
ASH	Average shifted histogram
C	Carbon
C1-6 or C_{1-6}	Carbon 1 to 6 of cellulose
CF	Carbon fibre
CHNS	Carbon, Hydrogen, Nitrogen, Sulfur Combustion
$-COO^-$	Carboxyl
CTBN	Carboxyl-terminated butadiene-acrylonitrile
CL	Cell lumen
CNC(s)	Cellulose nanocrystal(s)
CNF(s)	Cellulose nanofibre(s)
CNM(s)	Cellulose nanomaterial(s)
CTAB	Cetyltrimethylammonium bromide
CML	Compound middle lamella
CPS	Count per second

DSS	Degree of substitution
DI	Deionized
dW/dT	Derivative weight to derivative temperature
DSC	Differential scanning calorimetry
CA_c	Effective cross-sectional area
EM or YM	Elastic or Young's modulus
EHT	Electron high tension
DTG	First derivative of the thermogram
T_P	First derivative peak temperature
FTIR	Fourier transform infrared spectroscopy
GF	Glass fibre
HDPE	High density polyethylene
HR-XPS	High resolution x-ray photoelectron spectroscopy
HCl	Hydrochloric acid
H	Hydrogen
IR	Infrared
ID	Inner diameter
MCC	Microcrystalline cellulose
ML	Middle lamella
M-CNC	Modified cellulose nanocrystals
MW	Molecular weight
NP	Neat polymer
N	Nitrogen
N/C	Nitrogen to carbon ratio
NCH	Nylon clay hybrid
T_o	Onset temperature
O	Oxygen
O/C	Oxygen to carbon ratio
p-dAB	p-Aminobenzenediazonium
p-dAB+CNC	p-Aminobenzenediazonium modified cellulose nanocrystals
p-PD	p-Phenylenediamine
EAA	Poly(ethylene-co-acrylic acid) copolymer

PA11	Polyamide 11
PA6 or N6	Polyamide 6 or Nylon 6
PE	Polyethylene
PEG	Polyethylene glycol
PEO	Polyethylene oxide
PGMA	Polyglycidyl methacrylate
PLA	Polylactic acid
PMMA	Polymethyl methacrylate
PP	Polypropylene
PU	Polyurethane
PVA	Polyvinyl alcohol
KBr	Potassium bromide
KOH	Potassium hydroxide
P	Primary wall
PA	Propylamine
PA-CNC	Propylamine modified cellulose nanocrystals
RH	Relative humidity
rpm	Rotations per minute
SEM	Secondary electron microscopy
S1, 2, or 3	Secondary wall 1, 2, or 3
Na	Sodium
NaBr	Sodium bromide
NaOH	Sodium hydroxide
NaHClO	Sodium hypochlorite
$NaNO_2$	Sodium nitrite
$-OSO_3^-$	Sulfate half ester
S	Sulfur
H_2SO_4	Sulfuric acid
T	Temperature
HBF_4	Tetrafluoroboric Acid
TGA	Thermogravimetric analysis
3D	Three dimensional

TEM	Transmission electron microscopy
2D	Two dimensional
UTS or TS	Ultimate tensile strength or tensile strength
UM-CNC	Unmodified cellulose nanocrystals
v/v% or V	Volume per volume percent
wt/v%	Weight per volume percent
wt% or wt/wt%	Weight per weight percent
XRD	X-ray diffraction
XPS	X-ray photoelectron spectroscopy

Chapter 1. Introduction

1.1 Research Scope & Objectives

Alberta has become a leader in cellulose nanomaterial (CNM) production, specifically, of cellulose nanocrystals (CNC). The construction of a CNC pilot plant in Edmonton by Alberta-Pacific Forest Industries Inc. (ALPAC) and Innotech Alberta in late 2013 has encouraged CNC research across Alberta and Canada. The interest in cellulose as a feedstock for advanced functional materials stems from the sustainability and properties of the material itself. Cellulose is a natural product found in plant materials, and the majority of the material is extracted from wood by-products from the forestry industry. The crystalline regions of cellulose are then extracted to obtain CNC. CNC exhibits high specific strength and modulus for a high aspect ratio material that is crystalline and lightweight. The reactive surface also provides routes for modification and further functionality, as well as increased compatibilization in a variety of different matrices. A specific interest in CNC as fillers in polymers stems from the large reinforcing impact observed at low loadings.

This thesis explores the reinforcing capability of CNC in one of the most commonly used polymers in the world, Nylon 6 (or Polyamide 6), and reports the surface modification of CNC using diazonium chemistry as a route for increased compatibilization in organic matrices. Spin coating was used to produce freestanding thin films of Nylon 6 containing CNC. The films were used to initially investigate the reinforcing impact and effects of CNC on polymer crystallization. Solution electrospinning was then used to produce CNC-Nylon 6 nanofibres, and the reinforcing impact of CNC in both randomly distributed and aligned fibre mats is discussed. Finally, CNC was surface modified with diazonium salts using ex-situ and in-situ diazotization methods. The

diversion of the radical diazonium salt was also exploited for the surface modification of CNC with a short chain alkylamine. A quick study into the reinforcing impact of the modified CNCs in Nylon 6 is also described.

The experimental research objectives of this thesis include: 1) the fabrication of CNC-Nylon 6 freestanding thin films, 2) the influence of processing parameters on aligned Nylon 6 electrospun fibres using a rotating drum collector, 3) the effect of CNC on the morphology and crystallization of aligned Nylon 6 electrospun fibre mats, 4) the production of surface modified CNC with diazonium salts, and 5) the surface modification of CNC with an alkylamine using radical diazonium chemistry.

This Chapter introduces relevant topics that are crucial to understanding the structure and reinforcing capabilities of CNC, including an evaluation of various surface modifications used on CNC for the mechanical reinforcement of polymer matrices. An introduction to different polymer processing techniques used for CNC composites is also presented. Finally, Nylon 6 properties and composites are discussed.

1.2 Cellulose Nanocrystals

1.2.1 The Structure of Cellulose Nanocrystals

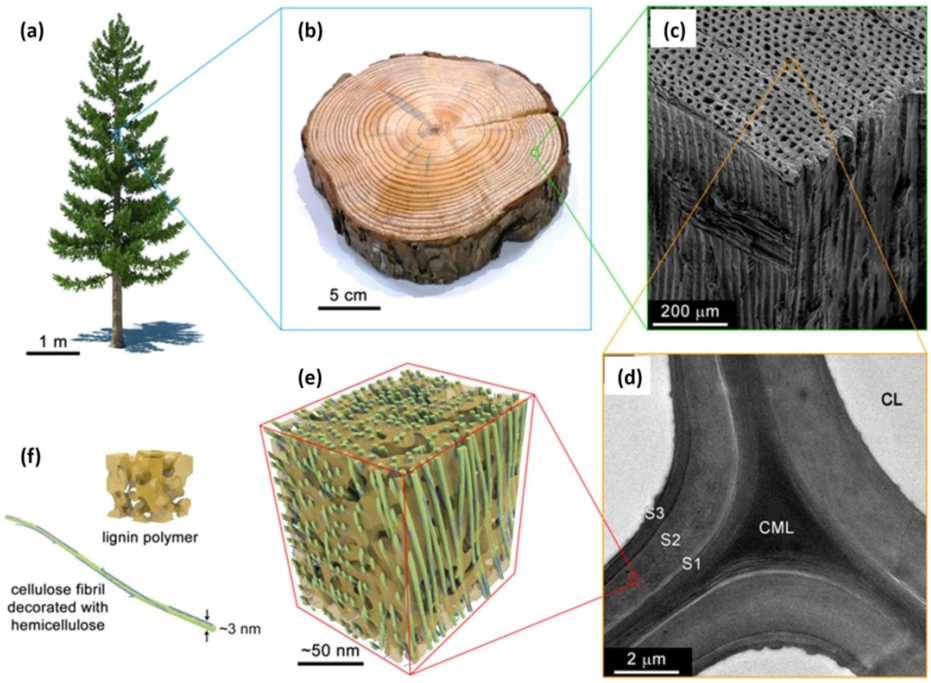

Figure 1-1. The hierarchal structure of cellulose from a tree: a) a pine tree, b) a cross-section of the tree trunk, c) SEM image of the tissue structure, d) TEM image of the layered cell wall, e) illustration of the lignocellulosic region, and f) illustration of extracted lignin and cellulose fibrils coated with hemicellulose. Reprinted with permission from Zhu, H.; Luo, W.; Ciesielski, P. N.; Fang, Z.; Zhu, J. Y.; Henriksson, G.; Himmel, M. E.; Hu, L., Wood-Derived Materials for Green Electronics, Biological Devices, and Energy Applications. *Chemical Reviews* 2016, 116 (16), 9305-9374. Copyright 2022 American Chemical Society.

Cellulose nanomaterials (CNM) are predominately derived from the naturally occurring cellulosic regions in the cell walls of wood plants.[1, 2] A closer look into the hierarchal structure of cellulose starting from a tree is illustrated in Figure 1-1.[3] The cell wall structure in Figure 1-1d shows a layered wall surrounded by the cell lumen (CL) – an empty air-filled space – that gives the cell walls an inherent mesoporosity.[4] The darker central region depicts the compound middle lamella (CML), which is deemed the primary cell wall. Between the CML and the CL is the secondary wall, which is comprised of three layers (S1, S2, and S3). The secondary cell wall is made up of three biopolymers: cellulose, hemicellulose, and lignin. Lignin is an amorphous

phenolic polymer that is hydrophobic, which acts to protect the rest of the polysaccharides in the cell wall (cellulose and hemicelluloses) from microbial decay.[5] Hemicellulose acts a bio-"glue" that binds the cellulose fibrils to each other and to lignin.[3] The hemicellulose decorated cellulose fibrils are called elementary fibrils (Fig. 1-1f), and the packing of these elementary fibrils form a larger microfibril.

The three secondary layers are labelled as the S1 outer layer, S2 middle layer, and S3 inner layer.[6] The S1 layer is a thin lignin-rich layer that protects the inner secondary walls.[4] The S2 layer is the region with the highest cellulose content, where cellulose is tightly packed into elementary fibrils that are bound together by lignin and hemicelluloses (Fig. 1-1e).[6, 7] This layer contains the rigid crystalline cellulose fibrils that provide structural support for the plant.[4, 8] Finally, the S3 layer has the lowest amount of lignin to allow for water to move up the plant.[4]

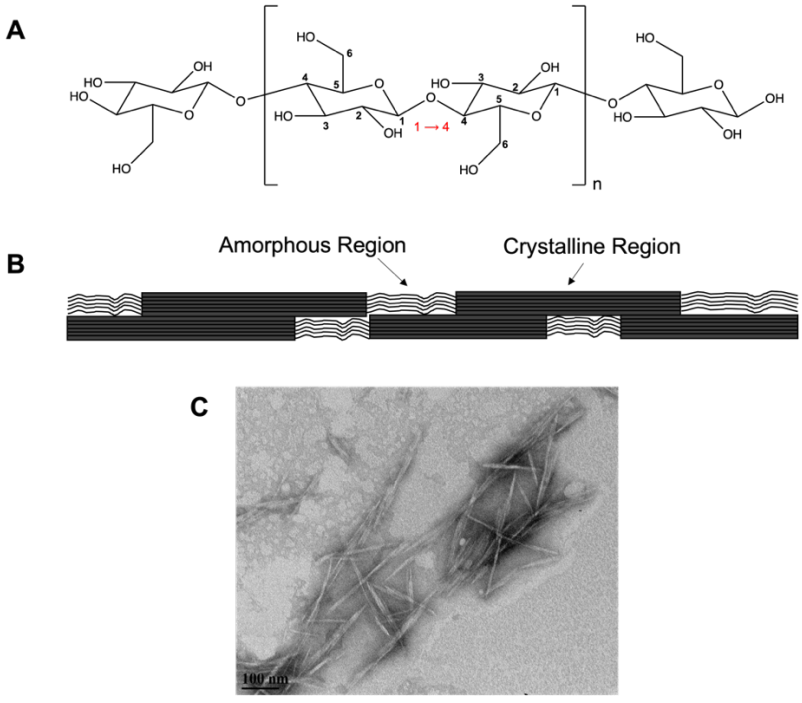

Figure 1-2. A) The chemical structure of cellulose with each carbon number labelled, B) the arrangement of amorphous and crystalline regions in untreated cellulose, and C) TEM image of CNCs.

Cellulose, which is predominantly found in the S2 layer, is comprised of repeat anhydroglucose units (AGUs) (Fig. 1-2A). In wood-derived celluloses, a single cellulose chain has around 15,000 AGUs.[9] The cellulose chains arrange as a mix of two phases: crystalline (highly ordered) and amorphous (disordered) regions (Fig. 1-2B).[10] Extracted fibrils that contain both the crystalline and amorphous regions are called cellulose nanofibres (CNFs), but it is the crystalline regions that are further extracted to obtain CNC.[6] The individual AGUs within cellulose are joined by β 1,4-glycosidic bonds, meaning that each unit is joined to adjacent units at Carbons 1 and 4, as shown in Figure 1-2A.[10] In CNC, this type of $1 \longrightarrow 4$ bonding creates a chain that has the carbon 6 methoxy group alternating between the "faces" of the chain. Since cellulose has this directionality between the chains, the packing of chains is known to have two configurations: parallel or anti-parallel.[10] In the parallel configuration, the $1 \longrightarrow 4$ glycosidic bonds of all cellulose chains are pointing in the same direction. In the antiparallel configuration, the $1 \longrightarrow 4$ glycosidic bonds are pointing in the opposite direction between chains. For CNC, the packing of the chains are in the parallel configuration.[10]

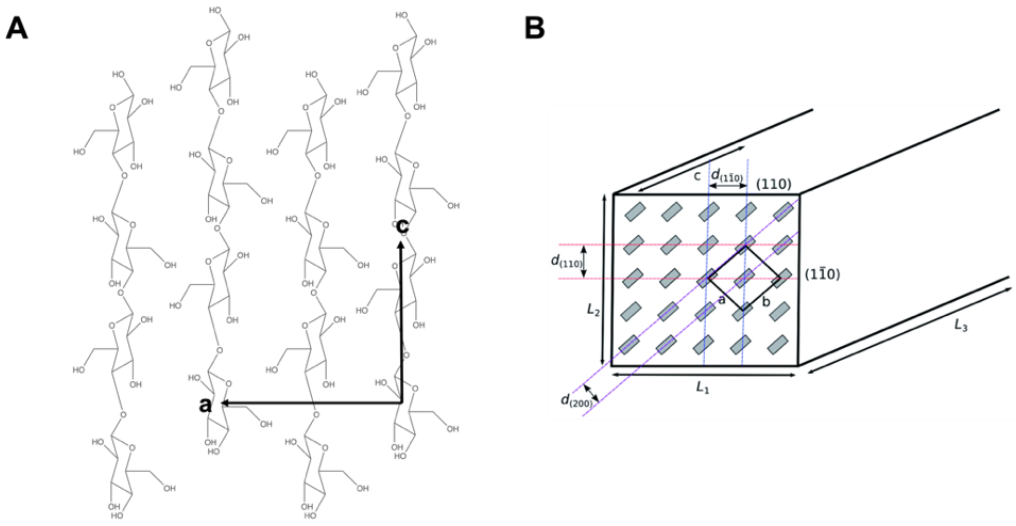

Figure 1-3. A) The packing of the Iβ polymorph of cellulose with black arrows showing the unit cell *a* and *c* edges and B) a cross-section of a CNC depicting the unit cell and lattice planes. Fig. 1-3B is adapted from S. Eyley and W. Thielemans, *Nanoscale*, 2014, 6, 7764 DOI: 10.1039/C4NR01756K with permission from the Royal Society of Chemistry, used under CC BY 3.0.

Due to the variations in cellulose chain packing, cellulose can arrange in four different polymorphs (I, II, III, and IV).[6, 11] Cellulose I is the native form, whereas Celluloses II, III, and IV are formed as a result of chemical or thermal treatments.[12] CNC is predominately comprised of the I polymorph of cellulose, which is further separated into two allomorphs: the Iα and Iβ allomorphs.[10, 13] It is the Iβ allomorph that is dominant in CNCs.[10] In this allomorph, the cellulose chains are in the parallel configuration and stack in such a way where the chains alternate in offset from each other, as pictured in Figure 1-3A.[10] This interchain packing creates a square unit cell with lattice planes of (200), (100), and $(1\bar{1}0)$,[10, 14] as shown in Figure 1-3B. Stacking also affects interchain hydrogen bonding, where the C_6-OH methoxy groups hydrogen bond with either the C_3-OH and or C_2-OH hydroxyl groups of adjacent chains (Fig. 1-2A).[10] The cross-section of this plane is also called the "hydrogen bonding plane",[10] which is visualized as the b-edge of the unit cell in Figure 1-3B or as the plane out of the page in Figure 1-3A.[14] It is suggested that the stiffness of CNC is due to the strong hydrogen bonding within this plane.[13]

1.2.2 Production of Cellulose Nanocrystals

Figure 1-4. General procedure for the production of CNC.

Since the majority of cellulose is found in the thin S2 layers of the plant cell walls, cellulose only accounts for 30-40% of the total wood content.[15] Therefore, the process of extraction in order to separate and obtain the purely crystalline form of cellulose from the rest of the cell wall components requires a large input of both mechanical and chemical energy. Foundational work on the extraction of crystalline cellulose using strong acids was performed by Nickerson and Habrle in 1947.[16] Nowadays, the process has been highly optimized for the large scale production of CNC.

A schematic outlining the general processing steps for obtaining CNC is presented in Figure 1-4.[1, 9] Natural wood fibres undergo two main chemical steps before CNC is extracted: 1) alkali and bleach pre-treatment and 2) acid hydrolysis.[1] The goal of the alkali and bleach pre-treatment is to remove all of the non-cellulosic materials, such as lignin, hemicelluloses, and pectin.[1] In a typical extraction, an alkali solution containing a strong base (typically, NaOH or KOH) is used first to solubilize the pectin and hemicelluloses from the wood fibres.[1] Then, a sodium hypochlorite and sodium acetate solution is used to breakdown the aromatic lignin as well as bleach the material.[1]

Once the contaminants are removed, long chains of cellulose containing both the amorphous and crystalline regions remain (Fig. 1-2B). In order to isolate the crystalline regions, a strong acid treatment in typically either sulfuric acid (H_2SO_4) or hydrochloric acid (HCl) is used to remove the amorphous cellulose regions.[1] In contrast to the crystalline regions, the amorphous

regions are loosely packed together. This allows for swelling of these regions in-solution and easy penetration of the acid that cleaves the cellulose β 1,4-glycosidic bonds.[1] In terms of processing parameters, the acid concentration, acid type, and hydrolysis time all affect the size of CNC;[1, 13, 17] however, the source of the plant material ultimately dictates the size.[1, 18] Hydrolysis at the ends of the cellulose chains cause tapering at the crystal tips forming a toothpick or whisker-like structure (Fig. 1-2C).[1, 19] The hydrolysis reaction is stopped by quenching with a base, such as NaOH.[17] Finally, the CNC is centrifuged down, dialyzed, filtered, and dried by either freeze-drying or spray-drying to obtain an off-white powder.[1, 17] In the end, CNCs are produced with lengths that range from 5-350 nm and widths ranging from 5-20 nm (aspect ratios of 5-30).[19]

The surface functionality of CNC depends on the type of acid used during hydrolysis. In the most commonly used sulfuric acid treatment, the hydroxyl groups on CNC are simultaneously esterified during hydrolysis to form negatively charged sulfate half ester ($-OSO_3^-$) groups that have a sodium counterion (Na^+) as a result of the quenching reaction.[20] In the HCl treatment, the hydroxyl groups are not affected thereby leaving them as uncharged -OH groups after quenching.[20] The stability of CNC in aqueous suspensions and the energy input to homogeneously disperse the particles in-solution is greatly affected by the surface charge. The sulfated CNCs impart good colloidal stability due to the electrostatic repulsion of the $-OSO_3^-$ functionalities on the surface between particles,[19] but the HCl treated CNCs require further oxidation of the hydroxyl groups in order to obtain good colloidal stability.[20] Typically, oxidization with a TEMPO (2,2,6,6-tetramethylpiperidine-1-oxyl) radical is done to obtain carboxylated ($-COO^-$) CNCs that exhibit better dispersion for HCl-treated CNC.[21]

1.3 Cellulose Nanocrystals as Polymer Additives

1.3.1 Surface Modification of Cellulose Nanocrystals

Surface modification of CNC opens the door to further functionalities, properties, and better dispersion in complex matrices. There are two main methods used for the modification of CNC: covalent bonding and adsorption. Additionally, as mentioned in the previous section, TEMPO oxidation and sulfonation of CNC can also be considered forms of covalent modification. An important consideration when surface modifying CNC is that only about 2% of the hydroxyl groups in a single CNC particle are accessible for modification due to the laminar stacking of the cellulose chains.[22] Of note, the C6 primary hydroxyl group is suggested to be the most reactive on CNCs; however, the sulfonation of CNCs during extraction may reduce the number of possible reactive hydroxyl sites.[22] Although there is a multitude of surface modifications used on CNC, modifications intended for the incorporation into polymer matrices will be the focus in this section.

The most common modification on CNC involves the covalent attachment of molecules to the CNC surface. For use in polymer matrices, CNC is typically modified with hydrophobic molecules with the goal of increased compatibilization with hydrophobic polymers and their solvents.[23] Grafting of polymers or long chain alkanes onto CNC is a common method for the incorporation into polymer matrices. This type of modification can be further separated into grafting *from* (or bottom-up) and grafting *to* (or top-down) approaches.[22] In the grafting *to* approach, a polymer chain and a coupling agent is mixed with CNC to allow coupling of the polymer onto the surface.[22] In the grafting *from* approach, a monomer and initiator is mixed with CNC to allow the building of a polymer chain from the surface.[22]

The type of grafted molecule can either be the same polymer as the target matrix, or a different polymer with similar hydrophobicity or has the possibility for increased interfacial

interactions with the target matrix. For example, Le Gars *et al.* incorporated poly(glycidyl methacrylate) (PGMA) modified CNC into hot pressed polylactic acid (PLA) films and found that the modified CNCs improved dispersion compared to unmodified CNC due to better adhesion between modified CNC and PLA.[24] In another study by Ogunsona *et al.*, modified CNC with carboxyl-terminated butadiene-acrylonitrile rubber (CTBN) were found to increase the tensile strength of PLA films by 25% compared to unmodified CNC.[25] An interesting study by Wohlhauser *et al.*, showed enhanced dispersion of modified CNC within a CNC-only film.[26] The authors produced "hairy CNC" by surface modifying CNC with poly(methyl methacrylate) (PMMA). The PMMA modified CNC was then solvent cast into films where the long PMMA chains acted as long chain groups that allowed for better dispersion of CNC within the film based on sterics and polymer chain entanglement.

The other general type of modification used on CNC involves non-covalent interactions of molecules at the surface. This type of modification relies on interactions such as hydrogen bonding, electrostatics, or van der Waals forces.[23] Typically, long chain alkanes with an ionized end group (also considered surfactants) are used to electrostatically interact with the ionized sulfonate or TEMPO oxidized carboxyl groups on CNC. The hydrophilic ionic end adsorbs to the CNC surface whereas the hydrophobic alkane end interacts with the non-polar solvent or polymer.[22] A common surfactant used for modification of CNC is cetyltrimethylammonium bromide (CTAB).[27] CTAB modified CNCs have been used in polypropylene (PP), PLA, and epoxy matrices for enhanced mechanical and corrosion properties.[28-30] The alkane backbone of CTAB utilizes the same compatibilization mechanism as polymer grafting, where the hydrophobization of CNC increases favourable interactions and dispersion within a hydrophobic polymer matrix.[30]

Additionally, the coating of molecules *via* adsorption onto the CNC surface has also been utilized.[22, 23, 31]

The addition of CNC for the mechanical reinforcement of polymers is the focus of this thesis. Thus, a few covalent and non-covalent modifications of CNC used in polymer composites are listed in Table 1-1. The table also compares the respective increase in elastic modulus compared to the neat polymer at the optimal CNC loading and compares this to the same wt% of unmodified CNC observed in each study. An increase in elastic modulus (EM) was observed for all modified CNC-polymer composites (M-CNC) compared to the neat polymer (NP). However, some modifications caused a decrease the EM when compared to unmodified CNC (UM-CNC), suggesting that the modification negatively influenced polymer-CNC interactions.

Table 1-1. Examples of modifications of CNC (M-CNC) in polymer composites with respective percent increase in elastic modulus (EM) results compared to the neat polymer (NP) and unmodified CNC (UM-CNC) at the optimal modified CNC loading.

Polymer	Modification on CNC	Composite Manufacturing	Optimal M-CNC (wt/wt%)	% Increase in EM from NP	% Increase in EM from UM-CNC	Ref
Acrylonitrile butadiene styrene (ABS)	Ring-opening polymerization of ε-caprolactone	Compression molding	0.5	4	-	[32]
Poly(ethylene-co-acrylic acid) copolymer (EAA)	*N,N*-diallyl-3-hydroxyazetidinium	Compression molding	10	168	(-6)	[33]
Polyamide 6 (PA6)	Aminopropyltri-ethoxysilane	Injection molding of masterbatch	3	49	6	[34]
Polyamide 11 (PA11)	Dodecanoic acid	Solvent casting then compression molding	3	40	21	[35]
Polyethylene (PE)	2-ureido-4[1H]pyrimidi-none	Solvent casting	15	137	-	[36]
Polylactic acid (PLA)	Carboxyl-terminated butadiene-acrylonitrile rubber (CTBN)	Solvent casting	1	48	0	[25]
	Cetyltrimethylammonium bromide (CTAB)	Solvent casting then extrusion	1	9	12	[29]
Polypropylene (PE)	Hexadecyl trimethylammonium bromide	Extrusion	3	28	(-28)	[37]
Polystyrene (PS)	Trifluoromethyl diazonium	Electrospinning	2	13	-	[38]
Polyurethane (PU)	(2-Dodecen-1-yl) succinic anhydride	Solvent casting	16	1888	-	[39]
	2-ureido-4[1H]pyrimidi-none	Solvent casting	75	67	(-14)	[40]
Polyvinyl alcohol (PVA)	TEMPO using polyacrylic acid as a crosslinker	Solvent casting	10	80	-	[41]

1.3.2 The Reinforcing Mechanism of Unmodified Cellulose Nanocrystals in Polymers

The interest in CNC as an additive in polymer manufacturing stems from the high modulus resulting from the stiffness of the crystalline material.[42] The stiffness of an individual CNC is directly related to the packing of the cellulose chains as described in Section 1.2.1.[13] As a result, the tensile strength along the length of a single CNC is around 7.5-7.7 GPa with an elastic modulus of around 120-143 GPa.[43, 44] Alternate properties, and an increase in the mechanical strength of a composite, can also be achieved by modifying CNC as described previously.

The advantage of using CNC to mechanically reinforce a polymer is attributed to a combination of percolation of CNC within the polymer matrix and strong CNC-polymer interfacial interactions.[10, 42, 45, 46] In the case of CNC composites, percolation describes a pathway of reinforcement related to the number of contact points between adjacent particles within a matrix, and is quantified using the aspect ratio of the CNC.[45, 46] Specifically, the strong hydrogen bonding between CNC particles within a matrix *without aggregating* is said to increase the rigidity, and thus stiffness, of the composite.[45] Therefore, polymer-CNC interface interactions, CNC interparticle interactions (and thus, aggregation and dispersion), particle orientation, and particle aspect ratio all influence the percolation of CNC.[45, 47]

There have been numerous reviews and reports describing the effects of percolation and dispersion of CNC in complex matrices.[42, 48-51] For example, in a report by Cao *et al.*, the authors compared CNC directly mixed with cement paste to CNC ultrasonicated prior to addition to the cement.[52] They found that the enhanced dispersion of CNC increased the strength of the cement samples. Above the percolation threshold, or the minimum volume of filler required for percolation, CNC aggregated leading to a decrease in the mechanical strength of the composite. Indeed, the dispersion of CNC remains an influential factor in composite processing.

1.3.3 Cellulose Nanocrystal Composite Processing Techniques

The processing of CNC-polymer composites can be broadly separated into two categories: melt-mixing and solvent dissolution. The technique chosen depends on the polymer properties and application of the composite. However, the compatibility of a polymer with either modified or unmodified CNC also dictates the processing technique used, especially when taking into consideration the surface energy of CNC and the polymer.

Melt-mixing is a solvent-free method for producing polymer composites, such as with extrusion or injection molding. In both cases, solid pellets of the polymer of choice are melted at high temperatures then dried CNC is added.[42] This compounding can be done prior to adding to the machine or done directly in the machine using a combination of melt and shear mixing,[42] such as with the twin screws often used inside extruders. The composite is then forced through a die or injected into a mold with dimensions specific to the final product desired.

A common problem faced when melt mixing CNC in a polymer is the degradation and burning of cellulose at the high processing temperatures required for high melting point polymers. For example, Peng *et al.* injection molded three types of CNMs (microcrystalline cellulose [MCC], CNF, and CNC) with Nylon 6.[53] At 10 wt%, all samples showed significant browning in colour due to burning of the CNMs at the 270˚C molding temperature.[53] Interestingly, all composites slightly increased in average elastic modulus and tensile strength despite the visual degradation observed. A decrease in impact strength was observed for all samples and was attributed to the poor dispersion quality of the CNMs in Nylon due to the innate incompatibility of the hydrophilic CNMs with the hydrophobic polymer matrix.[53]

Coating CNC with polymers by pre-mixing in-solution is utilized to overcome poor dispersion and aggregation of CNCs directly mixed with polymer melts. Inai *et al.* coated CNC

with polyethylene oxide (PEO) by dissolving both materials in water.[54] The dried PEO-coated CNCs were extruded with high density polyethylene (HDPE) and the filaments exhibited an elastic modulus that was significantly higher, at a max. loading of 1.5 wt%, than that for CNCs added directly to HDPE.[54] Nonetheless, the dispersion of CNC in a polymer by dispersing the nanocrystals prior to extrusion or molding is not viable for polymers that do have compatible solvents for dissolution or are dually incompatible with CNC. Therefore, surface modifications on CNC have been employed, as discussed in Section 1.3.1. However, percolation is no longer the dominating factor as interactions between modified CNC particles are inhibited by the surface groups.[46] Additionally, the orientation of the particles during melt mixing is not controlled thereby also reducing the percolation of CNC.[42]

At smaller scales, thin polymer films containing CNC are produced using solvent casting or spin coating. As the name suggests, solvent casting consists of dissolving a polymer in a solvent then depositing the solution onto a substrate where the solvent is left to evaporate. In spin coating, the process of evaporation is accelerated by spinning the substrate whilst also thinning the cast film.[55] The advantage of preparing thin films from solution is the ability to maintain the dispersion of CNC throughout film production compared to melt-mixing. Additionally, CNCs can orient radially due to the applied centripetal force during spin coating.[56] This orientation in films is also seen in solvent cast CNC-only films, where CNC exhibits long-range helical self-assembly called a chiral nematic phase.[57, 58] The alignment of CNC in thin films therefore lead to better interparticle interactions and thus an increase in the mechanical properties of the films.[58, 59] CNC composite films also have interesting applications in food packaging and membranes as they have exhibited increased vapor sorption,[60] increased barrier properties,[58] and even antimicrobial properties.[61]

1.3.4 Electrospun Nanofibres

Electrospinning is a processing technique to produce ultra-thin polymer fibres with diameters in the nanometer to micrometer range. There are two main types of electrospinning: solution or melt electrospinning. Solution electrospinning first dissolves a polymer in a solvent whereas melt electrospinning uses a polymer melt.[62] It is solution electrospinning that is the most common, and thus is the chosen method in this thesis.

In a typical solution electrospinning experiment, a polymer is dissolved in a solvent and loaded into a syringe with a blunt-end needle and placed in a syringe pump. A grounded metal substrate is placed some distance away from the needle and a power supply is used to apply a, typically, positive voltage to the needle. The polymer solution is electrostatically attracted to the collector and goes through a series of instabilities that causes whipping of the polymer jet. This causes fibres with random orientations to be deposited onto the collector; however, different types of collectors can be used depending on the desired final properties of the fibre mat. For example, a stationary collector can be used for randomly distributed fibres whilst a rotating drum collector can be used for aligning fibres.[62]

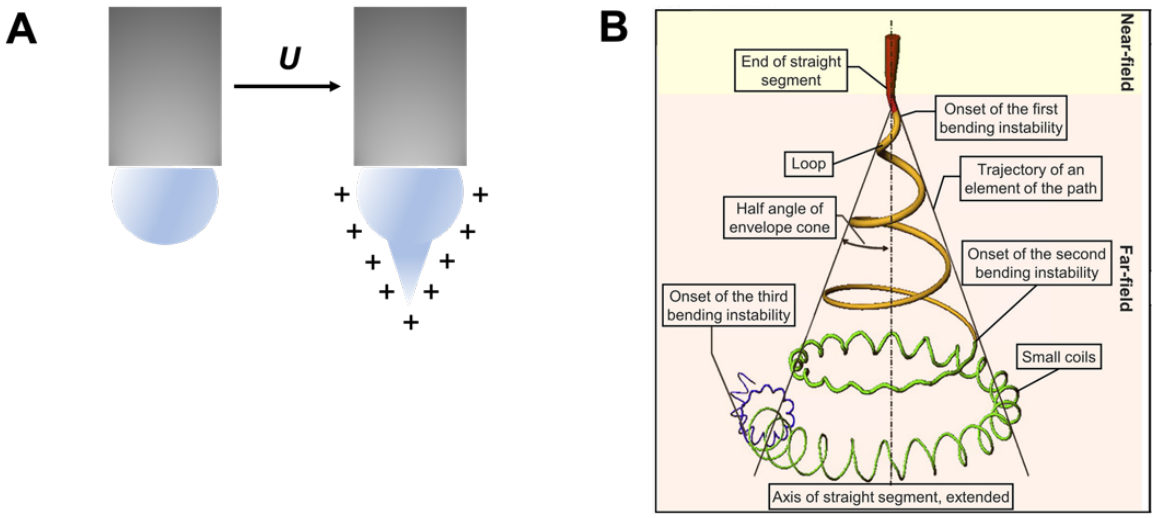

Figure 1-5. Visualization of the Taylor cone and bending instabilities of a polymer jet during electrospinning: A) The formation of the Taylor cone at the needle tip after a voltage is applied (*U*) and B) the trajectory of the jet going through a series of instabilities. Figure 1-5b is adapted with permission from Xue, J.; Wu, T.; Dai, Y.; Xia, Y., Electrospinning and Electrospun Nanofibers: Methods, Materials, and Applications. *Chemical Reviews* 2019, 119 (8), 5298-5415. Copyright 2022 American Chemical Society.

The electrospinning process starts when the syringe pump forces the polymer solution to be extruded from the syringe, which causes a polymer drop to form at the tip of the needle, as shown in Figure 1-5A. The applied voltage causes a buildup of charge, or Coulombic forces, on the surface of the polymer drop which is attracted to a grounded collector.[63] The repulsion of charges on the polymer drop causes the drop to form a conical shape (Fig. 1-5A). This shape is called the "Taylor cone", which is named after Sir Geoffrey Taylor who described the mechanics behind the formation of the cone.[64] After the formation of the Taylor cone, a polymer jet is ejected and is drawn towards the collector where it goes through a straight path followed by a series of bending instabilities before depositing onto the collector (Fig. 1-5B).[63] These bending instabilities are a result of electrostatic repulsions between the surface charges on the jet as it is drawn towards the collector.[62] This forces the jet to become increasingly more coiled due to a combination of the lateral electric forces and repulsive forces between each segment of the jet, which causes it to bend at about 90˚ thereby forming a series of loops, as shown in Figure 1-5B.[62, 65, 66] The bending

instabilities, increased coiling, and stretching of the jet towards the collector reduces the diameter of the jet thus thinning the fibres.[65] It is also during these instabilities that the solvent starts to evaporate where, eventually, fibres with diameters in the nanometer range are deposited onto the collector.[63]

The small diameters of electrospun nanofibres combined with the ease of production makes electrospinning an attractive processing technique for a multitude of applications. Fibres containing CNCs have been shown to have applications in textiles,[67] filtration,[68] and wound healing.[69] There are many advantages of using solution electrospinning to produce CNC composites. As with thin films, the use of a solvent allows for pre-dispersion of CNC prior to the addition of the polymer – similarly, this also limits the range of polymers to ones that have compatible solvents.[70] Secondly, CNC has been found to align parallel to the fibre axis.[71-73] The alignment of CNC in electrospun fibres can be due to a few possible reasons: 1) the electrostatic and physical alignment of the individual polymer chains while going through the bending instabilities may physically align the CNC, 2) the applied voltage could align the CNC in-solution, and 3) shear forces caused by the ejection of the polymer solution from the needle could force the alignment of CNC in the ejection direction.[71, 73, 74] The alignment of CNC can also increase interactions favourable for percolation. Nonetheless, CNCs with greater orientation within the polymer fibre exhibit a greater reinforcing impact.[74, 75]

1.4 Reinforced Nylon 6 Composites

1.4.1 Nylon 6 Properties and Characteristics

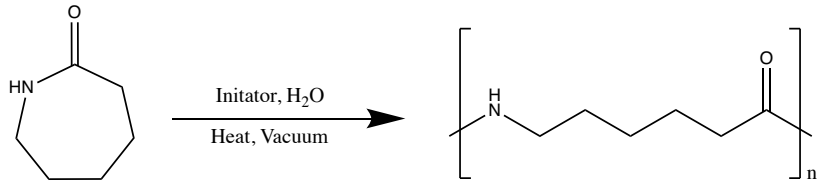

Figure 1-6. Summarized reaction for the synthesis of Nylon 6 from caprolactam.

Of the polyamides, Polyamide 6 is the most widely used due to its high tensile strength and chemical resistance.[76] The most common applications for Polyamide 6 include fibres for textiles and ropes, and molded plastics for automotive vehicles.[77-79] Polyamide 6, also called by its trade name Nylon 6 (N6), is formed by the water-initiated ring-opening polymerization (ROP) of caprolactam, as summarized in Figure 1-6.[78, 80] The final polymer has amide bonds separated by five carbons – the five-carbon separation plus the carbon that is part of the carbonyl is what gives Nylon *6* its name. The nitrogen end is terminated with an amine ($-NH_2$) and the carbonyl end is terminated as a carboxylic acid group (-COOH), giving it a linear formula of $H[HN-(CH_2)_5-CO]_nOH$.[78] Nylon 6 has a glass transition temperature of around 45˚C and a melting temperature of around 220˚C.[77]

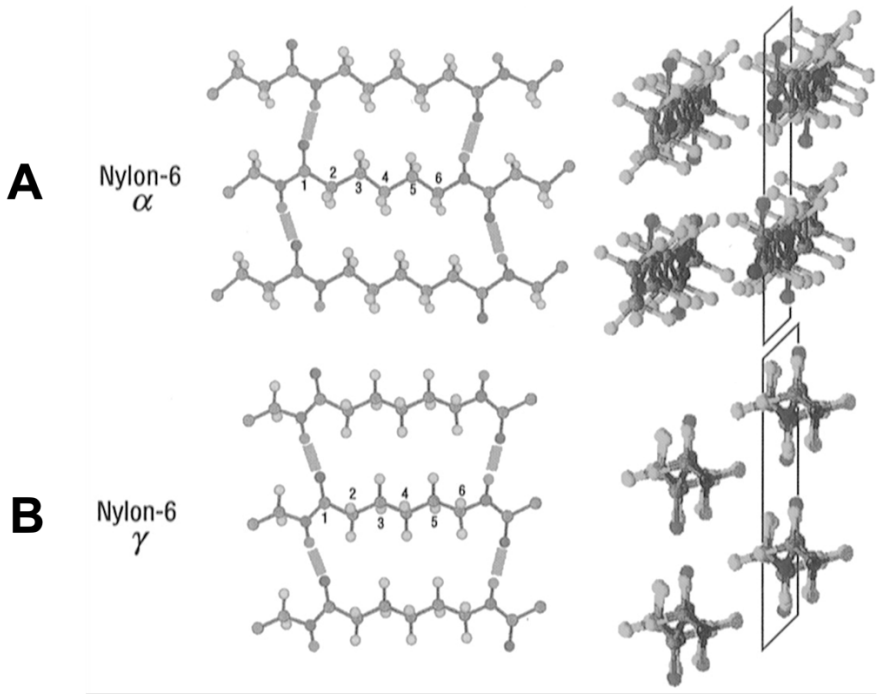

Figure 1-7. Crystal structure of the two dominant allomorphs of Nylon 6. A) Hydrogen bonding (left) and 3D packing (right) of α allomorph and B) hydrogen bonding (left) and 3D packing (right) of the γ allomorph. Adapted from Dasgupta, S.; Hammond, W. B.; Goddard, W. A., Crystal Structures and Properties of Nylon Polymers from Theory. Journal of the American Chemical Society 1996, 118 (49), 12291-12301. Copyright 2022 American Chemical Society.

Nylon 6 is a semicrystalline polymer, meaning it has both crystalline and amorphous regions. In the crystalline regions, it predominately crystallizes in two forms: the α and γ forms, as illustrated in Figure 1-7. The α allomorph is the most stable form as it consists of hydrogen bonding between antiparallel chains.[81, 82] The γ allomorph is less stable as it consists of hydrogen bonding between parallel twisted chains.[81, 82] As a result, the α form has a theoretical Young's modulus of around 235 GPa and the γ form has a theoretical Young's modulus of around 132 GPa.[82, 83] The formation of these allomorphs has been found to be dependent on the processing method – the α form is typically dominant in slow-drying processes such as solvent casting whereas the γ form is typically dominant in fast-drying processes such as electrospinning.[81] Furthermore, the γ form has been found to transform into the α form under additional external parameters after processing, such as temperature or pressure.[82, 84] Overall, processing parameters

and their effects on the crystallization of Nylon 6 is important to consider and will be discussed further in this thesis.

1.4.2 Fillers for the Mechanical Reinforcement of Nylon 6

Due to the widespread use of Nylon 6, further improvements and changes in properties with the addition of fillers have been extensively studied. The most reported (and one of the first) fillers used for the mechanical reinforcement of Nylon 6 is clay, specifically, montmorillonite (a silicon and aluminum oxide containing mineral).[76] Nylon clay hybrids (NCH) have been extensively studied and used in commercial products.[85-87] For example, Toyota's Central Research and Development Labs were the first to develop and produce NCH products and have used the composite in their vehicles, such as for timing belt covers.[88, 89] Other additive fillers, such as carbon fibres (CF) and glass fibres (GF), have also been commercialized in Nylon 6 composites, which are used as filaments for 3D printing.[90, 91]

Perhaps due to the mechanical improvements observed with CF and GF, fibrous cellulose nanomaterials, specifically CNC, have been of recent interest. Both solvent casting and melt-mixing techniques have been used to produce CNC-N6 composites, with the latter being the most common due to the relevance of the technique at large industrial production scales. The previous work done on CNC-N6 composites focus on improving dispersion quality and reducing degradation of CNC within the polymer. For example, Peng *et al.* used water as a plasticizer to reduce the compounding temperature to 30˚C thus preventing degradation of CNC.[92] Other studies have produced small polymer masterbatches containing CNC that are later diluted with N6 in order to achieve enhanced dispersion.[93, 94] A table summarizing previously reported CNC-Nylon 6 composite preparation and manufacturing methods is presented in Table 1-2. Since Nylon 6 is a

popular choice for textiles and filaments, the next progression of research will need to be towards fibre production either by extrusion or electrospinning.

Table 1-2. Previously reported CNC-Nylon 6 composite preparation and manufacturing methods.

Modification	Composite Preparation	Composite Manufacturing	Reference
Sulfate half ester (unmodified)	In-situ polymerization of N6 in the presence of CNC	Compression molding of CNC-N6 granules then injection molding	[95]
Sulfate half ester (unmodified)	Milling CNC and N6 pellets	Compression molding	[96]
Sulfate half ester (unmodified)	Dissolution of PA6 in formic acid + addition of dry CNC	Melt-pressed films from solvent cast films	[81]
Sulfate half ester (unmodified)	Dissolution of CNC in formic acid + addition of N6 pellets	Solvent cast films	[97]
Sulfate half ester (unmodified)	Dissolution of CNC in formic acid + addition of N6 pellets	Spin coated films	[98]
Sulfate half ester (unmodified)	Masterbatch (5 wt% CNC) diluted with N6	Injection molded foams	[93]
Sulfate half ester (unmodified)	Masterbatch (10 wt%) diluted with N6	Injection molding	[94]
Sulfate half ester (unmodified)	Not stated	Solvent cast CNC coating on electrospun N6 fibres	[99]
Sulfate half ester (unmodified)	Dissolution of CNC in formic acid + addition of N6 pellets	Electrospinning	[68]
Sulfate half ester (unmodified)	-	Melt compounding of N6 and CNC	[53]
Sulfate half ester (unmodified)	CNC aqueous solution added to N6 melt	Water-assisted compounding of N6 and CNC	[92]
Aminopropyltriethoxysilane (APS)	In-situ polymerization of N6 in the presence of CNC	Injection molding	[34]
Aminopropyltriethoxysilane (APS)	In-situ polymerization of N6 in the presence of CNC	Melt pressed	[100]

1.5 Thesis Outline

This thesis demonstrates the reinforcing capability of CNC in Nylon 6 electrospun nanofibres and spin coated thin films. Two types of surface modifications of CNC using diazonium chemistry are also described. The reinforcing impact of CNC in Nylon 6 fibres provides an exciting route towards stronger textiles and films, and the diazonium modification of CNC opens the door to dually strong and dyed fibres.

Chapter 2 presents the mechanical properties of CNC-Nylon 6 thin films and explores the effect of CNC on the crystallization of the polymer. Freestanding thin films were produced using spin-coating from formic acid. Tensile testing was performed, where the elastic moduli, tensile strength, and elongation at break are reported. Surface morphology and dispersion of CNC within the films are visualized using electron microscopy, specifically SEM and TEM. The chemical composition of the films was investigated using FTIR. Finally, the crystalline and thermal behaviour of the films was analyzed using DSC and TGA, respectively.

Chapter 3 investigates the effect of processing parameters in aligned electrospun Nylon 6 fibres using a drum collector. Nylon 6 fibres were collected onto a rotating drum collector, and the alignment and diameters of the fibres were visualized using SEM. The parameters investigated were drum rotation speed, applied voltage, needle-to-collector distance, and flow rate. Jet focusing was also explored by bending a piece of copper wire into a ring that was placed onto the needle. Photographs of the electrospinning set-up are presented.

Chapter 4 compares the mechanical properties of randomly distributed and aligned CNC-Nylon 6 electrospun nanofibre mats, with the elastic moduli, tensile strength, and strain at break reported. Both types of fibre mats were visualized using SEM and fibre diameters were measured. TEM images revealed the distribution and alignment of CNC within the aligned Nylon 6 fibres.

The chemical composition of the aligned fibres was investigated using FTIR, and DSC and XRD were used to probe the crystallinity of the fibres. Finally, the thermal stability of the aligned fibres was quantified using TGA.

Chapter 5 describes the surface functionalization of CNC with diazonium salts. Two methods of diazonium synthesis were performed: *ex-situ* and *in-situ* diazotization. The *ex-situ* method was first described, where 4-nitroaniline was converted into 4-nitrobenzenediazonium (4-dNB). The chemical composition of the modified CNC was evaluated using FTIR, CHNS, and XPS. The thermal stability of the modified CNC was also investigated using TGA. Then, *in-situ* diazotization was performed on p-phenylenediamine and 4-aminobenzylamine to obtain p-aminobenzenediazonium (p-dAB) and 4-aminobenzyldiazonium (4-dABA), respectively. CNC was modified with both diazonium salts, and the chemical composition of each was done using FTIR. Finally, the diazonium modified CNCs were incorporated into Nylon 6 and formic acid, then spin coated to produce thin films.

Chapter 6 presents the surface functionalization of CNC with propylamine using a diazonium radical initiated surface modification. 2,6-Dimethylaniline was converted into a diazonium salt using the *in-situ* diazotization method presented in Chapter 5, which was then used to form propylamine radicals that reacted with CNC. The chemical composition of the propylamine modified CNCs were done using FTIR, CHNS, and XPS, and thermal degradation is evaluated using TGA. The modified CNC was also visually compared to unmodified CNC using TEM. Finally, the propylamine modified CNC was incorporated into Nylon 6 and spin coated to create thin films.

1.6 References

1. Dufresne, A., 3. Preparation of cellulose nanocrystals. In *Nanocellulose: From Nature to High Performance Tailored Materials*, De Gruyter: 2017; pp 117-192.
2. Hamad, W. Y., Assembly and Structure in Native Cellulosic Fibers. In *Cellulose Nanocrystals*, 2017; pp 16-32.
3. Zhu, H.; Luo, W.; Ciesielski, P. N.; Fang, Z.; Zhu, J. Y.; Henriksson, G.; Himmel, M. E.; Hu, L., Wood-Derived Materials for Green Electronics, Biological Devices, and Energy Applications. *Chemical Reviews* **2016,** *116* (16), 9305-9374.
4. Wiedenhoeft, A.; Miller, R., 2 Structure and Function of Wood. *Handbook of Wood Chemistry and Wood Composites* **2005**.
5. Vanholme, R.; Demedts, B.; Morreel, K.; Ralph, J.; Boerjan, W., Lignin Biosynthesis and Structure. *Plant Physiology* **2010,** *153* (3), 895-905.
6. Nasir, M.; Hashim, R.; Sulaiman, O.; Asim, M., 11 - Nanocellulose: Preparation methods and applications. In *Cellulose-Reinforced Nanofibre Composites*, Jawaid, M.; Boufi, S.; H.P.S, A. K., Eds. Woodhead Publishing: 2017; pp 261-276.
7. Bajpai, P., Chapter 2 - Wood and Fiber Fundamentals. In *Biermann's Handbook of Pulp and Paper (Third Edition)*, Bajpai, P., Ed. Elsevier: 2018; pp 19-74.
8. Jakob, M.; Mahendran, A. R.; Gindl-Altmutter, W.; Bliem, P.; Konnerth, J.; Müller, U.; Veigel, S., The strength and stiffness of oriented wood and cellulose-fibre materials: A review. *Progress in Materials Science* **2022,** *125*, 100916.
9. Trache, D.; Tarchoun, A. F.; Derradji, M.; Hamidon, T. S.; Masruchin, N.; Brosse, N.; Hussin, M. H., Nanocellulose: From Fundamentals to Advanced Applications. *Frontiers in Chemistry* **2020,** *8* (392).
10. Moon, R. J.; Martini, A.; Nairn, J.; Simonsen, J.; Youngblood, J., Cellulose nanomaterials review: structure, properties and nanocomposites. *Chem Soc Rev* **2011,** *40* (7), 3941-94.
11. Mahmud, M. M.; Perveen, A.; Jahan, R. A.; Matin, M. A.; Wong, S. Y.; Li, X.; Arafat, M. T., Preparation of different polymorphs of cellulose from different acid hydrolysis medium. *International Journal of Biological Macromolecules* **2019,** *130*, 969-976.
12. Nunes, R. C. R., 13 - Rubber nanocomposites with nanocellulose. In *Progress in Rubber Nanocomposites*, Thomas, S.; Maria, H. J., Eds. Woodhead Publishing: 2017; pp 463-494.
13. Dufresne, A., Cellulose nanomaterial reinforced polymer nanocomposites. *Current Opinion in Colloid & Interface Science* **2017,** *29*, 1-8.
14. Eyley, S.; Thielemans, W., Surface modification of cellulose nanocrystals. *Nanoscale* **2014,** *6* (14), 7764-7779.
15. Postek, M.; Vladár, A.; Dagata, J.; Farkas, N.; Ming, B.; Wagner, R.; Raman, A.; Moon, R.; Sabo, R.; Wegner, T.; Beecher, J., Development of the metrology and imaging of cellulose nanocrystals. *Measurement Science and Technology* **2010,** *22*, 024005.
16. Nickerson, R. F.; Habrle, J. A., Cellulose Intercrystalline Structure. *Industrial & Engineering Chemistry* **1947,** *39* (11), 1507-1512.
17. Ngo, T.; Danumah, C.; Ahvazi, B., Production of Cellulose Nanocrystals at InnoTech Alberta. 2018.
18. Reid, M. S.; Villalobos, M.; Cranston, E. D., Benchmarking Cellulose Nanocrystals: From the Laboratory to Industrial Production. *Langmuir* **2017,** *33* (7), 1583-1598.
19. Foster, E. J.; Moon, R. J.; Agarwal, U. P.; Bortner, M. J.; Bras, J.; Camarero-Espinosa, S.; Chan, K. J.; Clift, M. J. D.; Cranston, E. D.; Eichhorn, S. J.; Fox, D. M.; Hamad, W. Y.;

Heux, L.; Jean, B.; Korey, M.; Nieh, W.; Ong, K. J.; Reid, M. S.; Renneckar, S.; Roberts, R.; Shatkin, J. A.; Simonsen, J.; Stinson-Bagby, K.; Wanasekara, N.; Youngblood, J., Current characterization methods for cellulose nanomaterials. *Chem Soc Rev* **2018,** *47* (8), 2609-2679.
20. Vanderfleet, O. M.; Cranston, E. D., Production routes to tailor the performance of cellulose nanocrystals. *Nature Reviews Materials* **2021,** *6* (2), 124-144.
21. Fraschini, C.; Chauve, G.; Bouchard, J., TEMPO-mediated surface oxidation of cellulose nanocrystals (CNCs). *Cellulose* **2017,** *24* (7), 2775-2790.
22. Dufresne, A., 5. Chemical modification of nanocellulose. In *Nanocellulose: From Nature to High Performance Tailored Materials*, De Gruyter: 2017; pp 221-286.
23. Habibi, Y., Key advances in the chemical modification of nanocelluloses. *Chem Soc Rev* **2014,** *43* (5), 1519-42.
24. Le Gars, M.; Bras, J.; Salmi-Mani, H.; Ji, M.; Dragoe, D.; Faraj, H.; Domenek, S.; Belgacem, N.; Roger, P., Polymerization of glycidyl methacrylate from the surface of cellulose nanocrystals for the elaboration of PLA-based nanocomposites. *Carbohydrate Polymers* **2020,** *234*, 115899.
25. Ogunsona, E. O.; Panchal, P.; Mekonnen, T. H., Surface grafting of acrylonitrile butadiene rubber onto cellulose nanocrystals for nanocomposite applications. *Composites Science and Technology* **2019,** *184*, 107884.
26. Wohlhauser, S.; Kuhnt, T.; Meesorn, W.; Montero de Espinosa, L.; Zoppe, J. O.; Weder, C., One-Component Nanocomposites Based on Polymer-Grafted Cellulose Nanocrystals. *Macromolecules* **2020,** *53* (3), 821-834.
27. Abitbol, T.; Marway, H.; Cranston, E. D., Surface modification of cellulose nanocrystals with cetyltrimethylammonium bromide. *Nordic Pulp & Paper Research Journal* **2014,** *29* (1), 46-57.
28. Clemons, C.; Reiner, R., Preparation of cellulose nanocrystal-polypropylene masterbatches by water-assisted thermokinetic mixing. *ANTEC 2020: The Virtual Edition. 6p.* **2020**.
29. Orellana, J. L.; Wichhart, D.; Kitchens, C. L., Mechanical and Optical Properties of Polylactic Acid Films Containing Surfactant-Modified Cellulose Nanocrystals. *Journal of Nanomaterials* **2018,** *2018*, 7124260.
30. Ly, M.; Mekonnen, T. H., Cationic surfactant modified cellulose nanocrystals for corrosion protective nanocomposite surface coatings. *Journal of Industrial and Engineering Chemistry* **2020,** *83*, 409-420.
31. Voronova, M.; Rubleva, N.; Kochkina, N.; Afineevskii, A.; Zakharov, A.; Surov, O., Preparation and Characterization of Polyvinylpyrrolidone/Cellulose Nanocrystals Composites. *Nanomaterials* **2018,** *8* (12), 1011.
32. Díaz de León, R.; Guzmán, E.; López González, R.; Díaz Elizondo, A.; Magaña, I.; Neira, G.; Castañeda Facio, A.; Valencia, L., Surface Modification of Cellulose Nanocrystals with Lactone Monomers via Plasma-Induced Polymerization and Their Application in ABS Nanocomposites. *Polymers* **2021,** *13* (16), 2699.
33. Forsgren, L.; Sahlin-Sjövold, K.; Venkatesh, A.; Thunberg, J.; Kádár, R.; Boldizar, A.; Westman, G.; Rigdahl, M., Composites with surface-grafted cellulose nanocrystals (CNC). *Journal of Materials Science* **2019,** *54* (4), 3009-3022.
34. Rahimi, S. K.; Otaigbe, J. U., The effects of the interface on microstructure and rheo-mechanical properties of polyamide 6/cellulose nanocrystal nanocomposites prepared by in-situ ring-opening polymerization and subsequent melt extrusion. *Polymer* **2017,** *127*, 269-285.

35. Peng, S. X.; Shrestha, S.; Youngblood, J. P., Crystal structure transformation and induction of shear banding in Polyamide 11 by surface modified Cellulose Nanocrystals. *Polymer* **2017,** *114*, 88-102.
36. Natterodt, J. C.; Sapkota, J.; Foster, E. J.; Weder, C., Polymer Nanocomposites with Cellulose Nanocrystals Featuring Adaptive Surface Groups. *Biomacromolecules* **2017,** *18* (2), 517-525.
37. Nagalakshmaiah, M.; El Kissi, N.; Dufresne, A., Ionic Compatibilization of Cellulose Nanocrystals with Quaternary Ammonium Salt and Their Melt Extrusion with Polypropylene. *ACS Applied Materials & Interfaces* **2016,** *8* (13), 8755-8764.
38. Kalantari, M.; Du, R.; Ayranci, C.; Boluk, Y., Effects of interfacial interactions and interpenetrating brushes on the electrospinning of cellulose nanocrystals-polystyrene fibers. *J Colloid Interface Sci* **2018,** *528*, 419-430.
39. Miao, C.; Hamad, W. Y., Alkenylation of cellulose nanocrystals (CNC) and their applications. *Polymer* **2016,** *101*, 338-346.
40. Tian, D.; Wang, F.; Yang, Z.; Niu, X.; Wu, Q.; Sun, P., High-performance polyurethane nanocomposites based on UPy-modified cellulose nanocrystals. *Carbohydrate Polymers* **2019,** *219*, 191-200.
41. Paralikar, S. A.; Simonsen, J.; Lombardi, J., Poly(vinyl alcohol)/cellulose nanocrystal barrier membranes. *Journal of Membrane Science* **2008,** *320* (1), 248-258.
42. Dufresne, A., Cellulose nanomaterials as green nanoreinforcements for polymer nanocomposites. *Philos Trans A Math Phys Eng Sci* **2018,** *376* (2112).
43. Šturcová, A.; Davies, G. R.; Eichhorn, S. J., Elastic Modulus and Stress-Transfer Properties of Tunicate Cellulose Whiskers. *Biomacromolecules* **2005,** *6* (2), 1055-1061.
44. Tang, J.; Sisler, J.; Grishkewich, N.; Tam, K. C., Functionalization of cellulose nanocrystals for advanced applications. *Journal of Colloid and Interface Science* **2017,** *494*, 397-409.
45. Dufresne, A., 9. Mechanical properties of nanocellulose-based nanocomposites. In *Nanocellulose: From Nature to High Performance Tailored Materials*, De Gruyter: 2017; pp 471-530.
46. Hamad, W. Y., *Cellulose Nanocrystals: Properties, Production and Applications*. Wiley: 2017.
47. Mariano, M.; Chirat, C.; El Kissi, N.; Dufresne, A., Impact of Cellulose Nanocrystal Aspect Ratio on Crystallization and Reinforcement of Poly(butylene adipate-co-terephthalate). *Journal of Polymer Science Part B-Polymer Physics* **2016,** *54* (22), 2284-2297.
48. Corder, R. D.; Adhikari, P.; Burroughs, M. C.; Rojas, O. J.; Khan, S. A., Cellulose nanocrystals for gelation and percolation-induced reinforcement of a photocurable poly(vinyl alcohol) derivative. *Soft Matter* **2020,** *16* (37), 8602-8611.
49. Jardin, J. M.; Zhang, Z.; Hu, G.; Tam, K. C.; Mekonnen, T. H., Reinforcement of rubber nanocomposite thin sheets by percolation of pristine cellulose nanocrystals. *International Journal of Biological Macromolecules* **2020,** *152*, 428-436.
50. Mariano, M.; El Kissi, N.; Dufresne, A., Cellulose nanocrystals and related nanocomposites: Review of some properties and challenges. *Journal of Polymer Science Part B: Polymer Physics* **2014,** *52* (12), 791-806.
51. Meree, C. E.; Schueneman, G. T.; Meredith, J. C.; Shofner, M. L., Rheological behavior of highly loaded cellulose nanocrystal/poly(vinyl alcohol) composite suspensions. *Cellulose* **2016,** *23* (5), 3001-3012.

52. Cao, Y.; Zavattieri, P.; Youngblood, J.; Moon, R.; Weiss, J., The relationship between cellulose nanocrystal dispersion and strength. *Construction and Building Materials* **2016,** *119*, 71-79.
53. Peng, Y. C.; Gardner, D. J.; Han, Y., Characterization of mechanical and morphological properties of cellulose reinforced polyamide 6 composites. *Cellulose* **2015,** *22* (5), 3199-3215.
54. Inai, N. H.; Lewandowska, A. E.; Ghita, O. R.; Eichhorn, S. J., Interfaces in polyethylene oxide modified cellulose nanocrystal - polyethylene matrix composites. *Composites Science and Technology* **2018,** *154*, 128-135.
55. Norrman, K.; Ghanbari-Siahkali, A.; Larsen, N. B., 6 Studies of spin-coated polymer films. *Annual Reports Section "C" (Physical Chemistry)* **2005,** *101* (0), 174-201.
56. Cranston, E. D.; Gray, D. G., Birefringence in spin-coated films containing cellulose nanocrystals. *Colloids and Surfaces A: Physicochemical and Engineering Aspects* **2008,** *325* (1), 44-51.
57. Lagerwall, J. P. F.; Schütz, C.; Salajkova, M.; Noh, J.; Hyun Park, J.; Scalia, G.; Bergström, L., Cellulose nanocrystal-based materials: from liquid crystal self-assembly and glass formation to multifunctional thin films. *NPG Asia Materials* **2014,** *6* (1), e80-e80.
58. Nuruddin, M.; Chowdhury, R. A.; Szeto, R.; Howarter, J. A.; Erk, K. A.; Szczepanski, C. R.; Youngblood, J. P., Structure–Property Relationship of Cellulose Nanocrystal–Polyvinyl Alcohol Thin Films for High Barrier Coating Applications. *ACS Applied Materials & Interfaces* **2021,** *13* (10), 12472-12482.
59. Tan, C.; Peng, J.; Lin, W.; Xing, Y.; Xu, K.; Wu, J.; Chen, M., Role of surface modification and mechanical orientation on property enhancement of cellulose nanocrystals/polymer nanocomposites. *European Polymer Journal* **2015,** *62*, 186-197.
60. Heise, K.; Kontturi, E.; Allahverdiyeva, Y.; Tammelin, T.; Linder, M. B.; Nonappa; Ikkala, O., Nanocellulose: Recent Fundamental Advances and Emerging Biological and Biomimicking Applications. *Advanced Materials* **2021,** *33* (3), 2004349.
61. Jackson, J. C.; Camargos, C. H. M.; Noronha, V. T.; Paula, A. J.; Rezende, C. A.; Faria, A. F., Sustainable Cellulose Nanocrystals for Improved Antimicrobial Properties of Thin Film Composite Membranes. *ACS Sustainable Chemistry & Engineering* **2021,** *9* (19), 6534-6540.
62. Xue, J.; Wu, T.; Dai, Y.; Xia, Y., Electrospinning and Electrospun Nanofibers: Methods, Materials, and Applications. *Chemical Reviews* **2019,** *119* (8), 5298-5415.
63. Reneker, D. H.; Yarin, A. L., Electrospinning jets and polymer nanofibers. *Polymer* **2008,** *49* (10), 2387-2425.
64. Taylor, G., Electrically Driven Jets. *Proceedings of the Royal Society of London. Series A, Mathematical and Physical Sciences* **1969,** *313* (1515), 453-475.
65. Wendorff, J. H.; Agarwal, S.; Greiner, A.; Agarwal, S., *Electrospinning : Materials, Processing, and Applications*. John Wiley & Sons, Incorporated: Hoboken, GERMANY, 2012.
66. Guerrero, J.; Rivero, J.; Gundabala, V. R.; Perez-Saborid, M.; Fernandez-Nieves, A., Whipping of electrified liquid jets. *Proceedings of the National Academy of Sciences* **2014,** *111* (38), 13763-13767.
67. Wang, W.-C.; Cheng, Y.-T.; Estroff, B., Electrostatic Self-Assembly of Composite Nanofiber Yarn. *Polymers* **2021,** *13* (1), 12.
68. Buyukada-Kesici, E.; Gezmis-Yavuz, E.; Aydin, D.; Cansoy, C. E.; Alp, K.; Koseoglu-Imer, D. Y., Design and fabrication of nano-engineered electrospun filter media with cellulose nanocrystal for toluene adsorption from indoor air. *Materials Science and Engineering: B* **2021,** *264*, 114953.

69. Ribeiro, A. S.; Costa, S. M.; Ferreira, D. P.; Calhelha, R. C.; Barros, L.; Stojković, D.; Soković, M.; Ferreira, I. C. F. R.; Fangueiro, R., Chitosan/nanocellulose electrospun fibers with enhanced antibacterial and antifungal activity for wound dressing applications. *Reactive and Functional Polymers* **2021,** *159*, 104808.
70. Fardioui, M.; Qaiss, A. e. K.; Bouhfid, R., 16 - Cellulose nanocrystal–based nanocomposites. In *Cellulose-Reinforced Nanofibre Composites*, Jawaid, M.; Boufi, S.; H.P.S, A. K., Eds. Woodhead Publishing: 2017; pp 373-389.
71. Song, W.; Liu, D.; Prempeh, N.; Song, R., Fiber Alignment and Liquid Crystal Orientation of Cellulose Nanocrystals in the Electrospun Nanofibrous Mats. *Biomacromolecules* **2017,** *18* (10), 3273-3279.
72. Shafizah, S.; Izwan, A. R. S.; Fatirah, F.; Hasraf, M. N. N., Review on cellulose nanocrystals (CNCs) as reinforced agent on electrospun nanofibers: mechanical and thermal properties. *IOP Conference Series: Materials Science and Engineering* **2018,** *440*, 012011.
73. Dong, H.; Strawhecker, K. E.; Snyder, J. F.; Orlicki, J. A.; Reiner, R. S.; Rudie, A. W., Cellulose nanocrystals as a reinforcing material for electrospun poly(methyl methacrylate) fibers: Formation, properties and nanomechanical characterization. *Carbohydrate Polymers* **2012,** *87* (4), 2488-2495.
74. Dong, H., Polymer Nanofibers Reinforced with Cellulose Nanocrystals. In *Handbook of Polymer Nanocomposites. Processing, Performance and Application: Volume C: Polymer Nanocomposites of Cellulose Nanoparticles*, Pandey, J. K.; Takagi, H.; Nakagaito, A. N.; Kim, H.-J., Eds. Springer Berlin Heidelberg: Berlin, Heidelberg, 2015; pp 323-341.
75. Zhou, C.; Chu, R.; Wu, R.; Wu, Q., Electrospun Polyethylene Oxide/Cellulose Nanocrystal Composite Nanofibrous Mats with Homogeneous and Heterogeneous Microstructures. *Biomacromolecules* **2011,** *12* (7), 2617-2625.
76. Feldman, D., Polyamide nanocomposites. *Journal of Macromolecular Science, Part A* **2017,** *54* (4), 255-262.
77. Deopura, B. L., 2 - Polyamide fibers. In *Polyesters and Polyamides*, Deopura, B. L.; Alagirusamy, R.; Joshi, M.; Gupta, B., Eds. Woodhead Publishing: 2008; pp 41-61.
78. Reimschuessel, H. K., Nylon 6. Chemistry and mechanisms. *Journal of Polymer Science: Macromolecular Reviews* **1977,** *12* (1), 65-139.
79. Matsuo, T., 17 - Automotive applications. In *Polyesters and Polyamides*, Deopura, B. L.; Alagirusamy, R.; Joshi, M.; Gupta, B., Eds. Woodhead Publishing: 2008; pp 525-541.
80. Sastri, V. R., 7 - Engineering Thermoplastics: Acrylics, Polycarbonates, Polyurethanes, Polyacetals, Polyesters, and Polyamides. In *Plastics in Medical Devices (Second Edition)*, Sastri, V. R., Ed. William Andrew Publishing: Oxford, 2014; pp 121-172.
81. Aitha, S.; Vasanthan, N., Effect of cellulose nanocrystals on crystallization, morphology and phase transition of polyamide 6. *Composite Interfaces* **2020,** *27* (4), 371-384.
82. Dasgupta, S.; Hammond, W. B.; Goddard, W. A., Crystal Structures and Properties of Nylon Polymers from Theory. *Journal of the American Chemical Society* **1996,** *118* (49), 12291-12301.
83. Li, Y.; Goddard, W. A., Nylon 6 Crystal Structures, Folds, and Lamellae from Theory. *Macromolecules* **2002,** *35* (22), 8440-8455.
84. Liu, Y.; Cui, L.; Guan, F.; Gao, Y.; Hedin, N. E.; Zhu, L.; Fong, H., Crystalline Morphology and Polymorphic Phase Transitions in Electrospun Nylon-6 Nanofibers. *Macromolecules* **2007,** *40* (17), 6283-6290.

85. Shah, R. K.; Paul, D. R., Nylon 6 nanocomposites prepared by a melt mixing masterbatch process. *Polymer* **2004,** *45* (9), 2991-3000.
86. Li, L.; Bellan, L. M.; Craighead, H. G.; Frey, M. W., Formation and properties of nylon-6 and nylon-6/montmorillonite composite nanofibers. *Polymer* **2006,** *47* (17), 6208-6217.
87. Paci, M.; Filippi, S.; Magagnini, P., Nanostructure development in nylon 6-Cloisite® 30B composites. Effects of the preparation conditions. *European Polymer Journal* **2010,** *46* (5), 838-853.
88. Usuki, A., Nylon 6-clay Hybrid: From Invention to Practical Use. *R&D Review of Toyota CRDL* **2016,** *47* (1), 45-55.
89. Kojima, Y.; Usuki, A.; Kawasumi, M.; Okada, A.; Fukushima, Y.; Kurauchi, T.; Kamigaito, O., Mechanical properties of nylon 6-clay hybrid. *Journal of Materials Research* **1993,** *8* (5), 1185-1189.
90. Chu, P. F.; Iwasawa, S.; Schell, P. L.; Lin, C.-Y., Carbon fiber versus glass fiber reinforcements: A novel, true comparison in thermoplastics. *Polymer Composites* **2021,** *42* (11), 6173-6181.
91. Singh, S.; Ramakrishna, S.; Berto, F., 3D Printing of polymer composites: A short review. *Material Design & Processing Communications* **2020,** *2* (2), e97.
92. Peng, J.; Walsh, P. J.; Sabo, R. C.; Turng, L.-S.; Clemons, C. M., Water-assisted compounding of cellulose nanocrystals into polyamide 6 for use as a nucleating agent for microcellular foaming. *Polymer* **2016,** *84*, 158-166.
93. Yousefian, H.; Rodrigue, D., Morphological, physical and mechanical properties of nanocrystalline cellulose filled Nylon 6 foams. *Journal of Cellular Plastics* **2017,** *53* (3), 253-271.
94. Yousefian, H.; Rodrigue, D., Effect of nanocrystalline cellulose on morphological, thermal, and mechanical properties of Nylon 6 composites. *Polymer Composites* **2016,** *37* (5), 1473-1479.
95. Rahimi, S. K.; Otaigbe, J. U., Polyamide 6 Nanocomposites Incorporating Cellulose Nanocrystals Prepared by In Situ Ring-Opening Polymerization: Viscoelasticity, Creep Behavior, and Melt Rheological Properties. *Polymer Engineering and Science* **2016,** *56* (9), 1045-1060.
96. Venkatraman, P.; Trotto, E.; Burgoyne, I.; Foster, E. J., Premixed cellulose nanocrystal reinforcement of polyamide 6 for melt processing. *Polymer Composites* **2020,** *41* (10), 4353-4361.
97. Sucharitpong, T.; Lam, N. T.; Sukyai, P., Production of Nylon-6/Cellulose Nanocrystal Composite Films Using Solvent Dissolution. *Sugar Tech* **2020,** *22* (2), 328-339.
98. Osorio, D. A.; Niinivaara, E.; Jankovic, N. C.; Demir, E. C.; Benkaddour, A.; Jarvis, V.; Ayranci, C.; McDermott, M. T.; de Lannoy, C.-F.; Cranston, E. D., Cellulose Nanocrystals Influence Polyamide 6 Crystal Structure, Spherulite Uniformity, and Mechanical Performance of Nanocomposite Films. *ACS Applied Polymer Materials* **2021,** *3* (9), 4673-4684.
99. Tan, X.; Peng, Q.; Yang, K.; Yang, T.; Saskova, J.; Wiener, J.; Venkataraman, M.; Militky, J.; Xiong, W.; Xu, J., Preparation and Characterization of corn husk nanocellulose coating on electrospun polyamide 6. *Alexandria Engineering Journal* **2022,** *61* (6), 4529-4540.
100. Rahimi, S. K.; Otaigbe, J. U., The role of particle surface functionality and microstructure development in isothermal and non-isothermal crystallization behavior of polyamide 6/cellulose nanocrystals nanocomposites. *Polymer* **2016,** *107*, 316-331.

Chapter 2. Spin Coated Cellulose Nanocrystal-Nylon 6 Thin Films[1]

2.1. Introduction

Nylon 6, also called Polyamide 6, is a semicrystalline polymer that is most soluble in the polar organic solvent formic acid.[1] It is one of the most used polyamides due to its excellent mechanical strength, chemical resistance, and ease in large-scale fabrication that leads to countless applications such as fibres for textiles and membranes as well as scaffolding used for tissue engineering.[1, 2] As a result of its widespread use, decades of research have been performed studying the crystal structure of Nylon 6 and the effect of processing parameters on the crystal structure during production.[3-7]

The amide group in Nylon 6 allows for interchain hydrogen bonding and provides a route for compatibilization of fillers for added strength.[8] Thus, multiple fillers have been studied for the reinforcement of Nylon 6 such as carbon nanotubes (CNT), graphene oxide (GO), clays, and glass fibres (GF).[2, 9] The incorporation of fillers can also improve the thermal and conductive properties of the polymer.[10, 11] More recently, cellulose nanocrystals (CNC) have been the focus of Nylon 6 reinforcement due to the high aspect ratio and stiffness, as well as the biorenewability, of the nanomaterial and the ability of CNC to form strong interfacial interactions *via* hydrogen bonding to the polymer matrix.[12]

[1] The contents of this Chapter have been copied and/or adapted from the following publication: Osorio, D.A.; Niinivaara, E.; Jankovic, N.C.; Demir, E.C; Benkaddour, A.; Jarvis, V.; Ayranci, C.; McDermott, M.T.; de Lannoy, C.-F.; and Cranston, E.D., Cellulose Nanocrystals Influence Polyamide 6 Crystal Structure, Spherulite Uniformity, and Mechanical Performance of Nanocomposite Films. *ACS Applied Polymer Materials* **2021**, *3*, 4673-4684.

Due to the potential for scaling-up at industrially-relevant levels, most of the focus on CNC reinforced Nylon 6 composites has been on melt processing for sample production.[13] For example, Yousefian and Rodrigue used a masterbatch of concentrated CNC in Nylon 6 (10 wt%) that was diluted with neat Nylon 6 to produce injection molded samples.[14] They found that the tensile modulus increased by 24% at 3 wt% CNC compared to neat Nylon 6 and did not vary significantly at higher loadings, which the authors attributed to a lower dispersion quality. The addition of CNC to Nylon 6 also significantly decreased the elongation at break at higher loadings. This again can be attributed to the potentially agglomerated CNC in the matrix which acts as stress concentration points within the composite leading to premature failure.

One strategy to improve CNC particle dispersion is reported by Rahimi and Otaigbe, where they polymerized Nylon 6 in-solution in the presence of CNC to obtain granules of polymer coated CNC. Then, they used compression molding to make test samples.[15] Similar to the study by Peng *et al.* mentioned in Chapter 1 of this thesis, the high molding temperature (235˚C) used by Rahimi and Otaigbe caused burning of CNC which changed the colour of the test samples to a dark brown.[16] Even with CNC degradation, the CNC-Nylon 6 samples improved the creep resistance (or the resistance to long-term deformation under constant stress levels) compared to neat Nylon 6. The authors attributed this to the ability of CNC to form strong interfacial interactions with Nylon and act as stiff springs in the matrix that physically prevented polymer chain slippage. They also observed a change in crystal structure as the glass transition temperature of the composite increased slightly with increasing CNC loading (0 to 2 wt%).

Solution-based composite processing is an alternative to the aforementioned melt-processing techniques that require high temperatures. These techniques provide a route for increased dispersion prior to composite processing due to the presence of the solvent that reduces

the viscosity of the system compared to molten materials. The most common solution-based methods include solvent casting or spin coating. In a study by Sucharitpong *et al.*, CNC produced from sugarcane bagasse was used in solvent cast Nylon 6 films.[17] They found that CNC increased the opacity of the cast films and had the greatest reinforcing impact at 1 wt% CNC loading (approx. 700 MPa) compared to neat Nylon 6 (approx. 400 MPa). The increase in mechanical properties was attributed to strong CNC-Nylon 6 interactions, such as hydrogen bonding. Though the authors did take a look into the crystalline structure of the cast films using XRD, and found that crystallinity decreased with increasing CNC loading, no direct link between the mechanical properties and the impact of crystallinity was discussed. This gap in the explanation for the reinforcement mechanism based on crystallization prompted us to explore its impact in CNC-Nylon 6 films – more specifically, the mechanical properties.

Other groups have explored the crystallization behaviour of CNC-Nylon composites. Specifically, Aitha and Vasanthan prepared solvent cast films of CNC and Nylon 6.[18] They used DSC and FTIR to study the crystalline structure of the composites and found that CNC induced the less stable γ crystal form of Nylon 6. The work done in this Chapter combines both reasonings for reinforcement (particle-matrix interactions and crystal structure) with morphological and crystallization changes in CNC-Nylon 6 films, which provides a more in-depth look into the reinforcing mechanism of CNC in Nylon 6.[19] More importantly, there is a focus on the reinforcing impact of unmodified CNC in order to probe the direct effect of CNC in a polyamide matrix, which is in contrast to many CNC-polymer studies that use surface modification for increased dispersion and interactions.[20, 21]

In this Chapter, CNC was combined with Nylon 6 in-solution using formic acid as the solvent. Then, the solutions were spin-coated onto glass slides and removed from the substrate to

obtain free-standing CNC-Nylon 6 thin films. The mechanical properties of the films were tested using a tensile tester, and the Young's modulus, ultimate tensile strength, and elongation at break are reported. The dispersity of CNC within the polymer matrix and the morphology of the films was visualized using TEM and SEM, respectively. An investigation into the chemical composition and crystalline structure of the composite films was performed using FTIR, then further studied using DSC. Finally, the thermal stability of the films was tested using TGA. This Chapter contains data and discussions reported by us in a multi-university collaboration.[19] The results presented here are those collected primarily by the University of Alberta team.

2.2 Experimental

2.2.1 Chemicals and Materials

All CNCs used in this study were provided by Celluforce Inc. (Montreal, QC, CA) and were produced from sulfuric acid hydrolysis of wood pulp. CNCs were received in the neutralized sodium salt form as a re-dispersible spray dried powder. Nylon 6 pellets (CAS No. 25038-54-4) and formic acid (98%) were purchased from Sigma-Aldrich (Oakville, ON, CA). All water used was deionized with a resistivity of 18.2 MΩ•cm. Non-frosted 22 mm x 75 mm glass microscope slides were purchased from VWR (Randor, PA, USA).

2.2.2 Preparation of Cellulose Nanocrystal and Nylon 6 Solutions

Spin coated solutions were prepared by adding CNC to formic acid (0 - 5 wt/wt%) and bath sonicating for 30 minutes. Then, Nylon 6 pellets were slowly added while magnetically stirring at room temperature. The total solids content (CNC+N6) in the solutions was 20 wt/v %. The solutions were left to stir overnight at ambient conditions until all the pellets were dissolved. Each

solution was sonicated for 5 minutes prior to spin coating. Solutions were used the following day to ensure that CNC was not potentially degraded by the acidic solvent.

2.2.3 Preparation of Spin Coated Films

A Specialty Coating Systems, Inc. Spincoater Model P6700 Series (Indianapolis, IN, USA) was used for spin coating. Glass microscope slides were cleaned thoroughly with ethanol and DI water, then dried with nitrogen gas. A syringe was used to deposit 2 mL of solution onto the cleaned microscope slide. The slide was tilted side-to-side to allow even spread of the solution across the entirety of the surface. The coated slides were affixed to the middle of the spin coater stage using double sided tape. Spin coating was performed at the following conditions: 300 rpm for 15 s, then 1000 rpm for 60 s, then 1300 rpm for 15 s, and repeated until the resultant spin coated film was dried (2-3 times). The films were left to sit for an hour before peeling from the glass substrate, then left to sit overnight to ensure full evaporation of solvent. Films were placed in a desiccator for at least 24 hours prior to testing.

2.2.4 Characterization

Mechanical testing was performed by Daniel Osorio at the Department of Chemical Engineering at McMaster University. Young's modulus, ultimate tensile strength, and elongation at break were determined through Instron tensile testing of the spin-coated CNC-Nylon 6 nanocomposite films (10 mm x 75 mm strips). A handheld digital micrometer (accuracy ± 0.00016 in or 0.004064 mm) was used to take average thickness measurements (n = 3) of the strips at three separate locations across the centre of the strip (iGaging; San Clemente, CA, USA). Strips were then loaded into a 3366 benchtop universal mechanical testing system (Instron Corporation;

Norwood, MA, USA) with custom-made poly(methyl methacrylate) (PMMA) grips. The PMMA grips were wrapped in Parafilm to reduce failure at the clamp grips and ensure failure in the centre of the samples. Samples were tested in accordance with ASTM d882-D tensile testing standards for free-standing films. Values shown are averages of n = 5 measurements with their corresponding standard deviation.

Differential scanning calorimetry (DSC) was performed by Eyup C. Demir at the nanoFAB at the University of Alberta. Approximately 5 mg of CNC-PA6 film was loaded into aluminum DSC pans, sealed, then analyzed using a TA Q1000 DSC (TA Instruments, DE, USA). Samples were run with heat and cool ramp of 10˚C/min. Temperature precision is up to 0.05 ˚C and the general error in identifying crystallinity is taken to be ± 2 %.

Thermogravimetric analysis (TGA) was completed by Analytical Instrumentation Services in the Department of Chemistry at the University of Alberta using a Mettler-Toledo TGA/DSC 1 (Columbus, OH, USA). Samples (4-5 mg) were placed in a platinum sample holder, then heated from 25˚C to 500˚C at heating rate of 10˚C/min and under nitrogen.

Fourier transform infrared (FTIR) analysis was completed by Analytical Instrumentation Services in the Department of Chemistry at the University of Alberta using a Thermo Nicolet 8700 FTIR Spectrometer (Waltham, MA, USA). A freestanding film was placed in the pathlength of the laser. All spectra were collected from 4000 to 650 cm^{-1} at 128 sample scans a resolution of 4.000.

Transmission electron microscopy (TEM) imaging was completed by the Microscopy Unit in the Department of Biological Sciences at the University of Alberta by Arlene Oatway. Images were collected using a Philips/FEI (Morgagni) transmission electron microscope with Gatan camera at 80 kV. The composite films were exposed to osmium tetroxide vapour for 1 hour then embedded in Spurr resin and cured overnight at 60˚C. A microtome was used to smooth the resin

blocks to the correct depth, then final sections were taken using a diamond knife and placed on a Cu mesh grid. The TEM images were provided by Abdelhaq Benkaddour and Akib Shahriar.

Scanning electron microscopy (SEM) images were taken using a Zeiss Sigma (Gemie) field emission scanning electron microscope at nanoFAB at the University of Alberta. The films were cut into 1 cm x 1 cm squares then placed onto SEM stubs using carbon tape. All samples were imaged at an EHT of 0.500 kV and using the InLens detector.

2.3 Results and Discussion

Solution Preparation and Spin Coating. Spin coating was chosen as the first processing technique for a CNC-Nylon 6 composite material investigated in this thesis as it is fast and produces uniform freestanding thin films that are easy to manipulate for tensile testing.[22] Furthermore, due to the low viscosity of the solutions used for spin coating, this technique produces an ideal specimen where CNC dispersion can be enhanced during processing compared to melt processes where dispersion is difficult to control.

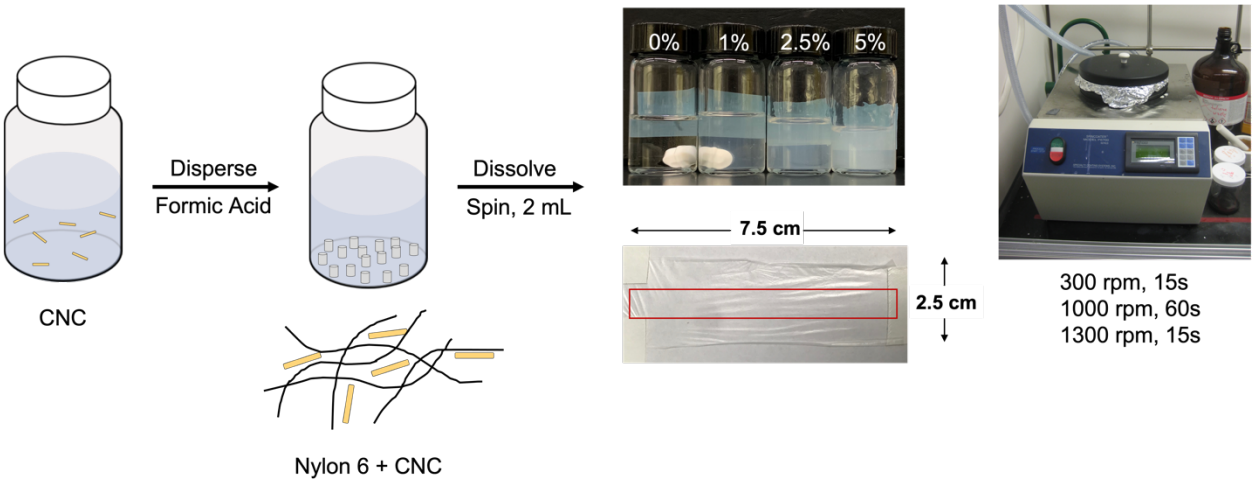

Figure 2-1. Schematic of the solution preparation, final CNC-Nylon 6 solutions, spin coating procedure and instrument, and an example of the final thin film after removal from the glass substrate. The red box indicates where the test strip was cut for tensile testing.

A schematic of the spin coating protocol is illustrated in Figure 2-1. Reproducible CNC-Nylon 6 nanocomposite films with CNC loadings of 0, 1, 2.5, and 5 wt% were prepared by spin coating CNC and Nylon 6 in formic acid. All solutions were sonicated prior to spin coating to maintain the dispersion of CNC in-solution. Most of the films were easily removed from the glass substrate after spinning; however, if the films were left on the substrate for an extended period of time (>1 day) they were difficult to remove, especially with higher CNC loadings (> 1 wt%).

Interestingly, it has been reported that CNC strongly adsorbs to glass substrates cast from acidic solvents.[23] Therefore, the use of formic acid as the solvent may be the reason for the difficulty in the removal of the composite films from the substrate. All films were removed from the glass substrates 1 hour after spinning to avoid this issue.

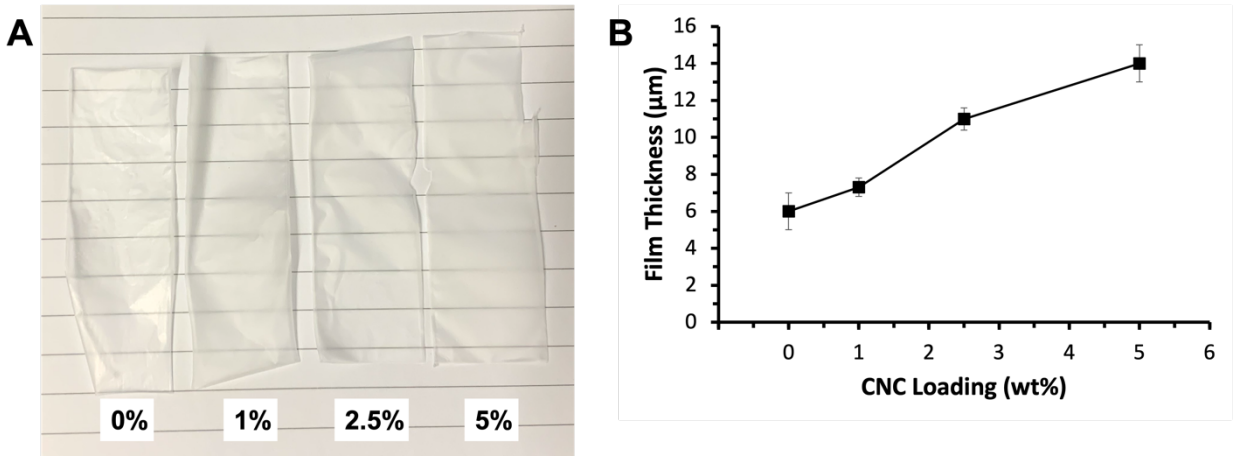

Figure 2-2. (A) Photographs of the thin films produced at CNC loadings of 0-5 wt% and (B) the corresponding thickness of the films at each CNC loading. The film thickness measurements were collected by Daniel Osorio.

Film Transparency and Thickness. The addition of CNC to Nylon 6 was found to decrease the transparency of the films and increase the film thickness, as shown in Figure 2-2. The pure Nylon 6 films were translucent but became opaque and visually non-uniform with 2.5 wt% and 5 wt% CNC, implying that the CNCs were no longer fully dispersed in-solution at higher loadings.[17] The increase in opacity for the spin-coated films is similar to what Sucharitpong *et al.* observed in solvent cast CNC-Nylon 6 films.[17] The film thickness doubled with the addition of 5 wt% CNC when compared to the neat Nylon 6 films even with the same volume of solution and the same film dimensions used for spin coating. The final films were also noticeably more fragile when handling.

It is important to note that the CNC-Nylon 6 solutions were increasingly more viscous and opaque with increasing CNC content. In other studies, CNC has been shown to increase the viscosity of many different polymers in a variety of different processing techniques.[24-26] Though we did not quantify the solution viscosity in this study, the solutions exhibited visible gelling with the addition of well-dispersed CNC due to the self-assembly of the nanoparticles in-solution.[27, 28] Furthermore, Rahimi and Otaigbe found that the addition of CNC to Nylon 6 increased the melt and complex viscosity of the polymer.[15]

Solution viscosity is directly proportional to film thickness in spin coating as shown in Equation 2-1,

$$h = k\eta_0{}^{\beta}\omega^{\alpha} \qquad \text{Eq. 2-1}$$

where h is the film thickness, ω is the angular velocity, η_0 is the initial solution viscosity, and k, β, and α are constants.[22] This means that with the observed increase in solution viscosities with increasing CNC loading, we expect an increase in film thickness. Thus, the non-uniform spreading of the composite solutions over the substrate, and the increase in film thickness at higher CNC loadings, is potentially due to an increase in solution viscosity.

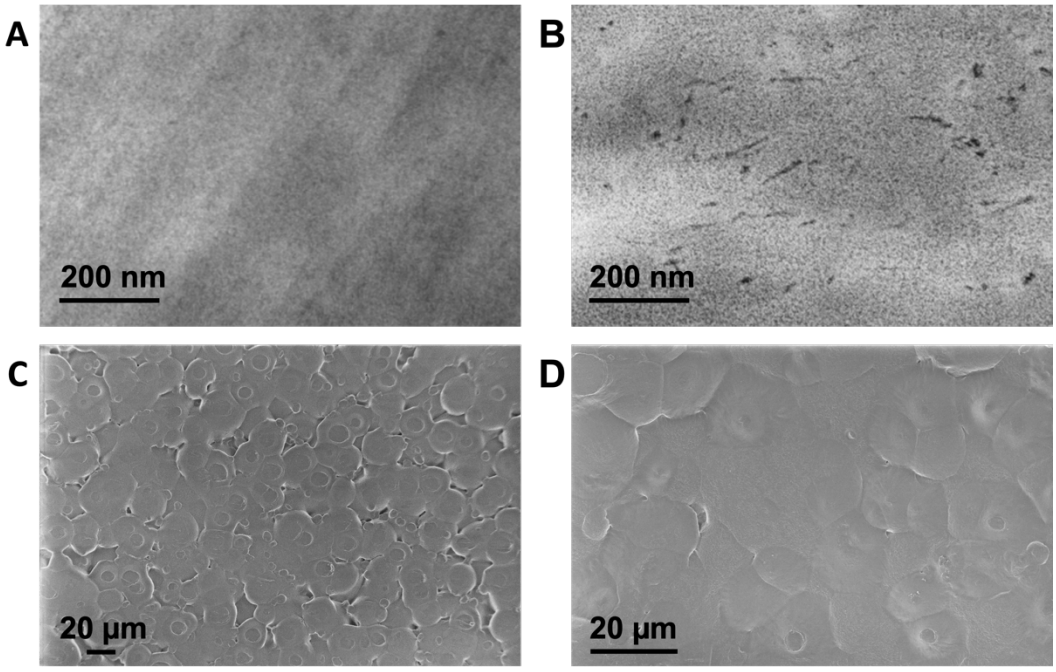

Figure 2-3. TEM images of (A) neat Nylon 6 film and (B) 5 wt% CNC film, and SEM images of (C) neat Nylon 6 film and (D) 5 wt% CNC film. The TEM images in Fig. 2-3A,B were provided by Abdelhaq Benkaddour and Akib Shahriar.

Electron Microscopy Imaging. Sonication of the solutions is expected to promote dispersion of individual CNC particles within the Nylon 6 matrix. Visualization of the dispersion quality was performed using bright field transmission electron microscopy (TEM). TEM images of neat Nylon 6 (0 wt% CNC) and 5 wt% CNC films are shown in Figure 2-3 A,B. The TEM image of the neat Nylon 6 film in Figure 2-3A is free of any particles, while the 5 wt% CNC film in Figure 2-3B clearly shows the presence of CNCs as dark, long fibrous particles. These particles are consistent with the shape and size of CNC, with particle lengths of around 150 nm.[29] CNC appears to be well dispersed within the film, with a few larger aggregates also visible.

The similarity in chemical composition of the carbon-rich CNC and carbon-rich Nylon 6 makes differentiation of CNC within the polymer matrix difficult using scanning electron microscopy (SEM). SEM, however, can provide insight into the morphological nature of the films. The SEM images in Figures 2-3C and 2-3D (neat Nylon 6 films and 5 wt% CNC film, respectively)

appear to reveal the formation of spherulite structures. Spherulites form due to the radial stacking of polymer chains around a crystal centre as a result of the drying of a crystalline polymer.[30] The formation of the spherulites (with imaging using Polarized Optical Microscopy) and their effect on the mechanical properties are discussed in detail by Osorio *et al.*[19] In brief, spherulites were found to pack closer together and decrease in size with increasing CNC loading. We proposed that well dispersed CNC act as nucleating sites for the spherulites. At high concentrations, CNC tends to aggregate which inhibits the formation of crystalline spherulite regions and instead increases the formation of amorphous regions.[31] The formation and density of these spherulites therefore play a role in influencing the mechanical properties of the composite.

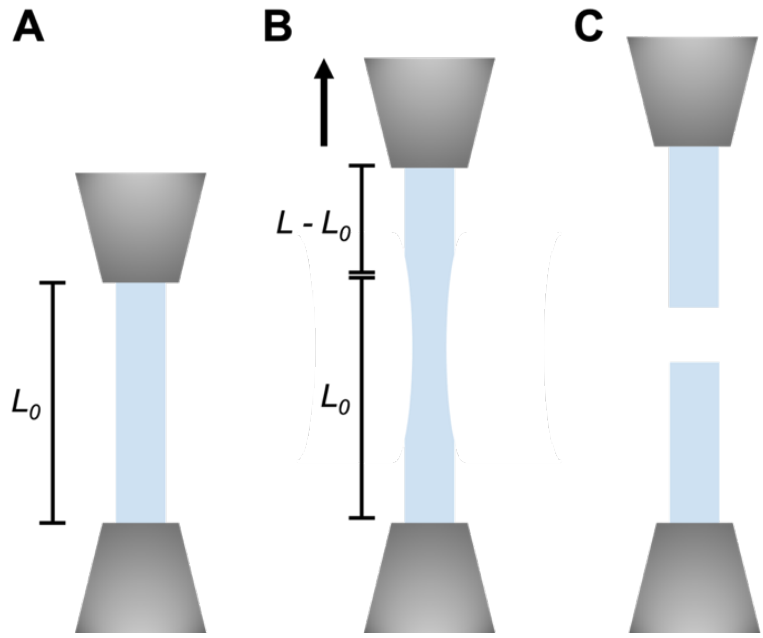

Figure 2-4. Schematic illustrating tensile testing of the spin coated films. A) Specimen (blue) loaded into the grips (grey) at the original length (L_0), B) specimen after displacement ($L-L_0$), and C) specimen after break. The black arrow indicates top grip displacement direction.

Mechanical Results. A schematic of a typical tensile test is illustrated in Figure 2-4. The polymer films were spin coated onto glass microscope slides, then test strips were cut from the

middle of the samples (Fig. 2-1) and loaded into the tensile testing instrument with some sort of support at or on the grips to prevent premature failure of the samples at the grips. The films are then stretched longitudinally (Fig. 2-4B) at a constant rate of 5 mm/min. In the end, a stress-strain curve is produced, where strain is the displacement over the original length and stress is the force per cross-sectional area of the sample. The quantification of the curve is according to Equations 2-2 and 2-3 below,

$$\varepsilon = \frac{L - L_0}{L_0} \qquad \text{Eq. 2-2}$$

$$\sigma = \frac{P}{A_0} \qquad \text{Eq. 2-3}$$

where ε is the engineering strain, L is the measured length, L_0 is the original length, σ is the engineering stress, P is the load in Newtons, and A_0 is the original cross-sectional area of the test strip (*i.e.* the cross-section prior to testing).[32] An example of a typical CNC-Nylon 6 stress-strain curve is presented in Figure 2-5.

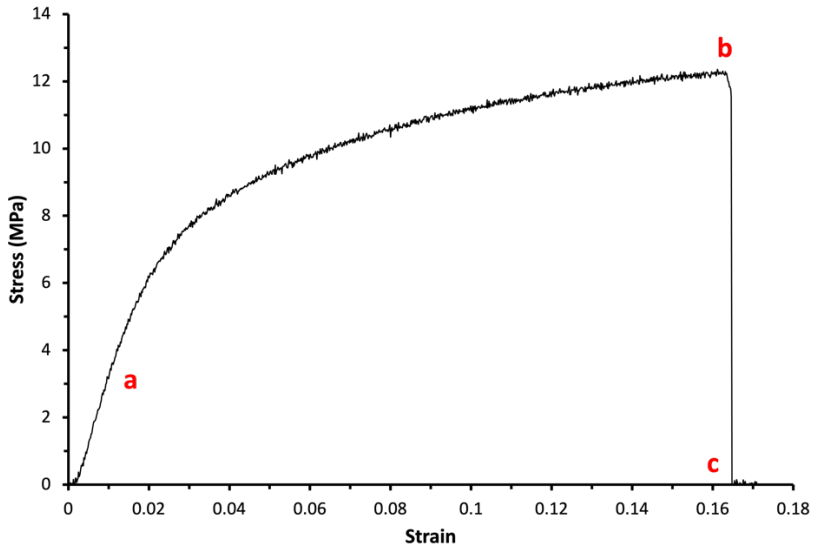

Figure 2-5. An example of a stress-strain curve for a 1 wt% CNC-Nylon 6 film. The points labelled on the curve are the (a) Young's modulus, (b) ultimate tensile strength, and (c) strain at break.

There are several mechanical parameters that can be derived from a stress-strain curve and three will be investigated here: Young's modulus, ultimate tensile strength, and strain at break or elongation at break. The Young's (or elastic) modulus is quantified as the slope of the initial linear portion of curve in the elastic region (Fig. 2-6a). It measures the material's resistance to elastic deformation.[33] The ultimate tensile strength (Fig. 2-6b) is the highest stress that the material undergoes during the test.[33] Finally, the point of failure (or the strain at break) is used to quantify the elongation of the sample when it breaks (Fig. 2-6c), which can also be quantified as the elongation at break. Depending on the type of material, the ultimate tensile strength and the maximum elongation at break may not necessarily happen at the same time, but in our case, all breaks happened immediately after the ultimate tensile strength point.

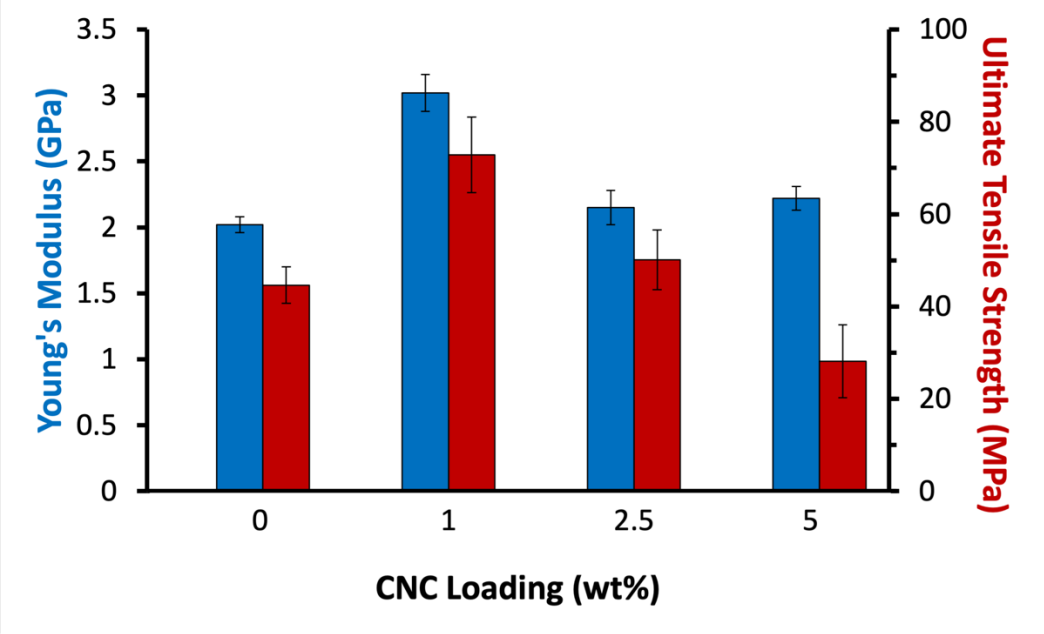

Figure 2-6. Young's modulus (blue) and ultimate tensile strength (red) results for the CNC-Nylon 6 films at 0-5 wt% loadings. The mechanical results were obtained by Daniel Osorio.

Table 2-1. Summary of mechanical properties of the CNC-Nylon 6 spin coated films.

% CNC	Young's Modulus (GPa)	Ultimate Tensile Strength (MPa)	Elongation at Break (%)
0	2.02 ± 0.06	45 ± 4	11 ± 5
1	3.0 ± 0.1	73 ± 8	10 ± 1
2.5	2.2 ± 0.1	50 ± 6	3.0 ± 0.8
5	2.22 ± 0.09	28 ± 8	2.0 ± 0.1

The Young's modulus (YM) and ultimate tensile strength (UTS) of the CNC-Nylon 6 films are presented in Figure 2-6, with a summary of all the mechanical results listed in Table 2-1. I was responsible for the preparation of the testing specimens for Daniel Osorio to perform tensile tests on. Pure Nylon 6 exhibits a YM of 2.02 ± 0.06 GPa which is comparable to previous studies.[15, 34, 35] The Young's modulus increased to 3.0 ± 0.1 GPa at 1 wt% CNC (an approximately 49% increase compared to the pure Nylon 6 films), then decreased to around 2.2 GPa for both 2.5 and 5 wt% CNC. The UTS showed a similar trend, with values of 45 ± 4 MPa for Nylon and an increase to 73 ± 8 at 1 wt% CNC (an approximately 62% increase compared to the pure Nylon 6 films), then a decrease at both 2.5 and 5 wt% CNC. It can be said that 1 wt% was the optimal loading for the Nylon 6 composite films. We did study lower loadings of CNC (0.25 and 0.5 wt%), but a loading of 1 wt% still gave the highest YM and UTS values.[19]

As seen in Figures 2-3C and 2-3D, the formation and density of spherulites is dependent on the amount of CNC added.[19] We expect CNC to be thoroughly dispersed at low loadings (1 wt%),[14, 15] thus individually dispersed CNCs are expected to increase the possibility for favourable interactions, such as such as hydrogen bonding, with Nylon 6.[17, 36, 37] Therefore, increased CNC-Nylon interactions and the stiffness imparted by CNC is the cause for the increase in YM and UTS

at 1 wt% loading (Fig. 2-6). On the other hand, CNC aggregates more readily at high loadings, and these aggregates can act as defect or local stress concentration points in the films making them weaker and more likely to fail prematurely.[38] Therefore, the decrease in spherulite density and increase in amorphous regions imparted by the high loadings of CNC negatively impacted the mechanical properties as seen by the decrease in YM, UTS, and elongation at break above 1 wt% (Table 2-1). Furthermore, the films were noticeably more fragile when removing from the glass substrates above 2.5 wt% CNC. This may also be due to an increase in stress concentrations at higher loadings. TEM images obtained in separate work by Akib Shahriar, a MSc student in our group, also revealed a higher density of aggregates at higher CNC loadings in Nylon 6 films further supporting the formation of aggregates (also shown in the 5 wt% CNC film TEM image in Fig. 2-3B).

The results presented here are in agreement with a previous report by Sucharitpong *et al.* on the reinforcing impact of CNC in Nylon 6 cast films, where a 1 wt% CNC loading had the largest reinforcing impact.[17] However, it is important to note that the processing technique chosen greatly affects the reinforcement capability of CNC. For example, previous studies of extruded or melt compounded Nylon 6 materials show an optimal CNC loading of 5 wt% or higher.[14, 39, 40] Nevertheless, the high reinforcement impact of CNC at such low loadings is the driving force for the use of these nanomaterials for industrial applications.[41]

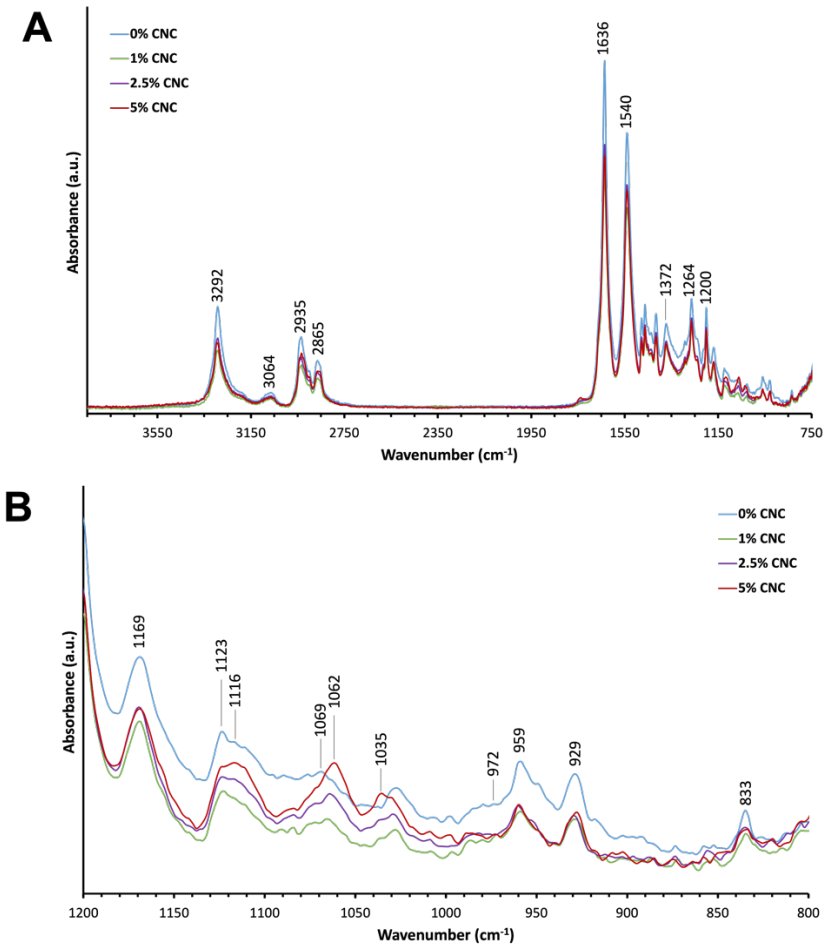

Figure 2-7. FTIR analysis of the spin-coated CNC-Nylon 6 films at 0 wt% CNC (blue), 1 wt% CNC (green), 2.5 wt% CNC (purple), and 5 wt% CNC (red).

FTIR Analysis. The chemical composition of the films was investigated using FTIR, as shown in Figure 2-7. The full spectra in Figure 2-7A show all expected peaks for Nylon 6 at 3292 cm^{-1} (H-bonded N-H str.), 3064 cm^{-1} (N-H), 2935 cm^{-1} (CH_2 asym.), 2865 cm^{-1} (CH_2 sym.), 1636 cm^{-1} (CONH [amide I]), 1540 cm^{-1} (CONH [amide II] + C-N str.), and 1372 cm^{-1} and 1264 cm^{-1} and 1200 cm^{-1} ([amide III] + CH_2 wag).[42, 43] The lower IR region presented in Figure 2-7B also show all expected peaks for Nylon 6 at 1169 cm^{-1} (CONH skeletal motion), 1123 cm^{-1} (C-C amorphous str.), 1069 cm^{-1} (C-C str.), and 833 cm^{-1} (CH_2 rocking).[18, 42] The appearance and increase of the glucose C2, C3, and C6 C-O stretching vibrations at 1116 cm^{-1}, 1062 cm^{-1}, and

1035 cm^{-1}, respectively, and the sharpening of the C-H band at 2935 cm^{-1} further confirm that CNC is present in the composites at all CNC loadings.[44]

The FTIR spectra can also provide insight into the crystalline microstructure of Nylon 6.[18] As mentioned previously, the crystal structure of Nylon 6 plays a large role in the mechanical properties of the polymer. Nylon 6 has two main crystal forms: the α allomorph and the γ allomorph.[18] The α allomorph is the most stable form as it is a result of the extended planar conformation of the polyamide chains, whereas the γ form is the less stable form as it is the result of some twisted chains.[18, 42, 43] In the spectra in Figure 2-7B, the band at 972 cm^{-1} is attributed to the CONH in-plane stretching of the γ allomorph of Nylon 6 and the bands at 959 and 929 cm^{-1} are attributed to the CONH in-plane stretching of the α crystal allomorph of Nylon 6.[18, 45] The peak at 972 cm^{-1} in all spectra is very weak suggesting that there is very little crystallization of the polymer in the γ form. However, the relative intensity of the peak does slightly increase with CNC loading, suggesting that CNC may induce crystallization of Nylon 6 in the γ form in spin-coated films.[19] The presence of the two bands at 959 and 929 cm^{-1} imply that the spin-coated films mainly crystallize in the α form. A full list of the FTIR band assignments is presented in Table 2-2.

Table 2-2. FTIR band assignments for the CNC-Nylon 6 spin-coated films.

Wavenumber (cm^{-1})	Nylon 6 Assignment	CNC Assignment	Reference
3292 (m)	H-bonded NH str.	1˚ and 2˚ O-H str.	*42, 44*
3064 (w)	NH fermi		*42*
2935 (m)	CH_2 asym. str.	C-H str.	*42, 44*
2865 (m)	CH_2 sym. str.		*42*
1636 (s)	C-ONH str. (amide I)		*42*
1540 (s)	CON-H in-plane bend (amide II) + CN str.		*42*
1372 (m)	CON-H str. (amide III) + CH_2 wag		*42*
1264 (m)	CON-H str. (amide III) + CH_2 wag		*42*
1200 (m)	α form CO-NH str. (amide III) + CH_2 wag		*42, 45*
1169 (w)	CO-NH skeletal	C-O-C str.	*42, 44*
1123 (w)	Amorphous C-C str.		*42*
1116 (m)		C-O str. (C2)	*44*
1069 (w)	C-C str.		*18, 42*
1062 (m)		C-O str. (C3)	*44*
1035 (w)		C-O str. (C4)	*44*
972 (w)	γ form CO-NH in-plane str.		*18, 42, 45*
959 (m)	α form CO-NH in-plane str.		*45*
929 (m)	α form CO-NH in-plane str.		*18, 42, 45*
833 (m)	CH_2 rocking		*18*

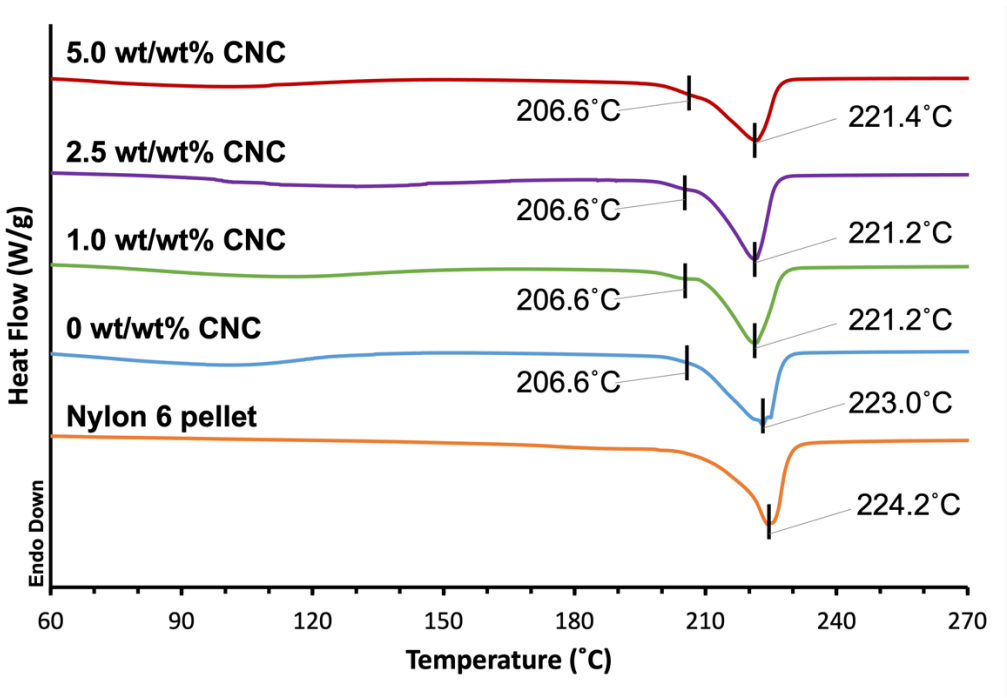

Figure 2-8. DSC analysis of the CNC-Nylon 6 films at 0 wt% CNC (blue), 1 wt% CNC (green), 2.5 wt% CNC (purple), and 5 wt% CNC (red). A comparison to the as-received Nylon 6 pellet is also included (orange).

DSC Analysis. Differential scanning calorimetry (DSC) was used to further investigate the crystallinity of the spin-coated films. In the DSC curves in Figure 2-8, the phase transition corresponding to the α allomorph appears at around 224˚C and that for the γ allomorph appears as a shoulder at around 206˚C. The small decrease in heat flow observed at around 100˚C is due to the evaporation of water absorbed and/or residual solvent (formic acid) on the films. The peak temperatures of the α allomorph in Figure 2-8 do not vary significantly between CNC loadings, even when compared to the as-received Nylon 6 pellet. The appearance of the γ allomorph at 206˚C in the spin-coated films and not in the pellet suggest that the spin-coating process intrinsically induces the γ crystallization of Nylon 6; however, the α form still remains the dominating crystal structure as shown by it being the largest peak in all samples. We expect that CNC interferes with intramolecular chain folding and induces intermolecular interactions with adjacent Nylon chains,[46] leading to formation of the γ crystal structure. Interestingly, CNCs are

known to be chiral in nature,[47] which may also induce the crystallization of Nylon 6 in the twisted γ structure.

It is also possible that the spin coating process may also induce the γ allomorph crystallization by causing preferential orientation of the polymer chains. The Nylon 6 chains and CNCs can orient radially in the direction of the centripetal force during spin-coating.[48] CNC has been suggested to impede polymer chain mobility and flexibility,[40] thus leading to the formation of the unstable γ crystal structure. Furthermore, the solutions were increasingly more viscous with the addition of CNC, as discussed previously. Increases in viscosity have been further suggested to rise from an increase in CNC-polymer bonding and entanglement, which may also inhibit the thermodynamic packing by preventing mobility of the Nylon chains.[20, 49] In the end, the reduction in crystallization supports the decrease in mechanical properties observed at high loadings (Table 2-1).

Finally, an intriguing result is that the CNC-Nylon 6 films had increased YM and UTS values even though a significant proportion of the unstable γ allomorph was formed. This is surprising given that the γ crystal structure exhibits a lower Young's modulus (135 GPa) than the α crystal structure (295 GPa) in neat Nylon 6.[5] Furthermore, we compared the relative percent of both the α and γ allomorphs in the films (with loadings of 0, 0.25, 0.5, 1, 1.75, 2.5, 3.75, and 5 wt% CNC) using x-ray diffraction (XRD).[19] We observed a decrease in the relative peak area of the α allomorph in the films with increasing CNC loadings and we saw an increase in relative peak area of the γ allomorph up to 1 wt% CNC. This suggests that the interaction between CNC and the polymer strengthened the composite and are sufficient enough to overcome a decrease in mechanical properties which would be solely due to the crystal structure of Nylon 6.

The degree of crystallinity was calculated from the DSC results using Equation 2-4,

$$\chi_C = \frac{\Delta H_f}{(1-\phi)\cdot \Delta H_f^{100}} \cdot 100\% \qquad \text{Eq. 2-4}$$

where ΔH_f is the heat of fusion of the composite, ϕ is the weight fraction of CNC, and ΔH_f^{100} is the heat of fusion of fully crystalline Nylon 6 (230 J/g).[50] The heat of fusion for each sample was determined by taking the area under the melting peak between 190˚C and 245˚C (Fig. 2-8). The degree of crystallinity of the polymer was not affected by CNC content, as the percent crystallinity values stayed between ± 0.7% (Table 2-3). Furthermore, the addition of CNC did not significantly impact the depth or width of the crystal peaks. A summary of the results from the DSC analysis is listed in Table 2-3.

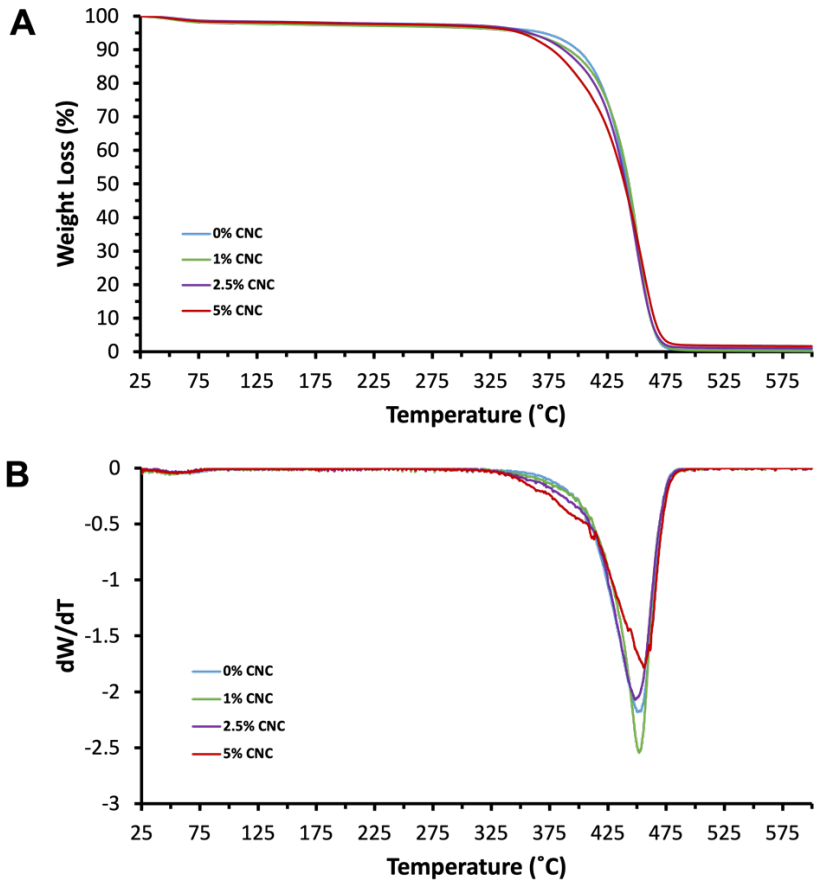

Figure 2-9. (A) TGA and (DTG) curves for the CNC-N6 films at 0 wt% (blue), 1 wt% (green), 2.5 wt% (purple), and 5 wt% (red).

Thermal Properties. Finally, the thermal stability of the composite films was studied using thermogravimetric analysis (TGA). In Figure 2-9A, all samples showed a small 1-2% weight loss at around 100˚C due to the loss of absorbed water and/or residual formic acid. Starting at around 325˚C, there is a larger weight loss from the degradation of both CNC and the polymer. The onset temperature (T_O) decreased with increasing CNC loading, from 421˚C for neat Nylon 6 (0 wt% CNC) to 409˚C for 5 wt% CNC (Table 2-3), as is expected since CNC starts to decompose at around 200˚C.[29] After 475˚C, the remaining mass is due to char left from the degradation of CNC,[29] which is slightly higher at 5 wt% CNC loading. On the other hand, the first derivative of the TGA curves (DTG) in Figure 2-9B show that the first derivative peak temperature (T_P) did not vary significantly between samples (listed in Table 2-3). The intensity of the peaks, however, decreased with increasing CNC loading which is a direct result of the earlier degradation of CNC. Overall, CNC slightly decreased the thermal stability of the Nylon 6 films. A summary of the data from the TGA and DTG curves are listed in Table 2-3.

Table 2-3. Summarized DSC and TGA results for the CNC-Nylon 6 films.

	DSC			TGA & DTG	
CNC (wt%)	**Peak$_\alpha$ (˚C)**	**ΔH_f (J/g)**	**χ_c (%)**	**To (˚C)**	**T_P (˚C)**
0 (pellet)	224.2	67.0	29.1	-	-
0	223.0	65.1	28.3	421	453
1	221.2	63.3	27.8	419	453
2.5	221.2	63.0	28.1	418	451
5	221.4	62.3	28.5	409	455

2.4 Conclusion

Spin coating was used to produce nanocomposite thin films of CNC and Nylon 6. The opacity and the thickness of the films increased with CNC loading. The presence of CNC in the films was visualized using TEM, and the formation of polymer spherulites was observed using SEM. The Young's modulus and ultimate tensile strength increased to an optimal CNC loading of 1 wt%, with values 1.5 and 1.6 times larger than that for neat Nylon 6, respectively. At loadings 2.5 wt% and higher, the films showed a reduction in all measured mechanical properties. The crystal microstructure of the films was investigated using FTIR and DSC, where the spin-coated films were found to predominately crystallize in the α allomorph for Nylon 6. The aggregation of CNC at high loadings was found to induce the crystallization of Nylon in the less stable γ form, supporting the decrease in mechanical properties at 2.5 and 5 wt%. Finally, the thermal stability of the composite films decreased slightly with CNC content due to the decomposition of CNC. The results presented in this Chapter demonstrate the feasibility and advantages of using CNC to reinforce Nylon films. These reinforced films have potential applications as coatings for the aerospace and automotive industries.

2.5 References

1. Shakiba, M.; Rezvani Ghomi, E.; Khosravi, F.; Jouybar, S.; Bigham, A.; Zare, M.; Abdouss, M.; Moaref, R.; Ramakrishna, S., Nylon—A material introduction and overview for biomedical applications. *Polymers for Advanced Technologies* **2021,** *32* (9), 3368-3383.
2. Feldman, D., Polyamide nanocomposites. *Journal of Macromolecular Science, Part A* **2017,** *54* (4), 255-262.
3. Dasgupta, S.; Hammond, W. B.; Goddard, W. A., Crystal Structures and Properties of Nylon Polymers from Theory. *Journal of the American Chemical Society* **1996,** *118* (49), 12291-12301.
4. Fornes, T. D.; Paul, D. R., Crystallization behavior of nylon 6 nanocomposites. *Polymer* **2003,** *44* (14), 3945-3961.
5. Li, Y.; Goddard, W. A., Nylon 6 Crystal Structures, Folds, and Lamellae from Theory. *Macromolecules* **2002,** *35* (22), 8440-8455.

6. Millot, C.; Fillot, L.-A.; Lame, O.; Sotta, P.; Seguela, R., Assessment of polyamide-6 crystallinity by DSC. *Journal of Thermal Analysis and Calorimetry* **2015,** *122* (1), 307-314.
7. Holmes, D. R.; Bunn, C. W.; Smith, D. J., The crystal structure of polycaproamide: Nylon 6. *Journal of Polymer Science* **1955,** *17* (84), 159-177.
8. O'Neill, A.; Bishop, D.; Dalton, B.; Archer, E.; McIlhagger, A.; Dixon, D., Preparation and properties of polyamide 6 nanocomposites covalently linked with amide functional graphene oxide. *Journal of Thermoplastic Composite Materials* **2018,** *31* (2), 162-180.
9. Cho, J. W.; Paul, D. R., Nylon 6 nanocomposites by melt compounding. *Polymer* **2001,** *42* (3), 1083-1094.
10. Zabegaeva, O. N.; Sapozhnikov, D. A.; Buzin, M. I.; Krestinin, A. V.; Kotelnikov, V. A.; Baiminov, B. A.; Afanasyev, E. S.; Pashunin, Y. M.; Vygodskii, Y. S., Nylon-6 and single-walled carbon nanotubes polyamide composites:Formulation and characterization. *High Performance Polymers* **2017,** *29* (4), 411-421.
11. Lu, Y.; Yu, G.; Wei, X.; Zhan, C.; Jeon, J.-W.; Wang, X.; Jeffryes, C.; Guo, Z.; Wei, S.; Wujcik, E. K., Fabric/multi-walled carbon nanotube sensor for portable on-site copper detection in water. *Advanced Composites and Hybrid Materials* **2019,** *2* (4), 711-719.
12. Lee, K.-Y.; Aitomäki, Y.; Berglund, L. A.; Oksman, K.; Bismarck, A., On the use of nanocellulose as reinforcement in polymer matrix composites. *Composites Science and Technology* **2014,** *105*, 15-27.
13. Wang, L.; Gardner, D. J.; Wang, J.; Yang, Y.; Tekinalp, H. L.; Tajvidi, M.; Li, K.; Zhao, X.; Neivandt, D. J.; Han, Y.; Ozcan, S.; Anderson, J., Towards industrial-scale production of cellulose nanocomposites using melt processing: A critical review on structure-processing-property relationships. *Composites Part B: Engineering* **2020,** *201*, 108297.
14. Yousefian, H.; Rodrigue, D., Effect of nanocrystalline cellulose on morphological, thermal, and mechanical properties of Nylon 6 composites. *Polymer Composites* **2016,** *37* (5), 1473-1479.
15. Rahimi, S. K.; Otaigbe, J. U., Polyamide 6 Nanocomposites Incorporating Cellulose Nanocrystals Prepared by In Situ Ring-Opening Polymerization: Viscoelasticity, Creep Behavior, and Melt Rheological Properties. *Polymer Engineering and Science* **2016,** *56* (9), 1045-1060.
16. Peng, Y. C.; Gardner, D. J.; Han, Y., Characterization of mechanical and morphological properties of cellulose reinforced polyamide 6 composites. *Cellulose* **2015,** *22* (5), 3199-3215.
17. Sucharitpong, T.; Lam, N. T.; Sukyai, P., Production of Nylon-6/Cellulose Nanocrystal Composite Films Using Solvent Dissolution. *Sugar Tech* **2020,** *22* (2), 328-339.
18. Aitha, S.; Vasanthan, N., Effect of cellulose nanocrystals on crystallization, morphology and phase transition of polyamide 6. *Composite Interfaces* **2020,** *27* (4), 371-384.
19. Osorio, D. A.; Niinivaara, E.; Jankovic, N. C.; Demir, E. C.; Benkaddour, A.; Jarvis, V.; Ayranci, C.; McDermott, M. T.; de Lannoy, C.-F.; Cranston, E. D., Cellulose Nanocrystals Influence Polyamide 6 Crystal Structure, Spherulite Uniformity, and Mechanical Performance of Nanocomposite Films. *ACS Applied Polymer Materials* **2021,** *3* (9), 4673-4684.
20. Rahimi, S. K.; Otaigbe, J. U., The role of particle surface functionality and microstructure development in isothermal and non-isothermal crystallization behavior of polyamide 6/cellulose nanocrystals nanocomposites. *Polymer* **2016,** *107*, 316-331.
21. Eyley, S.; Thielemans, W., Surface modification of cellulose nanocrystals. *Nanoscale* **2014,** *6* (14), 7764-7779.
22. Norrman, K.; Ghanbari-Siahkali, A.; Larsen, N. B., 6 Studies of spin-coated polymer films. *Annual Reports Section "C" (Physical Chemistry)* **2005,** *101* (0), 174-201.

23. Parker, R. M.; Guidetti, G.; Williams, C. A.; Zhao, T.; Narkevicius, A.; Vignolini, S.; Frka-Petesic, B., The Self-Assembly of Cellulose Nanocrystals: Hierarchical Design of Visual Appearance. *Advanced Materials* **2018,** *30* (19), 1704477.
24. Shojaeiarani, J.; Bajwa, D. S.; Stark, N. M.; Bajwa, S. G., Rheological properties of cellulose nanocrystals engineered polylactic acid nanocomposites. *Composites Part B: Engineering* **2019,** *161*, 483-489.
25. Goffin, A. L.; Raquez, J. M.; Duquesne, E.; Siqueira, G.; Habibi, Y.; Dufresne, A.; Dubois, P., Poly(ε-caprolactone) based nanocomposites reinforced by surface-grafted cellulose nanowhiskers via extrusion processing: Morphology, rheology, and thermo-mechanical properties. *Polymer* **2011,** *52* (7), 1532-1538.
26. Dufresne, A., 7. Processing of nanocellulose-based materials. In *Nanocellulose: From Nature to High Performance Tailored Materials*, De Gruyter: 2017; pp 351-418.
27. Peng, Y.; Via, B., The Effect of Cellulose Nanocrystal Suspension Treatment on Suspension Viscosity and Casted Film Property. *Polymers* **2021,** *13* (13), 2168.
28. Abitbol, T.; Kam, D.; Levi-Kalisman, Y.; Gray, D. G.; Shoseyov, O., Surface Charge Influence on the Phase Separation and Viscosity of Cellulose Nanocrystals. *Langmuir* **2018,** *34* (13), 3925-3933.
29. Reid, M. S.; Villalobos, M.; Cranston, E. D., Benchmarking Cellulose Nanocrystals: From the Laboratory to Industrial Production. *Langmuir* **2017,** *33* (7), 1583-1598.
30. Crist, B.; Schultz, J. M., Polymer spherulites: A critical review. *Progress in Polymer Science* **2016,** *56*, 1-63.
31. Roy, D.; Kotula, A. P.; Natarajan, B.; Gilman, J. W.; Fox, D. M.; Migler, K. B., Effect of cellulose nanocrystals on crystallization kinetics of polycaprolactone as probed by Rheo-Raman. *Polymer* **2018,** *153*, 70-77.
32. Tu, S.; Ren, X.; He, J.; Zhang, Z., Stress–strain curves of metallic materials and post-necking strain hardening characterization: A review. *Fatigue & Fracture of Engineering Materials & Structures* **2020,** *43* (1), 3-19.
33. International, A., *Atlas of Stress-strain Curves*. ASM International: 2002.
34. García, M.; van Zyl, W. E.; Verweij, H., Hybrid nylon-6/silica nanocomposites with improved mechanical properties. *MRS Online Proceedings Library* **2003,** *740* (1), I1.9.
35. Sridhara, P. K.; Vilaseca, F., High Performance PA 6/Cellulose Nanocomposites in the Interest of Industrial Scale Melt Processing. *Polymers* **2021,** *13* (9), 1495.
36. Fortunati, E.; Luzi, F.; Puglia, D.; Terenzi, A.; Vercellino, M.; Visai, L.; Santulli, C.; Torre, L.; Kenny, J. M., Ternary PVA nanocomposites containing cellulose nanocrystals from different sources and silver particles: Part II. *Carbohydrate Polymers* **2013,** *97* (2), 837-848.
37. Habibi, Y.; Lucia, L. A.; Rojas, O. J., Cellulose Nanocrystals: Chemistry, Self-Assembly, and Applications. *Chemical Reviews* **2010,** *110* (6), 3479-3500.
38. Li, W.; Zhao, X.; Huang, Z.; Liu, S., Nanocellulose fibrils isolated from BHKP using ultrasonication and their reinforcing properties in transparent poly (vinyl alcohol) films. *Journal of Polymer Research* **2013,** *20* (8), 210.
39. Yousefian, H.; Rodrigue, D., Morphological, physical and mechanical properties of nanocrystalline cellulose filled Nylon 6 foams. *Journal of Cellular Plastics* **2017,** *53* (3), 253-271.
40. Peng, J.; Walsh, P. J.; Sabo, R. C.; Turng, L. S.; Clemons, C. M., Water-assisted compounding of cellulose nanocrystals into polyamide 6 for use as a nucleating agent for microcellular foaming. *Polymer* **2016,** *84*, 158-166.

41. Dufresne, A., Cellulose nanomaterial reinforced polymer nanocomposites. *Current Opinion in Colloid & Interface Science* **2017,** *29*, 1-8.
42. Lee, K.-H.; Kim, K.-W.; Pesapane, A.; Kim, H.-Y.; Rabolt, J. F., Polarized FT-IR Study of Macroscopically Oriented Electrospun Nylon-6 Nanofibers. *Macromolecules* **2008,** *41* (4), 1494-1498.
43. Vasanthan, N.; Salem, D. R., FTIR spectroscopic characterization of structural changes in polyamide-6 fibers during annealing and drawing. *Journal of Polymer Science Part B: Polymer Physics* **2001,** *39* (5), 536-547.
44. Foster, E. J.; Moon, R. J.; Agarwal, U. P.; Bortner, M. J.; Bras, J.; Camarero-Espinosa, S.; Chan, K. J.; Clift, M. J. D.; Cranston, E. D.; Eichhorn, S. J.; Fox, D. M.; Hamad, W. Y.; Heux, L.; Jean, B.; Korey, M.; Nieh, W.; Ong, K. J.; Reid, M. S.; Renneckar, S.; Roberts, R.; Shatkin, J. A.; Simonsen, J.; Stinson-Bagby, K.; Wanasekara, N.; Youngblood, J., Current characterization methods for cellulose nanomaterials. *Chem Soc Rev* **2018,** *47* (8), 2609-2679.
45. Pagacz, J.; Raftopoulos, K. N.; Leszczyńska, A.; Pielichowski, K., Bio-polyamides based on renewable raw materials. *Journal of Thermal Analysis and Calorimetry* **2016,** *123* (2), 1225-1237.
46. Bazrafshan, Z., Multi-functional coating of polymeric spherulites for chiral photonic cellulose nanocrystal films. *Cellulose* **2020,** *27* (11), 6235-6247.
47. Usov, I.; Nyström, G.; Adamcik, J.; Handschin, S.; Schütz, C.; Fall, A.; Bergström, L.; Mezzenga, R., Understanding nanocellulose chirality and structure–properties relationship at the single fibril level. *Nature Communications* **2015,** *6* (1), 7564.
48. Cranston, E. D.; Gray, D. G., Birefringence in spin-coated films containing cellulose nanocrystals. *Colloids and Surfaces A: Physicochemical and Engineering Aspects* **2008,** *325* (1), 44-51.
49. Tousignant, M. N.; Rice, N. A.; Peltekoff, A.; Sundaresan, C.; Miao, C.; Hamad, W. Y.; Lessard, B. H., Improving Thin-Film Properties of Poly(vinyl alcohol) by the Addition of Low-Weight Percentages of Cellulose Nanocrystals. *Langmuir* **2020,** *36* (13), 3550-3557.
50. Klata, E.; Borysiak, S.; Van de Velde, K.; Garbarczyk, J.; Krucinska, I., Crystallinity of polyamide-6 matrix in glass fibre/polyamide-6 composites manufactured from hybrid yarns. *Fibres & Textiles in Eastern Europe* **2004,** *12* (3), 64-69.

Chapter 3. Effect of Electrospinning Parameters on Fibre Diameter and Alignment of Nylon 6 Fibres

3.1 Introduction

The electrospinning of polymers from solution is a quick and facile way of obtaining fibres with diameters in the nanometer range.[1] In a typical electrospinning experiment, a polymer solution is loaded into a syringe capped with a blunt-end needle. A syringe pump is used to force the solution out of the syringe and a voltage is applied to the needle. An electrostatic attraction between the charged needle and a grounded collector forces a polymer drop from the tip of the needle to be drawn to the collector. The jet goes through a stable straight phase before going through an series of unstable whipping phases that eventually leads to the deposition of thin polymer fibres onto the collector.[2] When using a stationary collector, the fibres are collected as a network of randomly orientated fibres and when using a rotating collector, the fibres are stretched and forced to align in the direction of rotation depending on the rotational velocity.[2]

In 1969, Sir Geoffrey Taylor was the first to theoretically describe that when the charge exceeds the surface tension of a viscous polymer drop at a needle tip when a voltage is applied, a cone forms (coined the "Taylor cone") and creates an electrically charged jet that is drawn to a grounded metal surface.[3] He suggested the following equation to explain the effect of applied voltage on the formation of the cone,

$$V_c^2 = 4\frac{H^2}{L^2}\left(\ln\frac{2L}{R} - \frac{3}{2}\right)(0.117\pi\gamma R) \qquad \text{Eq. 3-1}$$

where V_c is the critical voltage required to form the Taylor cone, H is the needle-to-collector distance, L is the length of the needle, R is the radius of the needle, and γ is the surface tension of the solution.[3, 4] Taylor's equation reinforces the importance of applied voltage during electrospinning and has led to many theoretical studies delving into the influence of Taylor cone formation on fibre diameter.[5-7] Fibre morphology and characteristics are therefore dependent on a multitude of solution and electrospinning processing parameters including, but not limited to, solution viscosity, solution concentration, polymer molecular weight, needle gauge and length, volatility and conductivity of the solvent, feed/flow rate, voltage, the distance between the tip of the needle and the collector (needle-to-collector distance), and type of collector.[8] The most common responding factor measured against these parameters is fibre diameter because it can be easily measured using scanning electron microscopy (SEM), transmission electron microscopy (TEM), or atomic force microscopy (AFM).[1] Since diameter also plays a large role in the end properties and applications of the fibres, it will be one of the main properties studied in this Chapter.

The radius of the jet decreases due to the series of stabilities and instabilities it undergoes while electrospinning, which is caused mostly by the electrostatic repulsion imparted by the applied voltage.[9] Therefore, the diameter of the jet is different at the nozzle (or not far after the Taylor cone) when compared to the final fibre diameter at the collector. A scaling law has been proposed to calculate the radius of the jet near the nozzle,

$$h = \left(\frac{6\mu\rho Q^2}{\pi I E}\right)^{\frac{1}{2}} \cdot \frac{1}{z} \qquad \text{Eq. 3-2}$$

where h is the radius of the jet, μ is the kinematic viscosity (or the viscosity divided by the density of the solution), ρ is the density of the fluid, Q is the flow rate, I is the current, E is the

electric field, and z is the needle-to-collector distance.[6] Another law is proposed to calculate the radius of the jet at the collector,

$$h = \left[\gamma\varepsilon\left(\frac{Q}{I}\right)^2 \cdot \frac{2}{\pi(2\ln\chi - 3)}\right]^{\frac{1}{3}} \qquad \text{Eq. 3-3}$$

where γ is the surface tension, ε is the dielectric constant of the outside medium (*i.e.* air), and χ is the slope of the jet's surface.[5, 6, 10, 11] Most importantly, these equations demonstrate that flow rate, current (or voltage), and collection distance play crucial roles in controlling fibre diameter during electrospinning.

Though numerous studies have been done on the effect of processing parameters on randomly distributed Nylon 6 fibre morphology,[12-14] there still exists a gap in studying the effect of these parameters on aligned Nylon 6 fibres using a drum collector. In this Chapter, multiple processing parameters for the electrospinning of neat Nylon 6 fibres are evaluated and the effect of these parameters on fibre diameter and alignment are reported. The parameters investigated are drum rotation speed, applied voltage, needle-to-collector distance, and flow rate. Scanning electron microscopy (SEM) imaging was used to both visualize and quantify the degree of alignment and fibre diameters. A detailed description of the electrospinning set-up and a small study into the effect of jet focusing is also presented.

3.2 Experimental

3.2.1 Chemicals and Materials

Nylon 6 pellets (CAS No. 25038-54-4) were purchased from Sigma-Aldrich (Oakville, ON, CA). BD PrecisionGlide needles (20g x 1 (0.9 mm x 25 mm)) and 3 mL luer lock BD syringes (I.D. = 8.56) were purchased from SigmaAldrich Canada (Oakville, ON, Canada). The needle tips

were sanded down using a Dremel rotary sander loaded with a 180 grit sanding disc to obtain blunt-end needles (Mount Prospect, IL, USA). Acros Organic Formic acid (FA, 98%+) and Saint-Gobain Tygon Ultra-Chemical-Resistant Tubing (Formula 2375) were purchased from Fisher Scientific Canada. Masterflex Fitting, Polypropylene, Straight Male and Female Luer Lock to Hosebarb Adapters (1/16-inch ID) were purchased from Cole-Parmer (Montreal, QC, Canada).

3.2.2 Preparation of Nylon 6 Solutions

Electrospinning solutions were prepared by slowly adding Nylon 6 pellets to formic acid at a loading of 20 wt/v%, then sonicating for 30 minutes. The solutions were left to stir overnight at ambient conditions until all the pellets were dissolved. Each solution was vortexed then sonicated for 5 minutes prior to electrospinning.

3.2.3 Electrospinning

Aligned electrospinning was performed using an 80 mm x 200 mm stainless steel drum collector from MTI Corporation (Richmond, CA, USA) and an external power supply. The stainless-steel drum was wrapped with aluminum foil. A single 3 mL syringe connected to a blunt-tip needle *via* tygon tubing was used and was kept stationary during electrospinning. A copper wire bent into a ring (d = 5 cm) was placed on the syringe needle to focus the electric field during spinning. Electrospinning time was 30-60 minutes for each sample and was performed in a plexiglass chamber to control humidity (RH ~ 25% and T ~ 18˚C) as shown in Figure 3-1.

A table of the all the electrospinning processing parameters studied is presented in Table 3-1. If rotation speed was ≤ 2500 rpm, the voltage was kept at 14 kV, the flow rate was kept at 2 µL/min, and the distance was kept at 10 cm. If rotation speed was ≥ 3000 rpm, the voltage was

kept at 21 kV, the flow rate was kept at 5 µL/min, and the distance was kept at 10 cm. When varying distance (5-13 cm), voltage was kept at 21 kV and flow rate was kept at 5 µL/min. When varying voltage (14-24 kV), distance was kept at 10 cm and flow rate was kept at 5µL/min. When varying flow rate, (1-7 µL/min) voltage was kept at 21 kV and distance was kept at 10 cm. A study on jet focusing was done at the faster rotational speeds (≥ 2500 rpm) using the Cu wire ring (pictured in Figure 2-3).

Table 3-1. Electrospinning parameters and the corresponding rotation speeds investigated in this chapter.

		Drum Rotation Speed (rpm)							
		0	100	500	1000	2000	2500	3000	4000
Voltage (kV)	14	*X*	*X*	*X*	*X*	*X*	*X*	*X*	
	17								*X*
	21						*X*	*X*	*X*
	24							*X*	*X*
Distance (cm)	5						*X*	*X*	*X*
	7								*X*
	8							*X*	
	10	*X*	*X*	*X*	*X*	*X*	*X*	*X*	*X*
	13								*X*
Flow Rate (µL/min)	1							*X*	
	2	*X*	*X*	*X*	*X*	*X*	*X*	*X*	*X*
	4								*X*
	5						*X*	*X*	*X*
	6								*X*
	7							*X*	*X*
Jet Focusing							*X*	*X*	*X*

3.2.4 Characterization

Scanning electron microscopy (SEM) images were taken using a Zeiss Sigma (Gemie) field emission scanning electron microscope at nanoFAB. Electrospun samples were kept on the aluminum foil and cut into 1cm x 1cm squares then placed onto SEM stubs using carbon tape. All samples were imaged using an EHT of 1.00 kV and using the SE2 Everhart-Thornley or InLens detector. Image analysis was completed using the ImageJ software. For fibre diameter analysis, n

= 30 for all samples. For degree of alignment analysis, n = 90 for the samples collected with jet focusing and n = 30 for the remaining samples. The degree of alignment of each fibre was corrected in respect to the spinning direction.

3.3 Results and Discussion

Humidity Chamber. Humidity plays a crucial role in the efficacy of electrospinning and consistency in the morphology of the fibres.[15] Therefore, in order to maintain the humidity during electrospinning, I designed a custom 5-walled plexiglass chamber with the Mechanical Shop in the Department of Chemistry, as shown below in Figure 3-1.

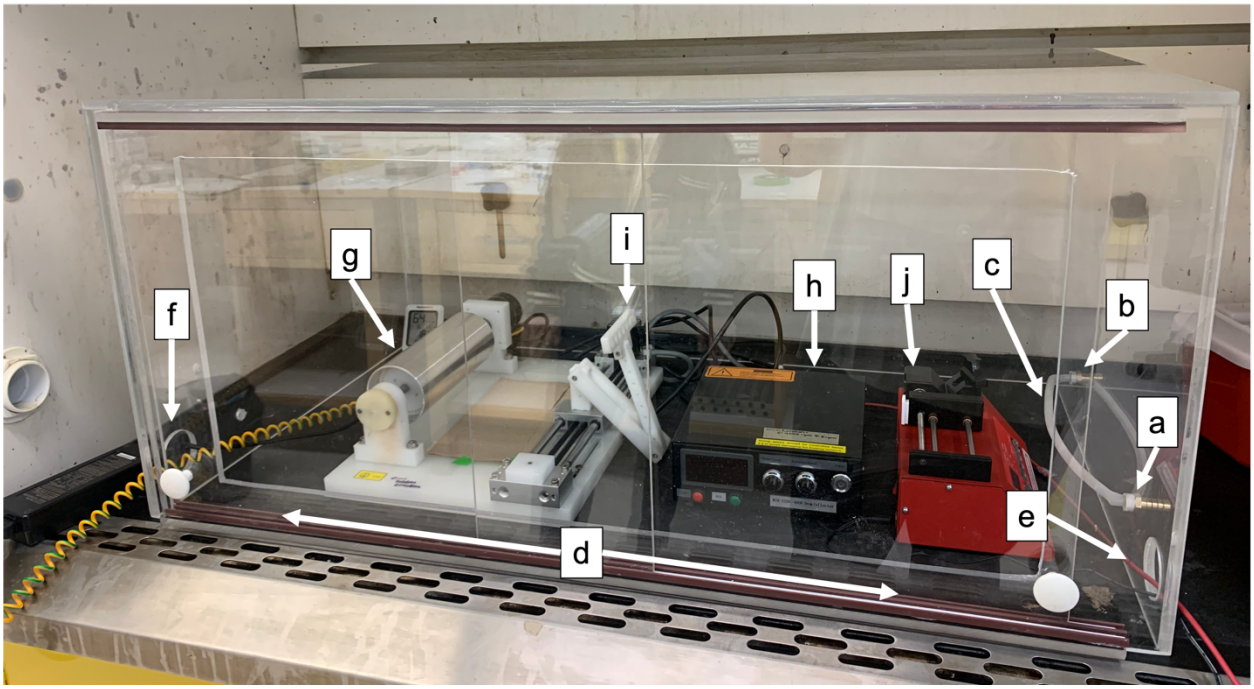

Figure 3-1. Photograph of the rotating drum electrospinner set-up inside the plexiglass chamber. Each of the components are labelled as follows: a) air inlet, b) air outlet, c) air disperser, d) sliding door, e) cord connected to power supply, f) grounding wire, g) rotating drum, h) drum control box, i) arm that holds syringe(s), and j) syringe pump.

The chamber is made of 1” thick plexiglass sheets bound together by chloroform. An inlet on the side of the chamber (Fig. 3-1a) allowed for dry air to be pumped into the box, and the outlet (Fig. 3-1b) prevented pressure buildup in the box. Holes were drilled along the length of a polyethylene hose that was fashioned into a disperser (Fig. 3-1c), which was connected between the inlet and outlet to prevent excess airflow during electrospinning. Sliding plexiglass doors in the front allowed for easy access into the chamber as well as a way to control humidity (Fig. 3-1d). The bottom of the chamber was open so that the counter of the fumehood was exposed. All power cords and connectors were fed through holes drilled into the sides of the chamber (Fig. 3-1e,f), then covered with tape to trap air flow in the box. The humidity and temperature were measured with a portable monitor in the chamber. The relative humidity and temperature for the fibre mats collected and characterized in this Chapter were measured at ~ 25% and ~ 18˚C, respectively.

The chamber houses all instrumentation *sans* the external power supply for electrospinning. The rotating drum electrospinner consists of a rotating drum (Fig. 3-1g) and a control box (Fig. 3-1h). The control box changes the drum rotation speed and the transverse speed of the moveable arm that holds the syringe needle (Fig. 3-1i); however, in this study, the moveable arm was kept stationary at the centre of the drum. Finally, the syringe pump was also placed inside the chamber (Fig. 3-1j). The wiring and alligator clip connected to the power supply (the red wire in Fig. 3-1) were fed through one of the holes on the side of the chamber (Fig. 3-1e). The grounding wire for the rotating drum (the yellow and green coiled wire) was fed through the other hole on the other side of the chamber (Fig 3-1f). Each wire and cord were also wrapped with a paper towel at any place of contact between wires to mitigate charge buildup on the coatings of the wires/cords fed through the same hole.

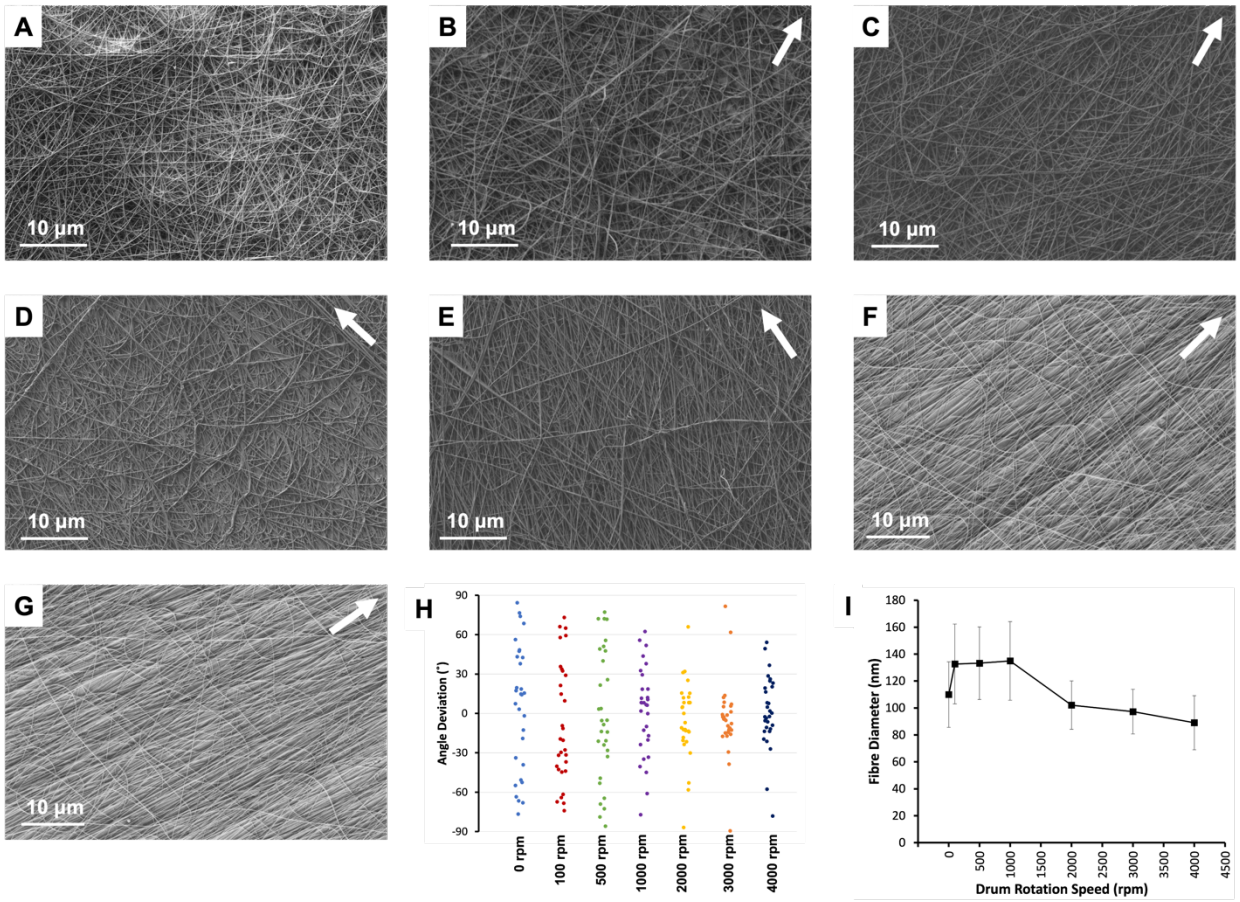

Figure 3-2. SEM images of electrospun mats collected at increasing drum rotation speeds: A) 0 rpm, B) 100 rpm, C) 500 rpm, D) 1000 rpm, E) 2000 rpm, F) 3000 rpm, G) 4000 rpm, H) a jitter plot of the angles of deviance for the fibres in each mat, and I) a plot of the fibre diameters for each fibre mat. The white arrows indicate drum rotation direction.

Varying Drum Rotation Speed. The alignment of the Nylon 6 fibres with increasing drum rotational speeds was first studied. Scanning electron microscopy (SEM) images of the resultant fibre mats are presented in Figures 3-2 A to G. A jitter plot visualizing the spread of the angles of deviance of the fibres with respect to spinning direction in each mat is presented in Figure 3-2H and a plot of the fibre diameters for each sample is presented in Figure 3-2I. The fibres at all collection speeds were long, smooth, and thin. All fibre mats had super-fine "spider-web" fibres in addition to the thicker fibres. Islam *et al.* suggested that the amide groups in Nylon 6 are ionized in formic acid when a high voltage is applied during electrospinning, which causes electrostatic

repulsion between individual polymer chains and thereby reduces the viscosity in small regions of the solution.[16] Though these "spider-web" fibres are present, the morphology of the larger fibres was not affected.

The degree of alignment of individual fibres is directly related to the collection speed when using a rotating drum,[1, 12] therefore, the differences in the alignment and diameter of the fibres were quantified using SEM. At 0 rpm (or randomly distributed fibres), the fibres are orientated in numerous different directions and have an average diameter of 110 nm (Fig. 3-2A). When the drum rotation speed is increased to 500 rpm (Fig. 3-2B), there is an increase in average fibre diameter to 133 nm due to a change from the stationary collector used at 0 rpm and the rotating drum used at 500 rpm; however, the alignment of the fibres does not differ significantly from the randomly distributed fibres (Fig. 3-2H). The alignment deviations and the average fibre diameters stay relatively the same until 2000 rpm (Fig. 3-2E), where the fibre diameter decreases to an average of 102 nm and the alignment angles become less deviant and start to become more centralized around the norm. This is also visually observed as the fibres appear more aligned in Figure 3E. At 3000 rpm (Fig. 3-2F), a significant portion of the fibres fall within 30˚ of the norm and the fibre diameters decrease slightly to an average of 97 nm. Finally, at 4000 rpm (Fig. 3-2G), the angles of deviation of the fibres are relatively similar to those collect at 3000 rpm; however, the average diameter decreases further to 89 nm. The decrease in diameter over increasing drum rotation speeds is due to the process of aligning the fibres, which is caused by the drum collector physically stretching the fibres into alignment. At increasing collection speeds, the stretching tensile force also increases which further thins the fibres.[17] Overall, the fibres were more aligned and thinner with increasing drum rotation speed.

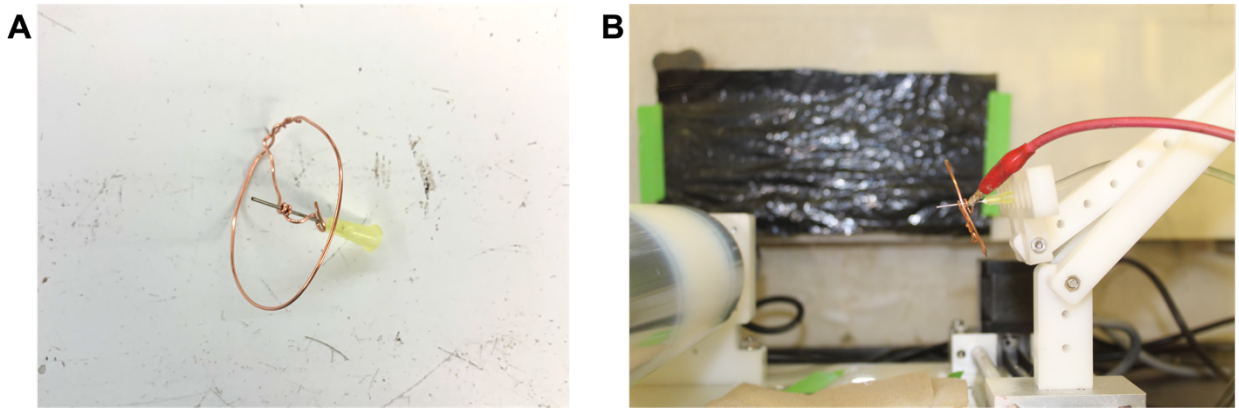

Figure 3-3. Photographs of the copper wire ring placed onto the syringe needle for jet focusing.

Jet Focusing. In order to achieve greater alignment, a copper wire was fashioned into a ring and placed onto the syringe needle while electrospinning, as depicted in Figure 3-3. The wire acts as a conductive ring that confines the jet by constraining the electric field.[17] The main goals of focusing the jet and electric field around the jet is to inhibit the whipping motion of the jet early-on during spinning, which results in a decrease in the spot size for fibre collection.[17] By stabilizing the movement of the jet during this unstable whipping stage, the fibres are less likely to orient randomly onto the collector. The copper wire ring reported here is a quick and simple approach compared to the use of complex electrodes for improved fibre alignment reported in previous studies.[2, 18]

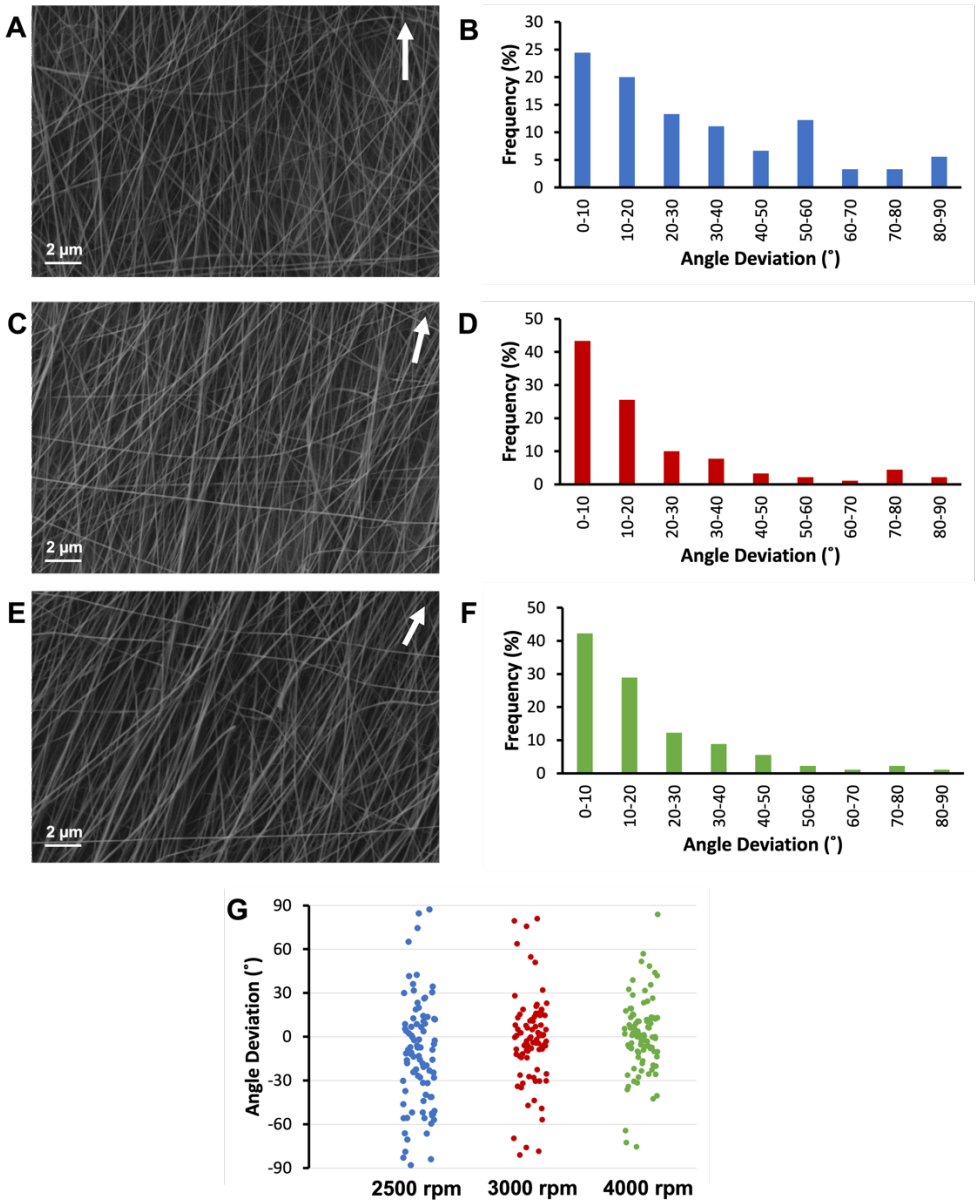

Figure 3-4. Effect of jet focusing on the alignment of fibres. SEM images of focusing done at A) 2500 rpm, C) 3000 rpm, and D) 4000 rpm. Distribution frequency for the angle of alignment of fibres collected at B) 2500 rpm, D) 3000 rpm, and F) 4000 rpm, and G) a jitter plot of the angles of deviance for each of the fibre mats. The white arrows indicate drum rotation direction.

The effect of jet focusing was visualized and quantified using SEM, as shown in Figure 3-4. Three drum rotation speeds were investigated: 2500 rpm (Fig. 3-4 A, B), 3000 rpm (Fig. 3-4 C, D), and 4000 rpm (Fig. 3-4 E, F). No changes in fibre morphology were found when jet focusing was used (Fig. 3-4 A, C, D). As expected, the alignment of the fibres increased with increasing

rotational speeds. In the 2500 rpm fibre mats, 58% of the fibres fell within 30˚ of the norm (Fig. 3-4B), which drastically increased to 79% at 3000 rpm (Fig. 3-4D). Alignment further increased at 4000 rpm where 83% of fibres fell within 30˚ of the norm (Fig. 3-4F). The alignment impact is also visualized in the jitter plot in Figure 3-4G, where the fibres spun at 2500 rpm have a larger spread of angles whereas the fibres spun at 4000 rpm have a higher number of fibres aligned closer to the norm (or 0˚). The combination of focusing and high drum rotation speed appear to have a large impact on Nylon 6 fibre alignment. The remainder of the data presented in this Chapter was collected using jet focusing.

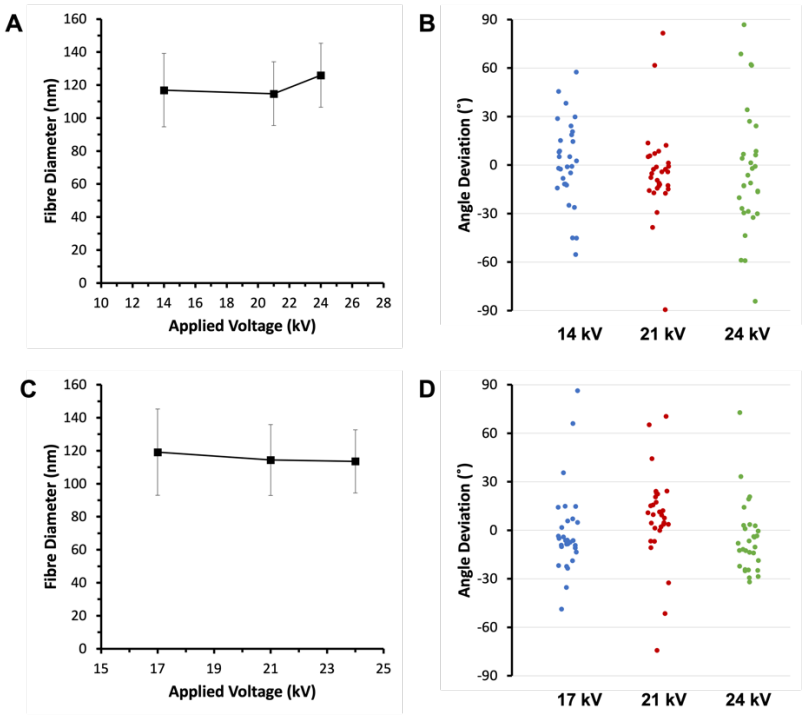

Figure 3-5. Effect of varying voltage on fibres collected at 3000 rpm on A) fibre diameters and B) alignment, and at 4000 rpm on C) fibre diameters and D) alignment.

Varying Voltage. In electrospinning, an external power supply is used to apply a high voltage to the blunt-end metal needle of a syringe containing a polymer solution. By applying a

high voltage, a charge is built up on the needle and propagated to the surface of a polymer drop at the needle tip.[2] The drop is attracted to a grounded metal collector (in this case, a drum collector) and fibres are deposited on the surface. Figure 3-5 shows the fibre diameters and angles of deviance when fibres were collected at 3000 rpm (Fig. 3-5 A, B) and at 4000 rpm (Fig. 3-5 C, D) with varying voltages between 14 and 24 kV. In both cases, the fibre diameters did not differ significantly between voltages; however, the fibres collected at 3000 rpm did increase slightly in average diameter when spun with an applied voltage of 24 kV and the fibres collected at 4000 rpm decreased slightly in average diameter when spun with increasing applied voltages. According to Equation 3-1, an increase in applied voltage will decrease fibre diameter, which is in agreement with the data presented in Figure 3-5. This is also consistent with a previous report from Bazbouz *et al.* showing that randomly distributed Nylon 6 fibres decreased in fibre diameter with increasing voltage.[13] The jitter plots visualizing the spread of the angles of deviance in Figure 3-5 B,D show that most fibres stayed within 30˚ of the spinning direction, but at 21 kV, there are a higher proportion of fibres closer to the norm.

Varying Flow Rate. In solution electrospinning, a syringe loaded with a polymer solution is placed in a syringe pump that depresses the plunger of the syringe at a constant rate. The rate at which the solution is expelled from the syringe has a direct effect on the stability of the polymer drop at the tip of the needle, and therefore an effect on the stability and formation of the Taylor cone.[7, 9] It has been found that increasing the flow rate also increases fibre diameter because a larger polymer drop is formed at the needle tip; however, a faster flow rate comes at the cost of slower solvent evaporation and lower charge density.[19] Additionally, a study done on the effect of flow rate on randomly distributed Nylon 6 fibre mats showed that a faster flow rate increased the deposition area on the stationary collector.[7]

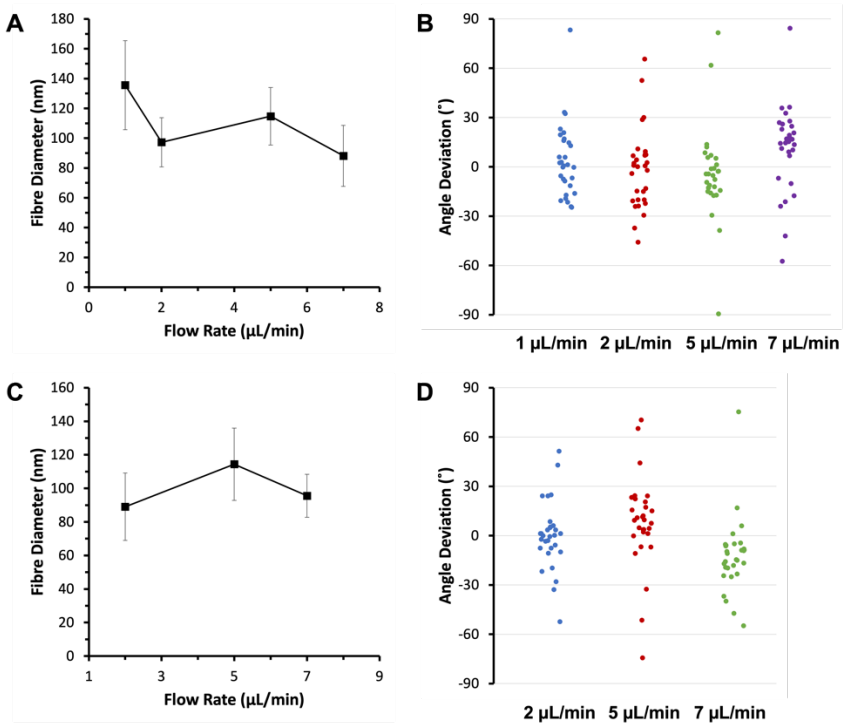

Figure 3-6. Effect of varying flow rate on fibres collected at 3000 rpm on A) fibre diameters and B) alignment, and at 4000 rpm on C) fibre diameters and D) alignment.

Figure 3-6 shows the effect of flow rate on the fibre diameter and alignment of fibres collected at 3000 rpm (Fig. 3-6 A, B) and at 4000 rpm (Fig. 3-6 C, D). Interestingly, the average fibre diameters decreased by approx. 50 nm with increasing flow rates when collected at 3000 rpm (Fig. 3-6A). The fibre diameters increased to a max of 114 nm at 5 µL/min then decreased to 95 nm at 7 µL/min when collected at 4000 rpm (Fig. 3-6C). Both collection speeds showed the smallest fibre diameter at 2 µL/min, with average values of 97 nm for 3000 rpm and 89 nm for 4000 rpm. The decrease in diameter at 4000 rpm is due to the faster collection speed, which thins the fibres as explained previously. Though this seems to be contrary to what was stated previously about increasing fibre diameters with increasing flow rates, it is important to note that the applied voltage was not altered at each flow rate. This means that at a higher flow rate there was less charge per area on the polymer drop,[20] which is shown by the increase in fibre diameter at 5 µL/min at

both collection speeds. Equation 3-3 also shows that an increase in flow rate while keeping all other parameters constant will also increase fibre diameter at the collector. There was no significant effect on the alignment of fibres with varying flow rates, as shown in Figures 3-6B and 3-6D. Finally, none of the fibres collected in this study had beading, meaning that the flow rates used here are below the critical flow rate for the electrospinning of Nylon 6 fibres.[19]

Varying Needle-to-Collector Distance. Finally, the effect of needle-to-collector distance on fibre diameter and alignment was investigated. By varying the distance, a few processes can be affected: 1) the solvent evaporation rate, 2) the area of the stable and unstable whipping regions, and 3) the thickness and deposition area of the fibre mat.[19] The whipping instabilities during electrospinning causes thinning of the fibres before deposition. By decreasing the area of this region, the jet goes through less (and sometimes no) whipping which generates thicker fibres. Too slow or too fast evaporation rates can also cause fusion of the fibres after collection.[19] A previous study on the collection distance on randomly distributed Nylon 6 fibres also showed that the diameter of the resultant fibre mat decreased with decreasing distances.[21]

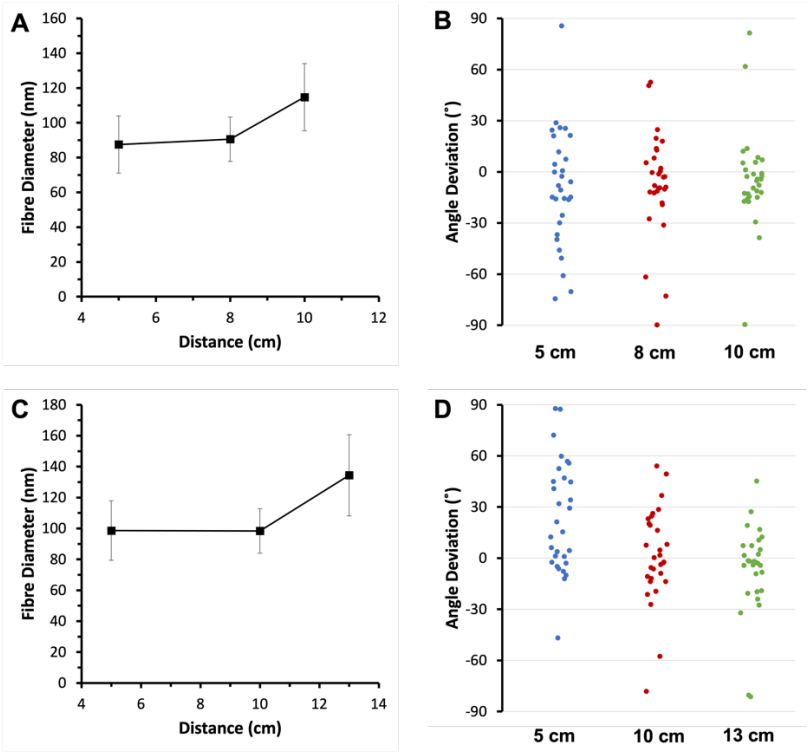

Figure 3-7. Effect of varying needle-to-collector distance on fibres collected at 3000 rpm on A) fibre diameters and B) alignment, and at 4000 rpm on C) fibre diameters and D) alignment.

Figure 3-7 shows the effect of collection distance on the fibre diameter and alignment for fibres collected at 3000 rpm (Fig. 3-7 A,B) and at 4000 rpm (Fig. 3-7 C,D). Surprisingly, at both drum rotation speeds, the average fibre diameter increased with increasing collector distance (Fig. 3-7 A,C). On the other hand, the alignment of the fibres improved with farther collection distances (Fig. 3-7 B,D). Again, it is important to note that the voltage and flow rate was kept consistent at all distances studied. A larger needle to collector distance means that the electric field area is larger which leads to a decrease in the attraction of the charged jet to the grounded collector, as described in the simplified electric field equation below,

$$E = \frac{U}{d} \qquad \text{Eq. 3-4}$$

where, E is the electric field strength, U is the voltage, and d is the needle-to-collector distance.[10] According to Equation 3-4, if the needle-to-collector distance is increased, then the

electric field strength decreases when U is constant. This means that the jet is experiencing a weaker E which reduces the sharpness of the Taylor cone thereby increasing fibre diameter.[19] This phenomenon is also described by Equation 3-2 where an increase in z (or needle-to-collector distance) will cause an increase in fibre diameter at the collector when all other parameters are constant.[6]

3.4 Conclusion

The effect of processing parameters on Nylon 6 fibre diameter and alignment in aligned electrospinning was studied. The parameters investigated were: 1) drum rotation speed, 2) jet focusing, 3) applied voltage, 4) flow rate, and 5) needle-to-collector distance. In order to control humidity during spinning, a custom-built humidity chamber was used to house the electrospinning set-up. Drum rotation speeds from 0 to 4000 rpm were investigated, where fibre diameter decreased and alignment increased with increasing collection speed. Degree of alignment increased when a copper wire fashioned into a ring was placed onto the needle to focus the jet while spinning, thus jet focusing was used for the rest of the study to obtain good alignment of the fibre mats. Varying applied voltage did not significantly alter fibre diameter, but a voltage of 21 kV gave rise to better fibre alignment. Fibre diameter increased at a flow rate of 5 μL/min but decreased at flow rates above and below this feed rate. There was also a slightly better alignment at this value. Finally, increasing collection distance produced thicker fibres and slightly better alignment at 10 cm.

3.5 References

1. Xue, J.; Wu, T.; Dai, Y.; Xia, Y., Electrospinning and Electrospun Nanofibers: Methods, Materials, and Applications. *Chemical Reviews* **2019,** *119* (8), 5298-5415.
2. Sahay, R.; Thavasi, V.; Ramakrishna, S., Design Modifications in Electrospinning Setup for Advanced Applications. *Journal of Nanomaterials* **2011,** *2011*, 317673.
3. Taylor, G., Electrically Driven Jets. *Proceedings of the Royal Society of London. Series A, Mathematical and Physical Sciences* **1969,** *313* (1515), 453-475.
4. Ko, F. K.; Wan, Y., 4.2 Fundamentals of Process Modeling. In *Introduction to Nanofiber Materials*, Cambridge University Press.
5. Fridrikh, S. V.; Yu, J. H.; Brenner, M. P.; Rutledge, G. C., Controlling the Fiber Diameter during Electrospinning. *Physical Review Letters* **2003,** *90* (14), 144502.
6. Cramariuc, B.; Cramariuc, R.; Scarlet, R.; Manea, L. R.; Lupu, I. G.; Cramariuc, O., Fiber diameter in electrospinning process. *Journal of Electrostatics* **2013,** *71* (3), 189-198.
7. Zargham, S.; Bazgir, S.; Tavakoli, A.; Rashidi, A. S.; Damerchely, R., The Effect of Flow Rate on Morphology and Deposition Area of Electrospun Nylon 6 Nanofiber. *Journal of Engineered Fibers and Fabrics* **2012,** *7* (4), 155892501200700414.
8. Khajavi, R.; Abbasipour, M., 5 - Controlling nanofiber morphology by the electrospinning process. In *Electrospun Nanofibers*, Afshari, M., Ed. Woodhead Publishing: 2017; pp 109-123.
9. Wendorff, J. H.; Agarwal, S.; Greiner, A.; Agarwal, S., *Electrospinning : Materials, Processing, and Applications*. John Wiley & Sons, Incorporated: Hoboken, GERMANY, 2012.
10. Yang, Y.; Jia, Z.; Liu, J.; Li, Q.; Hou, L.; Wang, L.; Guan, Z., Effect of electric field distribution uniformity on electrospinning. *Journal of Applied Physics* **2008,** *103* (10), 104307.
11. Laudenslager, M. J.; Sigmund, W. M., Electrospinning. In *Encyclopedia of Nanotechnology*, Bhushan, B., Ed. Springer Netherlands: Dordrecht, 2012; pp 769-775.
12. Lee, K.-H.; Kim, K.-W.; Pesapane, A.; Kim, H.-Y.; Rabolt, J. F., Polarized FT-IR Study of Macroscopically Oriented Electrospun Nylon-6 Nanofibers. *Macromolecules* **2008,** *41* (4), 1494-1498.
13. Bazbouz, M. B.; Stylios, G. K., Alignment and optimization of nylon 6 nanofibers by electrospinning. *Journal of Applied Polymer Science* **2008,** *107* (5), 3023-3032.
14. Borges, A. L. S.; Münchow, E. A.; de Oliveira Souza, A. C.; Yoshida, T.; Vallittu, P. K.; Bottino, M. C., Effect of random/aligned nylon-6/MWCNT fibers on dental resin composite reinforcement. *Journal of the Mechanical Behavior of Biomedical Materials* **2015,** *48*, 134-144.
15. Pelipenko, J.; Kristl, J.; Janković, B.; Baumgartner, S.; Kocbek, P., The impact of relative humidity during electrospinning on the morphology and mechanical properties of nanofibers. *Int J Pharm* **2013,** *456* (1), 125-34.
16. Islam, M. S.; McCutcheon, J. R.; Rahaman, M. S., A high flux polyvinyl acetate-coated electrospun nylon 6/SiO2 composite microfiltration membrane for the separation of oil-in-water emulsion with improved antifouling performance. *Journal of Membrane Science* **2017,** *537*, 297-309.
17. Beachley, V.; Katsanevakis, E.; Zhang, N.; Wen, X., Highly Aligned Polymer Nanofiber Structures: Fabrication and Applications in Tissue Engineering. In *Biomedical Applications of Polymeric Nanofibers*, Jayakumar, R.; Nair, S., Eds. Springer Berlin Heidelberg: Berlin, Heidelberg, 2012; pp 171-212.
18. Yuan, H.; Zhou, Q.; Zhang, Y., 6 - Improving fiber alignment during electrospinning. In *Electrospun Nanofibers*, Afshari, M., Ed. Woodhead Publishing: 2017; pp 125-147.

19. Haider, A.; Haider, S.; Kang, I.-K., A comprehensive review summarizing the effect of electrospinning parameters and potential applications of nanofibers in biomedical and biotechnology. *Arabian Journal of Chemistry* **2018,** *11* (8), 1165-1188.
20. Tijing, L. D.; Woo, Y. C.; Yao, M.; Ren, J.; Shon, H. K., 1.16 Electrospinning for Membrane Fabrication: Strategies and Applications. In *Comprehensive Membrane Science and Engineering (Second Edition)*, Drioli, E.; Giorno, L.; Fontananova, E., Eds. Elsevier: Oxford, 2017; pp 418-444.
21. Hekmati, A. H.; Rashidi, A.; Ghazisaeidi, R.; Drean, J.-Y., Effect of needle length, electrospinning distance, and solution concentration on morphological properties of polyamide-6 electrospun nanowebs. *Textile Research Journal* **2013,** *83* (14), 1452-1466.

Chapter 4. Influence of Cellulose Nanocrystals on the Mechanical Properties and Crystallization of Aligned Nylon 6 Electrospun Fibre Mats

4.1 Introduction

In Chapter 3, the effect of electrospinning parameters on neat Nylon 6 fibre alignment was investigated. As mentioned previously, by using a rotating drum collector, the orientation of the produced fibres within the mat can be controlled. Stationary collectors give rise to randomly distributed fibres. Both the syringe needle and the substrate are kept stationary, which allows for the bending instabilities of the polymer jet to randomly deposit fibres onto the substrate as a multilayered non-woven network.[1] The final mat has fibres with vastly varying alignments. The use of a network of randomly distributed fibres are desirable for many different applications, including drug delivery and adsorption.[2, 3] On the other hand, fibres can be forced into alignment using two main methods: electrostatic repulsion between two collectors while spinning or physical stretching of the polymer fibres into alignment using a rotating collector.[4-6] As was shown in Chapter 3, by increasing the rotational speed of the drum collector, fibres became increasingly aligned with the spinning direction. By aligning the fibres with respect to each other, the stress transfer is dissipated along the axis of the fibres thus increasing the elastic modulus and tensile strength.[6, 7] The alignment of polymer fibres can be used further for processing into braided yarns or ropes for a variety of applications including textiles, sutures, and sensors.[8-11]

The next step is to incorporate CNC into electrospun Nylon 6 fibres. The interest in cellulose nanomaterials has expanded over the past few decades. The use of a cellulose-based nanomaterial in polymer composites is appealing as a bio-based reinforcing filler due to the biorenewability and biodegradability of the material itself.[12] As mentioned previously, CNC has been widely used in composites as it gives rise to large increases in elastic modulus with very little loading percentages.[12, 13] CNCs can favourably interact with a polymer matrix *via* hydrogen bonding, and alongside the highly crystalline and stiff nature of CNCs, they can ultimately increase the mechanical properties of a composite.[12] However, the main concern when using CNC is the prevention of inter-particle aggregation that tends to lead to lower mechanical properties, as has been extensively discussed in the previous Chapters.[14, 15] Therefore, solvent mixing and sonication in aqueous or highly polar solvents, such as for solution cast thin films and electrospinning, is used to obtain uniform dispersions of CNC within a composite rather than direct mixing such as in melt extrusion or compounding.[16]

Nylon 6 is one of the most commonly used polymers for the production of industrial fibres, ropes, and thin films.[17] It is a semi-crystalline polymer that changes crystal structure depending on processing technique used, temperature, or with the addition of fillers.[18] As was observed in Chapter 2, CNC has been shown to influence changes in the crystalline structure of Nylon 6 thin films.[14, 19] Other than one report by Buyukada-Kesici *et al.* looking into the adsorptive properties of CNC-Nylon 6 randomly distributed electrospun fibre mats,[3] no studies investigating the influence of CNC on the crystal structure of electrospun Nylon 6 fibres have been previously reported.

Herein, this Chapter describes the mechanical results of CNC-Nylon 6 composite fibres using either a stationary or rotating drum collector. Then, the chemical and thermal properties, as

well as the crystallization, of the aligned Nylon 6 fibres is investigated using FTIR, DSC, and XRD. The influence on these properties when CNC is added is discussed. To my knowledge, this is the first report of aligned CNC-Nylon 6 fibres using in-solution electrospinning.

4.2 Experimental

4.2.1 Chemicals and Materials

Nylon 6 pellets (CAS No. 25038-54-4) were purchased from SigmaAldrich Canada (Oakville, ON, CA). Spray-dried sulfate half-ester Na-form cellulose nanocrystals (CNC) were purchased from Celluforce (Montreal, QC, CA). BD PrecisionGlide needles (20 g x 1 (0.9 mm x 25 mm)) and 3 mL luer lock BD syringes (I.D. = 8.56) were purchased from SigmaAldrich Canada (Oakville, ON, CA). The needle tips were sanded down using a Dremel rotary sander loaded with a 180 grit sanding disc to obtain blunt-end needles (Mount Prospect, IL, USA). Acros Organic Formic acid (FA, 98%+) and Saint-Gobain Tygon Ultra-Chemical-Resistant Tubing (Formula 2375) were purchased from Fisher Scientific Canada. Masterflex Fitting, Polypropylene, Straight Male and Female Luer Lock to Hosebarb Adapters (1/16-inch ID) were purchased from Cole-Parmer (Montreal, QC, CA).

4.2.2 Preparation of Cellulose Nanocrystal and Nylon 6 Solutions

Electrospinning solutions of 20 wt/v% (total solids/solvent) were prepared by adding cellulose nanocrystals to formic acid (1, 2.5, and 5 wt/wt% CNC/Nylon 6) and bath sonicating for 30 minutes. Nylon 6 pellets were added to the CNC solution (100, 99, 97.5, and 95 wt/wt% Nylon 6/CNC) while magnetically stirring. The total solids in solution was 20 wt/v%. The solutions were left to stir overnight at ambient conditions until all the pellets were dissolved. Each solution was

vortexed then sonicated for 5 minutes prior to electrospinning and used no more than 2 weeks after preparation to prevent using CNCs that could be acid hydrolyzed by formic acid.

4.2.3 Production of Randomly Distributed Electrospun Fibre Mats

Randomly distributed electrospun fibres were collected on a 20 cm x 20 cm stainless steel plate that was covered with aluminum foil. A single 3 mL syringe with a blunt-tip needle was used. Electrospinning was performed with a constant flow rate of 2 µL/min, a constant voltage of 21 kV, and a working distance (tip of syringe needle-to-collector distance) of 10 cm. Electrospinning time was 3 hours for each sample and done at ambient conditions (RH ~ 37% and T ~ 21˚).

4.2.4 Production of Aligned Electrospun Fibre Mats

Aligned electrospinning was done using an 80 mm x 200 mm drum collector from MTI Corporation (Richmond, CA, USA). The stainless-steel drum was wrapped with aluminum foil. A single 3 mL syringe connected to a blunt-tip needle *via* tygon tubing was used and kept stationary during the electrospinning process. A copper wire bent into a ring (d = 5cm) was placed on the syringe needle to focus the electric field during spinning. The aligned fibre mats used for mechanical testing were produced using optimal conditions for each solution concentration dependent on the formation of the Taylor Cone, thus, flow rate and voltage differed between samples because of a change in solution viscosity due to the addition of CNC. Keeping working distance and rotational speed constant (10 cm and 4000 rpm, respectively), the following flow rates and voltages were used: 2 µL/min & 18 kV (100% Nylon 6), 1.5 µL/min & 20 kV (1 wt% CNC), 1 µL/min & 20 kV (2.5 wt% CNC), and 0.8 µL/min & 21 kV (5 wt% CNC). Electrospinning

time was 3 hours for each sample and was done in a plexiglass chamber to control humidity (RH ~ 25% and T ~ 18˚C).

4.2.5 Characterization

Scanning electron microscopy (SEM) images were taken using a Zeiss Sigma (Gemie) field emission scanning electron microscope at nanoFAB. Electrospun samples were kept on the aluminum foil and cut into 1cm x 1cm squares then placed onto SEM stubs using carbon tape. All samples were imaged using an EHT of 3.00 kV and using the SE2 Everhart-Thornley or InLens detector for the aligned or randomly distributed fibres, respectively. Image analysis was completed using the ImageJ software. Fibre diameter visualization was created using an open-source program and represented as an average shifted histogram (ASH) plot.[20]

Transmission electron microscopy (TEM) images were completed by the Microscopy Facility in the Department of Biological Sciences using a Philips/FEI (Morgagni) transmission electron microscope with Gatan camera at 80 kV. Samples were cut from the aligned electrospun mats and exposed to osmium tetroxide vapour for 1 hour, then embedded in Spurr resin and cured overnight at 60˚. A microtome was used to smooth the resin blocks to the correct depth, then final sections were taken using a diamond knife and placed on a Cu mesh grid.

Fourier transform infrared (FTIR) analysis was completed by the Analytical Instrumentation Lab in the Department of Chemistry using a Thermo Nicolet 8700 FTIR Spectrometer. A freestanding sample was cut from the fibre mat and placed in the pathlength of the laser. All spectra were collected from 4000 to 650 cm^{-1} at 128 sample scans and a resolution of 4.000.

Differential scanning calorimetry (DSC) was completed using a TA Instruments DSC-Q1000 at nanoFAB. Samples (4-5mg) were placed in a hermetic aluminum DSC pan, then heated from 25˚C to 250˚C at a heating rate of 10˚C/min and under nitrogen. In the percent crystallinity calculations, a value of 230 J/g for ΔH_f^{100} of Nylon 6 was used. Data was processed using the TA Universal Analysis software.

Thermogravimetric analysis (TGA) was competed using a TA Instruments Discovery TGA at nanoFAB. Samples (4-5mg) were placed in a platinum sample holder, then heated from 25˚C to 500˚C at heating rate of 10˚C/min and under nitrogen. Data was processed using the TA Universal Analysis software.

X-Ray diffraction (XRD) analysis was completed using a Rigaku Ultima IV XRD at nanoFAB. It was equipped with a Cu x-ray target, with operating voltage of 40 kV and 44 mA. The parallel beam was used at a scan axis of 2theta with glancing angle omega at 0.5˚. Scan mode was continuous, sampling width was 0.05˚ with a range from 8˚ to 38˚, and a scan speed of 2˚/min was used. The divergence slit was 0.1˚. Data was processed using Jade 9.0 with ICDD database 2010.

Mechanical tests were performed using the TA Instruments ElectroForce 3200 uniaxial testing machine (10 N max. capacity load cell) by Eyup C. Demir and Jiawei Chen, PhD students in the Department of Mechanical Engineering. Test strips were prepared from the electrospun samples by cutting with a rotary cutter to obtain sample dimensions of 10mm x 75mm then peeling the mats from the aluminum foil. All samples were stored in a desiccator for at least 12 hours to remove excess moisture and residual solvent. The tensile tester instrument has grips that hold 25mm of the test strip, therefore gauge length was set to 50mm between the grips. A C-shaped mechanical testing frame made from paper was used to hold the samples in the grips to prevent

sliding of and reduce stress concentration on the samples during testing. All samples were placed between the grips in a way where the alignment direction of fibres was parallel to the testing direction. All tests were performed at ambient conditions. The strain rate was set at 0.1 mm/mm•min (5mm/min). The results were averaged over 4-5 measurements according to the ASTM 882-12 standard.

4.3 Results and Discussion

The most commonly used solvent for the dissolution of Nylon 6 is formic acid. It is an organic acid that has a pKa of 3.75 and a boiling point of 100.8˚C. Formic acid has also been used to prepare CNCs from pulp as an alternative to sulfuric acid.[21] Not surprisingly, because of the use of formic acid in the preparation of CNCs, the CNCs used in this project were readily dispersed in-solution after sonication. A short study investigating the effect of storage of CNC in formic acid was previously done, as mentioned in Chapter 2. We found that the crystallinity of CNC did not significantly change after storage in formic acid after 7 days (data not shown here). However, all solutions were still used within 2 weeks of preparation to prevent using CNCs that may be potentially acid hydrolyzed by the solvent.

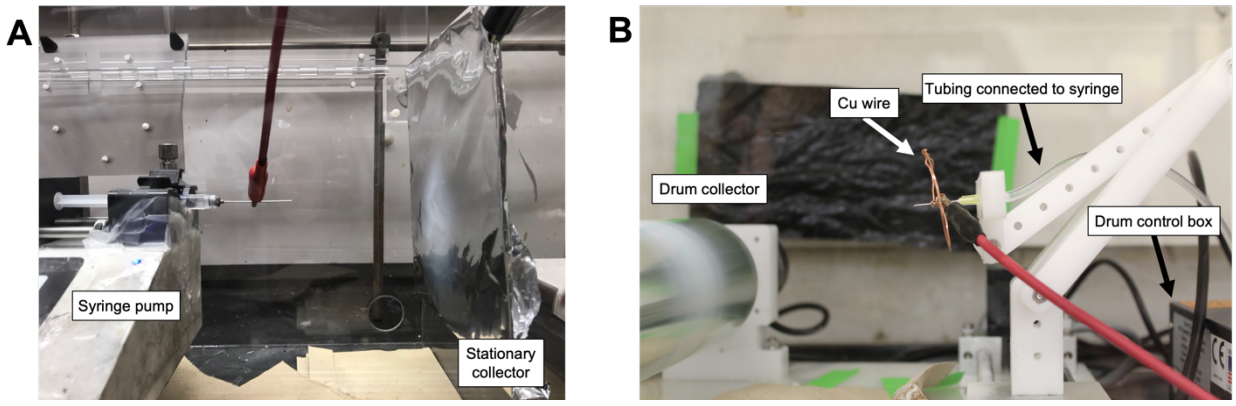

Figure 4-1. Electrospinning set-up for (A) the randomly distributed fibre mats and (B) the aligned fibre mats.

Electrospinning Set-Up. A comparison of the experimental set-up for the randomly distributed and aligned electrospinning methods is pictured in Figure 4-1. In the randomly distributed fibre mats, a 20 x 20 cm metal collector was placed 10 cm away from the tip of the syringe needle, as shown in Figure 4-1A. Fibres were deposited onto an aluminum foil sheet covering the square stationary collector. This collector was chosen for the collection of the randomly distributed fibre mats over a stationary drum collector due to the larger surface area of the sheet, thereby producing larger mats that were later cut for mechanical testing. For the aligned fibre mats, the electrospinning set-up was the same as the one presented in Chapter 3. Briefly, an 80 mm x 200 mm drum collector was rotated at 4000 rpm and a copper wire was used to focus the jet during spinning, as shown in Figure 4-1B. By rotating a drum while electrospinning, the fibres are stretched and forced to physically align in the same direction as rotation. A more detailed description of the rotating drum set-up can be found in Chapter 3.

The surface area of the drum collector is much larger than the stationary collector thus the effective cross-sectional area (or thickness) of the mats was much smaller than the randomly distributed fibre mats when collected over the same electrospinning time. Sample calculations to

find the effective cross-sectional areas of the fibre mat are shown in Equations 4-1 to 4-4 below, with the corresponding values listed in Table 4-1.

The effective cross-sectional area of the composite was calculated by first determining the volume fraction of CNC (Eq. 4-1) and Nylon 6 (Eq. 4-2),

$$V_{CNC} = \frac{\emptyset_{CNC}\rho_{CNC}}{\emptyset_{CNC}\rho_{CNC} + \emptyset_{N6}\rho_{N6}} \qquad \text{Eq. 4-1}$$

$$V_{N6} = \frac{\emptyset_{N6}\rho_{N6}}{\emptyset_{CNC}\rho_{CNC} + \emptyset_{N6}\rho_{N6}} \qquad \text{Eq. 4-2}$$

where, V_{CNC} is the volume fraction of CNC, V_{N6} is the volume fraction of Nylon 6, $\emptyset_{CNC}$ is the mass fraction of CNC, ρ_{CNC} is the density of CNC (1.5 g/cm^3 at 25˚C)[22], $\emptyset_{N6}$ is the mass fraction of Nylon 6, and ρ_{N6} is the density of Nylon 6 (1.084 g/mL at 25˚C).

Then, the composite density (Eq. 4-3) and, finally, the effective cross-sectional area was calculated (Eq. 4-4),

$$\rho_c = V_{CNC}\rho_{CNC} + V_{N6}\rho_{N6} \qquad \text{Eq. 4-3}$$

$$CA_c = \frac{m_c}{\rho_c\, l_s} \qquad \text{Eq. 4-4}$$

where, ρ_c is the density of the composite, m_c is the mass of the composite, CA_C is the effective cross-sectional area of the composite, and l_s is the length of the sample.

Table 4-1. Calculated effective cross-sectional areas of the randomly distributed and aligned fibre mats.

	Effective Cross-Sectional Area (m^2)	
wt% CNC	**Random**	**Aligned**
0	4 ± 1 x10^{-5}	2.1 ± 0.1 x10^{-8}
1	4.0 ± 0.5 x10^{-5}	2.1 ± 0.2 x10^{-8}
2.5	3.4 ± 0.5 x10^{-5}	1.7 ± 0.3 x10^{-8}
5	3.3 ± 0.8 x10^{-5}	1.4 ± 0.1 x10^{-8}

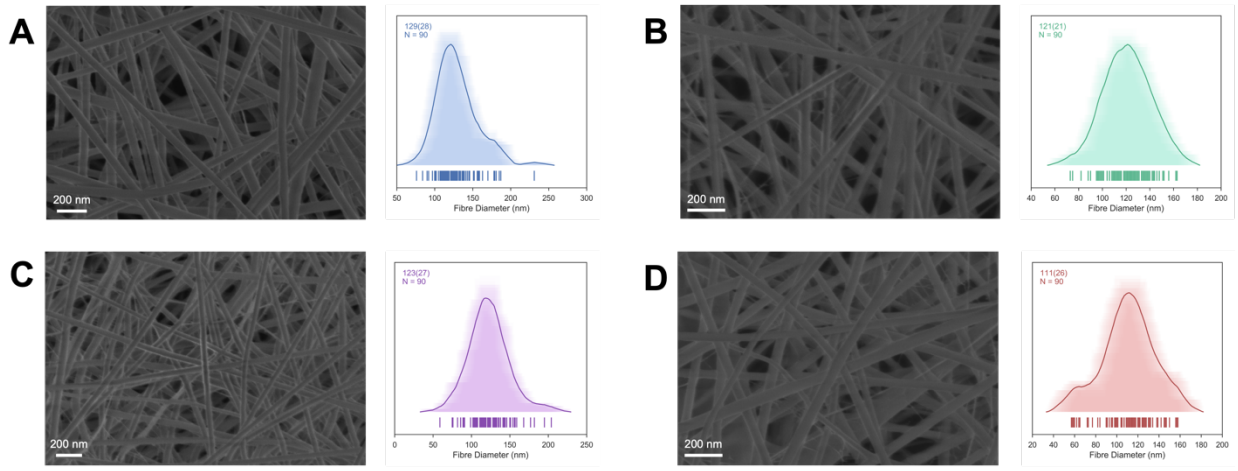

Figure 4-2. SEM images of randomly distributed electrospun fibre mats at A) 0 wt% CNC, B) 1 wt% CNC, C) 2.5 wt% CNC, and D) 5 wt% CNC. The inset images are average shifted histogram (ASH) plots for each sample.

Visualization of Randomly Distributed CNC-Nylon 6 Fibres. The collection of fibres directly onto a stationary collector is expected to produce fibre mats consisting of randomly orientated fibres. SEM was used to confirm the random orientation of the fibres and also provide information about fibre morphology and diameter. The SEM images of the randomly distributed electrospun fibres are shown in Figure 4-2, with average shifted histogram (ASH) plots representing the fibre diameters beside each respective image. All fibres produced with the randomly distributed protocol are smooth with no beading. Average fibre diameter does not differ significantly between CNC loadings, with values at 129 ± 28 nm for 0 wt% CNC, 121 ± 21 nm for 1 wt% CNC, 123 ± 27 nm for 2.5 wt% CNC, and 111 ± 26 nm for 5 wt% CNC. In all the samples, there are secondary super-fine "spider-web" structures in addition to the larger, thicker fibres, which is more apparent with higher CNC loadings, as shown in Figure 4-3A. The most common explanation for these secondary structures was suggested by Islam *et al.*, where the authors suggested that the amide groups in Nylon 6 are ionized in the acid solvent (*i.e.* formic acid) when a high voltage is applied during electrospinning.[23] The ionization of the polymer causes in increase in electrostatic forces between individual polymer chains thereby disentangling some regions of

the polymer in-solution and ultimately leading to a reduction in solution viscosity.[24, 25] The addition of the sulfate half-ester CNCs may also lead to increased electrostatic repulsion between CNC and ionized Nylon 6 causing the formation of the super-fine fibres. Even though these thin "spider-web" fibres are present in all samples, the overall morphology of the thicker, larger fibres appear unaffected with increased CNC loading.

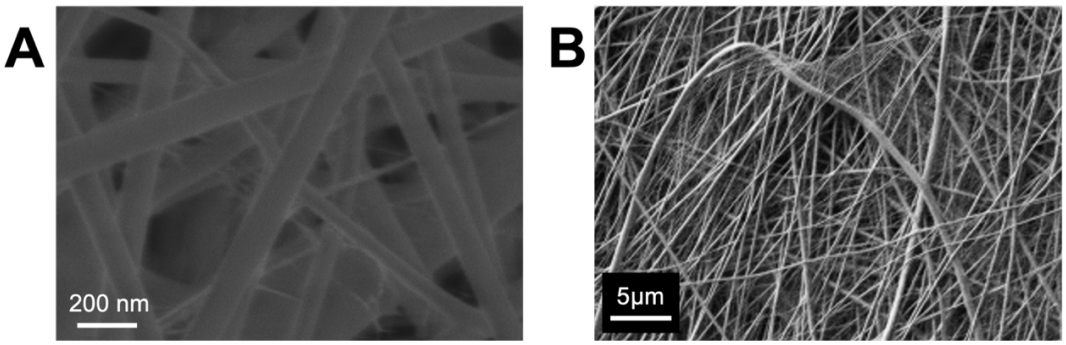

Figure 4-3. Close-up SEM images of the spider-web structures for the 5% CNC randomly distributed fibre mats (A) and aligned fibre mats (B).

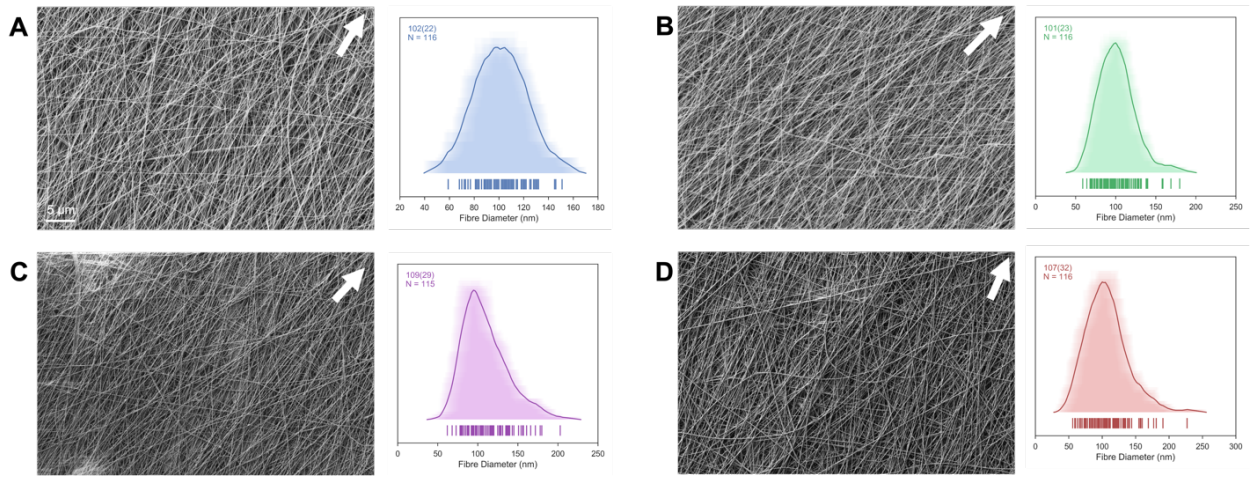

Figure 4-4. SEM images of aligned electrospun fibre mats at A) 0 wt% CNC, B) 1 wt% CNC, C) 2.5 wt% CNC, and D) 5 wt% CNC. The white arrows indicate drum rotation direction, and the inset images are average shifted histogram (ASH) plots for each sample.

Visualization of Aligned CNC-Nylon 6 Fibres. After confirmation of successful electrospinning using a stationary collector, fibres were produced using a rotating drum collector. As stated previously, it is expected that the rotating drum collector physically forces the alignment of the fibres. SEM was used to gauge alignment of the fibres and to obtain information about the morphology and diameters of the fibres. The SEM images of the aligned electrospun fibres are shown in Figure 4-4, with the ASH plots representing fibre diameters beside each respective image. All aligned fibres are smooth and also show no beading, as observed for the randomly distributed fibres. Similar to the randomly distributed fibres, super-fine "spider-web" structures were also seen in the aligned fibre samples (Fig. 4-3B). The average fibre diameter decreased by around 15 nm compared to the randomly distributed fibres, with values at 102 ± 22 for 0 wt% CNC, 101 ± 23 nm for 1 wt% CNC, 109 ± 29 nm for 2.5 wt% CNC, and 107 ± 32 nm for 5 wt% CNC. This decrease in diameter compared to the randomly distributed fibres is expected as the stretching of the fibres when aligning causes further thinning of the fibres and therefore a decrease in fibre diameter.[5, 26] Even with the difference in applied voltages and flow rates at each CNC

loading in order to maintain the Taylor cone, the fibres did not vary in diameter between each of the loadings. Though the majority of fibres are aligned, there are some fibres that deviate from the alignment direction (as presented in the Figure 3-4F of Chapter 3). This deviation is attributed to three possible factors: an increase in charge repulsion by the outermost layer of fibres, an increase in fibre density that decreases the apparent charge on the drum collector, and the snapping of some fibres at high rotational speeds.[27-29] Though all these factors may play a role in the misalignment of fibres, over 83% of the fibres collected in this study fall within an angle deviation of 30˚ from the spinning direction (Figure 3-4F of Chapter 3).

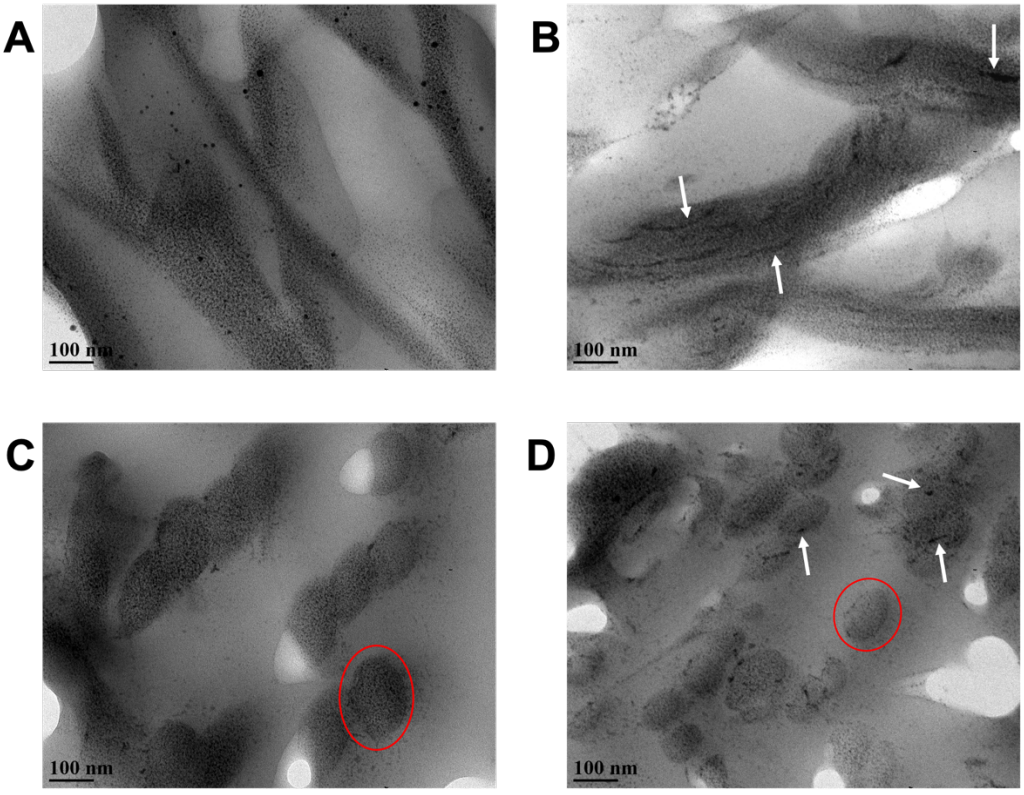

Figure 4-5. TEM images of neat Nylon 6 along the fibre axis (A) and of the cross section (C), and of 5 wt% CNC along the fibre axis (B) and of the cross section (D). The red circles indicate a cross-section of a fibre, and the white arrows point to CNCs.

TEM Images of the Aligned Fibres. The physical alignment of the fibres alongside the electric field alignment during electrospinning may play a role in CNC alignment in individual fibres. Thus, transmission electron microscopy (TEM) was used to confirm the presence of CNC and to visualize the dispersion and alignment of CNCs within the aligned fibres, as shown in Figure 4-5. Fibre mats of neat Nylon 6 and 5 wt% CNC were embedded in resin and sections of the resin block were cut along the axis of the embedded fibres and across the width (or cross-section) of the fibres. The neat Nylon 6 fibres in Figure 4-5 A,C show no presence of CNCs; however, there are few small dark spots attributed to dried stain particles. The 5 wt% CNC fibres in Figure 4-5B clearly show the presence of CNCs as long fibrous particles along the length of the fibres. At 5 wt% CNC, there is the presence of a few agglomerates of CNCs but most of the CNC particles are dispersed well along the axis of the fibre, which suggests that the electrospinning process may orient the CNCs in the spinning and collection direction.[30, 31] When viewing the cross sections of the fibres in Figure 4-5D, the dark spots are cross-sections of CNCs within the fibres (circled in red). The lengths and widths of the particles present in the TEM images are consistent with those for CNC.[32]

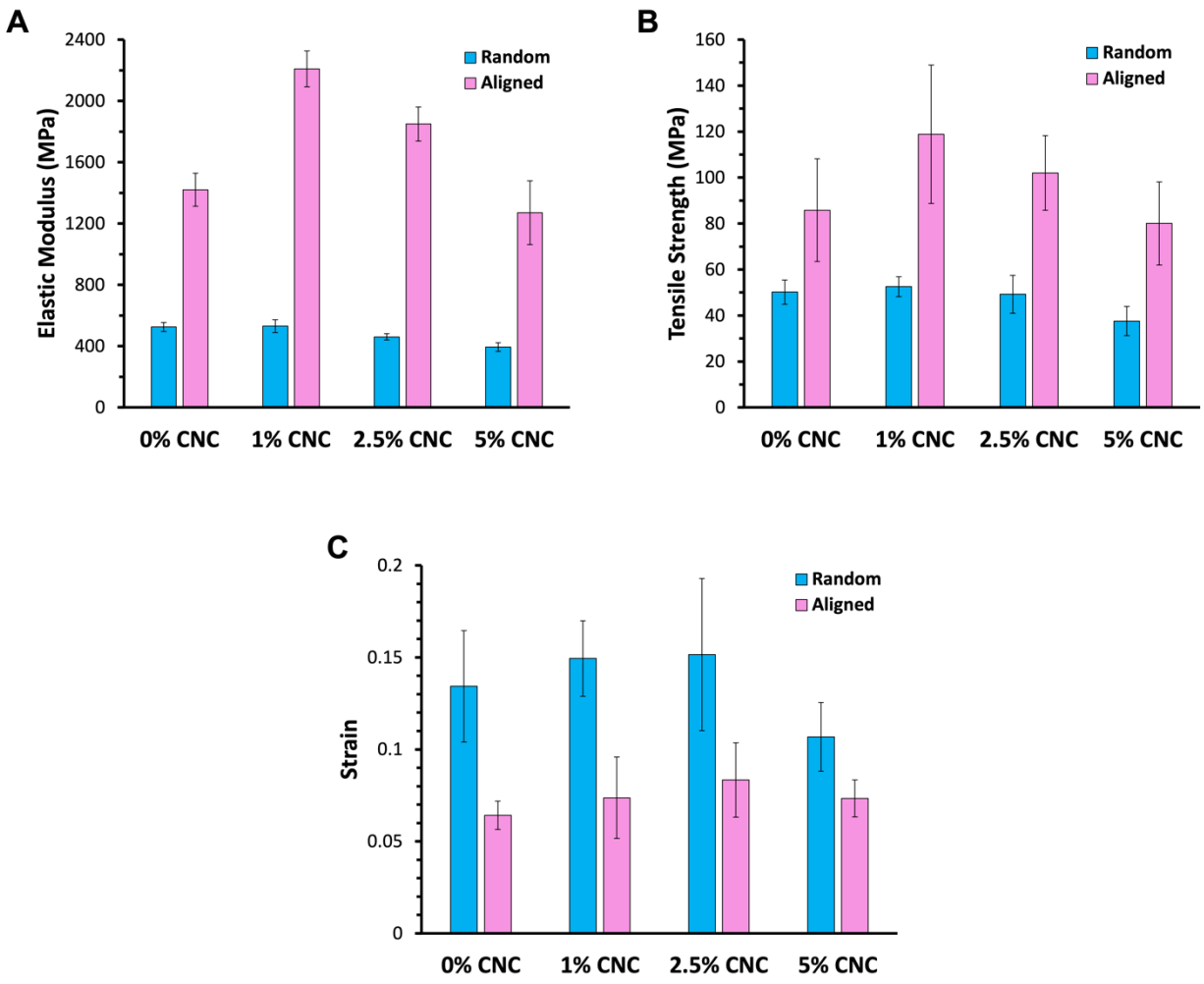

Figure 4-6. Mechanical results comparing randomly distributed (blue) and aligned (pink) fibre mats at increasing CNC loadings (0, 1, 2.5, and 5 wt%): A) Elastic Modulus, B) Tensile Strength, and C) Strain at Break.

Table 4-2. Summarized mechanical results for the random and aligned fibre mats.

wt% CNC	Random			Aligned		
	Elastic Modulus (MPa)	Tensile Strength (MPa)	Strain at Break (a.u.)	Elastic Modulus (MPa)	Tensile Strength (MPa)	Strain at Break (a.u.)
0	525 ± 29	50 ± 5	0.13 ± 0.03	1420 ± 107	85 ± 22	0.06 ± 0.01
1	530 ± 42	53 ± 4	0.15 ± 0.02	2208 ± 117	118 ± 30	0.07 ± 0.02
2.5	460 ± 20	49 ± 8	0.15 ± 0.05	1849 ± 111	102 ± 16	0.08 ± 0.02
5	394 ± 28	38 ± 6	0.11 ± 0.02	1270 ± 208	80 ± 18	0.07 ± 0.01

Mechanical Results. As mentioned previously, the mechanical properties of the fibre mats are expected to differ with fibre alignment. Aligned electrospun fibres are proven to be mechanically stiffer than their randomly distributed counterparts.[5, 33] In aligned fibre mats, the stress transfer when testing is being exerted on the individual fibres rather than on a network of randomly distributed fibres. The aligned fibre mats have the majority of the fibres orientated in the same direction as testing, thus the fibres become taut at low strain rates due to there being a lack of movement of the individual fibres prior to displacement. On the other hand, the randomly distributed fibres are orientated in numerous different directions in addition to the testing direction, therefore movement and realignment of individual fibres is greater while displacement occurs during testing, especially of fibres that are perpendicular to the testing direction. This wider distribution of fibre direction allows for greater stretching of the fibre mat thus a higher strain is required to break the samples.[7]

Tensile tests of the fibre mats were performed, and elastic modulus (EM), tensile strength (TS), and strain-at-break were quantified. Figure 4-6 and Table 4-2 show the mechanical results of both the randomly distributed and aligned electrospun CNC-Nylon 6 fibres. Both the EM and TS are significantly higher for the aligned fibre mats than for the randomly distributed fibre mats. In the case of the randomly distributed mats, the average EM did not significantly change after the addition of 1% CNC. On the other hand, the aligned fibre mats increased in EM by 55% for 0 wt% and 1 wt% CNC, respectively. There was also no significant difference in average TS for the randomly distributed or aligned fibre mats after the addition of 1 wt% CNC. At CNC loadings above 1 wt%, EM and TS decreased for all samples to values below those for neat Nylon 6. This is consistent with other studies that show a decrease in mechanical properties of CNC-Nylon composites at higher CNC loadings.[3, 14, 34] As seen for the films presented in Chapter 2, there is an

increased probability of aggregation at high loadings. These aggregates can act as defect or local stress points in the fibres causes premature failure. A decrease in crystallinity may also decrease the mechanical properties, which will be discussed in the following sections. The strain at break values of all the aligned fibre mats are also almost half than those for the randomly distributed mat samples (Table 4-2). This is due to the freedom of the individual fibres in the randomly distributed mats to align in the testing direction.[35] Overall, the tensile strength and elastic moduli of the aligned fibre samples are over 2 and 3 times larger on average than those of their randomly distributed counterparts, respectively.

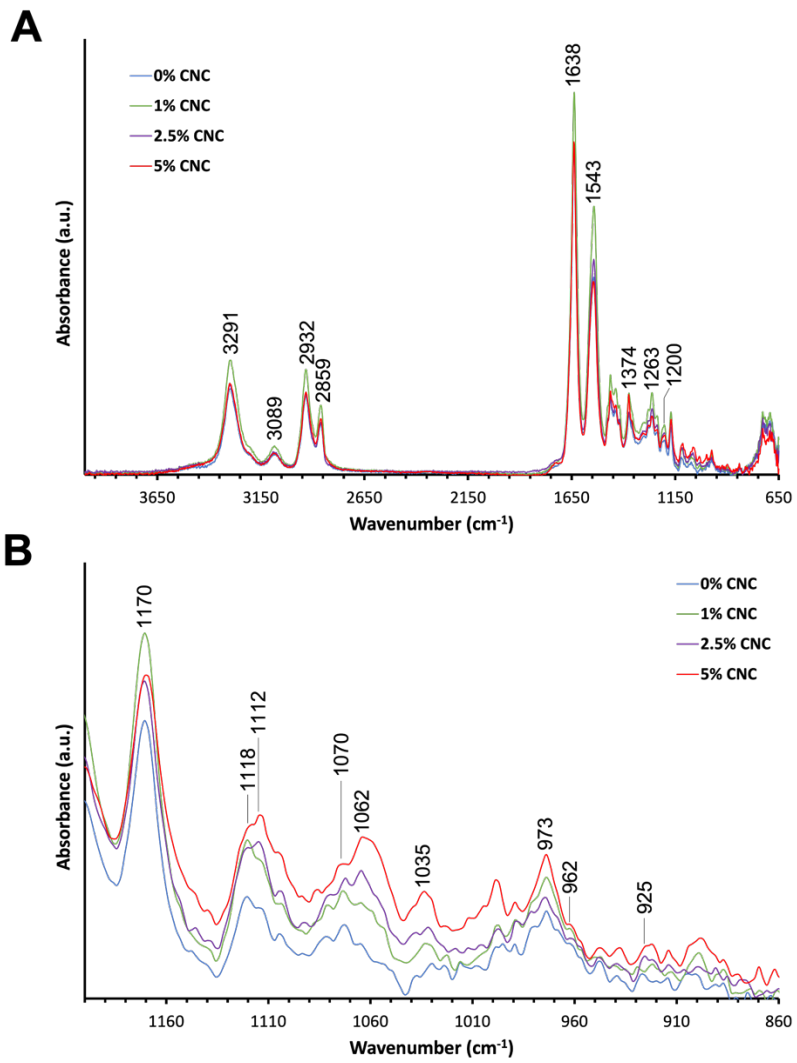

Figure 4-7. FTIR analysis of aligned CNC-Nylon 6 electrospun mats at 0 wt% CNC (blue), 1 wt% CNC (green), 2.5 wt% CNC (purple), and 5 wt% CNC (red).

FTIR Analysis. The chemical structure of the aligned fibre mats was investigated using FTIR, as presented in Figure 4-7. All spectra from 0 to 5 wt% CNC in Figure 4-7A show predicted Nylon 6 bands at 3291 cm^{-1} (N-H str.), 3089 cm^{-1} (N-H str.), 2932 cm^{-1} (CH_2 asym.), 2859 cm^{-1} (CH_2 sym.), 1638 cm^{-1} (amide I), 1543 cm^{-1} (amide II), and 1374 cm^{-1} and 1263 cm^{-1} and 1200 cm^{-1} (amide III + CH_2 wag).[36] In the lower IR region from 1200-860 cm^{-1} in Figure 4-7B, there is also the presence of predicted Nylon 6 bands at 1170 cm^{-1} (CONH skeletal motion), 1118 cm^{-1} (C-

C amorphous str.), and 1070 cm^{-1} and 1062 cm^{-1} (C-C str.). The appearance and increase of the glucose C2, C3, and C6 C-O stretching vibrations at 1112 cm^{-1}, 1062 cm^{-1}, and 1035 cm^{-1}, respectively, confirm that CNC is present in the composites.[37] A full list of the FTIR band assignments is presented in Table 4-3.

The FTIR spectra also provide insight into the crystalline microstructure of Nylon 6. The bands at 973 cm^{-1} and 925 cm^{-1} are attributed to the CONH in-plane stretching of the γ and α crystal allomorphs of Nylon 6, respectively.[19] The α allomorph is the most stable form as it is a result of the extended planar conformation of the polyamide chains, whereas the γ form is the less stable form as it is the result of some twisted chains.[36, 38] Both allomorph bands at 973 and 925 cm^{-1} have increasingly larger peak intensities and band broadening with increasing CNC loading (Fig. 4-7B). Electrospun Nylon 6 fibres predominately crystallize in the γ form,[36, 39-41] therefore any changes in the crystallization of the α form must be due to the addition of CNC. The fast collection speed during electrospinning in this study (4000 rpm) allow for only a short period of time for the fibres to dry and crystallize, which is consistent with the fact that the γ allomorph forms as a result of fast crystallization.[18] These observations are in contrast with CNC-Nylon 6 thin films, where Nylon 6 crystallizes in a predominately α form due to the slow drying of the films and the addition of CNC instead induces the γ form.[14, 19] Though the γ form is known to be weaker than the α form, we still observed an increase in the EM of the aligned fibres with the addition of CNC (Fig. 4-6). This is similar to what was observed in the films presented in Chapter 2, where the stress transfer and interactions between Nylon 6 and CNC overcame the potential decrease in mechanical properties of the fibres solely due to changes in crystallinity.

Table 4-3. FTIR band assignments for the CNC-Nylon 6 spin-coated films.

Wavenumber (cm^{-1})	Nylon 6 Assignment	CNC Assignment	Reference
3291 (m)	H-bonded NH str.	1˚ and 2˚ O-H str.	*36, 37*
3089 (w)	NH str.		*36*
2932 (m)	CH_2 asym. str.	C-H str.	*36, 37*
2859 (m)	CH_2 sym. str.		*36*
1638 (s)	C-ONH str. (amide I)		*36*
1543 (s)	CON-H in-plane bend (amide II) + CN str.		*36*
1374 (m)	CON-H str. (amide III) + CH_2 wag		*36*
1263 (m)	CON-H str. (amide III) + CH_2 wag		*36*
1200 (m)	α form CO-NH str. (amide III) + CH_2 wag		*36*
1170 (w)	CO-NH skeletal	C-O-C str.	*36, 37*
1118 (w)	Amorphous C-C str.		*36*
1112 (m)		C-O str. (C2)	*37*
1070 (w)	C-C str.		*36*
1062 (m)		C-O str. (C3)	*37*
1035 (w)		C-O str. (C4)	*37*
973 (w)	γ form CO-NH in-plane str.		*19*
962 (m)	α form CO-NH in-plane str.		*19*
929 (m)	α form CO-NH in-plane str.		*19*

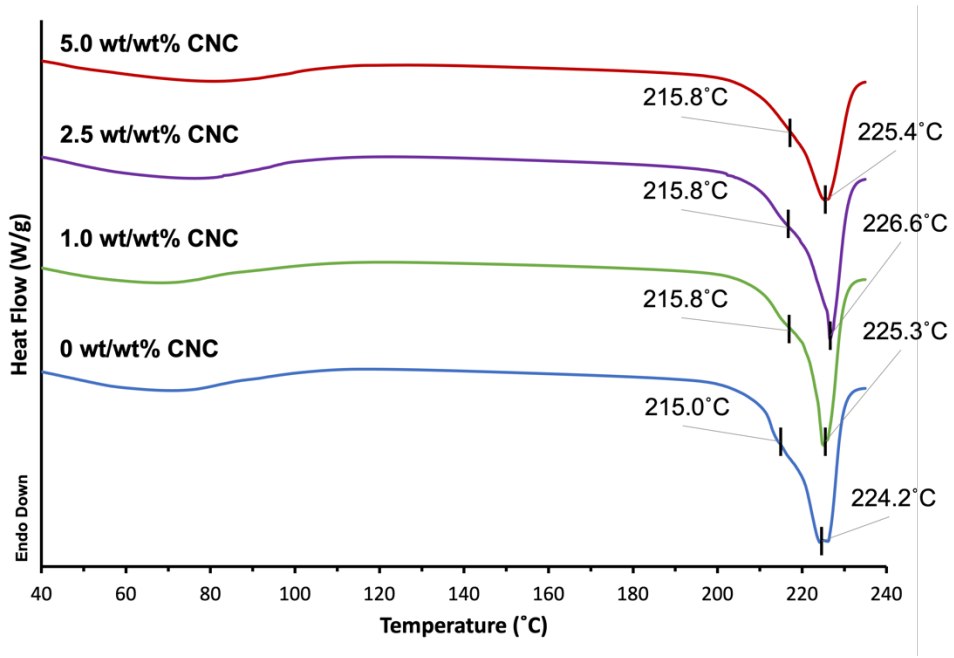

Figure 4-8. DSC analysis of aligned CNC-Nylon 6 electrospun mats at 0 wt% CNC (blue), 1 wt% CNC (green), 2.5 wt% CNC (purple), and 5 wt% CNC (red).

DSC Analysis. An investigation into the effect of CNC on the crystalline and melting behaviour of Nylon 6 was also done using DSC. In the DSC spectra in Figure 4-8, the α and γ forms appear at approx. 225˚C and 215˚C, respectively. The α allomorph at 225˚C appears to dictate the crystallization temperature of the composites, however, there is a shoulder at 215˚C attributed to the γ allomorph peak. The 215˚C γ peak is higher in temperature than the melting temperatures reported for CNC-Nylon 6 thin films, suggesting that the γ allomorph is stabilized when Nylon 6 is electrospun.[14, 19] The heat flow of the 215˚C γ allomorph also appears to decrease with increasing CNC content. The presence of both the α and γ allomorphs in all samples, including neat Nylon 6, suggests that the formation of electrospun fibres induces both crystal forms.[42] However, the forceable alignment of the fibres during electrospinning can induce an alignment of the polymer chains, which may lead to a more planar conformation similar to that of the α form of Nylon 6,[43] which supports the fact that the α allomorph is the dominant form as seen

in DSC. There is also a decrease in the heat flow with increasing CNC content as a result of a decrease of the peak area of the α allomorph. There is no significant difference in crystallization temperature seen between each CNC loading as the peak maxima lies between 224-226˚C. The small decrease in heat flow between 40 and 100˚C is attributed to water and residual solvent loss.

The degree of crystallinity of each composite was calculated from the DSC results using Equation 4-5 (the same as Eq. 2-4),

$$\chi_C = \frac{\Delta H_f}{(1-\phi)\cdot \Delta H_f^{100}} \cdot 100\% \qquad \text{Eq. 4-5}$$

where ΔH_f is the heat of fusion of the composite, ϕ is the weight fraction of CNC, and ΔH_f^{100} is the heat of fusion of fully crystalline Nylon 6 (230 J/g).[44] The heat of fusion of each sample was determined by taking the area under the peak between 200˚C and 240˚C, and was found to decrease with increasing CNC content – from 81.6 J/g for 0 wt% CNC to 74.2 J/g for 5 wt% CNC. The degree of crystallinity therefore also decreased with increasing CNC loading, from 35.5% for 0 wt% CNC to 34.0% for 5 wt% CNC. A summary of the results from the DSC analysis are found in Table 4-4. It can be said that CNC did not significantly influence the overall crystallinity of the electrospun Nylon 6 fibres.

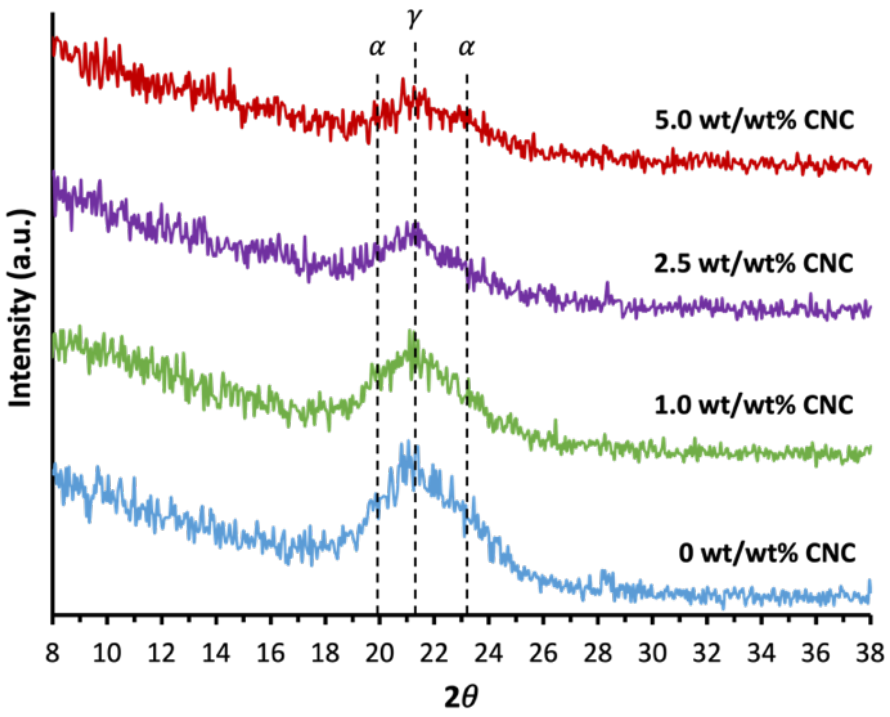

Figure 4-9. XRD patterns for the aligned CNC-Nylon 6 electrospun mats at 0 wt% (blue), 1 wt% (green), 2.5 wt% (purple), and 5 wt% (red) CNC. The theoretical peak positions for the α and γ allomorphs are denoted with the vertical dotted lines.

XRD Analysis. A final investigation into the crystallinity of the aligned fibres was done using XRD, as shown in Figure 4-9. The XRD patterns show two diffraction peaks at 20.3˚ and 23.2˚for the α allomorph, and one peak at 21.2˚ for the γ allomorph.[18] As stated previously, electrospun Nylon 6 fibres have been shown to predominately crystallize in the γ form, which is confirmed by the largest intensity peak staying at 21.2˚ in the XRD patterns for all samples. As CNC content increased, the intensity of the γ peak decreased while the α peak became more pronounced. The findings in this study are consistent with previous reports that show high cellulose content induces the formation of the α allomorph in Nylon 6.[14, 19, 43] At higher CNC loadings, there is a greater chance of inter-particle CNC aggregation. This aggregation may reduce favourable interactions between CNC and Nylon 6 in the electrospun fibres and thus force the transition of

the polymer to the α form. Of note, CNC is chiral in nature and this innate structural conformation may also interact favourably with the twisted conformation of the γ allomorph in Nylon 6,[14, 45, 46] thus also providing an additional explanation for the high reinforcement seen in the mechanical results.

It is also important to note that the solutions were increasingly more viscous with increasing CNC content. This change in viscosity can greatly affect the ability of the individual polymer chains to thermodynamically crystallize and may also slow down the evaporation of solvent absorbed by CNC.[43, 47] Therefore, the possible slower drying with higher CNC loadings due to more adsorption of the solvent may also result in the transition to the more stable α form.[41] This is quantified by the decrease in intensity of the γ allomorph peak seen in XRD with increasing CNC loading (Fig. 4-9).

The data obtained from DSC and XRD suggest that higher loadings of CNC inhibit the crystallization of Nylon 6, which directly coincides with the mechanical results from Figure 4-6. At 1 wt% CNC, there appears to be little difference in crystallization behaviour when compared to neat Nylon 6. At 5.0 wt%, there is a decrease in the crystallization of Nylon 6 in both the α and γ forms implying that there is no preferred crystal orientation.[48] At these high loadings, CNC may aggregate thereby reducing favourable interactions with the polymer matrix and ultimately restricting the mobility of the individual polymer chains during crystallization.[47] Thus, the elastic modulus, tensile strength, and strain at break values were the same or lower for 5 wt% CNC when compared to neat Nylon 6.

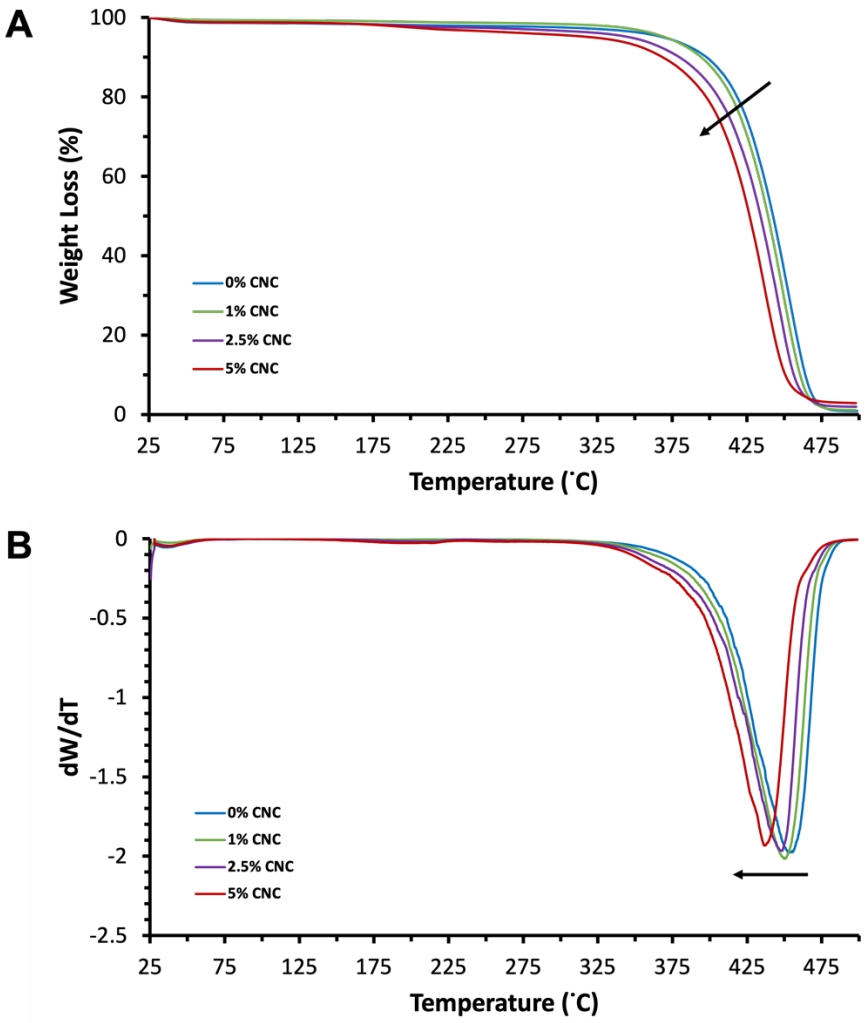

Figure 4-10. TGA (A) and DTG (B) analysis of aligned CNC-Nylon 6 electrospun mats at 0 wt% CNC (blue), 1 wt% CNC (green), 2.5 wt% CNC (purple), and 5 wt% CNC (red). The black arrows denote the trend with increasing CNC loading.

Thermal Properties. Finally, TGA and DTG was used to investigate the thermal properties of the aligned electrospun fibres, as shown in Figure 4-10. The TGA curves in Figure 4-10A show a small 2% decrease in weight loss at temperatures below 100˚C which is attributed to water and/or residual solvent loss. Beginning at around 200˚C, there is another small decrease in weight loss which is greater for the 5% CNC sample due to the earlier degradation of CNCs at temperatures around 200˚C.[32] The onset temperature (T_O) significantly decreased with increasing CNC loading – from 413.0˚C for 0 wt% CNC to 390.3˚C for 5 wt% CNC. After 450˚C, there is a

small remaining mass that is greater with higher CNC loading due to the residual char leftover from CNC after degradation.[32] In the DTG curves in Figure 4-10B, the first derivative peak temperature (T_P) also decreased with increasing CNC loading, from 451.8˚C for 0 wt% CNC to 437.1˚C for 5 wt% CNC. The intensity and width of the T_P peaks do not vary significantly between samples. Overall, the thermal stability of the composite decreased with increasing CNC loading due to the earlier decomposition of CNCs. The decrease of both the T_O and T_P of the composites also directly coincides with a decrease in the more stable α allomorph, as seen by DSC and XRD. A summary of the data from TGA is presented in Table 4-4.

Table 4-4. Summarized DSC and TGA data for the aligned CNC-Nylon 6 fibres.

	DSC			TGA	
CNC (wt%)	**Peak$_\alpha$ (˚C)**	**ΔH_f (J/g)**	**χ_c (%)**	**To (˚C)**	**T_P (˚C)**
0	224.2	81.6	35.5	413.0	451.8
1	225.3	80.4	35.3	406.3	449.4
2.5	226.6	75.8	33.8	390.3	447.6
5	225.4	74.2	34.0	390.3	437.1

4.4 Conclusion

Nylon 6 reinforced with CNC was electrospun from formic acid. A comparison of the fibre morphologies and mechanical properties were performed on randomly distributed and aligned fibre mats. There was a significant increase in elastic modulus and tensile strength when the fibres were aligned at all CNC loadings with values that were 2 and 3 times larger than the randomly

distributed fibre mats, respectively. A CNC loading of 1 wt% showed the highest reinforcing impact in both the randomly distributed and aligned fibre mats. All other mechanical properties decreased at loadings of 2.5 wt% and above. The results from FTIR, DSC, and XRD of the aligned fibres all showed that the process of aligning the fibres induces the formation of both the γ and α crystal allomorph in Nylon 6, where the aligned fibre mats predominately crystallized in the γ form. The presence of CNC in the composite fibres reduced the crystallization of the polymer in the γ form and ultimately inhibited crystallization. The decrease in the more stable α form with higher CNC loadings coincides with a decrease in mechanical properties at loadings above 2.5 wt%. The percent crystallinity of Nylon 6 was calculated from the DSC results and decreased by 1.5% with the addition of CNC. Finally, the thermal stability of the polymer also decreased with increasing CNC content due to the earlier degradation of CNC as well as a reduction in the crystallization of Nylon 6 in the more thermally stable α crystal form. The work presented here demonstrates the mechanical reinforcing capability of CNC in electrospun Nylon 6 fibres. Of note, this is the first time that CNC particle alignment along the axis of the electrospun Nylon 6 fibres was visualized using TEM. This study opens the door to the use of CNC reinforced Nylon fibres for textile applications such as in strengthened fishing lines or ropes.

4.5 References

1. Xue, J.; Wu, T.; Dai, Y.; Xia, Y., Electrospinning and Electrospun Nanofibers: Methods, Materials, and Applications. *Chemical Reviews* **2019,** *119* (8), 5298-5415.
2. Agarwal, S.; Greiner, A.; Wendorff, J. H., Functional materials by electrospinning of polymers. *Progress in Polymer Science* **2013,** *38* (6), 963-991.
3. Buyukada-Kesici, E.; Gezmis-Yavuz, E.; Aydin, D.; Cansoy, C. E.; Alp, K.; Koseoglu-Imer, D. Y., Design and fabrication of nano-engineered electrospun filter media with cellulose nanocrystal for toluene adsorption from indoor air. *Materials Science and Engineering: B* **2021,** *264*, 114953.

4. Li, B.; Pan, S.; Yuan, H.; Zhang, Y., Optical and mechanical anisotropies of aligned electrospun nanofibers reinforced transparent PMMA nanocomposites. *Composites Part A: Applied Science and Manufacturing* **2016,** *90*, 380-389.
5. Fryer, C.; Scharnagl, M.; Helms, C., Electrostatic alignment of electrospun PEO fibers by the gap method increases individual fiber modulus in comparison to non-aligned fibers of similar diameter. *AIP Advances* **2018,** *8* (6), 065023.
6. Isaac, B.; Taylor, R. M.; Reifsnider, K., Mechanical and Dielectric Properties of Aligned Electrospun Fibers. *Fibers* **2021,** *9* (1), 4.
7. Liu, S.-d.; Li, D.-s.; Yang, Y.; Jiang, L., Fabrication, mechanical properties and failure mechanism of random and aligned nanofiber membrane with different parameters. *Nanotechnology Reviews* **2019,** *8* (1), 218-226.
8. Hu, J.; Song, Y.; Zhang, C.; Huang, W.; Chen, A.; He, H.; Zhang, S.; Chen, Y.; Tu, C.; Liu, J.; Xuan, X.; Chang, Y.; Zheng, J.; Wu, J., Highly Aligned Electrospun Collagen/Polycaprolactone Surgical Sutures with Sustained Release of Growth Factors for Wound Regeneration. *ACS Applied Bio Materials* **2020,** *3* (2), 965-976.
9. Li, D.; Tao, L.; Shen, Y.; Sun, B.; Xie, X.; Ke, Q.; Mo, X.; Deng, B., Fabrication of Multilayered Nanofiber Scaffolds with a Highly Aligned Nanofiber Yarn for Anisotropic Tissue Regeneration. *ACS Omega* **2020,** *5* (38), 24340-24350.
10. Zheng, J.; Yan, X.; Li, M.-M.; Yu, G.-F.; Zhang, H.-D.; Pisula, W.; He, X.-X.; Duvail, J.-L.; Long, Y.-Z., Electrospun Aligned Fibrous Arrays and Twisted Ropes: Fabrication, Mechanical and Electrical Properties, and Application in Strain Sensors. *Nanoscale Research Letters* **2015,** *10* (1), 475.
11. Liu, J.; Zhai, H.; Sun, Y.; Wu, S.; Chen, S., Developing high strength poly(L-lactic acid) nanofiber yarns for biomedical textile materials: A comparative study of novel nanofiber yarns and traditional microfiber yarns. *Materials Letters* **2021,** *300*, 130229.
12. Dufresne, A., Cellulose nanomaterials as green nanoreinforcements for polymer nanocomposites. *Philos Trans A Math Phys Eng Sci* **2018,** *376* (2112).
13. Liu, D.; Sui, G.; Dong, Y., 5 - Electrospun polymeric composite nanofibers with cellulose nanocrystals and their applications. In *Electrospun Polymers and Composites*, Dong, Y.; Baji, A.; Ramakrishna, S., Eds. Woodhead Publishing: 2021; pp 147-178.
14. Osorio, D. A.; Niinivaara, E.; Jankovic, N. C.; Demir, E. C.; Benkaddour, A.; Jarvis, V.; Ayranci, C.; McDermott, M. T.; de Lannoy, C.-F.; Cranston, E. D., Cellulose Nanocrystals Influence Polyamide 6 Crystal Structure, Spherulite Uniformity, and Mechanical Performance of Nanocomposite Films. *ACS Applied Polymer Materials* **2021,** *3* (9), 4673-4684.
15. Desmaisons, J.; Rueff, M.; Bras, J.; Dufresne, A., Impregnation of paper with cellulose nanocrystal reinforced polyvinyl alcohol: synergistic effect of infrared drying and CNC content on crystallinity. *Soft Matter* **2018,** *14* (46), 9425-9435.
16. Dufresne, A., 9. Mechanical properties of nanocellulose-based nanocomposites. In *Nanocellulose: From Nature to High Performance Tailored Materials*, De Gruyter: 2017; pp 471-530.
17. Deopura, B. L., 2 - Polyamide fibers. In *Polyesters and Polyamides*, Deopura, B. L.; Alagirusamy, R.; Joshi, M.; Gupta, B., Eds. Woodhead Publishing: 2008; pp 41-61.
18. Liu, Y.; Cui, L.; Guan, F.; Gao, Y.; Hedin, N. E.; Zhu, L.; Fong, H., Crystalline Morphology and Polymorphic Phase Transitions in Electrospun Nylon-6 Nanofibers. *Macromolecules* **2007,** *40* (17), 6283-6290.

19. Aitha, S.; Vasanthan, N., Effect of cellulose nanocrystals on crystallization, morphology and phase transition of polyamide 6. *Composite Interfaces* **2020,** *27* (4), 371-384.
20. Anderson, S. L.; Luber, E. J.; Olsen, B. C.; Buriak, J. M., Substance over Subjectivity: Moving beyond the Histogram. *Chemistry of Materials* **2016,** *28* (17), 5973-5975.
21. Li, B.; Xu, W.; Kronlund, D.; Määttänen, A.; Liu, J.; Smått, J.-H.; Peltonen, J.; Willför, S.; Mu, X.; Xu, C., Cellulose nanocrystals prepared via formic acid hydrolysis followed by TEMPO-mediated oxidation. *Carbohydrate Polymers* **2015,** *133*, 605-612.
22. Dufresne, A., Nanocellulose: a new ageless bionanomaterial. *Materials Today* **2013,** *16* (6), 220-227.
23. Islam, M. S.; McCutcheon, J. R.; Rahaman, M. S., A high flux polyvinyl acetate-coated electrospun nylon 6/SiO2 composite microfiltration membrane for the separation of oil-in-water emulsion with improved antifouling performance. *Journal of Membrane Science* **2017,** *537*, 297-309.
24. Chen, Y.; Waghmare, P. R.; Ayranci, C., Fabrication and characterization of electrospun mats of Nylon 6/Silica nanocomposite fibers. *Journal of Engineered Fibers and Fabrics* **2019,** *14*, 1558925019843225.
25. Kim, H. J.; Pant, H. R.; Amarjargal, A.; Kim, C. S., Incorporation of silver-loaded ZnO rods into electrospun nylon-6 spider-web-like nanofibrous mat using hydrothermal process. *Colloids and Surfaces A: Physicochemical and Engineering Aspects* **2013,** *434*, 49-55.
26. Yan, J.; Qiang, L.; Gao, Y.; Cui, X.; Zhou, H.; Zhong, S.; Wang, Q.; Wang, H., Effect of fiber alignment in electrospun scaffolds on keratocytes and corneal epithelial cells behavior. *Journal of Biomedical Materials Research Part A* **2012,** *100A* (2), 527-535.
27. Bazbouz, M. B.; Stylios, G. K., Alignment and optimization of nylon 6 nanofibers by electrospinning. *Journal of Applied Polymer Science* **2008,** *107* (5), 3023-3032.
28. Kim, J. I.; Hwang, T. I.; Aguilar, L. E.; Park, C. H.; Kim, C. S., A Controlled Design of Aligned and Random Nanofibers for 3D Bi-functionalized Nerve Conduits Fabricated via a Novel Electrospinning Set-up. *Scientific Reports* **2016,** *6* (1), 23761.
29. Conte, A. A.; Sun, K.; Hu, X.; Beachley, V. Z., Effects of Fiber Density and Strain Rate on the Mechanical Properties of Electrospun Polycaprolactone Nanofiber Mats. *Frontiers in Chemistry* **2020,** *8* (610).
30. Song, W.; Liu, D.; Prempeh, N.; Song, R., Fiber Alignment and Liquid Crystal Orientation of Cellulose Nanocrystals in the Electrospun Nanofibrous Mats. *Biomacromolecules* **2017,** *18* (10), 3273-3279.
31. Zhou, C.; Chu, R.; Wu, R.; Wu, Q., Electrospun Polyethylene Oxide/Cellulose Nanocrystal Composite Nanofibrous Mats with Homogeneous and Heterogeneous Microstructures. *Biomacromolecules* **2011,** *12* (7), 2617-2625.
32. Reid, M. S.; Villalobos, M.; Cranston, E. D., Benchmarking Cellulose Nanocrystals: From the Laboratory to Industrial Production. *Langmuir* **2017,** *33* (7), 1583-1598.
33. Borges, A. L. S.; Münchow, E. A.; de Oliveira Souza, A. C.; Yoshida, T.; Vallittu, P. K.; Bottino, M. C., Effect of random/aligned nylon-6/MWCNT fibers on dental resin composite reinforcement. *Journal of the Mechanical Behavior of Biomedical Materials* **2015,** *48*, 134-144.
34. Sucharitpong, T.; Lam, N. T.; Sukyai, P., Production of Nylon-6/Cellulose Nanocrystal Composite Films Using Solvent Dissolution. *Sugar Tech* **2020,** *22* (2), 328-339.
35. Lee, J.; Deng, Y., Increased mechanical properties of aligned and isotropic electrospun PVA nanofiber webs by cellulose nanowhisker reinforcement. *Macromolecular Research* **2012,** *20* (1), 76-83.

36. Lee, K.-H.; Kim, K.-W.; Pesapane, A.; Kim, H.-Y.; Rabolt, J. F., Polarized FT-IR Study of Macroscopically Oriented Electrospun Nylon-6 Nanofibers. *Macromolecules* **2008,** *41* (4), 1494-1498.
37. Foster, E. J.; Moon, R. J.; Agarwal, U. P.; Bortner, M. J.; Bras, J.; Camarero-Espinosa, S.; Chan, K. J.; Clift, M. J. D.; Cranston, E. D.; Eichhorn, S. J.; Fox, D. M.; Hamad, W. Y.; Heux, L.; Jean, B.; Korey, M.; Nieh, W.; Ong, K. J.; Reid, M. S.; Renneckar, S.; Roberts, R.; Shatkin, J. A.; Simonsen, J.; Stinson-Bagby, K.; Wanasekara, N.; Youngblood, J., Current characterization methods for cellulose nanomaterials. *Chem Soc Rev* **2018,** *47* (8), 2609-2679.
38. Vasanthan, N.; Salem, D. R., FTIR spectroscopic characterization of structural changes in polyamide-6 fibers during annealing and drawing. *Journal of Polymer Science Part B: Polymer Physics* **2001,** *39* (5), 536-547.
39. Kimura, N.; Kim, B.-S.; Kim, I.-S., Effects of Fe2+ ions on morphologies, microstructures and mechanical properties of electrospun nylon-6 nanofibers. *Polymer International* **2014,** *63* (2), 266-272.
40. Gururajan, G.; Sullivan, S. P.; Beebe, T. P.; Chase, D. B.; Rabolt, J. F., Continuous electrospinning of polymer nanofibers of Nylon-6 using an atomic force microscope tip. *Nanoscale* **2011,** *3* (8), 3300-3308.
41. Stephens, J. S.; Chase, D. B.; Rabolt, J. F., Effect of the Electrospinning Process on Polymer Crystallization Chain Conformation in Nylon-6 and Nylon-12. *Macromolecules* **2004,** *37* (3), 877-881.
42. Li, Y.; Goddard, W. A., Nylon 6 Crystal Structures, Folds, and Lamellae from Theory. *Macromolecules* **2002,** *35* (22), 8440-8455.
43. Joshi, M. K.; Tiwari, A. P.; Maharjan, B.; Won, K. S.; Kim, H. J.; Park, C. H.; Kim, C. S., Cellulose reinforced nylon-6 nanofibrous membrane: Fabrication strategies, physicochemical characterizations, wicking properties and biomimetic mineralization. *Carbohydr Polym* **2016,** *147*, 104-113.
44. Klata, E.; Borysiak, S.; Van de Velde, K.; Garbarczyk, J.; Krucinska, I., Crystallinity of polyamide-6 matrix in glass fibre/polyamide-6 composites manufactured from hybrid yarns. *Fibres & Textiles in Eastern Europe* **2004,** *12* (3), 64-69.
45. Usov, I.; Nyström, G.; Adamcik, J.; Handschin, S.; Schütz, C.; Fall, A.; Bergström, L.; Mezzenga, R., Understanding nanocellulose chirality and structure–properties relationship at the single fibril level. *Nature Communications* **2015,** *6* (1), 7564.
46. Ogawa, Y., Electron microdiffraction reveals the nanoscale twist geometry of cellulose nanocrystals. *Nanoscale* **2019,** *11* (45), 21767-21774.
47. Zhu, R.; Yadama, V.; Liu, H.; Lin, R. J. T.; Harper, D. P., Fabrication and characterization of Nylon 6/cellulose nanofibrils melt-spun nanocomposite filaments. *Composites Part a-Applied Science and Manufacturing* **2017,** *97*, 111-119.
48. Paci, M.; Filippi, S.; Magagnini, P., Nanostructure development in nylon 6-Cloisite® 30B composites. Effects of the preparation conditions. *European Polymer Journal* **2010,** *46* (5), 838-853.

Chapter 5. Surface Modification of Cellulose Nanocrystals with Diazonium Salts

5.1 Introduction

During the processing of CNC, the strong acid treatment imparts surface functionalization dependent on the type of acid used. The most commonly seen functionalizations are with $-OSO_3^-$ and -OH groups as seen with sulfuric or hydrochloric acid treatments, respectively.[1] The hydroxyl groups make homogenous dispersions difficult due to strong interparticle hydrogen bonding, thus the treatment with sulfuric acid is favoured because of the enhanced interparticle repulsions that drive the colloidal stability and dispersion of CNC in aqueous solutions.[2] However, this limits composite processing to aqueous or polar matrices, which is in contrast to the hydrophobicity of most polymers.[3] Consequently, grafting of additional hydrophobic molecules is typically performed to increase dispersion and increase favourable filler-polymer interactions.[4, 5]

As discussed previously, one of the biggest difficulties faced when using CNC as a filler in polymers is the incompatibility of the nanoparticles and the polymer causing poor distribution of individual CNCs within the matrix.[6] To overcome this, a multitude of surface functionalizations have been utilized for the compatibilization of CNCs in polymer matrices.[3, 4, 7] With a focus on composite production, surface modifications range from covalent and ionic bonding to physisorption of molecules onto CNC.[4, 6] Most importantly, the type of molecule chosen dictates the strength and type of interactions at the CNC-molecule and CNC-matrix interfaces, where most of the previously reported work has focused on the grafting of alkyl-rich molecules onto CNC.[4, 8] With our group's expertise in aryl diazonium chemistry on conductive surfaces,[9-11] we wanted to

expand upon the methods used for CNC modification to include multilayer aryl radical functionalization. Of note, previous reports on radical grafting onto CNCs typically use some type of radical polymerization, such as atom transfer radical polymerization (ATRP) for polymer growth from the surface.[12, 13]

Diazonium salts are a proven versatile starting material for the modification of a variety of materials including carbon, metal, and polymer surfaces.[14, 15] The aryl radical generated electrochemically[16], thermally[17], or spontaneously[18] bonds to 2D or 3D surfaces in monolayers or multilayers depending on reaction conditions.[19] The wide array of substituents available on diazonium salts also allow for precise tailoring of the surface in order to obtain additional properties of the material. More relevant to the work in this thesis, effects of surface modification range from improved dispersion in solvents,[16] to increased interface interactions,[20] to the possibility for further reactivity and formation bi-functional multilayers on surfaces *via* coupling through the bound diazonium molecule.[21, 22]

Two methods for the formation of diazonium salts (also called *diazotization*) are the *ex-situ* and *in-situ* methods. In the *ex-situ* method, the diazonium salt is prepared prior to modification of a surface.[15, 23] An aniline precursor is reacted with a reducing agent, typically sodium nitrite, in an aqueous acidic solution at 0˚C. Sodium nitrite reduces the aryl amine to the cationic diazonium ion, with the counterion being the base pair of the acid in solution. Finally, a two-step purification is required to obtain the final dried diazonium salt. Though the *ex-situ* method is the most common, there are dangers to consider when preparing diazonium salts in this manner. Firstly, the reaction must take place at or near 0˚C to prevent excess nitrous acid and nitrogen gas formation, as well as to prevent spontaneous decomposition of the salt at room temperature.[24] Secondly, the choice of the acid reaction medium is crucial in preventing further decomposition. It has been found that

diazonium salts synthesized using the *ex-situ* method with tetrafluoroborate or sulfonate counterions are more stable than those with chloride counterions.[25] Lastly, some functionalized diazonium salts are unstable when purifying from solvent, limiting the choice of functionalities on the diazonium cation.[26] However, one advantage of preparing diazonium salts using this method is that they can be prepared ahead of time in larger batches. There are a handful of reports in the literature that list all hazards and to prepare researchers in their laboratories when synthesizing diazonium molecules *ex-situ*,[24, 27] but so long as thorough precautionary measures are taken, it is still a powerful tool when preparing diazonium salts.

Contrary to the *ex-situ* method, it may be desirable to prepare diazonium salts *in-situ*. In this method, the diazonium salt is formed in the same reaction medium as the surface under ambient conditions. Alternative acids that give more stable counterions and/or are less corrosive are used with an optionally more stable reducing agent (*e.g.* isopentyl nitrite or t-butyl nitrite).[28] When ready to use the diazonium salt for surface modification, the entirety of the diazonium solution is added to the surface without prior purification, preventing any unwanted decomposition due to instability. Different solvents that are more compatible with the surface or diazonium salt can also be used. For example, Baranton and Belanger grafted 4-bromophenyl diazonium, 4-nitrophenyl diazonium, and anthraquinone-1-diazonium to a glassy carbon electrode using acetonitrile.[29] The authors compared the *in-situ* grafting with pre-prepared (*ex-situ*) diazonium salts dissolved in acetonitrile and found that the electrochemical properties of the modified electrode did not vary significantly between methods. Nonetheless, the choice of using either the *ex-situ* or *in-situ* method depends on the reaction medium for surface modification as well as the solubility and stability of the functionalized diazonium salt.

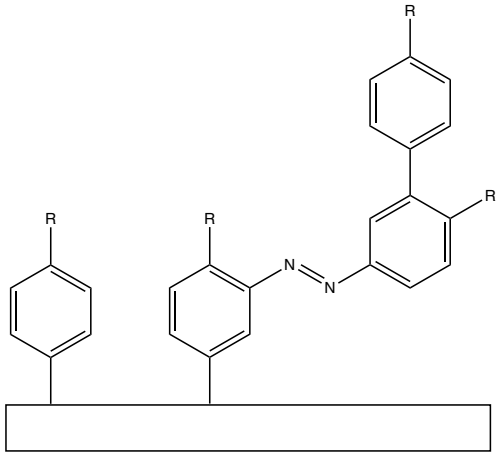

Figure 5-1. Proposed monolayer and multilayer bonding of diazonium molecules on a surface.

Azo coupling of diazonium molecules to surfaces take advantage of the capability of the cationic $-N_2^+$ group on the diazonium cation to form covalent bonds with the surface. Under particular conditions, diazonium cations spontaneously form multilayers on surfaces where an unreacted diazonium cation binds to the aromatic benzene ring of a bound diazonium in positions ortho to the *p*-substituents.[30] The thickness, or degree of grafting, of the diazonium multilayer can be controlled by varying the functional groups, grafting time, or type of reducing agent.[9, 31, 32] In the case of multilayer formation, the covalent bonds formed between diazonium molecules and between the diazonium and the surface are suggested to be a combination of carbon-carbon (C-C) linkages and azo (-C-N=N-C-) bridges,[33, 34] as illustrated in Figure 5-1. The functionalization of a surface with a layer of hydrophobic aryl groups can promote greater dispersion, adhesion, and stress transfer to the filler in a hydrophobic polymer, thereby also increasing the thermal and/or mechanical properties of the polymer as a result.[15, 35]

The ease of spontaneous modification, the introduction of hydrophobic aryl groups, and the possibility for additional grafting *via* substituents on the aryl groups make diazonium surface modification an attractive route for compatibilization of carbon-based fillers in polymer matrices.

This has been taken advantage of when preparing surface modified fillers for mechanical reinforcement purposes. For example, Valles *et al.* used p-aminobenzenediazonium as a covalent interlayer between graphene and poly(methyl methacrylate) (or PMMA) for increased mechanical properties in PMMA.[36] By adding a layer of PMMA around the graphene, favourable dispersion of the graphene-diazonium-PMMA filler in PMMA was achieved thereby increasing both the elastic modulus and tensile strength of the polymer compared to unmodified graphene-PMMA.

Another common method to increase interface interactions is by choosing an R group on the phenyl that will form favourable interactions between the filler and the polymer *via* Van der Waals forces – most commonly, hydrogen bonding.[15] Yu *et al.* modified graphite oxide (GO) layers with 4-aminoazobenzene-4'sulfonatediazonium for incorporation into poly(vinyl alcohol) (or PVA).[37] The authors suggested that the sulfonate group on the phenyl and the hydroxyl groups on GO formed strong hydrogen bonds, which increased interfacial adhesion as well as dispersion of GO in PVA. The combination of favourable interactions led to a significant increase in elastic modulus compared to pure PVA. Regardless of the mode of reinforcement, the role of the filler is to provide a route of stress transfer between the filler and the polymer matrix where surface modification provides a further increase in adhesion at the filler-matrix interface.[38]

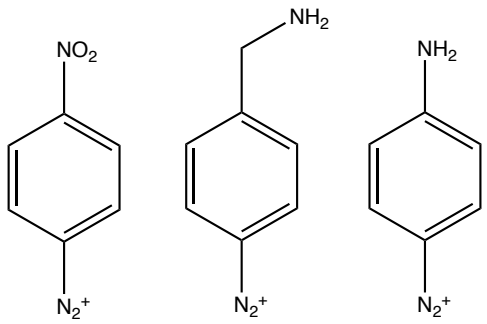

Figure 5-2. Structures of diazonium cations used for surface modification of CNC. From left to right: 4-nitrobenzenediazonium, 4-aminobenzyldiazonium, and p-aminobenzenediazonium.

In this Chapter, we test the hypothesis that diazonium cations can be used to chemically modify the surface of CNC. Three p-substituted diazonium molecules were utilized for surface functionalization of CNC. The structures of the diazonium cations used are illustrated in Figure 5-2. The diazonium molecules in this study were chosen due to the strong signatures of the nitrogen-containing functional groups during characterization as well as the possibility of increased hydrogen bonding between CNC and Nylon 6. Two methods of diazotization were used: *ex-situ* and *in-situ* synthesis. The efficacy of the modification was characterized to confirm grafting and to investigate chemical and thermal properties. Finally, a short study of the mechanical properties of modified CNC-Nylon 6 thin films is presented. Members of our collaborative team have previously reported the use of diazonium cations to modify CNC for the incorporation into electrospun polystyrene fibres.[39, 40] The work in this Chapter provides a thorough characterization of CNC modified with diazonium precursors.

5.2 Experimental

5.2.1 Chemicals and Materials

Cellulose nanocrystals (CNC) were supplied by Innotech Alberta (Edmonton, Canada). The CNCs were received in the sulfate-half ester form as a spray-dried powder, with an apparent particle size as determined by DLS as 100-230 nm, a surface charge of < -30 mV at pH 6.5-7, a total sulfur content of 0.5-1 wt%, and a thermal stability of 240-275˚C. L-Ascorbic acid, ethanol, acetonitrile, acetone, diethyl ether, sodium nitrite, tetrafluoroboric acid (5%), hydrochloric acid, 4-aminobenzylamine, p-phenylenediamine, 4-nitroaniline, and 4-nitrobenzenediazonium tetrafluoroborate were purchased from Sigma Aldrich (Oakville, Ontario). The GXF/GHP membrane (25mm diameter, pore size 0.45 μm) Acrodisc filters and BD syringes were also

purchased from Sigma Aldrich (Oakville, Ontario). Deionized (DI) water measured at 18.2Ω was used in all instances of water.

5.2.2 Purification of 4-Nitrobenzenediazonium Tetrafluoroborate (4-dNB)

The as-purchased 4-nitrobenzenediazonium tetrafluoroborate (4-dNB) salts were purified via a two-solvent recrystallization method using acetonitrile and diethyl ether. Acetonitrile and diethyl ether was placed in an ice bath to cool. In a beaker in the ice bath containing the 4-dNB, acetonitrile was added to just dissolve the diazonium salts. Then, diethyl ether was added dropwise until all the diazonium salts were precipitated out. The salts were subsequently vacuum dried and washed with more cold diethyl ether until the ether wash ran colourless.

5.2.3 Ex-Situ Diazonium Salt Synthesis and Cellulose Nanocrystal Modification

The *ex-situ* method was adapted from a previously reported procedure by Solak *et al.*[41] A 2M solution of the aniline precursor of the desired diazonium salt in tetrafluoroboric acid was stirred in an ice bath at 0˚C. Then, a 0˚C solution of a 3:1 ($NaNO_2$:aniline) molar ratio of aqueous $NaNO_2$ (in DI water until just dissolved) was added dropwise to the aniline solution ensuring the temperature of the solution did not exceed 4˚C. After all the $NaNO_2$ was added, the solution was left to stir for 30 minutes. The resultant diazonium salt was vacuum filtered and washed with ice cold diethyl ether until the solution ran colourless. Finally, to ensure all unreacted precursors were removed, a two-solvent recrystallization of the diazonium salt in ice cold acetonitrile and diethyl ether was performed, followed by another vacuum filtration and wash with ice cold diethyl ether. The solid diazonium salt was stored in the freezer until used.

A 1.0 wt/v% aqueous CNC solution was prepared by bath sonicating CNCs in DI water for 10 min. After sonication, the CNCs were filtered using a 0.45μm syringe filter to remove any large agglomerates that were not dispersed during sonication. The purified diazonium salts and 4 v/v% of 0.05 M l-ascorbic acid was added to the filtered CNC solution, bath sonicated for 1 hour, then left to stir at ambient conditions overnight. The diazonium modified CNCs were purified *via* centrifugation in acetonitrile at 5000 rpm for 30 minutes 3 times. The final diazonium modified CNCs were freeze dried from water.

5.2.4 In-Situ Diazonium Salt Synthesis and Cellulose Nanocrystal Modification

The *in-situ* method was adapted from a previously reported procedure by Breton and Belanger.[31] A 0.2 M solution of the aniline precursor of the desired diazonium was prepared in 0.5 M HCl and stirred magnetically until dissolved at ambient conditions. Then, an equal volume of 0.2 M of aqueous $NaNO_2$ was added and stirred for 15 minutes. After diazonium salt formation, an equal volume of 1.0 wt/v% of cellulose nanocrystals in DI water was added. Finally, 10 v/v% of 0.05 M l-ascorbic acid was added and the solution was bath sonicated for 1 hour, then left to stir at ambient conditions overnight. The diazonium modified CNCs were purified *via* centrifugation in acetonitrile at 5000 rpm for 30 minutes 3 times. The final diazonium modified CNCs were freeze dried from water.

5.2.5 Characterization

Fourier transform infrared (FT-IR) analysis was completed by Analytical Services in the Department of Chemistry (Edmonton, Alberta) using a Thermo Nicolet 8700 FTIR Spectrometer.

Freeze-dried samples were drop cast from methanol on a KBr plate and examined from 4000 to 600 cm^{-1}.

X-ray photoelectron spectroscopy (XPS) analysis was completed at by characterization staff at nanoFAB (Edmonton, Alberta) using a Kratos AXIS-165 spectrometer with a monochromatic AI Kα source (1486.69 eV) at 126 W. The CasaXPS software was used for data processing. The library was set to CasaXPS_KratosAxis-F1.lib and the high-resolution spectra was adjusted by setting the C1s peak to the 285.00 eV binding energy.

Elemental analysis by combustion of Carbon, Hydrogen, Nitrogen, Sulfur (CHNS) was completed by Analytical Services in the Department of Chemistry (Edmonton, Alberta) using a Thermo Flash 2000 Elemental Analyzer for CHNS and Oxygen.

Thermogravimetric Analysis (TGA) was completed by Analytical Services in the Department of Chemistry (Edmonton, Alberta) using a Perkin Elmer Pyris 1 TGA instrument. All samples were heated from 25-600˚C at a heating rate of 10˚C/min and using Argon as the carrier gas.

Contact angle measurements were prepared and collected by Dr. Rongbing Du. To prepare the samples for analysis, 1 mL of 1 wt/v% of unmodified or modified CNC in deionized water was drop cast onto a 1 cm x 1 cm silicon wafer then left to air dry. An FTA 200 Contact Analyzer (First Angstroms, Virginia, USA) was used for analysis. All measurements were carried out at ambient conditions. The captured images were analyzed using the FTA image analysis software.

X-Ray diffraction (XRD) measurements were prepared by Dr. Rongbing Du. Analysis was done by the Nanotechnology Research Centre Characterization Facility in the National Research Council Canada (Edmonton, Alberta). A Bruker D8 Discover XRD instrument with an IμS Cu Kα

source and Vantec 500 2D detector was used. Measurements were analyzed using a 2θ coverage from 4 frames, a scan range of 5-95˚, and a step size of 0.2˚.

5.3 Results and Discussion

5.3.1 Surface Modification of CNC Using the Ex-Situ Method

Diazonium salts were prepared using modified procedures from two different methods: *ex-situ* or *in-situ* diazotization. The results of the most commonly used *ex-situ* method of synthesizing diazonium salts reported by Bourdillon *et al.* will be described first.[42] A summarized reaction scheme is presented in Figure 5-3. Briefly, the aniline (in this study, 4-nitroaniline) was dissolved in tetrafluoroboric acid and cooled to 0˚C, then sodium nitrite was added dropwise. The resultant diazonium cation was purified *via* vacuum filtration and two-solvent recrystallization method to remove unreacted aniline. The final product was stored in the freezer until used. Either the as-purchased or freshly synthesized 4-dNB was used for modification. The solid diazonium salts were combined with a sonicated CNC aqueous solution. Finally, l-ascorbic acid, a water-soluble reducing agent, was added to initiate formation of diazonium radicals for surface modification. The final diazonium modified CNC was centrifuged in acetonitrile (ACN) then freeze-dried from water to obtain a dried, solid product.

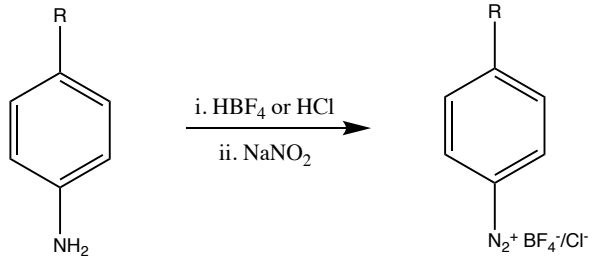

Figure 5-3. Summarized reaction scheme for the synthesis of diazonium salts. HBF_4 is used for the *ex-situ* method and HCl is used for the *in-situ* method. R = NO_2, NH_2, or CH_2NH_2.

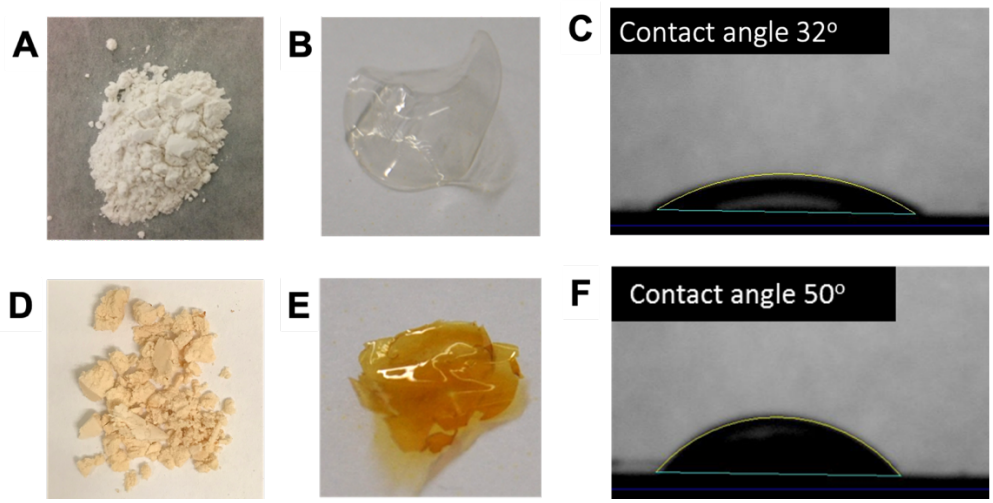

Figure 5-4. Contact angle measurements and photographs of CNCs. (A) Photographs of unmodified CNC dried powder and (B) unmodified CNC spin coated film, (C) contact angle measurement of unmodified CNC spin coated film, (D) photographs of 4-dNB+CNC freeze dried material and (E) 4-dNB+CNC spin coated film, and (F) contact angle measurement of 4-dNB+CNC spin coated film.

Wettability. Successful attachment of diazonium derived aryl groups to CNC particles is expected to change the wettability of the CNC surface, thus the contact angle of water was measured on solvent cast films of unmodified and modified CNC. The as-received spray dried CNC material is a white powder as shown in Figure 5-4A. A solvent cast film of this material appears clear and colourless (Fig. 5-4 B). The contact angle of water with the film is 32˚ (Fig. 5-4C), a value reflective of a relatively strong interaction between water and the CNC film. It is expected and known that water interacts with CNC *via* polar interactions and H-bonding resulting in a lower contact angle. The reaction between CNC and 4-nitrobenzenediazonium tetrafluoroborate (4-dNB) is expected to modify the CNC surface with nitrobenzene (NB) groups. The reaction results in an orange-coloured solid material as shown in Figure 5-4D. Nitrobenzene has an absorbance maximum at around 370 nm giving the solid material its orange color,[29] thus the solvent cast film is also orange in color (Fig. 5-4E). Therefore, the change in color from white to orange is consistent with modification of the CNC surface with nitrobenzene groups. The contact angle for the NB modified CNC film is 50˚, a value substantially higher than that on

unmodified CNC. It would be expected that a nitrobenzene layer will weaken the interaction between water and the CNC particles, thus the value of 50˚ is consistent of a film composed of CNCs containing NB groups on their surface.

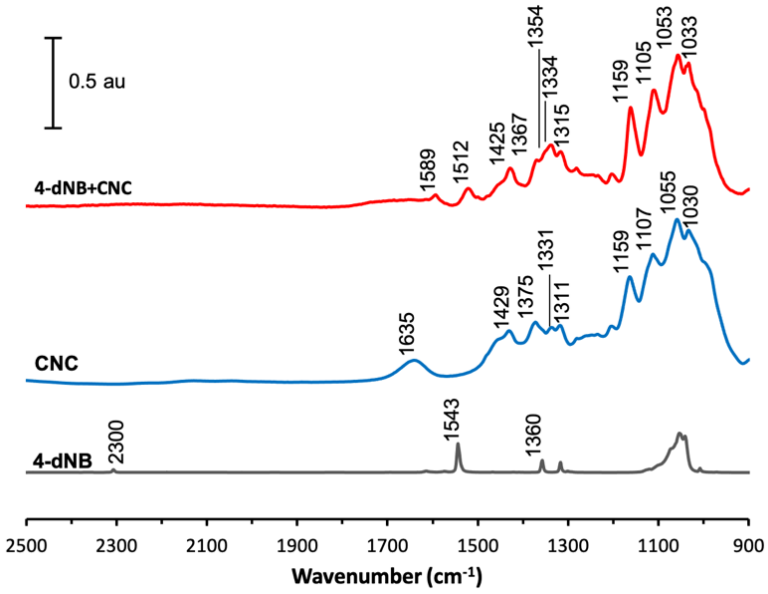

Figure 5-5. FTIR spectra of 4-nitrobenzenediazonium tetrafluoroborate (4-dNB), cellulose nanocrystals (CNC), and the material resulting from the reaction of 4-dNB and CNC (4-dNB+CNC).

FT-IR Analysis. 4-Nitrobenzenediazonium tetrafluoroborate (4-dNB) was used as the initial diazonium salt for examination of reactivity with CNC due to the strong signature of the nitro group in vibrational spectroscopy. The reactions between 4-dNB and CNC were first examined by FTIR. Figure 5-5 is the FTIR spectra of the two starting materials and the resulting surface modified material. The 4-dNB spectrum features all predicted bands at 2300 cm^{-1} ($-N_2^+$), 1543 cm^{-1} ($-NO_2$ asym.), and 1360 cm^{-1} ($-NO_2$ sym.).[11] The CNC spectrum is consistent with spectra presented in the literature, showing bands at 1429 cm^{-1} ($-CH_2-$), 1375-1311 cm^{-1} (1˚ and 2˚ -OH), 1159 cm^{-1} (glycosidic C-O-C), and 1107-1030 cm^{-1} (C-O of C2, C3, and C6 of glucose).[43] In addition to all the CNC bands, the modified 4-dNB+CNC spectrum shows the appearance of

the -NO_2 asymmetric and symmetric stretches at 1512 cm^{-1} and 1354 cm^{-1}, respectively, as well as the presence of the aromatic ring stretch at 1589 cm^{-1}. In cellulose membranes, diazonium cations are suggested to bind to the C6 methoxy group on cellulose.[44]

The disappearance of the diazonium -N_2^+ stretch at ~2300 cm^{-1} in the 4-dNB+CNC spectrum suggests that no free, unreacted diazonium molecules are adsorbed to CNC. The small, broad peak at 1630 cm^{-1} in the unmodified sample is attributed to water adsorbed by CNC,[45] which is significantly reduced after modification with 4-dNB. This suggests that the purification of 4-dNB+CNC in organic solvent (acetonitrile) in addition to the final freeze-drying step removed the majority of residual water. The removal of water is crucial for further processing in polymer composites where water can affect solution turbidity and final composite properties.[46-48] The results from Figure 5-5 are consistent with the bonding of diazonium derived 4-nitrobenzene with the surface of CNC.

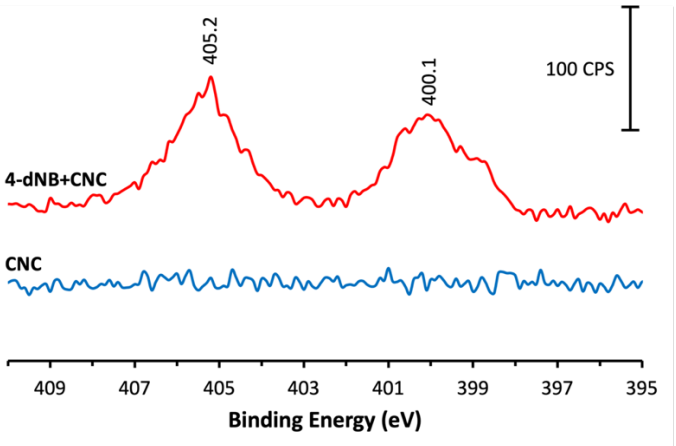

Figure 5-6. HR-XPS spectra in the N1s region for cellulose nanocrystals (CNC) and the material resulting from the reaction of 4-dNB and CNC (4-dNB+CNC).

HR-XPS. Further characterization of bonding was performed using HR-XPS. As shown in Figure 5-6, there is no detectable nitrogen in the N1s high resolution spectrum of unmodified CNC.

The 4-dNB+CNC N1s high resolution spectrum shows two peaks at 405.2 eV and 400.1 eV attributed to -NO_2 and reduced nitrogen (-N=N- or -NH_2), respectively. The appearance of a reduced nitrogen species is commonly seen in surfaces functionalized by 4-dNB.[49-51] Toupin and Belanger electrochemically modified carbon black with three different diazonium molecules, one of which was 4-dNB.[34] They suggested that the peak at ~400 eV is attributed to an azo (-C-N=N-C-) linkage between the diazonium molecules grafted onto the surface.[34] Therefore, it can be inferred that the presence of the peak at 400.1 eV is due to a multilayer of diazonium molecules that has formed on the surface of CNC *via* azo bridges. Additionally, it is possible that the nitro group in 4-dNB is reduced *in vacuo* during XPS measurements, also contributing to the presence of the reduced nitrogen species in the form of -NH_2.

Table 5-1. CHNS analysis of cellulose nanocrystals (CNC) and the material resulting from the reaction of 4-dNB and CNC (4-dNB+CNC).

	N (%)	C (%)	H (%)	S (%)
CNC	0.00	40.85	6.14	0.60
4-dNB+CNC	0.20	42.67	5.96	0.31

CHNS Elemental Analysis. CHNS analysis was done to further confirm the presence of the nitrogen-rich 4-nitrobenzenediazonium molecule. Table 5-1 lists the elemental analysis results for CNC and 4-dNB+CNC using CHNS analysis. The unmodified CNC sample shows expected atomic percentages for each of the elements detected,[52-55] with values at 0% nitrogen (N), 40.85% carbon (C), 6.14% hydrogen (H), and 0.60% sulfur (S). After the reaction of 4-dNB with CNC, the %N increases to 0.20% due to the presence of the nitro groups from 4-dNB and azo bridges in the multilayer. The addition of carbon-rich aryl groups also increased the C content by 1.8%. Interestingly, both the H and S content decreased slightly by 0.18% and 0.29%, respectively. This

can be attributed to hydrogen extraction during the redox of the diazonium molecule and CNC,[56] as well as the displacement of the labile sulfate half esters on CNC under the reaction conditions.[57, 58]

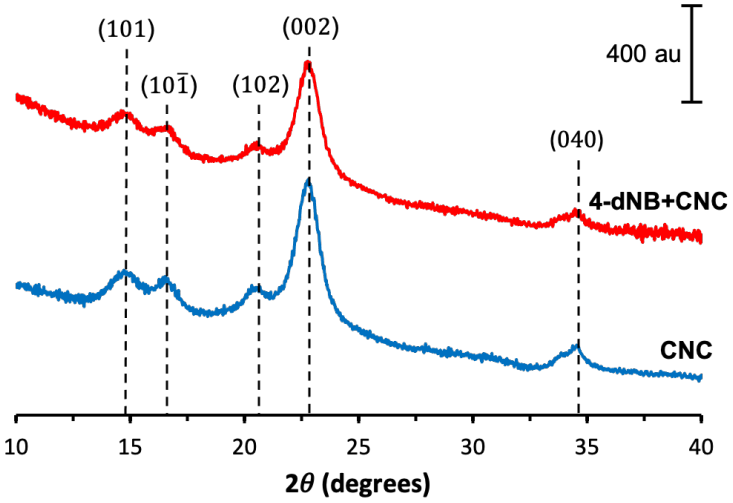

Figure 5-7. XRD analysis of cellulose nanocrystals (CNC) and the material resulting from the reaction of 4-dNB and CNC (4-dNB+CNC).

XRD Analysis. A potential change in crystallinity is an important factor to consider when incorporating surface functionalized CNCs in polymers with the goal of increased mechanical strength, as the crystallinity of CNC plays a key role in its reinforcing potential.[59] Therefore, XRD was used to study the effect of surface modification on CNC crystallinity, as depicted in Figure 5-7. Both the unmodified CNC and 4-dNB+CNC spectra show all characteristic cellulose I peaks at 101, 10$\bar{1}$, 102, 002, and 040.[43] There is no significant change in crystallinity or apparent crystal faces present after modification with 4-dNB.

Thermal Properties. There are numerous different polymer composite processing techniques ranging from solvent evaporation to heating methods, as described in previous Chapters. Though CNC is known for its strong mechanical reinforcement properties,[60, 61] it suffers

from burning and discoloration at elevated temperatures,[45] which pose a problem when utilizing high processing temperatures in melt mixing. Therefore, it is important to investigate the thermal stability of surface functionalized CNC for applications in polymer composites.

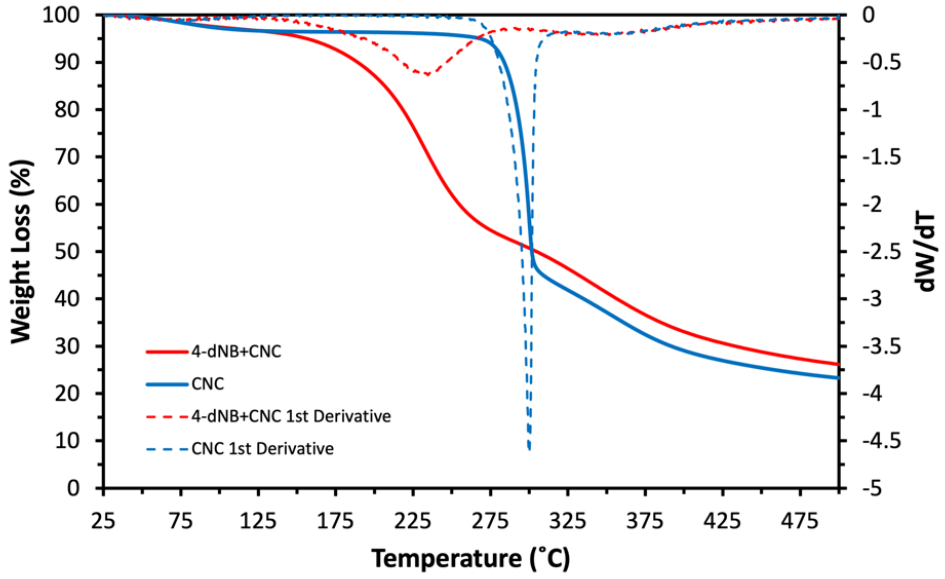

Figure 5-8. Thermogravimetric analysis (TGA) and the first derivative thermograms (DTG) of CNC (blue) and 4-dNB+CNC (red). The Weight Loss (%) axis on the left is for the TGA spectra (solid lines) and the dW/dT axis on the left is for the DTG spectra (dashed lines).

Thermogravimetric analysis (TGA) and the first derivative of the thermograms (DTG) were used to compare the thermal stability of the unmodified and modified CNCs, as shown in Figure 5-8. Both the CNC and 4-dNB+CNC samples show a small 5% weight decrease in the first 225˚C, which is attributed to water loss due to the hydroscopic nature of CNCs.[45] From 25˚C to 300˚C, there is a gradual 45% weight loss of 4-dNB+CNC that can be attributed to the degradation of the 4-nitrobenzenediazonium moieties, which has a melting point of 144˚C.[62] The initial degradation of 4-dNB+CNC starts at a lower onset temperature (T_O) than for unmodified CNC, 193˚C compared to 295˚C, respectively, also attributed to the earlier degradation of 4-dNB. The DTG of unmodified CNC shows a 1st derivative peak temperature (T_P) at 300˚C, whereas the T_P

of 4-dNB+CNC decreases to 234˚C. The decrease in thermal stability after the addition of 4-dNB is consistent with literature reports of radical initiated attachment of molecules to surfaces, where radically formed bonds degrade at lower temperatures.[34, 63] With both the T_O and T_P values appearing at temperatures above the expected onset of CNC degradation at 190˚C, we can confirm that the 4-dNB molecules are covalently grafted onto the CNC surface. Past the T_P, the remaining mass is attributed to char consisting of mostly low molecular weight hydrocarbons.[45] Though both modified and unmodified CNC TGA curves follow the same trend past 300˚C, the curve for 4-dNB+CNC has a higher residue yield compared to CNC due to remaining char from the carbon-rich diazonium multilayer. Considering the overall decrease in thermal stability observed, I recommend that diazonium modified CNCs be used for non-heat or low-heat polymer composite processing, such as spin coating or electrospinning, to prevent degradation of the diazonium molecules at high processing temperatures.

5.3.2 Surface Modification of CNC Using the In-Situ Method

Another method to synthesize diazonium cations *in-situ* was investigated using a modified procedure from Breton and Belanger.[31] Different from the *ex-situ* method, the *in-situ* method is fast (15 minutes compared to >1 hours) and does not require purification of the resultant diazonium salt prior to use for surface modification. The summarized reaction scheme is presented in Figure 5-4. Briefly, the chosen aniline form of the diazonium was dissolved in 0.5 M HCl. An equal volume of 0.2 M sodium nitrite to the aniline precursor solution was combined and stirred at ambient conditions for 15 minutes. The entirety of the resultant diazonium salt solution was used for surface modification with CNC using the same procedure as the *ex-situ* method. 4-Aminobenzylamine (4-ABA) and p-phenylenediamine (p-PD) were used in the *in-situ* method to

yield 4-aminobenzyldiazonium (4-dAB) and p-aminobenzenediazonium (p-dAB), respectively. The structures of the diazonium cations are illustrated in Figure 5-3. Similar to the choice of using 4-dNB in the *ex-situ* method, the presence of the nitrogen-containing amine groups in 4-ABA and p-PD also make them easily distinguishable from cellulose during characterization.

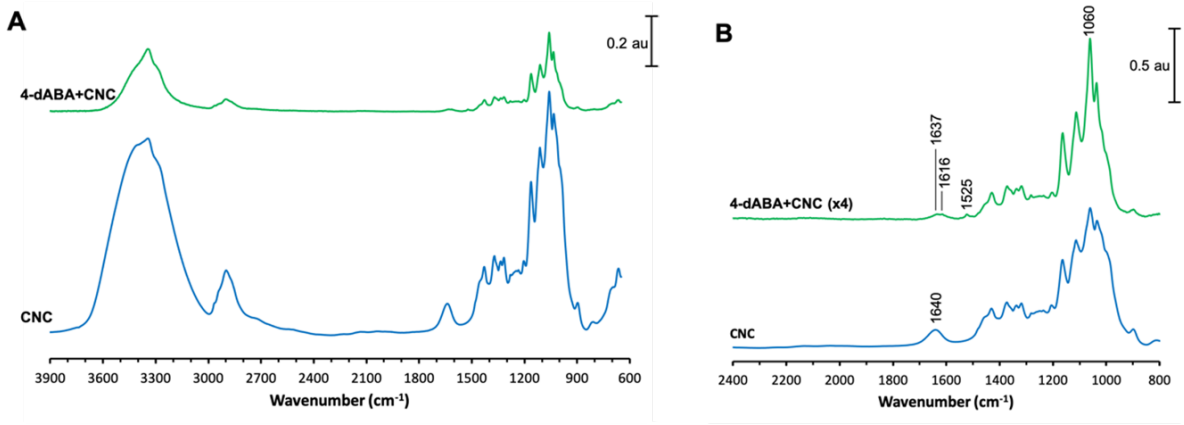

Figure 5-9. FTIR spectra of 4-dABA+CNC and CNC. (A) FTIR spectra of cellulose nanocrystals (CNC) and the materials resulting from the reaction of 4-dABA and CNC (4-dABA+CNC), and (B) enlarged FTIR spectra of CNC and 4-dABA+CNC in the 2400-800 cm^{-1} region. The absorbance intensity of the 4-dABA+CNC spectrum in (B) is increased by a factor of 4 to better show the peaks.

FTIR Analysis of 4-dABA+CNC. FTIR spectroscopy was used to assess the modification of CNC with 4-aminobenzyldiazonium (4-dABA+CNC) using the *in-situ* method, as shown in Figure 5-9. Both the CNC and 4-dABA+CNC spectra in Figure 5-9A show all expected peaks corresponding to cellulose.[43] The 4-dANA+CNC spectrum in Figure 5-9A shows a sharp peak in the -OH region at 3338 cm^{-1} corresponding to the $-NH_2$ bend of the methylamine group in 4-dABA. When comparing the lower IR regions in Figure 5-9B, there is the appearance of a weak $-NH_2$ stretch at 1616 cm^{-1} and a weak aromatic ring stretch at 1525 cm^{-1} in the 4-dABA+CNC spectrum. There is also an increase in intensity of the peak at 1060 cm^{-1} relative to its adjacent peaks, which is a result of the combined intensity of the C-N stretch from 4-dABA and from the C-O stretch of C2 in CNC. As was observed in the *ex-situ* method, there is also a reduction of the absorbed water

peak at 1637 cm^{-1} for 4-dABA+CNC compared to unmodified CNC due to the purification in organic solvent as well as freeze-drying.

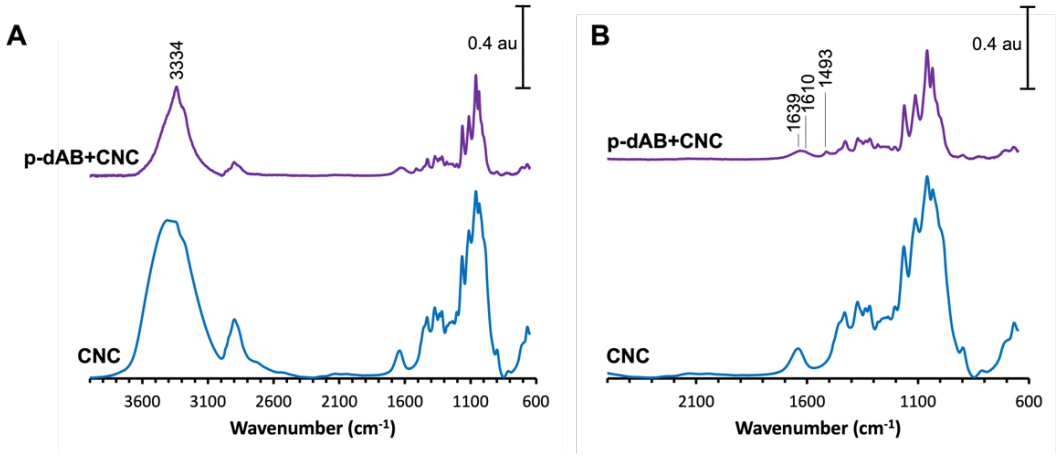

Figure 5-10. FTIR spectra of p-dAB+CNC and CNC. (A) FTIR spectra of cellulose nanocrystals (CNC) and the materials resulting from the reaction of p-dAB and CNC (p-dAB+CNC), and (B) Enlarged FTIR spectra of CNC and p-dAB+CNC in the 2500-600 cm^{-1} region.

FTIR Analysis of p-dAB+CNC. p-Phenylenediamine to form p-aminobenzenediazonium (p-dAB) was also synthesized using the *in-situ* method.[64] FTIR analysis of the material resulting from the reaction of p-aminobenzenediazonium and CNC (p-dAB+CNC) was performed, as presented in Figure 5-10. Like the spectra shown in Figures 5-5 and 5-9, Figure 5-10A shows all expected peaks for cellulose in both the CNC and p-dAB+CNC spectra. In the lower IR regions presented in Figure 5-10B, the p-dAB+CNC spectrum has the appearance of two weak peaks at 1493 cm^{-1} and 1610 cm^{-1} which is attributed to the aromatic ring stretch and $-NH_2$ stretch, respectively. There is also a decrease in the peak absorbance of absorbed water at 1639 cm^{-1} for p-dAB+CNC.

Interestingly, though the p-phenylenediamine precursor has two amine groups that can form the $-N_2^+$ cation during diazotization,[65] no evidence of a band at around 2300 cm^{-1} correlating

to the $-N_2^+$ is present in the FTIR spectrum reported here. Instead, there is a sharp increase in peak absorbance at 3334 cm^{-1} and the appearance of the 1610 cm^{-1} peak in the p-dAB+CNC spectrum that corresponds to the $-NH_2$ group, as shown in Figure 5-10A. The availability of the unreacted amine group provides a pathway towards further reactivity. It has been shown that the free amine group can undergo an additional hydrolysis to form linear multilayers on boron nitride nanotubes.[66] The potential for different multilayer morphologies provides interesting routes for countless tunable surface properties and applications for diazonium modified CNCs. Furthermore, this is the first time that the *in-situ* formation of diazonium cations for the modification of CNC has been reported.

5.3.3 Proposed Mechanism

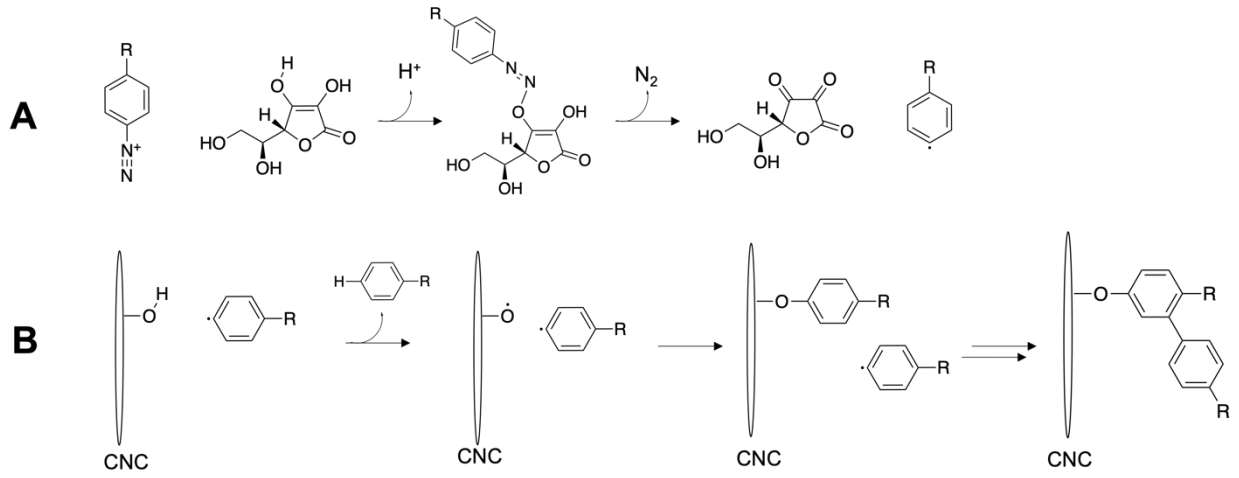

Figure 5-11. Proposed mechanism for the formation of aryl radicals from diazonium cations (A) and the attachment of the aryl molecules onto CNC (B).

Proposed Mechanism for the Attachment of Aryl Radicals on CNC. A proposed mechanism based on the data presented here and previous reports on the attachment of aryl molecules onto CNC using diazonium chemistry is presented in Figure 11. In Figure 5-11A, the

diazonium cation reacts with l-ascorbic acid where the $-N_2^+$ is removed resulting in a radical aryl molecule.[67] Since aryl radical formation and CNC modification are carried out in the same reaction vessel, the aryl radical then extracts a hydrogen from a C6 methoxy group on CNC leaving a radical on the surface, as illustrated in Figure 5-11B.[44] It has been suggested that the C6 group is the most reactive hydroxyl group on cellulose due to the free rotation of the group compared to the C2 or C3 hydroxyls that are bound directly to the chair.[68, 69] In an uncontrolled environment, we expect that another aryl radical binds to the bound aryl forming a multilayer, as has been observed on conductive surfaces.[9, 70] Specifically, multilayer formation starts when a free aryl radical binds to positions ortho to the substituent on the bound aryl group.[71, 72] Further electrochemical studies should be performed in order to gauge the thickness of the grafted layer.[9]

5.3.4 Diazonium Modified CNC and Nylon 6 Thin Films

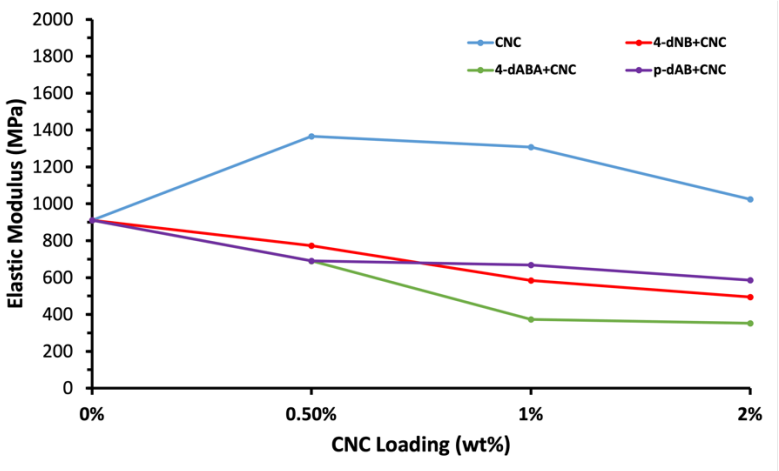

Figure 5-12. Elastic modulus results for the diazonium modified CNC and Nylon 6 thin films at CNC loadings of 0, 0.5, 1, and 2 wt%**.** The blue line is unmodified CNC, the red line is 4-dNB+CNC, the green line is 4-dABA+CNC, and the purple line is p-dAB+CNC.

Effect of Aryl Modification on CNC-Nylon 6 Composite Films. The modification of additives opens the door to the incorporation of countless nanomaterials in otherwise incompatible matrices. More specifically, diazonium modification of fillers has been used for composite reinforcement using carbon nanotubes (CNTs), graphene oxide (GO), and silica nanoparticles with the goal of increasing filler-polymer adhesion and promoting better dispersion of the filler within the matrix[15, 22] Thus, a short study into the reinforcing impact of the modified CNCs in Nylon 6 was performed. Thin films were prepared using the same solution preparation and spin coating procedure reported in Chapter 2. The elastic moduli of the films are presented in Figure 5-12, where only one film per loading was tested. The incorporation of the diazonium modified CNC in Nylon 6 decreased the elastic moduli at all loadings compared to the unmodified CNC films. Overall, the elastic modulus decreased with increasing CNC loading suggesting that the modified CNCs did not form favourable interactions with Nylon 6. Additionally, an observed poor dispersion of the modified CNCs in formic acid led to aggregates which may act as fracture points in the films (not shown here). This is contrary to our initial thoughts, where we expected the nitrogen-containing groups on the aryl molecules to form hydrogen bonds with the amide groups in Nylon.[73, 74] Therefore, the mechanical results suggest that the interfacial adhesion between CNC and Nylon is inhibited by the aryl multilayer. Though diazonium modified CNC did not increase the mechanical properties of Nylon 6, other more compatible polymers and solvents may benefit from the addition of aryl modified CNCs, such as aryl-rich polystyrene as presented in a previous paper from our group.[39]

5.4 Conclusion

Cellulose nanocrystals were modified with three different diazonium salts using two diazotization methods. The diazonium molecules in this study were chosen because of the strong signatures of the nitrogen-containing R groups when characterized using spectroscopic techniques, as well as the possibility of increased compatibilization of CNC in Nylon 6. First, CNC was modified with 4-nitrobenzenediazonium using an *ex-situ* method where the diazonium salt was prepared and purified before modification. Grafting was confirmed using FTIR, HR-XPS, and CHNS. The results of the characterization are consistent with the bonding of diazonium molecules onto a surface. Crystallinity of CNC was unchanged after modification, as shown by XRD. The thermal stability of the modified CNC, as evaluated by TGA, decreased due to the instability of diazonium molecules at high temperatures. Therefore, it is recommended that diazonium modified CNC be used as fillers in low temperature or solvent processing composite techniques. Secondly, CNC was modified with 4-aminobenzyldiazonium and p-aminobenzenediazonium using the *in-situ* method where the diazonium salt was prepared in-solution. Grafting was confirmed using FTIR. This study showed that both the *ex-situ* and *in-situ* methods are valid options for modification of cellulose nanocrystals with diazonium salts. Finally, composite films containing each of the diazonium modified CNCs in Nylon 6 were produced, where the modified CNCs decreased the elastic modulus of the films at all loadings compared to unmodified CNC.

5.5 References

1. Vanderfleet, O. M.; Cranston, E. D., Production routes to tailor the performance of cellulose nanocrystals. *Nature Reviews Materials* **2021,** *6* (2), 124-144.
2. Dufresne, A., 3. Preparation of cellulose nanocrystals. In *Nanocellulose: From Nature to High Performance Tailored Materials*, De Gruyter: 2017; pp 117-192.
3. Dufresne, A., 5. Chemical modification of nanocellulose. In *Nanocellulose: From Nature to High Performance Tailored Materials*, De Gruyter: 2017; pp 221-286.

4. Eyley, S.; Thielemans, W., Surface modification of cellulose nanocrystals. *Nanoscale* **2014,** *6* (14), 7764-7779.
5. Kargarzadeh, H.; Mariano, M.; Huang, J.; Lin, N.; Ahmad, I.; Dufresne, A.; Thomas, S., Recent developments on nanocellulose reinforced polymer nanocomposites: A review. *Polymer* **2017,** *132*, 368-393.
6. Shi, Z.; Li, S.; Li, M.; Gan, L.; Huang, J., Surface modification of cellulose nanocrystals towards new materials development. *Journal of Applied Polymer Science* **2021,** *138* (48), 51555.
7. Mariano, M.; El Kissi, N.; Dufresne, A., Cellulose nanocrystals and related nanocomposites: Review of some properties and challenges. *Journal of Polymer Science Part B: Polymer Physics* **2014,** *52* (12), 791-806.
8. Grishkewich, N.; Mohammed, N.; Tang, J. T.; Tam, K. C., Recent advances in the application of cellulose nanocrystals. *Current Opinion in Colloid & Interface Science* **2017,** *29*, 32-45.
9. Kariuki, J. K.; McDermott, M. T., Formation of Multilayers on Glassy Carbon Electrodes via the Reduction of Diazonium Salts. *Langmuir* **2001,** *17* (19), 5947-5951.
10. Laurentius, L.; Stoyanov, S. R.; Gusarov, S.; Kovalenko, A.; Du, R.; Lopinski, G. P.; McDermott, M. T., Diazonium-Derived Aryl Films on Gold Nanoparticles: Evidence for a Carbon–Gold Covalent Bond. *ACS Nano* **2011,** *5* (5), 4219-4227.
11. Shewchuk, D. M.; McDermott, M. T., Comparison of Diazonium Salt Derived and Thiol Derived Nitrobenzene Layers on Gold. *Langmuir* **2009,** *25* (8), 4556-4563.
12. Zhang, Z.; Sèbe, G.; Hou, Y.; Wang, J.; Huang, J.; Zhou, G., Grafting polymers from cellulose nanocrystals via surface-initiated atom transfer radical polymerization. *Journal of Applied Polymer Science* **2021,** *138* (48), 51458.
13. Peng, S.; Luo, Q.; Zhou, G.; Xu, X., Recent Advances on Cellulose Nanocrystals and Their Derivatives. *Polymers* **2021,** *13* (19), 3247.
14. Knirsch, K. C.; Berner, N. C.; Nerl, H. C.; Cucinotta, C. S.; Gholamvand, Z.; McEvoy, N.; Wang, Z.; Abramovic, I.; Vecera, P.; Halik, M.; Sanvito, S.; Duesberg, G. S.; Nicolosi, V.; Hauke, F.; Hirsch, A.; Coleman, J. N.; Backes, C., Basal-Plane Functionalization of Chemically Exfoliated Molybdenum Disulfide by Diazonium Salts. *ACS Nano* **2015,** *9* (6), 6018-6030.
15. Sandomierski, M.; Voelkel, A., Diazonium Modification of Inorganic and Organic Fillers for the Design of Robust Composites: A Review. *Journal of Inorganic and Organometallic Polymers and Materials* **2021,** *31* (1), 1-21.
16. Bahr, J. L.; Yang, J.; Kosynkin, D. V.; Bronikowski, M. J.; Smalley, R. E.; Tour, J. M., Functionalization of Carbon Nanotubes by Electrochemical Reduction of Aryl Diazonium Salts: A Bucky Paper Electrode. *Journal of the American Chemical Society* **2001,** *123* (27), 6536-6542.
17. Kindt, S.; Wicht, K.; Heinrich, M. R., Thermally Induced Carbohydroxylation of Styrenes with Aryldiazonium Salts. *Angewandte Chemie International Edition* **2016,** *55* (30), 8744-8747.
18. Lehr, J.; Williamson, B. E.; Downard, A. J., Spontaneous Grafting of Nitrophenyl Groups to Planar Glassy Carbon Substrates: Evidence for Two Mechanisms. *The Journal of Physical Chemistry C* **2011,** *115* (14), 6629-6634.
19. Marcoux, P. R.; Hapiot, P.; Batail, P.; Pinson, J., Electrochemical functionalization of nanotube films: growth of aryl chains on single-walled carbon nanotubes. *New Journal of Chemistry* **2004,** *28* (2), 302-307.

20. Szabó, L.; Imanishi, S.; Kawashima, N.; Hoshino, R.; Takada, K.; Hirose, D.; Tsukegi, T.; Ninomiya, K.; Takahashi, K., Carbon fibre reinforced cellulose-based polymers: intensifying interfacial adhesion between the fibre and the matrix. *RSC Advances* **2018,** *8* (40), 22729-22736.
21. Griffete, N.; Lamouri, A.; Herbst, F.; Felidj, N.; Ammar, S.; Mangeney, C., Synthesis of highly soluble polymer-coated magnetic nanoparticles using a combination of diazonium salt chemistry and the iniferter method. *RSC Advances* **2012,** *2* (3), 826-830.
22. Gautier, C.; López, I.; Breton, T., A post-functionalization toolbox for diazonium (electro)-grafted surfaces: review of the coupling methods. *Materials Advances* **2021,** *2* (9), 2773-2810.
23. Mahouche-Chergui, S.; Gam-Derouich, S.; Mangeney, C.; Chehimi, M. M., Aryl diazonium salts: a new class of coupling agents for bonding polymers, biomacromolecules and nanoparticles to surfaces. *Chem Soc Rev* **2011,** *40* (7), 4143-66.
24. Firth, J. D.; Fairlamb, I. J. S., A Need for Caution in the Preparation and Application of Synthetically Versatile Aryl Diazonium Tetrafluoroborate Salts. *Organic Letters* **2020,** *22* (18), 7057-7059.
25. Bonin, H.; Fouquet, E.; Felpin, F.-X., Aryl Diazonium versus Iodonium Salts: Preparation, Applications and Mechanisms for the Suzuki–Miyaura Cross-Coupling Reaction. *Advanced Synthesis & Catalysis* **2011,** *353* (17), 3063-3084.
26. Hossain, M. Z.; Shimizu, N., In Situ Functionalization of Graphene with Reactive End Group through Amine Diazotization. *The Journal of Physical Chemistry C* **2017,** *121* (45), 25223-25228.
27. Sheng, M.; Frurip, D.; Gorman, D., Reactive chemical hazards of diazonium salts. *Journal of Loss Prevention in the Process Industries* **2015,** *38*, 114-118.
28. Oger, N.; d'Halluin, M.; Le Grognec, E.; Felpin, F.-X., Using Aryl Diazonium Salts in Palladium-Catalyzed Reactions under Safer Conditions. *Organic Process Research & Development* **2014,** *18* (12), 1786-1801.
29. Baranton, S.; Bélanger, D., In situ generation of diazonium cations in organic electrolyte for electrochemical modification of electrode surface. *Electrochimica Acta* **2008,** *53* (23), 6961-6967.
30. Hetemi, D.; Hazimeh, H.; Decorse, P.; Galtayries, A.; Combellas, C.; Kanoufi, F.; Pinson, J.; Podvorica, F. I., One-Step Formation of Bifunctionnal Aryl/Alkyl Grafted Films on Conducting Surfaces by the Reduction of Diazonium Salts in the Presence of Alkyl Iodides. *Langmuir* **2015,** *31* (19), 5406-5415.
31. Breton, T.; Belanger, D., Modification of carbon electrode with aryl groups having an aliphatic amine by electrochemical reduction of in situ generated diazonium cations. *Langmuir* **2008,** *24* (16), 8711-8718.
32. Anariba, F.; DuVall, S. H.; McCreery, R. L., Mono- and Multilayer Formation by Diazonium Reduction on Carbon Surfaces Monitored with Atomic Force Microscopy "Scratching". *Analytical Chemistry* **2003,** *75* (15), 3837-3844.
33. Doppelt, P.; Hallais, G.; Pinson, J.; Podvorica, F.; Verneyre, S., Surface Modification of Conducting Substrates. Existence of Azo Bonds in the Structure of Organic Layers Obtained from Diazonium Salts. *Chemistry of Materials* **2007,** *19* (18), 4570-4575.
34. Toupin, M.; Bélanger, D., Thermal Stability Study of Aryl Modified Carbon Black by in Situ Generated Diazonium Salt. *The Journal of Physical Chemistry C* **2007,** *111* (14), 5394-5401.
35. Islam, S.; Hasan, M.; Ahmad, M. B., Chemical Modification and Properties of Cellulose-Based Polymer Composites. In *Lignocellulosic Polymer Composites*, 2014; pp 301-324.

36. Vallés, C.; Papageorgiou, D. G.; Lin, F.; Li, Z.; Spencer, B. F.; Young, R. J.; Kinloch, I. A., PMMA-grafted graphene nanoplatelets to reinforce the mechanical and thermal properties of PMMA composites. *Carbon* **2020,** *157*, 750-760.
37. Yu, D. S.; Kuila, T.; Kim, N. H.; Lee, J. H., Enhanced properties of aryl diazonium salt-functionalized graphene/poly(vinyl alcohol) composites. *Chemical Engineering Journal* **2014,** *245*, 311-322.
38. Robles, E.; Labidi, J.; Halász, K.; Csóka, L., 18 - Key issues in reinforcement involving nanocellulose. In *Cellulose-Reinforced Nanofibre Composites*, Jawaid, M.; Boufi, S.; H.P.S, A. K., Eds. Woodhead Publishing: 2017; pp 401-425.
39. Kalantari, M.; Du, R.; Ayranci, C.; Boluk, Y., Effects of interfacial interactions and interpenetrating brushes on the electrospinning of cellulose nanocrystals-polystyrene fibers. *J Colloid Interface Sci* **2018,** *528*, 419-430.
40. Du, R.; Kaufman, G.; McDermott, M. In *Surface modification of cellulose nanocrystals (CNCs) with diazonium salts and their application in nanocomposites*, TAPPI International Conference on Nanotechnology for Renewable Materials 2016, 2016; pp 633-643.
41. Solak, A. O.; Eichorst, L. R.; Clark, W. J.; McCreery, R. L., Modified Carbon Surfaces as "Organic Electrodes" That Exhibit Conductance Switching. *Analytical Chemistry* **2003,** *75* (2), 296-305.
42. Bourdillon, C.; Delamar, M.; Demaille, C.; Hitmi, R.; Moiroux, J.; Pinson, J., Immobilization of glucose oxidase on a carbon surface derivatized by electrochemical reduction of diazonium salts. *Journal of Electroanalytical Chemistry* **1992,** *336* (1), 113-123.
43. Foster, E. J.; Moon, R. J.; Agarwal, U. P.; Bortner, M. J.; Bras, J.; Camarero-Espinosa, S.; Chan, K. J.; Clift, M. J. D.; Cranston, E. D.; Eichhorn, S. J.; Fox, D. M.; Hamad, W. Y.; Heux, L.; Jean, B.; Korey, M.; Nieh, W.; Ong, K. J.; Reid, M. S.; Renneckar, S.; Roberts, R.; Shatkin, J. A.; Simonsen, J.; Stinson-Bagby, K.; Wanasekara, N.; Youngblood, J., Current characterization methods for cellulose nanomaterials. *Chem Soc Rev* **2018,** *47* (8), 2609-2679.
44. Credou, J.; Volland, H.; Dano, J.; Berthelot, T., A one-step and biocompatible cellulose functionalization for covalent antibody immobilization on immunoassay membranes. *Journal of Materials Chemistry B* **2013,** *1* (26), 3277-3286.
45. Reid, M. S.; Villalobos, M.; Cranston, E. D., Benchmarking Cellulose Nanocrystals: From the Laboratory to Industrial Production. *Langmuir* **2017,** *33* (7), 1583-1598.
46. Pillay, S.; Vaidya, U. K.; Janowski, G. M., Effects of moisture and UV exposure on liquid molded carbon fabric reinforced nylon 6 composite laminates. *Composites Science and Technology* **2009,** *69* (6), 839-846.
47. Titone, V.; Correnti, A.; La Mantia, F. P., Effect of Moisture Content on the Processing and Mechanical Properties of a Biodegradable Polyester. *Polymers* **2021,** *13* (10), 1616.
48. Pelipenko, J.; Kristl, J.; Janković, B.; Baumgartner, S.; Kocbek, P., The impact of relative humidity during electrospinning on the morphology and mechanical properties of nanofibers. *Int J Pharm* **2013,** *456* (1), 125-34.
49. Su, J.; Calderón Gómez, J. C.; Grundmeier, G.; González Orive, A., Electrografting of 4-Nitrobenzenediazonium Salts on Al-7075 Alloy Surfaces—The Role of Intermetallic Particles. *Nanomaterials* **2021,** *11* (4), 894.
50. Pan, L.; Duan, L.; Zheng, Z.; Hu, Y.; Aamir, A.; Bhuwan, S.; Tao, J.; Zhao, T.; Du, Z., Surface characteristics and adhesive strength to polyetheretherketone of titanium electrografted with aryl diazonium salt. *Materials & Design* **2016,** *95*, 555-562.

51. Baranton, S.; Belanger, D., Electrochemical derivatization of carbon surface by reduction of in situ generated diazonium cations. *J Phys Chem B* **2005,** *109* (51), 24401-10.
52. Carneiro de Oliveira, J.; Rigolet, S.; Marichal, C.; Roucoules, V.; Laborie, M.-P., Grafting Diels-Alder moieties on cellulose nanocrystals through carbamation. *Carbohydrate Polymers* **2020,** *250*, 116966.
53. Mariano, M.; Chirat, C.; El Kissi, N.; Dufresne, A., Impact of Cellulose Nanocrystal Aspect Ratio on Crystallization and Reinforcement of Poly(butylene adipate-co-terephthalate). *Journal of Polymer Science Part B-Polymer Physics* **2016,** *54* (22), 2284-2297.
54. Le Gars, M.; Roger, P.; Belgacem, N.; Bras, J., Role of solvent exchange in dispersion of cellulose nanocrystals and their esterification using fatty acids as solvents. *Cellulose* **2020,** *27* (8), 4319-4336.
55. Saha, S.; Hemraz, U. D.; Boluk, Y., The Effects of High Pressure and High Temperature in Semidilute Aqueous Cellulose Nanocrystal Suspensions. *Biomacromolecules* **2020,** *21* (2), 1031-1035.
56. Pinson, J.; Podvorica, F. I., Surface modification of materials: Electrografting of organic films. *Current Opinion in Electrochemistry* **2020,** *24*, 44-48.
57. Lin, N.; Dufresne, A., Surface chemistry, morphological analysis and properties of cellulose nanocrystals with gradiented sulfation degrees. *Nanoscale* **2014,** *6* (10), 5384-5393.
58. Habibi, Y.; Lucia, L. A.; Rojas, O. J., Cellulose Nanocrystals: Chemistry, Self-Assembly, and Applications. *Chemical Reviews* **2010,** *110* (6), 3479-3500.
59. Dufresne, A., 9. Mechanical properties of nanocellulose-based nanocomposites. In *Nanocellulose: From Nature to High Performance Tailored Materials*, De Gruyter: 2017; pp 471-530.
60. Yong, C.; Mei, C.; Guan, M.; Wu, Q.; Sun, X.; Xu, B.; Wang, K., Interfacial modification mechanism of nanocellulose as a compatibilizer for immiscible binary poly(vinyl alcohol)/poly(ethylene oxide) blends. **2018,** *135* (9), 45896.
61. Shojaeiarani, J.; Bajwa, D. S.; Stark, N. M., Spin-coating: A new approach for improving dispersion of cellulose nanocrystals and mechanical properties of poly (lactic acid) composites. *Carbohydr Polym* **2018,** *190*, 139-147.
62. Bondarev, A. A.; Naumov, E. V.; Kassanova, A. Z.; Krasnokutskaya, E. A.; Stankevich, K. S.; Filimonov, V. D., First Study of the Thermal and Storage Stability of Arenediazonium Triflates Comparing to 4-Nitrobenzenediazonium Tosylate and Tetrafluoroborate by Calorimetric Methods. *Organic Process Research & Development* **2019,** *23* (11), 2405-2415.
63. Li, M.; Liu, X.; Liu, N.; Guo, Z.; Singh, P. K.; Fu, S., Effect of surface wettability on the antibacterial activity of nanocellulose-based material with quaternary ammonium groups. *Colloids and Surfaces A: Physicochemical and Engineering Aspects* **2018,** *554*, 122-128.
64. Flavel, B. S.; Gross, A. J.; Garrett, D. J.; Nock, V.; Downard, A. J., A simple approach to patterned protein immobilization on silicon via electrografting from diazonium salt solutions. *ACS Appl Mater Interfaces* **2010,** *2* (4), 1184-90.
65. Marshall, N.; Rodriguez, A.; Crittenden, S., Diazonium-functionalized thin films from the spontaneous reaction of p-phenylenebis(diazonium) salts. *RSC Advances* **2018,** *8* (12), 6690-6698.
66. Wang, Z.; Li, Q.; Liu, J.; Li, H.; Zheng, S., Covalent Surface Functionalization of Boron Nitride Nanotubes Fabricated with Diazonium Salt. *Journal of Nanomaterials* **2018,** *2018*, 6717046.

67. Liu, S.; Cheng, P.; Liu, W.; Zeng, J.-G., Ascorbic Acid-Initiated Tandem Radical Cyclization of N-Arylacrylamides to Give 3,3-Disubstituted Oxindoles. *Molecules (Basel, Switzerland)* **2015,** *20* (9), 15631-15642.
68. Roy, D.; Semsarilar, M.; Guthrie, J. T.; Perrier, S., Cellulose modification by polymer grafting: a review. *Chemical Society Reviews* **2009,** *38* (7), 2046-2064.
69. Hebeish, A.; Guthrie, J. T., Grafting on Chemically Modified Cellulose. In *The Chemistry and Technology of Cellulosic Copolymers*, Springer Berlin Heidelberg: Berlin, Heidelberg, 1981; pp 196-244.
70. Olguín, C. F.; Agurto, N.; Silva, C. P.; Candia, C. P.; Santander-Nelli, M.; Oyarzo, J.; Gómez, A.; Silva, J. F.; Pavez, J., Tuning the Covering on Gold Surfaces by Grafting Amino-Aryl Films Functionalized with Fe(II) Phthalocyanine: Performance on the Electrocatalysis of Oxygen Reduction. *Molecules* **2021,** *26* (6), 1631.
71. Allongue, P.; Delamar, M.; Desbat, B.; Fagebaume, O.; Hitmi, R.; Pinson, J.; Savéant, J.-M., Covalent Modification of Carbon Surfaces by Aryl Radicals Generated from the Electrochemical Reduction of Diazonium Salts. *Journal of the American Chemical Society* **1997,** *119* (1), 201-207.
72. Pinson, J.; Podvorica, F., Attachment of organic layers to conductive or semiconductive surfaces by reduction of diazonium salts. *Chemical Society Reviews* **2005,** *34* (5), 429-439.
73. Yu, S.; Oh, K. H.; Hwang, J. Y.; Hong, S. H., The effect of amino-silane coupling agents having different molecular structures on the mechanical properties of basalt fiber-reinforced polyamide 6,6 composites. *Composites Part B: Engineering* **2019,** *163*, 511-521.
74. Wang, Z.; Li, Q.; Chen, Z.; Liu, J.; Liu, T.; Li, H.; Zheng, S., Enhanced Comprehensive Properties of Nylon-6 Nanocomposites by Aniline-Modified Boron Nitride Nanosheets. *Industrial & Engineering Chemistry Research* **2018,** *57* (32), 11005-11013.

Chapter 6. Diazonium Radical Mediated Surface Modification of Cellulose Nanocrystals with an Alkylamine

6.1 Introduction

The poor dispersibility of cellulose nanocrystals (CNC) in organic solvents and most polymers have motivated the development of methods for the attachment of alkyl or carbon-rich moieties onto CNC. Modification methods range from esterification[1, 2] to adsorption[3] to grafting-from methods like ring-opening polymerizations.[4-6] All surface modification methods aim at reducing the interparticle hydrogen bonding that make dispersion of CNC difficult in non-polar matrices.[6] Additionally, longer chain molecules grafted onto CNC could intersperse within a polymer matrix and become entangled in the polymer chains further improving interactions favourable for mechanical reinforcement.[7] The choice of surface group can also tailor the properties and interactions of CNC, from biological compatibility[8] to increased thermal properties.[9] In the previous chapter, this reasoning was used when grafting a hydrophobic aryl layer on CNC.

The use of 2,2,6,6-tetramethylpiperidine-1-oxyl (TEMPO) for the oxidation of the CNC surface is one of the most common intermediate methods for the attachment of molecules on cellulose.[10] The TEMPO radical reacts with hydroxyl groups on CNC to form a carboxyl group that is used as a linkage between an alkyl group and CNC.[11, 12] TEMPO oxidation and the ionic sulfate ester groups formed after acid hydrolysis of cellulose enhance electrostatic interactions that makes CNC colloidally stable in aqueous solutions compared to hydroxyl-only groups.[13] However, these functionalities limit the types of interactions to polar or hydrophilic. Therefore, additional

grafting must be done in order to shift CNC-matrix interactions to non-polar and hydrophobic ones that promote better dispersion.[7]

A recent report from Hetemi *et al.* using the diversion of aryl radicals to functionalize a polymeric surface intrigued us.[14] In the paper, the authors indirectly modified polymethyl methacrylate (PMMA) and high-density polyethylene (HDPE) with a 6-hexanoic acid molecule. Contrary to typical aryl radical modifications, a sterically hindered diazonium molecule with two methyl groups ortho to the azo group prevented the binding of the molecule to the polymer surface. Instead, the ortho substituted aryl radical was used to abstract the bromine from 6-bromohexanoic acid forming a 6-hexanoic acid radical that binds to the polymer. In order to confirm grafting of the 6-hexanoic acid group, the modified PMMA or HDPE were post-functionalized with different aromatic amines (4-nitroaniline, 1-aminoanthraquinone, and Neutral Red) using 1-ethyl-3-(-3-dimethylaminopropyl) carbodiimide hydrochloride (EDC) and N-hydroxysuccinimide (NHS), which is a common coupling treatment between carboxylic acid groups and amine-terminated molecules.[11] When non-functionalized (*i.e.* neat) polymer was reacted with EDC/NHS and the aromatic amines, no modification was observed which confirmed the mechanism of 6-hexanoic functionalization on the surface. Further characterization using FTIR and XPS of the post-functionalized polymers confirmed the binding of the aromatic amine molecules. This was observed as the presence of the -NO_2 stretching bands in FTIR for polymer post-functionalized with 4-nitraniline, the presence of a peak in the N1s region in XPS for post-functionalization with the anthraquinone, and the absence of peaks associated with bromine.[14]

Prior to the modification of polymers, Hetemi *et al.* used the same modification mechanism to functionalize glassy carbon (GC) electrodes with a perfluoroalkyl ($(CH_2)_5CF_3$) group,[15] and even co-functionalized conductive surfaces (Au and GC) by forming mixed alkyl and aryl layers.[16]

Electrochemical studies from Pinson's group further confirms the modification of a surface using the indirect method using cyclic voltammetry.[17] They showed that the wave shape and intensity did not change after 10 scans when the electrode was placed in a solution with the dimethyl diazonium, suggesting that the diazonium is unable to bind to the electrode surface due the steric hinderance as previously stated.[17]

Herein, this chapter investigates an alternate one-pot synthetic method for the alkyl modification of CNC using diazonium radical mediated surface functionalization without pre-treatment of the CNC surface. Cellulose nanocrystals are functionalized with propylamine using an adapted diazonium radical mediated modification previously reported by Hetemi *et al.*[14, 15] Propylamine is the alkyl molecule of choice in this study as the terminal amine group may provide both increased hydrogen bonding of CNC with Nylon 6 as well as increased hydrophobicity of CNC due to the carbon-rich chain of the alkyl group. The propylamine modified CNC (PA-CNC) was chemically and thermally characterized using FTIR, CHNS, XPS, and TGA. Finally, a short look into the reinforcing capability of PA-CNC in Nylon 6 thin films is studied. To our knowledge, this is the first time that CNC has been functionalized using diazonium mediated radical formation.

6.2 Experimental

6.2.1 Chemicals and Materials

2,6-Dimethylaniline, 3-bromopropylamine hydrobromide, acetone, acetonitrile, and ethanol (100%), and isopentyl nitrite was purchased from SigmaAldrich (Oakville, ON, CA). Spray-dried sodium-form cellulose nanocrystals (CNC) were provided by InnoTech Alberta (Edmonton, AB, CA).

6.2.2 Surface Modification of Cellulose Nanocrystals with Propylamine

Surface modification of the cellulose nanocrystals (CNC) was done using a modified method previously reported by Hetemi *et al.*[14] 2,6-Dimethylaniline (100 mM) and 3-bromopropylamine hydrobromide (50 mM) were stirred magnetically at 60˚C in neat isopentyl nitrite until dissolved. Dry cellulose nanocrystals (5 wt/v %) were added slowly to the isopentyl nitrite solution and stirred at 60˚C overnight. The resultant propylamine modified cellulose nanocrystals (PA-CNC) were purified via vacuum filtration and washed with neat acetone, acetonitrile, and ethanol until the supernatant ran colourless. The product was dried over vacuum at ambient conditions.

6.2.3 Characterization

Fourier transform infrared (FTIR) analysis was completed using a Nicolet 8700 continuum FTIR microscope. One milligram of dried sample and 100 mg of KBr powder were ground together using a mortar and pestle, then pressed to form discs. Each sample was examined between 600 to 4000 cm^{-1}, with a resolution of 4 cm^{-1}.

X-ray photoelectron spectroscopy (XPS) analysis was completed using a Kratos AXIS-165 spectrometer with a monochromatic AI K(alpha) source (1486.69 eV) for unmodified CNC and an achromatic Mg source (1253.6 eV) for modified CNC. Both survey and high-resolution spectra were obtained. The CasaXPS software was used for data processing. The library was set to CasaXPS_KratosAxis-F1.lib and the high-resolution spectra was adjusted by setting the C1s peak to 285.00 eV binding energy. For all peak fittings, a Gaussian-Lorentzian line shape and a Shirley background was used.

CHNS (Carbon, Hydrogen, Nitrogen, Sulfur) characterization was completed using a Thermo Flash 2000 Elemental Analyzer for CHNS and Oxygen. The temperature was increased from room temperature (25˚C) to 600˚C at a rate of 10˚C/min. The sample weight used was approximately 1.2 mg. Samples were run in duplicates and the percentages reported are the average of the two measurements.

Transmission electron microscopy (TEM) imaging was completed by Arlene Oatway at the Microscopy Facility in the Department of Biological Sciences at the University of Alberta. A Philips/FEI (Morgagni) Transmission Electron Microscope was used. The samples were first dispersed in ethanol at 0.5 mg/mL then bath sonicated for 5 minutes. The samples were drop-casted onto a TEM copper mesh grid and left to dry for 10 minutes then double-stained with uranyl acetate for 1 hour. Samples were imaged at 80 kV. Image analysis was completed using the ImageJ software.

Mechanical tests were performed using the TA Instruments ElectroForce 3200 (10 N max. capacity load cell) by Eyup C. Demir, a PhD student in the Department of Mechanical Engineering. Test strips were prepared from the spin coated samples by cutting with a rotary cutter to obtain sample dimensions of 10mm x 75mm. All samples were stored in a desiccator for at least 12 hours to remove excess moisture and residual solvent. The tensile tester instrument has grips that hold 25mm of the test strip, therefore gauge length was set to 50mm between the grips. A C-shaped mechanical testing frame made from paper was used to hold the samples in the grips to prevent sliding of and reduce stress concentration on the samples during testing. All tests were performed at ambient conditions. The strain rate was set at 0.1 mm/mm•min (5mm/min). The results were averaged over 5 measurements according to the ASTM 882-12 standard.

6.3 Results and Discussion

Proposed Reaction Mechanism. Cellulose nanocrystals (CNC) were modified with an alkylamine using an adapted diazonium radical mediated method previously reported by Hetemi *et al.* for the surface modification of polymers.[14] Briefly, 2,6-dimethyldiazonium (2,6-dDM) (pale yellow in colour) was prepared *in-situ* using 2,6-dimethylaniline as the aniline precursor and isopentyl nitrite as the reducing agent. When heated to 60˚C, 2,6-dDM decomposes homolytically to form a diazonium radical and the solution colour changes from light yellow to dark orange. In the presence of an alkyl halide (in this case, 3-bromopropylamine), the 2,6-dDM radical abstracts the halide thus forming an alkyl radical. Then, the unhindered alkyl radical recombines with a radical on the CNC surface and forms a covalent bond, leading to the formation of propylamine modified CNC (PA-CNC) that is yellow in colour (Fig. 6-2 and 6-3). Proposed reaction schemes for both the formation of the alkyl radical and the surface modification of CNC are presented in Figure 6-1.

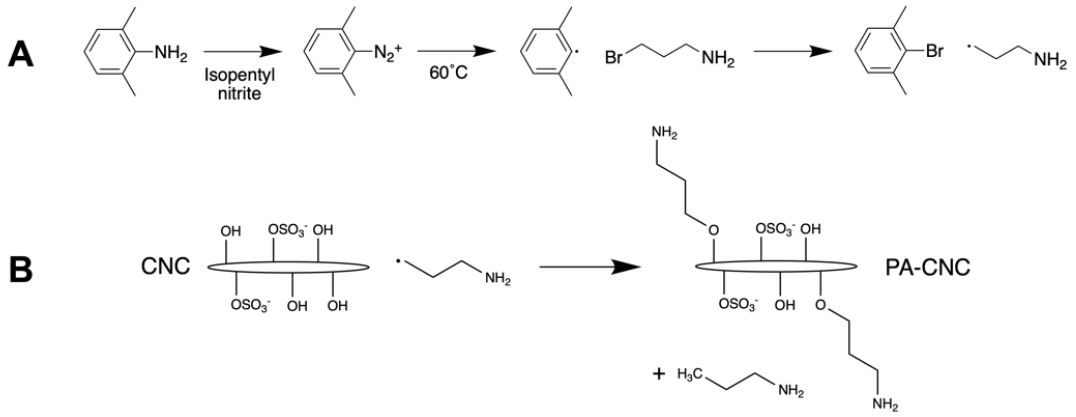

Figure 6-1. A) In-situ diazotization of 2,6-dimethylaniline and subsequent radical formation of 3-bromopropylamine and B) proposed mechanism for the surface modification of CNC with the propylamine radical.

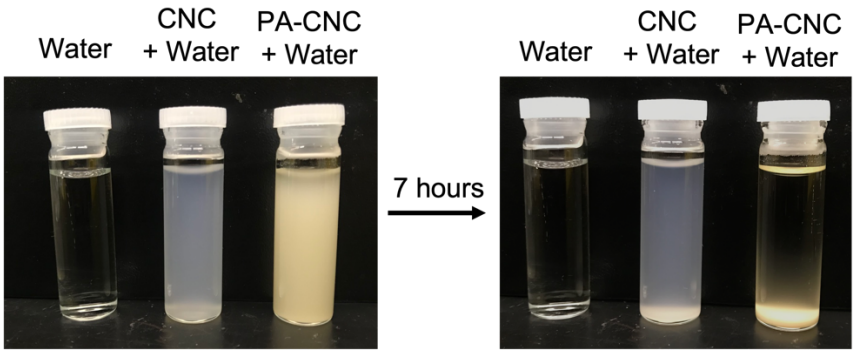

Figure 6-2. Photographs of (left) water, 5 wt% CNC and 5 wt% PA-CNC dispersed in water, and (right) the same solutions after they were left to stand for 7 hours.

Colloidal Stability in Aqueous Solutions. After modification of CNC with propylamine (PA-CNC), the colour of the final dried powder changed from off-white to light yellow, as shown in Figures 6-2 and 6-3. An investigation into the colloidal stability of the alkyl modified CNCs was performed by dispersing unmodified CNC and PA-CNC in deionized water, then leaving the samples to sit at ambient conditions. After 7 hours, the unmodified CNCs remained dispersed whereas the PA-CNCs fully settled to the bottom of the vial, as shown in Figure 6-2. In aqueous solutions, CNC exhibits colloidal stability *via* long-range electrostatic repulsions between the individual particles imparted by the charged surface groups – ($-COO^-$) in the case of TEMPO oxidized CNC and ($-OSO_3^-$) in the case of sulfate ester modified CNC. We know this to be true as non-modified native CNC (*i.e.,* CNCs with only hydroxyl (-OH) groups) are not colloidally stable.[13] When a carbon-rich alkylamine is bound to the CNC surface as presented here, the ionic groups ($-OSO_3^-$) are covered thereby decreasing the stability in water. Additionally, the addition of propylamine may also displace the sulfate ester groups on CNC thus also decreasing its colloidal stability. Therefore, the settling of PA-CNC overtime is consistent with the grating of a hydrophobic layer on CNC.

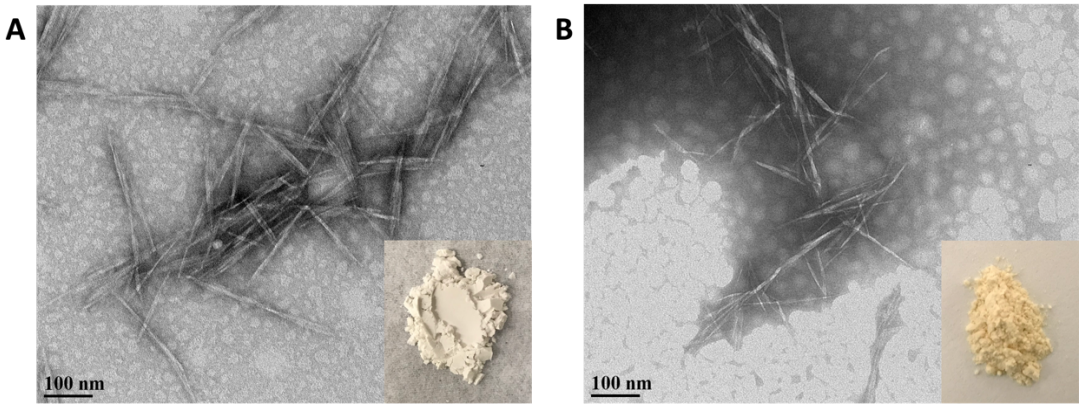

Figure 6-3. TEM images of A) unmodified CNC and B) PA-CNC. The inset photographs are of the dried powders corresponding to each CNC sample.

TEM Images. Figure 6-3 shows the TEM images of CNC and PA-CNC, with photos of the dried powders for each sample inset in the images. No significant differences are observed between the modified and unmodified CNC. Particle diameters and lengths were measured from the TEM images, yielding aspect ratios of 18 ± 7 for CNC and 20 ± 7 for PA-CNC. These values are consistent with literature values for unmodified CNC.[18] With no significant change in aspect ratio after modification, we can conclude that the reaction conditions and modification do not alter the shape of CNC.

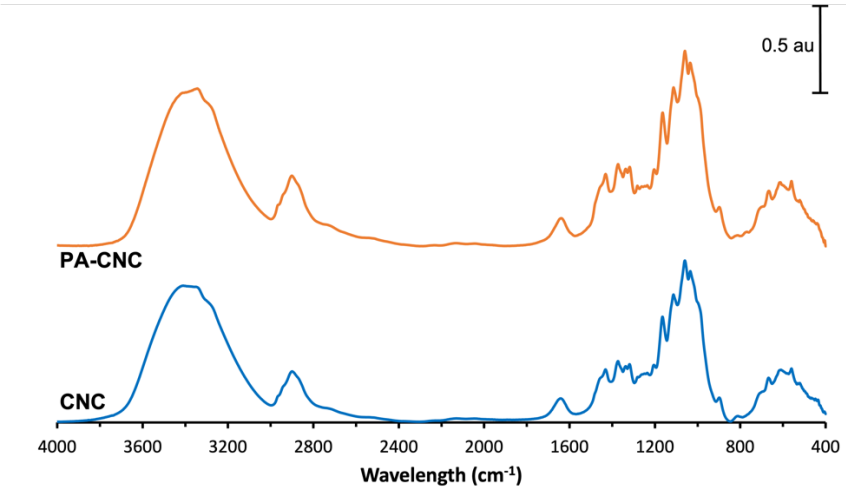

Figure 6-4. FT-IR spectra of unmodified CNC and PA-CNC. The blue line is unmodified CNC and the orange line is PA-CNC.

FTIR Analysis. The FTIR spectra of CNC and PA-CNC are presented in Figure 6-4. Both spectra show predicted bands for CNC at 3345 cm^{-1} (OH str.), 2900 cm^{-1} (C-H str.), 1638 cm^{-1} (absorbed water), 1430 cm^{-1} ($-CH_2-$), 1372-1317 cm^{-1} (1˚ and 2˚ -OH), 1163 cm^{-1} (glycosidic C-O-C), and 1112-1034 cm^{-1} (C-O of C2, C3, and C6 of glucose).[19] Additionally, the lack of bands associated with 2,6-dDM suggest very little is adsorbed to CNC even with the change in colour observed in Figures 6-2 and 6-3. Due to the strong signature of the hydroxyl and C-O groups in CNC, it is difficult to differentiate between the unmodified and modified CNC spectra, especially in the IR regions expected for primary amines (~3300 cm^{-1} and ~1600 cm^{-1}). Therefore, further characterization using alternate techniques was performed, as described in the following sections.

Table 6-1. CHNS analysis of CNC and PA-CNC.

	N (%)	C (%)	H (%)	S (%)
CNC	0.00	41.03	6.01	0.76
PA-CNC	0.20	42.67	5.96	0.31

CHNS Elemental Analysis. CHNS elemental analysis was performed to confirm grafting of propylamine on CNC. Table 6-1 lists the CHNS results of both CNC and PA-CNC. The unmodified CNC sample show all expected atomic percentages for each of the elements detected, with values at 0% for nitrogen (N), 41.03% for carbon (C), 6.01% for hydrogen (H), and 0.76% for sulfur (S).[20] Once grafted with propylamine, CHNS confirms the presence of propylamine in PA-CNC with an increase of %N to 0.20% due to the primary amine group on propylamine (PA), as well as an increase in %C by 1.64% due to the addition of the alkyl backbone of PA. Both the

%H and %S content decreased slightly by 0.05% and 0.45%, respectively, similar to the results obtained for diazonium modified CNC presented in the previous Chapter. This is due to the abstraction of hydrogen from the redox reaction between the radical propylamine molecule and CNC,[14, 21] as well as the displacement of the sulfate ester groups on CNC at the elevated reaction temperature and by the radical PA molecules.[22] This coincides with the stability observations as part of Figure 6-2, where the loss of sulfur correlates to a loss of the ionic $-OSO_3^-$ groups thus reducing interparticle repulsion. The CHNS data is consistent with the presence of propylamine bound to CNC.

The degree of substitution of propylamine on the CNC surface was calculated from the CHNS values using the follow equation reported by Carneiro de Oliveira *et al.*,[20]

$$DSS = \frac{\emptyset_N \bullet MW_{AGU}}{MW_N - MW_{PA} \bullet \emptyset_N} \qquad \text{Eq. 6-1}$$

where DSS is the degree of substitution of the surface, $\emptyset_N$ is the mass fraction of nitrogen from CHNS (0.2%), MW_{AGU} is the molecular weight of a single repeating anhydroglucose unit in CNC (162 g/mol), MW_{PA} is the molecular weight of the propylamine moiety (58 g/mol), and MW_N is the molecular weight of nitrogen (14 g/mol). The DSS of PA-CNC was calculated as 0.25, which is rather low when compared to the estimated value of <1 for CNC when assuming all possible hydroxyl groups are fully modified.[23] This may be due to a few possible reasons. First, the poor dispersibility of unmodified CNC in neat isopentyl nitrite reduces the availability of C6 hydroxyl groups during modification. Second, alkyl radical formation may be increased by utilizing a better halogen leaving group on propylamine, such as iodine.[24] Lastly, the aryl and alkyl radicals may form byproducts thus lowering the concentration of available alkyl radicals to react with CNC. We are also assuming that propylamine forms a monolayer on CNC and not a multilayer similar to the functionalization with aryl radicals, as proposed in Chapter 5. The results presented here are

comparable to the nitrogen content of the post-functionalized polyethylene (0.6% nitrogen) from XPS reported by Hetemi *et al.*, suggesting the diazonium mediated modification has an expected low yield.[14]

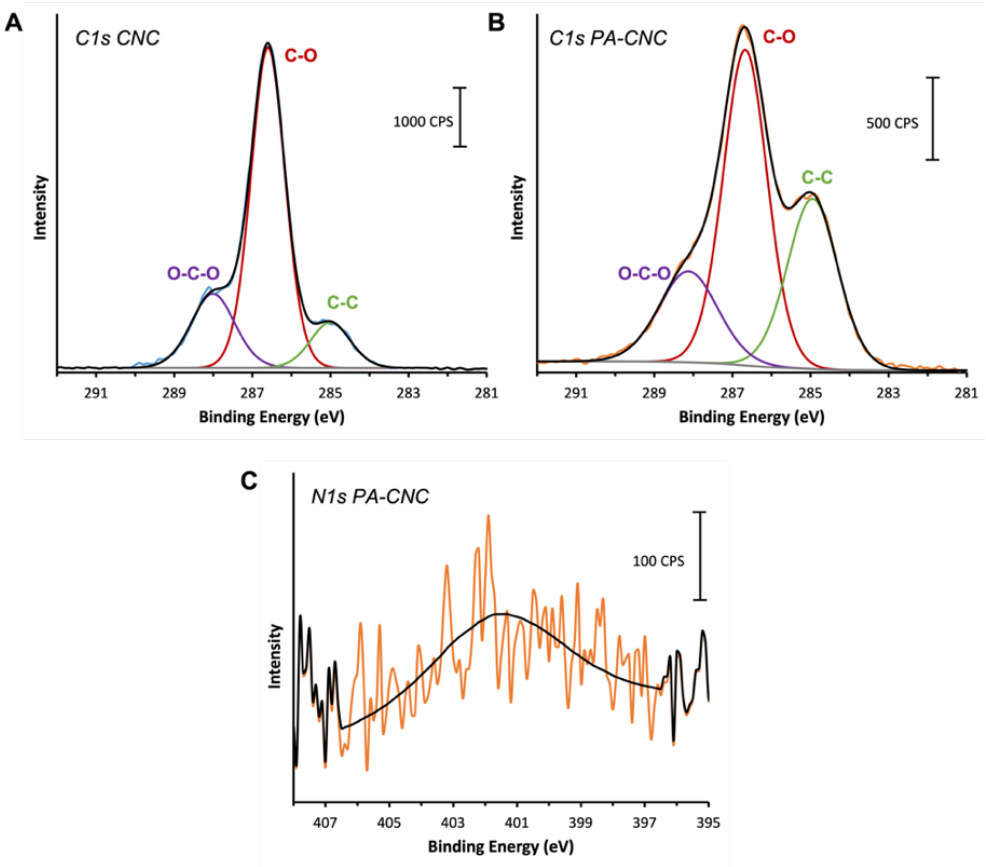

Figure 6-5. HR-XPS of A) the C1s region for unmodified CNC, B) the C1s region for PA-CNC, and C) the N1s region for PA-CNC.

XPS and HR-XPS. Further characterization to confirm the grafting of propylamine onto CNC was done using high resolution x-ray photoelectron spectroscopy (HR-XPS), as shown in Figure 6-5. The HR-XPS of the C1s region for CNC in Figure 6-5A is consistent with those reported in the literature, with three peaks at binding energies of 284.9 eV for adventitious carbon and C-C bonds (or C1), 286.5 eV for C-O bonds (or C2), and 287.9 eV for O-C-O bonds (or C3).[18,

[25] In the PA-CNC sample in Figure 6-5B, there is also the presence of all three expected peaks, but there is an increase in the peak intensity at 284.9 eV relative to the other two peaks. Since CNC does not contain any C-C linkages because the glucose backbone has only C-O bonds,[18] the large increase in C-C content must be due to the addition of propylamine. The low intensity peak at 284.9 eV in the unmodified CNC spectrum is attributed to hydrocarbon contaminants, such as lignin, that are not fully removed during the production of CNC.[18, 26] This increase in intensity for the PA modified CNC coincides with a 19.2% increase in atomic percent of the C1 peak at 284.9 eV in PA-CNC compared to CNC (Table 6-2). Finally, there is the appearance of a low intensity peak in the N1s region of PA-CNC at 401 eV attributed to the C-NH_2 bond of the terminal amine group in propylamine,[15] as shown in Figure 6-5C. A summary of the information from the deconvolution of the C1s regions for unmodified CNC and PA-CNC samples is presented in Table 6-2.

Table 6-2. Summarized HR-XPS data in the C1s regions for CNC and PA-CNC.

Sample	Deconvolution Binding Energy (eV)	Deconvolution Atomic %	Assignment
CNC	284.9	11.9	C-C (C1)
	286.5	68.0	C-O (C2)
	287.9	20.1	O-C-O (C3)
PA-CNC	284.9	31.1	C-C (C1)
	286.6	49.9	C-O (C2)
	288.0	19.0	O-C-O (C3)

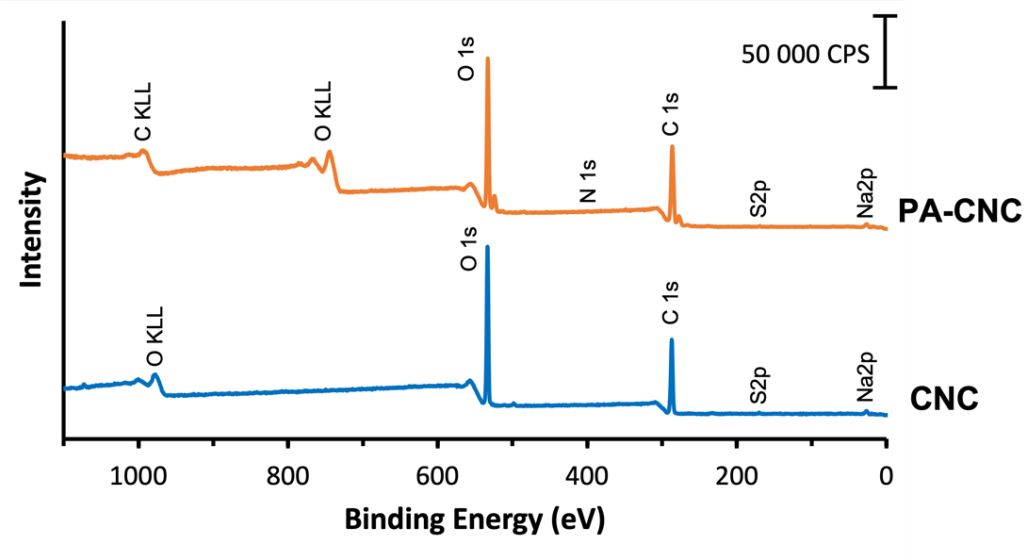

Figure 6-6. XPS survey spectra of CNC and PA-CNC. The blue line is unmodified CNC and the orange line is PA-CNC.

Table 6-3. Summarized XPS survey scan data for CNC and PA-CNC.

Element	CNC		PA-CNC	
	Binding Energy (eV)	Atomic %	Binding Energy (eV)	Atomic %
C1s	287.1	56.0	286.6	62.8
N1s	402.1	0.0	400.6	1.3
O1s	533.1	39.9	533.1	32.1
S2p	170.1	0.86	169.1	0.55
Na2p	26.6	3.2	27.1	3.2

The XPS survey spectra and a summary of the survey spectra data for CNC and PA-CNC are presented in Figure 6-6 and Table 6-3, respectively. The survey spectra for both samples show peaks at binding energies of ~276 eV for C1s, ~533 eV for O1s, ~170 eV for S2p, and ~27 eV for Na2p. The presence of the S2p and Na2p peaks are due to the ionic sulfate half ester groups formed during the production of CNC.[19] The lack of a peak at ~68 eV corresponding to Br3d confirms that there is no unreacted 3-bromopropylamine adsorbed onto the CNC surface. The shift in the O KLL

and C KLL peaks in PA-CNC compared to CNC is due to the difference in x-ray source used in the XPS instrumentation when each spectrum was obtained.[27] The data in Table 6-3 show that PA-CNC has an increase in carbon atomic percent by 6.8% and in nitrogen atomic percent by 1.3% compared to unmodified CNC. This is further corroborated by the increase in N/C ratio by 0.02 and the decrease in O/C ratio by 0.20 after modification. Again, this is due to the addition of the carbon-rich and amine-terminated propylamine group grafted on CNC. There is a decrease in the oxygen atomic percent by 7.8% and in the sulfur atomic percent by 0.31% in PA-CNC due to the displacement of some sulfate half ester groups during modification, which is consistent with the data obtained from CHNS. The information derived from XPS is also consistent with the binding of propylamine on CNC.

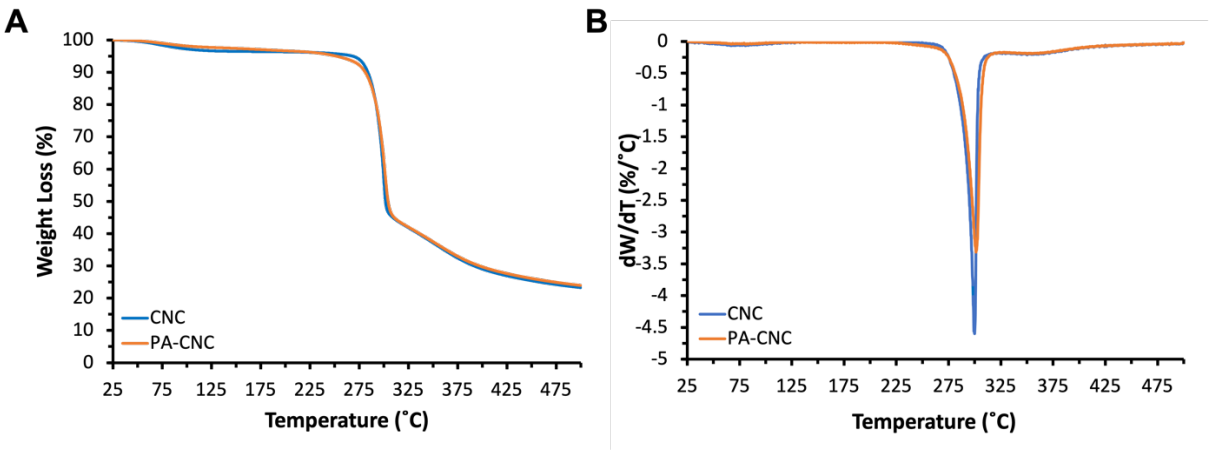

Figure 6-7. A) TGA and B) DTG thermograms of CNC and PA-CNC.

Thermal Properties. Finally, the thermal stability of the modified CNC was evaluated using TGA, as shown in Figure 6-7. The TGA spectrum of PA-CNC in Figure 6-7A shows small differences from the unmodified CNC spectrum. The small weight loss until 100˚C in both spectra is attributed to water loss from absorbed water on CNC, however, PA-CNC has a slightly lower weight loss (2% compared to 4% for CNC) as a result of less water absorption due to the

hydrophobic nature imparted onto CNC because of the alkyl surface groups. Although there is a slight earlier degradation of PA-CNC at around 275˚C in Figure 6-7A (and as visualized as the smaller dW/dT intensity in Figure 6-7B), the onset temperature (T_O) of both the CNC and PA-CNC are the same, with values at 289˚C. Between 120˚C and 320˚C, CNC has a 48% weight loss, whereas PA-CNC has an increase in weight loss to 52% due to the degradation of the added alkyl groups. The remaining mass for both samples are attributed to char from the degradation of cellulose.[19] CNC and PA-CNC also have the same first derivative peak temperature (T_P) of 300˚C, as shown in Figure 6-7B. The data from the thermograms confirm that the propylamine modification of CNC does not significantly affect the thermal stability of CNC.

Effect of Propylamine Modification on CNC-Nylon 6 Composite Films. As mentioned previously, one of the most common challenges when using CNC in polymer composites is the dispersion of the particles to allow for adequate interface interactions. For CNCs, the polar-hydrophilic and nonpolar-hydrophobic interactions of CNC and the matrix, respectively, are deemed responsible for poor dispersibility leading to irreversible agglomeration.[28] By modifying the CNC surface, the surface energy is lowered thus promoting favourable non-polar interactions with the polymer matrix.[29, 30] This has been demonstrated in multiple studies where modified CNC exhibits lower surface energies and better dispersion in organic solvents and non-polar polymers.[30, 31] More specifically, the modification of CNC with alkyl molecules is favoured as the long chains can interact with and entangle in the polymer chains, as well as potentially co-crystallize with the polymer creating an interphase between CNC and the polymer.[7, 28] Thus, we expect that the addition of the propylamine on CNC may promote these interactions.

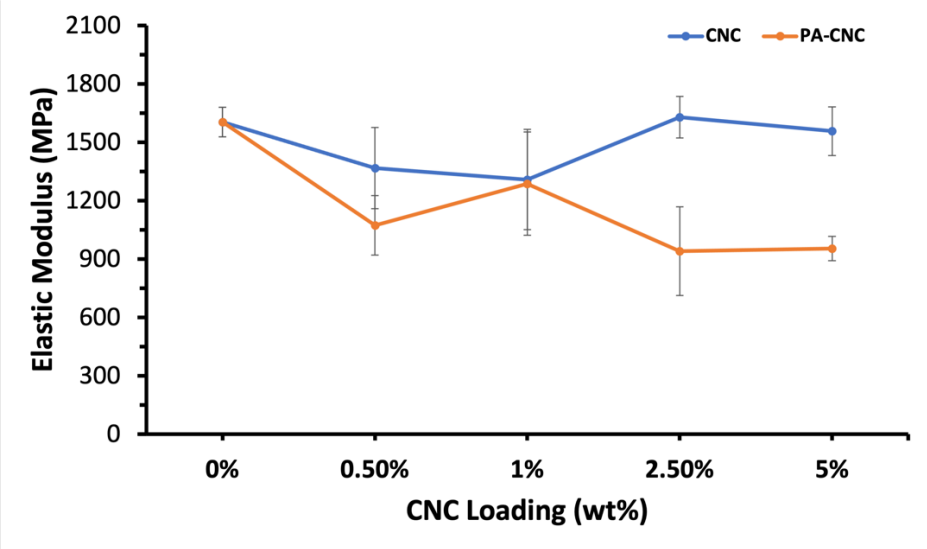

Figure 6-8. Elastic moduli for the CNC or PA-CNC and Nylon 6 composite films. The blue line is for unmodified CNC and the orange line is for PA-CNC.

The elastic moduli for the films are presented in Figure 6-8B. The addition of unmodified CNC increased the elastic modulus of the films to a maximum of 2.50 wt% CNC. For the modified PA-CNC films, the elastic moduli of Nylon 6 decreased at all PA-CNC loadings compared to neat Nylon 6. Though the alkylamine molecule on CNC was thought to increase filler-matrix interactions, the poor dispersity of the individual CNCs in formic acid may cause aggregation and therefore decrease the ability of PA-CNC to interact with Nylon 6. As seen with the CNC-Nylon 6 films in Chapters 2 and 5, CNC aggregates can act as fracture points thus lowering the reinforcing potential of the additive in the films. Additionally, the three-carbon alkyl molecule chosen here may be too short to adequately interact and disperse within Nylon.[32] It has been found that long chain alkyl molecules on CNC can favourably interact with polymer matrices,[9, 12] therefore further work using longer chain alkylamines or additional grafting *via* the terminal amine to form longer chains can provide alternate routes for compatibilization using the modification method presented in this Chapter.

6.4 Conclusion

Cellulose nanocrystals were modified with an alkylamine group using diazonium mediated surface functionalization. This is the first time this reaction has been applied to nanosized CNC. First, a dimethyl diazonium molecule was prepared *in-situ*. Due to the steric hinderance of the two methyl groups ortho to the diazonium functionality, radical formation was diverted from the CNC surface to an alkyl halide. The radical alkyl halide then forms a covalent bond with the CNC surface, forming a propylamine modified CNC (PA-CNC). The colour of the final modified product changed from off-white to yellow and did not stay dispersed in water overtime compared to unmodified CNC. Due to the large characteristic peaks of CNC in FTIR, other methods, including CHNS and XPS were used to confirm grafting. Both characterization methods showed an increased in nitrogen and carbon content after modification, which is consistent with bonding of an alkylamine on the surface. The degree of substitution was calculated using the nitrogen content as determined by CHNS, with a value of DSS = 0.25. The thermal stability of CNC did not significantly change after modification as evaluated by TGA and DTG. Finally, thin films containing the modified CNCs in Nylon 6 were produced, where the elastic modulus of the thins were similar to unmodified CNC films up to 1 wt%. At 2.5wt% and higher, the PA-CNCs decreased the elastic modulus of the films significantly compared to unmodified CNC. The quick and facile nature of the surface modification presented in this chapter opens up numerous pathways for increased compatibilization of CNC in hydrophobic matrices or for further reactivity of the CNC surface *via* the terminal amine group. Alternate alkyl halides with various functionalities or chain lengths may also be used for the modification of CNC using this method to tailor surface properties for use in composites or other functional materials.

6.5 References

1. Le Gars, M.; Roger, P.; Belgacem, N.; Bras, J., Role of solvent exchange in dispersion of cellulose nanocrystals and their esterification using fatty acids as solvents. *Cellulose* **2020,** *27* (8), 4319-4336.
2. Leszczyńska, A.; Radzik, P.; Szefer, E.; Mičušík, M.; Omastová, M.; Pielichowski, K., Surface Modification of Cellulose Nanocrystals with Succinic Anhydride. *Polymers* **2019,** *11* (5), 866.
3. Padalkar, S.; Capadona, J. R.; Rowan, S. J.; Weder, C.; Won, Y.-H.; Stanciu, L. A.; Moon, R. J., Natural Biopolymers: Novel Templates for the Synthesis of Nanostructures. *Langmuir* **2010,** *26* (11), 8497-8502.
4. Carlsson, L.; Ingverud, T.; Blomberg, H.; Carlmark, A.; Larsson, P. T.; Malmström, E., Surface characteristics of cellulose nanoparticles grafted by surface-initiated ring-opening polymerization of ε-caprolactone. *Cellulose* **2015,** *22* (2), 1063-1074.
5. Wohlhauser, S.; Delepierre, G.; Labet, M.; Morandi, G.; Thielemans, W.; Weder, C.; Zoppe, J. O., Grafting Polymers from Cellulose Nanocrystals: Synthesis, Properties, and Applications. *Macromolecules* **2018,** *51* (16), 6157-6189.
6. Carlmark, A.; Larsson, E.; Malmström, E., Grafting of cellulose by ring-opening polymerisation – A review. *European Polymer Journal* **2012,** *48* (10), 1646-1659.
7. Mariano, M.; El Kissi, N.; Dufresne, A., Cellulose nanocrystals and related nanocomposites: Review of some properties and challenges. *Journal of Polymer Science Part B: Polymer Physics* **2014,** *52* (12), 791-806.
8. Tortorella, S.; Vetri Buratti, V.; Maturi, M.; Sambri, L.; Comes Franchini, M.; Locatelli, E., Surface-Modified Nanocellulose for Application in Biomedical Engineering and Nanomedicine: A Review. *Int J Nanomedicine* **2020,** *15*, 9909-9937.
9. Lee, J. H.; Park, S. H.; Kim, S. H., Surface Alkylation of Cellulose Nanocrystals to Enhance Their Compatibility with Polylactide. *Polymers* **2020,** *12* (1), 178.
10. Fraschini, C.; Chauve, G.; Bouchard, J., TEMPO-mediated surface oxidation of cellulose nanocrystals (CNCs). *Cellulose* **2017,** *24* (7), 2775-2790.
11. Le Gars, M.; Delvart, A.; Roger, P.; Belgacem, M. N.; Bras, J., Amidation of TEMPO-oxidized cellulose nanocrystals using aromatic aminated molecules. *Colloid and Polymer Science* **2020,** *298* (6), 603-617.
12. Tan, C.; Peng, J.; Lin, W.; Xing, Y.; Xu, K.; Wu, J.; Chen, M., Role of surface modification and mechanical orientation on property enhancement of cellulose nanocrystals/polymer nanocomposites. *European Polymer Journal* **2015,** *62*, 186-197.
13. Vanderfleet, O. M.; Cranston, E. D., Production routes to tailor the performance of cellulose nanocrystals. *Nature Reviews Materials* **2021,** *6* (2), 124-144.
14. Hetemi, D.; Medard, J.; Kanoufi, F.; Combellas, C.; Pinson, J.; Podvorica, F. I., Surface Modification of Polymers by Reaction of Alkyl Radicals. *Langmuir* **2016,** *32* (2), 512-8.
15. Hetemi, D.; Kanoufi, F.; Combellas, C.; Pinson, J.; Podvorica, F. I., Electrografting of alkyl films at low driving force by diverting the reactivity of aryl radicals derived from diazonium salts. *Langmuir* **2014,** *30* (46), 13907-13.
16. Hetemi, D.; Hazimeh, H.; Decorse, P.; Galtayries, A.; Combellas, C.; Kanoufi, F.; Pinson, J.; Podvorica, F. I., One-Step Formation of Bifunctionnal Aryl/Alkyl Grafted Films on Conducting Surfaces by the Reduction of Diazonium Salts in the Presence of Alkyl Iodides. *Langmuir* **2015,** *31* (19), 5406-5415.

17. Combellas, C.; Kanoufi, F.; Pinson, J.; Podvorica, F. I., Sterically Hindered Diazonium Salts for the Grafting of a Monolayer on Metals. *Journal of the American Chemical Society* **2008,** *130* (27), 8576-8577.
18. Reid, M. S.; Villalobos, M.; Cranston, E. D., Benchmarking Cellulose Nanocrystals: From the Laboratory to Industrial Production. *Langmuir* **2017,** *33* (7), 1583-1598.
19. Foster, E. J.; Moon, R. J.; Agarwal, U. P.; Bortner, M. J.; Bras, J.; Camarero-Espinosa, S.; Chan, K. J.; Clift, M. J. D.; Cranston, E. D.; Eichhorn, S. J.; Fox, D. M.; Hamad, W. Y.; Heux, L.; Jean, B.; Korey, M.; Nieh, W.; Ong, K. J.; Reid, M. S.; Renneckar, S.; Roberts, R.; Shatkin, J. A.; Simonsen, J.; Stinson-Bagby, K.; Wanasekara, N.; Youngblood, J., Current characterization methods for cellulose nanomaterials. *Chem Soc Rev* **2018,** *47* (8), 2609-2679.
20. Carneiro de Oliveira, J.; Rigolet, S.; Marichal, C.; Roucoules, V.; Laborie, M.-P., Grafting Diels-Alder moieties on cellulose nanocrystals through carbamation. *Carbohydrate Polymers* **2020,** *250*, 116966.
21. Pinson, J.; Podvorica, F. I., Surface modification of materials: Electrografting of organic films. *Current Opinion in Electrochemistry* **2020,** *24*, 44-48.
22. Lin, N.; Dufresne, A., Surface chemistry, morphological analysis and properties of cellulose nanocrystals with gradiented sulfation degrees. *Nanoscale* **2014,** *6* (10), 5384-5393.
23. Eyley, S.; Thielemans, W., Surface modification of cellulose nanocrystals. *Nanoscale* **2014,** *6* (14), 7764-7779.
24. Hetemi, D.; Combellas, C.; Kanoufi, F.; Podvorica, F. I., Direct vs Indirect Grafting of Alkyl and Aryl Halides. *ChemPhysChem* **2021,** *22* (18), 1844-1849.
25. Tian, C.; Fu, S.; Habibi, Y.; Lucia, L. A., Polymerization Topochemistry of Cellulose Nanocrystals: A Function of Surface Dehydration Control. *Langmuir* **2014,** *30* (48), 14670-14679.
26. Habibi, Y.; Goffin, A.-L.; Schiltz, N.; Duquesne, E.; Dubois, P.; Dufresne, A., Bionanocomposites based on poly(ε-caprolactone)-grafted cellulose nanocrystals by ring-opening polymerization. *Journal of Materials Chemistry* **2008,** *18* (41), 5002-5010.
27. Haasch, R. T., X-Ray Photoelectron Spectroscopy (XPS) and Auger Electron Spectroscopy (AES). In *Practical Materials Characterization*, Sardela, M., Ed. Springer New York: New York, NY, 2014; pp 93-132.
28. Khattab, M. M.; Abdel-Hady, N. A.; Dahman, Y., 21 - Cellulose nanocomposites: Opportunities, challenges, and applications. In *Cellulose-Reinforced Nanofibre Composites*, Jawaid, M.; Boufi, S.; H.P.S, A. K., Eds. Woodhead Publishing: 2017; pp 483-516.
29. Trache, D.; Tarchoun, A. F.; Derradji, M.; Hamidon, T. S.; Masruchin, N.; Brosse, N.; Hussin, M. H., Nanocellulose: From Fundamentals to Advanced Applications. *Frontiers in Chemistry* **2020,** *8* (392).
30. Khoshkava, V.; Kamal, M. R., Effect of Surface Energy on Dispersion and Mechanical Properties of Polymer/Nanocrystalline Cellulose Nanocomposites. *Biomacromolecules* **2013,** *14* (9), 3155-3163.
31. Fox, D. M.; Rodriguez, R. S.; Devilbiss, M. N.; Woodcock, J.; Davis, C. S.; Sinko, R.; Keten, S.; Gilman, J. W., Simultaneously Tailoring Surface Energies and Thermal Stabilities of Cellulose Nanocrystals Using Ion Exchange: Effects on Polymer Composite Properties for Transportation, Infrastructure, and Renewable Energy Applications. *ACS Applied Materials & Interfaces* **2016,** *8* (40), 27270-27281.
32. Junior de Menezes, A.; Siqueira, G.; Curvelo, A. A. S.; Dufresne, A., Extrusion and characterization of functionalized cellulose whiskers reinforced polyethylene nanocomposites. *Polymer* **2009,** *50* (19), 4552-4563.

Chapter 7. Conclusions and Future Directions

7.1 Chapter Summaries

The motivation of the work presented in this thesis was to investigate the effect of CNC in Nylon 6 nanocomposites and to study the surface modification of CNC using diazonium chemistry. This thesis presented two polymer processing techniques, spin coating to obtain freestanding thin films and electrospinning to obtain nanofibre mats. The effect of electrospinning parameters on the alignment and morphology of fibres obtained with a rotating drum collector was also discussed. Finally, CNC was surface modified with diazonium cations and with an alkylamine using diazonium cations with a brief study into the incorporation of the modified CNC in Nylon 6 thin films. This thesis emphasizes the reinforcing capabilities of CNC in polymer matrices, which provides an exciting route for industrial polymer applications.

In Chapter 2, CNC-Nylon 6 freestanding thin films were produced using spin coating. Tensile testing was used to measure the mechanical properties of the films, which showed an increase in Young's modulus and ultimate tensile strength up to 1 wt% CNC loading then a decrease at 2.5 and 5 wt% CNC loading. The decrease in mechanical properties was attributed to aggregation of CNC at high loadings and the influence of CNC on the crystal microstructure of Nylon 6, as shown using FTIR and DSC. In neat Nylon 6 films, the α allomorph was the predominant crystal form. With the addition of CNC, the γ allomorph was formed and became increasingly more apparent at 5 wt% CNC. DSC also revealed a decrease in the heat of fusion and in percent crystallinity with increasing CNC loading. The appearance of this less stable γ allomorph and the small decrease in percent crystallinity with the increase in CNC loading

supports the decrease in the mechanical properties. The thermal stability of the films also decreased with increasing CNC, with the T_O decreasing in 12˚C at 5 wt% CNC. This is due to the degradation of CNCs as temperatures below that of Nylon 6. This chapter emphasizes the importance of dispersion and crystal structure when preparing CNC-polymer composites with the goal of increased mechanical properties.

In Chapter 3, five different processing parameters were investigated for the electrospinning of aligned Nylon 6 fibres using a rotating drum collector. The parameters investigated were drum rotation speed, jet focusing, applied voltage, flow rate, and needle-to-collector distance. The alignment of the fibres improved with increasing drum rotation speed from 0 to 4000 rpm. The diameters of the fibres decreased with increasing drum rotation speed due to the faster pulling and stretching of the fibres while spinning. In order to obtain greater alignment of the fibres, a copper wire was fashioned into a ring and placed on the needle to focus the jet while spinning. At 2500 rpm, only 58% of the fibres were aligned within 30˚ of the norm. When increased to 4000 rpm, 83% of the fibres were aligned within 30˚. Though fibre diameter did not vary significantly at 3000 or 4000 rpm when changing the applied voltage, flow rate, or distance, small trends were observed, and the alignment of the fibres were improved in some cases. When changing applied voltage (14-24 kV), the fibre diameters stayed consistent, but the fibre alignment was the best at 21 kV. When changing flow rate (1-7 μL/min), the fibre diameters decreased at 7μL/min and were the thickest at 5 μL/min, and the alignment was not significantly affected. When changing distance (5-13 cm), the fibre diameter increased with increasing distance at 13 cm and showed the best alignment also at 13 cm. This chapter emphasizes the importance in choosing processing parameters when obtaining optimally aligned fibres during electrospinning.

In Chapter 4, CNC was incorporated into Nylon 6 and the solutions were electrospun using either a stationary or rotating drum collector, which yielded randomly distributed and aligned fibres, respectively. The aligned fibres had smaller fibre diameters at all CNC loadings compared to the randomly distributed ones, as described in the previous Chapter. TEM was used to visualize the aligned fibres, and it was found that CNCs were aligned parallel to the fibre axis. The aligned fibres also had significantly higher elastic moduli and tensile strengths compared to the random fibres at all CNC loadings. This is due to the higher stiffness of the fibres when they are aligned in the testing direction. However, the randomly distributed fibres exhibited higher strain at breaks due to the greater freedom of the individual fibres to move during testing. In either the randomly distributed or aligned fibre mats, a loading of 1 wt% CNC showed the highest mechanical properties. Similar to the thin films, the decrease in mechanical strength above 1 wt% CNC was attributed to the aggregation of CNC and its influence on the crystal microstructure of Nylon 6. FTIR and XRD showed that electrospinning induced the crystallization of Nylon 6 predominantly in the γ form, and CNC decreased the crystallization of Nylon in both the α and γ forms causing the fibres to become more amorphous. This is also seen in DSC by the slight decrease in percent crystallinity and a decrease in the heat of fusion with increasing CNC loading. Again, CNCs decreased the thermal stability of the fibres, with a decrease in the T_O by 23˚C and T_P by 15˚C at 5 wt% CNC. This chapter emphasizes the difference between electrospun randomly distributed and aligned fibres, and the importance of CNC dispersion and polymer crystallinity on the mechanical properties of the composite fibres.

In Chapter 5, CNC was surface modified with diazonium cations. The synthesis of the diazonium cations were performed using either ex-situ or in-situ diazotization. 4-Nitrobenzenediazonium (4-dNB) was used as a benchmark molecule for characterization, which

utilized the ex-situ diazotization. The surface modification of CNC with 4-dNB was confirmed using FTIR, CHNS, and XPS. TGA was used to characterize the thermal stability of the modified CNC product and was found to decrease with the addition of the diazonium multilayer. In-situ diazotization was used to form 4-aminobenzyldiazonium (4-dABA) and p-aminobenzenediazonium (p-dAB), and the grafting of the diazonium molecules on CNC was confirmed using FTIR. Finally, the modified CNCs were incorporated into Nylon 6 solutions and spin coated to create thin films. The preliminary mechanical results of the samples showed that the modification of CNC with a diazonium multilayer decreased the elastic moduli, regardless of diazonium molecule used, up to 2 wt%. This chapter emphasizes the modification of CNC with diazonium cations, which has not been previously reported in the literature.

In Chapter 6, CNC was surface modified with propylamine using a diazonium mediated reaction. 2,6-Dimethylaniline was converted into a diazonium cation, but due to the steric hinderance of the ortho methyl groups cannot bind to CNC. Instead, radical formation is diverted to the small 3-bromopropylamine molecule which then forms a propylamine (PA) radical. The PA radical then reacts with the CNC surface to yield alkyl modified CNC. The alkylation of CNCs caused them to become more hydrophobic, as seen visually when PA-CNC did not stay dispersed in water when left over time. The modified CNCs also did not differ significantly in aspect ratio compared to unmodified CNCs, as shown by TEM. The surface modification was confirmed using FTIR, CHNS, and XPS. TGA was used to characterization the thermal stability of the modified CNC product and was found to decrease with the addition of PA on the surface. This chapter emphasizes the use of indirect modification of CNC using diazonium chemistry to obtain hydrophobic alkyl modified CNC.

7.2 Future Directions

7.2.1 Post-Functionalization of Diazonium or Propylamine Modified CNC

The diversity of functionalities on diazonium cations opens the door to countless additional reactivities. As presented in Chapters 5 and 6, amine terminated molecules can be successfully grafted onto CNC. The primary amine groups provide further reactivity that can be exploited using covalent or electrostatic crosslinking. For example, a recent article published by Adel-Mehraban *et al.* reduced both ends of the p-aminobenzenediazonium (p-dAB) molecule I presented in Chapter 5.[1] The molecule was bound to a Cu substrate then a graphene layer was covalently bound to the substrate *via* the para $-N_2^+$ end of the p-dAB molecule. This mechanism can also be utilized to crosslink individual CNCs together or to crosslink CNCs between the polymer chains for enhanced composite toughness.[2, 3]

7.2.2 Incorporation of Modified CNC in Nylon 6 Electrospun Fibres

The mechanical results presented in Chapter 4 showcase the reinforcing impact of unmodified CNCs in electrospun fibres. The next step for the use of CNC is surface modification in order to obtain different or enhanced properties. For example, our group recently published a paper reporting the modification of CNC with stearic acid and the increase in the mechanical properties of Nylon 6 films with the addition of the modified CNC. For use in electrospinning, the long 18 carbon stearic acid molecule may cause favourable chain alignment or entanglement as well as enhanced CNC-polymer interactions,[4] especially in aligned fibres. This may drastically increase the elastic moduli of modified CNC-Nylon 6 aligned fibre mats.

7.2.3 CNC-Polymer Electrospun Yarns

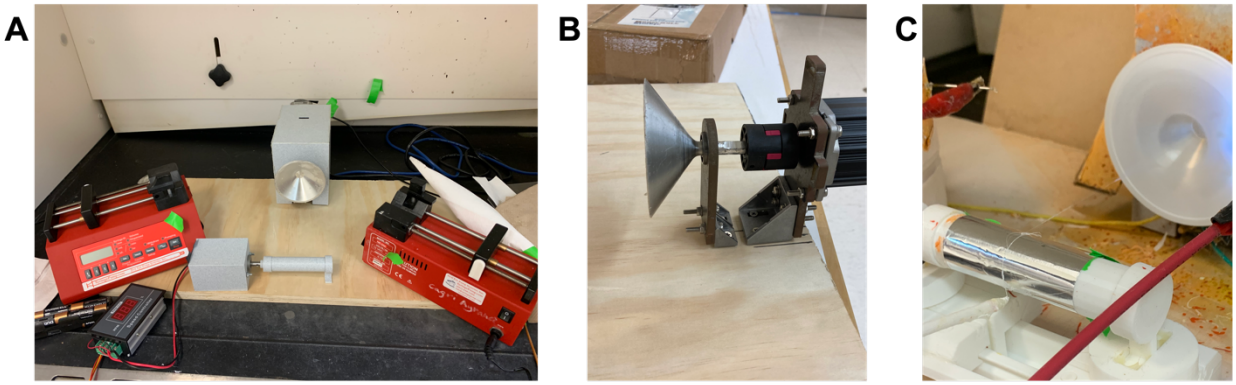

Figure 7-1. Photographs depicting the yarn spinning of Nylon 6 solutions: A) yarn spinning setup with the two syringe pumps, cone collector, and drum collector, B) side-view of cone collector and motor powering the rotation of the cone, and C) collection of the polymer yarn onto the rotating drum collector.

The scaling up of electrospun fibre mats includes post-processing the fibres into yarns for use in ropes or textiles.[5] I have done some preliminary work on the yarn spinning of Nylon 6. The electrospinning setup that myself and Jiawei Chen, a PhD student in Dr. Ayranci's group, made is pictured in Figure 7-1A. In yarn spinning, two syringes have voltages of opposite charges applied to them. A concave metallic cone is placed between the syringes and the fibres are collected on the cone while it spins (Figure 7-1B). Once a sufficient number of fibres are collected across the base of the cone, the fibres are carefully pulled from the centre of the base and the bundle of fibres is placed on a rotating drum collector (Figure 7-1C). The combination of the rotation of the cone and the rotation of the drum collector causes twisted yarns to be produced.

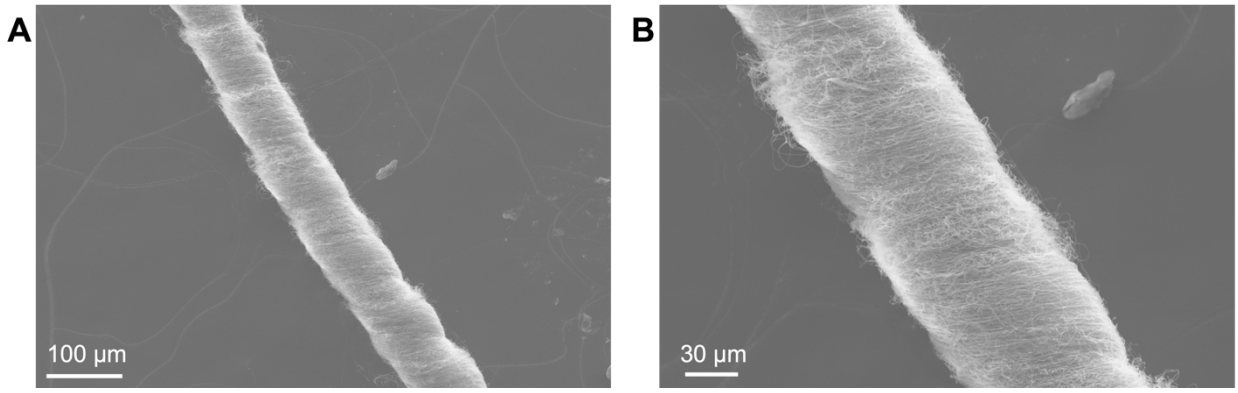

Figure 7-2. SEM images of electrospun Nylene yarns.

Figure 7-2 shows preliminary SEM images using Nylene, an extrusion grade Nylon 6. The individual fibres formed during electrospinning are twisted into fibre bundles that end up as yarns. Optimization would need to be done to obtain yarns of consistent thickness and toughness to prevent snapping of the yarns during collection. Then, the next steps for the yarn spinning would be the addition of CNC to Nylon and the production of spools of yarn that could eventually be braided into ropes using a yarn braiding machine.[6, 7] Other polymers could also be yarn spun with CNC, such as polyethylene glycol (PEG) or polyvinyl alcohol (PVA), and the addition of surface molecules on CNC that change its colour could also act as dual reinforcing and dyeing agents.[8]

7.3 References

1. Adel-Mehraban, F.; Raeissi, K.; Karimzadeh, F.; Pedersen, S. U.; Salehzadeh, H.; Daasbjerg, K., A novel approach toward attachment of graphene oxide on copper using electrochemical grafting of an organic interlayer with enhanced corrosion performance. *Progress in Organic Coatings* **2021,** *154*, 106185.
2. Gautier, C.; López, I.; Breton, T., A post-functionalization toolbox for diazonium (electro)-grafted surfaces: review of the coupling methods. *Materials Advances* **2021,** *2* (9), 2773-2810.
3. Tanpichai, S.; Oksman, K., Cross-linked nanocomposite hydrogels based on cellulose nanocrystals and PVA: Mechanical properties and creep recovery. *Composites Part A: Applied Science and Manufacturing* **2016,** *88*, 226-233.

4. Perween, S.; Khan, Z.; Singh, S.; Ranjan, A., PVA-PDMS-Stearic acid composite nanofibrous mats with improved mechanical behavior for selective filtering applications. *Scientific Reports* **2018,** *8* (1), 16038.
5. Dai, Z.; Wang, N.; Yu, Y.; Lu, Y.; Jiang, L.; Zhang, D.-A.; Wang, X.; Yan, X.; Long, Y.-Z., One-Step Preparation of a Core-Spun Cu/P(VDF-TrFE) Nanofibrous Yarn for Wearable Smart Textile to Monitor Human Movement. *ACS Applied Materials & Interfaces* **2021,** *13* (37), 44234-44242.
6. Liu, J.; Zhai, H.; Sun, Y.; Wu, S.; Chen, S., Developing high strength poly(L-lactic acid) nanofiber yarns for biomedical textile materials: A comparative study of novel nanofiber yarns and traditional microfiber yarns. *Materials Letters* **2021,** *300*, 130229.
7. Zhao, X.; Li, W.; Li, F.; Hou, Y.; Lu, T.; Pan, Y.; Li, J.; Xu, Y.; He, J., Wearable yarn supercapacitors coated with twisted PPy@GO nanosheets and PPy@PAN-GO nanofibres. *Journal of Materials Science* **2021,** *56* (32), 18147-18161.
8. Arju, S. N.; Afsar, A. M.; Das, D. K.; Khan, M. A., Role of Reactive Dye and Chemicals on Mechanical Properties of Jute Fabrics Polypropylene Composites. *Procedia Engineering* **2014,** *90*, 199-205.

Bibliography (Alphabetical by First Author)

Abitbol, T.; Kam, D.; Levi-Kalisman, Y.; Gray, D. G.; Shoseyov, O., Surface Charge Influence on the Phase Separation and Viscosity of Cellulose Nanocrystals. *Langmuir* **2018,** *34* (13), 3925-3933.

Abitbol, T.; Marway, H.; Cranston, E. D., Surface modification of cellulose nanocrystals with cetyltrimethylammonium bromide. *Nordic Pulp & Paper Research Journal* **2014,** *29* (1), 46-57.

Adel-Mehraban, F.; Raeissi, K.; Karimzadeh, F.; Pedersen, S. U.; Salehzadeh, H.; Daasbjerg, K., A novel approach toward attachment of graphene oxide on copper using electrochemical grafting of an organic interlayer with enhanced corrosion performance. *Progress in Organic Coatings* **2021,** *154*, 106185.

Agarwal, S.; Greiner, A.; Wendorff, J. H., Functional materials by electrospinning of polymers. *Progress in Polymer Science* **2013,** *38* (6), 963-991.

Aitha, S.; Vasanthan, N., Effect of cellulose nanocrystals on crystallization, morphology and phase transition of polyamide 6. *Composite Interfaces* **2020,** *27* (4), 371-384.

Allongue, P.; Delamar, M.; Desbat, B.; Fagebaume, O.; Hitmi, R.; Pinson, J.; Savéant, J.-M., Covalent Modification of Carbon Surfaces by Aryl Radicals Generated from the Electrochemical Reduction of Diazonium Salts. *Journal of the American Chemical Society* **1997,** *119* (1), 201-207.

Anariba, F.; DuVall, S. H.; McCreery, R. L., Mono- and Multilayer Formation by Diazonium Reduction on Carbon Surfaces Monitored with Atomic Force Microscopy "Scratching". *Analytical Chemistry* **2003,** *75* (15), 3837-3844.

Anderson, S. L.; Luber, E. J.; Olsen, B. C.; Buriak, J. M., Substance over Subjectivity: Moving beyond the Histogram. *Chemistry of Materials* **2016,** *28* (17), 5973-5975.

Arju, S. N.; Afsar, A. M.; Das, D. K.; Khan, M. A., Role of Reactive Dye and Chemicals on Mechanical Properties of Jute Fabrics Polypropylene Composites. *Procedia Engineering* **2014,** *90*, 199-205.

Bahr, J. L.; Yang, J.; Kosynkin, D. V.; Bronikowski, M. J.; Smalley, R. E.; Tour, J. M., Functionalization of Carbon Nanotubes by Electrochemical Reduction of Aryl Diazonium Salts: A Bucky Paper Electrode. *Journal of the American Chemical Society* **2001,** *123* (27), 6536-6542.

Bajpai, P., Chapter 2 - Wood and Fiber Fundamentals. In *Biermann's Handbook of Pulp and Paper (Third Edition)*, Bajpai, P., Ed. Elsevier: 2018; pp 19-74.

Baranton, S.; Belanger, D., Electrochemical derivatization of carbon surface by reduction of in situ generated diazonium cations. *J Phys Chem B* **2005,** *109* (51), 24401-10.

Baranton, S.; Bélanger, D., In situ generation of diazonium cations in organic electrolyte for electrochemical modification of electrode surface. *Electrochimica Acta* **2008,** *53* (23), 6961-6967.

Bazbouz, M. B.; Stylios, G. K., Alignment and optimization of nylon 6 nanofibers by electrospinning. *Journal of Applied Polymer Science* **2008,** *107* (5), 3023-3032.

Bazrafshan, Z., Multi-functional coating of polymeric spherulites for chiral photonic cellulose nanocrystal films. *Cellulose* **2020,** *27* (11), 6235-6247.

Beachley, V.; Katsanevakis, E.; Zhang, N.; Wen, X., Highly Aligned Polymer Nanofiber Structures: Fabrication and Applications in Tissue Engineering. In *Biomedical Applications of Polymeric Nanofibers*, Jayakumar, R.; Nair, S., Eds. Springer Berlin Heidelberg: Berlin, Heidelberg, 2012; pp 171-212.

Bondarev, A. A.; Naumov, E. V.; Kassanova, A. Z.; Krasnokutskaya, E. A.; Stankevich, K. S.; Filimonov, V. D., First Study of the Thermal and Storage Stability of Arenediazonium Triflates Comparing to 4-Nitrobenzenediazonium Tosylate and Tetrafluoroborate by Calorimetric Methods. *Organic Process Research & Development* **2019,** *23* (11), 2405-2415.

Bonin, H.; Fouquet, E.; Felpin, F.-X., Aryl Diazonium versus Iodonium Salts: Preparation, Applications and Mechanisms for the Suzuki–Miyaura Cross-Coupling Reaction. *Advanced Synthesis & Catalysis* **2011,** *353* (17), 3063-3084.

Borges, A. L. S.; Münchow, E. A.; de Oliveira Souza, A. C.; Yoshida, T.; Vallittu, P. K.; Bottino, M. C., Effect of random/aligned nylon-6/MWCNT fibers on dental resin composite reinforcement. *Journal of the Mechanical Behavior of Biomedical Materials* **2015,** *48*, 134-144.

Bourdillon, C.; Delamar, M.; Demaille, C.; Hitmi, R.; Moiroux, J.; Pinson, J., Immobilization of glucose oxidase on a carbon surface derivatized by electrochemical reduction of diazonium salts. *Journal of Electroanalytical Chemistry* **1992,** *336* (1), 113-123.

Breton, T.; Belanger, D., Modification of carbon electrode with aryl groups having an aliphatic amine by electrochemical reduction of in situ generated diazonium cations. *Langmuir* **2008,** *24* (16), 8711-8718.

Buyukada-Kesici, E.; Gezmis-Yavuz, E.; Aydin, D.; Cansoy, C. E.; Alp, K.; Koseoglu-Imer, D. Y., Design and fabrication of nano-engineered electrospun filter media with cellulose nanocrystal for toluene adsorption from indoor air. *Materials Science and Engineering: B* **2021,** *264*, 114953.

Cao, Y.; Zavattieri, P.; Youngblood, J.; Moon, R.; Weiss, J., The relationship between cellulose nanocrystal dispersion and strength. *Construction and Building Materials* **2016,** *119*, 71-79.

Carlmark, A.; Larsson, E.; Malmström, E., Grafting of cellulose by ring-opening polymerisation – A review. *European Polymer Journal* **2012,** *48* (10), 1646-1659.

Carlsson, L.; Ingverud, T.; Blomberg, H.; Carlmark, A.; Larsson, P. T.; Malmström, E., Surface characteristics of cellulose nanoparticles grafted by surface-initiated ring-opening polymerization of ε-caprolactone. *Cellulose* **2015,** *22* (2), 1063-1074.

Carneiro de Oliveira, J.; Rigolet, S.; Marichal, C.; Roucoules, V.; Laborie, M.-P., Grafting Diels-Alder moieties on cellulose nanocrystals through carbamation. *Carbohydrate Polymers* **2020,** *250*, 116966.

Chen, Y.; Waghmare, P. R.; Ayranci, C., Fabrication and characterization of electrospun mats of Nylon 6/Silica nanocomposite fibers. *Journal of Engineered Fibers and Fabrics* **2019,** *14*, 1558925019843225.

Cho, J. W.; Paul, D. R., Nylon 6 nanocomposites by melt compounding. *Polymer* **2001,** *42* (3), 1083-1094.

Chu, P. F.; Iwasawa, S.; Schell, P. L.; Lin, C.-Y., Carbon fiber versus glass fiber reinforcements: A novel, true comparison in thermoplastics. *Polymer Composites* **2021,** *42* (11), 6173-6181.

Clemons, C.; Reiner, R., Preparation of cellulose nanocrystal-polypropylene masterbatches by water-assisted thermokinetic mixing. *ANTEC 2020: The Virtual Edition. 6p.* **2020**.

Combellas, C.; Kanoufi, F.; Pinson, J.; Podvorica, F. I., Sterically Hindered Diazonium Salts for the Grafting of a Monolayer on Metals. *Journal of the American Chemical Society* **2008,** *130* (27), 8576-8577.

Conte, A. A.; Sun, K.; Hu, X.; Beachley, V. Z., Effects of Fiber Density and Strain Rate on the Mechanical Properties of Electrospun Polycaprolactone Nanofiber Mats. *Frontiers in Chemistry* **2020,** *8* (610).

Corder, R. D.; Adhikari, P.; Burroughs, M. C.; Rojas, O. J.; Khan, S. A., Cellulose nanocrystals for gelation and percolation-induced reinforcement of a photocurable poly(vinyl alcohol) derivative. *Soft Matter* **2020,** *16* (37), 8602-8611.

Cramariuc, B.; Cramariuc, R.; Scarlet, R.; Manea, L. R.; Lupu, I. G.; Cramariuc, O., Fiber diameter in electrospinning process. *Journal of Electrostatics* **2013,** *71* (3), 189-198.

Cranston, E. D.; Gray, D. G., Birefringence in spin-coated films containing cellulose nanocrystals. *Colloids and Surfaces A: Physicochemical and Engineering Aspects* **2008,** *325* (1), 44-51.

Credou, J.; Volland, H.; Dano, J.; Berthelot, T., A one-step and biocompatible cellulose functionalization for covalent antibody immobilization on immunoassay membranes. *Journal of Materials Chemistry B* **2013,** *1* (26), 3277-3286.

Crist, B.; Schultz, J. M., Polymer spherulites: A critical review. *Progress in Polymer Science* **2016,** *56*, 1-63.

Dai, Z.; Wang, N.; Yu, Y.; Lu, Y.; Jiang, L.; Zhang, D.-A.; Wang, X.; Yan, X.; Long, Y.-Z., One-Step Preparation of a Core-Spun Cu/P(VDF-TrFE) Nanofibrous Yarn for Wearable Smart Textile to Monitor Human Movement. *ACS Applied Materials & Interfaces* **2021,** *13* (37), 44234-44242.

Dasgupta, S.; Hammond, W. B.; Goddard, W. A., Crystal Structures and Properties of Nylon Polymers from Theory. *Journal of the American Chemical Society* **1996,** *118* (49), 12291-12301.

Deopura, B. L., 2 - Polyamide fibers. In *Polyesters and Polyamides*, Deopura, B. L.; Alagirusamy, R.; Joshi, M.; Gupta, B., Eds. Woodhead Publishing: 2008; pp 41-61.

Desmaisons, J.; Rueff, M.; Bras, J.; Dufresne, A., Impregnation of paper with cellulose nanocrystal reinforced polyvinyl alcohol: synergistic effect of infrared drying and CNC content on crystallinity. *Soft Matter* **2018,** *14* (46), 9425-9435.

Díaz de León, R.; Guzmán, E.; López González, R.; Díaz Elizondo, A.; Magaña, I.; Neira, G.; Castañeda Facio, A.; Valencia, L., Surface Modification of Cellulose Nanocrystals with Lactone Monomers via Plasma-Induced Polymerization and Their Application in ABS Nanocomposites. *Polymers* **2021,** *13* (16), 2699.

Dong, H., Polymer Nanofibers Reinforced with Cellulose Nanocrystals. In *Handbook of Polymer Nanocomposites. Processing, Performance and Application: Volume C: Polymer Nanocomposites of Cellulose Nanoparticles*, Pandey, J. K.; Takagi, H.; Nakagaito, A. N.; Kim, H.-J., Eds. Springer Berlin Heidelberg: Berlin, Heidelberg, 2015; pp 323-341.

Dong, H.; Strawhecker, K. E.; Snyder, J. F.; Orlicki, J. A.; Reiner, R. S.; Rudie, A. W., Cellulose nanocrystals as a reinforcing material for electrospun poly(methyl methacrylate) fibers: Formation, properties and nanomechanical characterization. *Carbohydrate Polymers* **2012,** *87* (4), 2488-2495.

Doppelt, P.; Hallais, G.; Pinson, J.; Podvorica, F.; Verneyre, S., Surface Modification of Conducting Substrates. Existence of Azo Bonds in the Structure of Organic Layers Obtained from Diazonium Salts. *Chemistry of Materials* **2007,** *19* (18), 4570-4575.

Du, R.; Kaufman, G.; McDermott, M. In *Surface modification of cellulose nanocrystals (CNCs) with diazonium salts and their application in nanocomposites*, TAPPI International Conference on Nanotechnology for Renewable Materials 2016, 2016; pp 633-643.

Dufresne, A., Nanocellulose: a new ageless bionanomaterial. *Materials Today* **2013,** *16* (6), 220-227.

Dufresne, A., Cellulose nanomaterial reinforced polymer nanocomposites. *Current Opinion in Colloid & Interface Science* **2017,** *29*, 1-8.

Dufresne, A., 9. Mechanical properties of nanocellulose-based nanocomposites. In *Nanocellulose: From Nature to High Performance Tailored Materials*, De Gruyter: 2017; pp 471-530.

Dufresne, A., 7. Processing of nanocellulose-based materials. In *Nanocellulose: From Nature to High Performance Tailored Materials*, De Gruyter: 2017; pp 351-418.

Dufresne, A., 3. Preparation of cellulose nanocrystals. In *Nanocellulose: From Nature to High Performance Tailored Materials*, De Gruyter: 2017; pp 117-192.

Dufresne, A., 5. Chemical modification of nanocellulose. In *Nanocellulose: From Nature to High Performance Tailored Materials*, De Gruyter: 2017; pp 221-286.

Dufresne, A., Cellulose nanomaterials as green nanoreinforcements for polymer nanocomposites. *Philos Trans A Math Phys Eng Sci* **2018,** *376* (2112).

Eyley, S.; Thielemans, W., Surface modification of cellulose nanocrystals. *Nanoscale* **2014,** *6* (14), 7764-7779.

Fardioui, M.; Qaiss, A. e. K.; Bouhfid, R., 16 - Cellulose nanocrystal–based nanocomposites. In *Cellulose-Reinforced Nanofibre Composites*, Jawaid, M.; Boufi, S.; H.P.S, A. K., Eds. Woodhead Publishing: 2017; pp 373-389.

Feldman, D., Polyamide nanocomposites. *Journal of Macromolecular Science, Part A* **2017,** *54* (4), 255-262.

Firth, J. D.; Fairlamb, I. J. S., A Need for Caution in the Preparation and Application of Synthetically Versatile Aryl Diazonium Tetrafluoroborate Salts. *Organic Letters* **2020,** *22* (18), 7057-7059.

Flavel, B. S.; Gross, A. J.; Garrett, D. J.; Nock, V.; Downard, A. J., A simple approach to patterned protein immobilization on silicon via electrografting from diazonium salt solutions. *ACS Appl Mater Interfaces* **2010,** *2* (4), 1184-90.

Fornes, T. D.; Paul, D. R., Crystallization behavior of nylon 6 nanocomposites. *Polymer* **2003,** *44* (14), 3945-3961.

Forsgren, L.; Sahlin-Sjövold, K.; Venkatesh, A.; Thunberg, J.; Kádár, R.; Boldizar, A.; Westman, G.; Rigdahl, M., Composites with surface-grafted cellulose nanocrystals (CNC). *Journal of Materials Science* **2019,** *54* (4), 3009-3022.

Fortunati, E.; Luzi, F.; Puglia, D.; Terenzi, A.; Vercellino, M.; Visai, L.; Santulli, C.; Torre, L.; Kenny, J. M., Ternary PVA nanocomposites containing cellulose nanocrystals from different sources and silver particles: Part II. *Carbohydrate Polymers* **2013,** *97* (2), 837-848.

Foster, E. J.; Moon, R. J.; Agarwal, U. P.; Bortner, M. J.; Bras, J.; Camarero-Espinosa, S.; Chan, K. J.; Clift, M. J. D.; Cranston, E. D.; Eichhorn, S. J.; Fox, D. M.; Hamad, W. Y.; Heux, L.; Jean, B.; Korey, M.; Nieh, W.; Ong, K. J.; Reid, M. S.; Renneckar, S.; Roberts, R.; Shatkin, J. A.; Simonsen, J.; Stinson-Bagby, K.; Wanasekara, N.; Youngblood, J., Current characterization methods for cellulose nanomaterials. *Chem Soc Rev* **2018,** *47* (8), 2609-2679.

Fox, D. M.; Rodriguez, R. S.; Devilbiss, M. N.; Woodcock, J.; Davis, C. S.; Sinko, R.; Keten, S.; Gilman, J. W., Simultaneously Tailoring Surface Energies and Thermal Stabilities of Cellulose Nanocrystals Using Ion Exchange: Effects on Polymer Composite Properties for Transportation, Infrastructure, and Renewable Energy Applications. *ACS Applied Materials & Interfaces* **2016,** *8* (40), 27270-27281.

Fraschini, C.; Chauve, G.; Bouchard, J., TEMPO-mediated surface oxidation of cellulose nanocrystals (CNCs). *Cellulose* **2017,** *24* (7), 2775-2790.

Fridrikh, S. V.; Yu, J. H.; Brenner, M. P.; Rutledge, G. C., Controlling the Fiber Diameter during Electrospinning. *Physical Review Letters* **2003,** *90* (14), 144502.

Fryer, C.; Scharnagl, M.; Helms, C., Electrostatic alignment of electrospun PEO fibers by the gap method increases individual fiber modulus in comparison to non-aligned fibers of similar diameter. *AIP Advances* **2018,** *8* (6), 065023.

García, M.; van Zyl, W. E.; Verweij, H., Hybrid nylon-6/silica nanocomposites with improved mechanical properties. *MRS Online Proceedings Library* **2003,** *740* (1), I1.9.

Gautier, C.; López, I.; Breton, T., A post-functionalization toolbox for diazonium (electro)-grafted surfaces: review of the coupling methods. *Materials Advances* **2021,** *2* (9), 2773-2810.

Goffin, A. L.; Raquez, J. M.; Duquesne, E.; Siqueira, G.; Habibi, Y.; Dufresne, A.; Dubois, P., Poly(ε-caprolactone) based nanocomposites reinforced by surface-grafted cellulose nanowhiskers via extrusion processing: Morphology, rheology, and thermo-mechanical properties. *Polymer* **2011,** *52* (7), 1532-1538.

Griffete, N.; Lamouri, A.; Herbst, F.; Felidj, N.; Ammar, S.; Mangeney, C., Synthesis of highly soluble polymer-coated magnetic nanoparticles using a combination of diazonium salt chemistry and the iniferter method. *RSC Advances* **2012,** *2* (3), 826-830.

Grishkewich, N.; Mohammed, N.; Tang, J. T.; Tam, K. C., Recent advances in the application of cellulose nanocrystals. *Current Opinion in Colloid & Interface Science* **2017,** *29*, 32-45.

Guerrero, J.; Rivero, J.; Gundabala, V. R.; Perez-Saborid, M.; Fernandez-Nieves, A., Whipping of electrified liquid jets. *Proceedings of the National Academy of Sciences* **2014,** *111* (38), 13763-13767.

Gururajan, G.; Sullivan, S. P.; Beebe, T. P.; Chase, D. B.; Rabolt, J. F., Continuous electrospinning of polymer nanofibers of Nylon-6 using an atomic force microscope tip. *Nanoscale* **2011,** *3* (8), 3300-3308.

Haasch, R. T., X-Ray Photoelectron Spectroscopy (XPS) and Auger Electron Spectroscopy (AES). In *Practical Materials Characterization*, Sardela, M., Ed. Springer New York: New York, NY, 2014; pp 93-132.

Habibi, Y., Key advances in the chemical modification of nanocelluloses. *Chem Soc Rev* **2014,** *43* (5), 1519-42.

Habibi, Y.; Goffin, A.-L.; Schiltz, N.; Duquesne, E.; Dubois, P.; Dufresne, A., Bionanocomposites based on poly(ε-caprolactone)-grafted cellulose nanocrystals by ring-opening polymerization. *Journal of Materials Chemistry* **2008,** *18* (41), 5002-5010.

Habibi, Y.; Lucia, L. A.; Rojas, O. J., Cellulose Nanocrystals: Chemistry, Self-Assembly, and Applications. *Chemical Reviews* **2010,** *110* (6), 3479-3500.

Haider, A.; Haider, S.; Kang, I.-K., A comprehensive review summarizing the effect of electrospinning parameters and potential applications of nanofibers in biomedical and biotechnology. *Arabian Journal of Chemistry* **2018,** *11* (8), 1165-1188.

Hamad, W. Y., Assembly and Structure in Native Cellulosic Fibers. In *Cellulose Nanocrystals*, 2017; pp 16-32.

Hamad, W. Y., *Cellulose Nanocrystals: Properties, Production and Applications*. Wiley: 2017.

Hebeish, A.; Guthrie, J. T., Grafting on Chemically Modified Cellulose. In *The Chemistry and Technology of Cellulosic Copolymers*, Springer Berlin Heidelberg: Berlin, Heidelberg, 1981; pp 196-244.

Heise, K.; Kontturi, E.; Allahverdiyeva, Y.; Tammelin, T.; Linder, M. B.; Nonappa; Ikkala, O., Nanocellulose: Recent Fundamental Advances and Emerging Biological and Biomimicking Applications. *Advanced Materials* **2021,** *33* (3), 2004349.

Hekmati, A. H.; Rashidi, A.; Ghazisaeidi, R.; Drean, J.-Y., Effect of needle length, electrospinning distance, and solution concentration on morphological properties of polyamide-6 electrospun nanowebs. *Textile Research Journal* **2013,** *83* (14), 1452-1466.

Hetemi, D.; Combellas, C.; Kanoufi, F.; Podvorica, F. I., Direct vs Indirect Grafting of Alkyl and Aryl Halides. *ChemPhysChem* **2021,** *22* (18), 1844-1849.

Hetemi, D.; Hazimeh, H.; Decorse, P.; Galtayries, A.; Combellas, C.; Kanoufi, F.; Pinson, J.; Podvorica, F. I., One-Step Formation of Bifunctionnal Aryl/Alkyl Grafted Films on Conducting Surfaces by the Reduction of Diazonium Salts in the Presence of Alkyl Iodides. *Langmuir* **2015,** *31* (19), 5406-5415.

Hetemi, D.; Kanoufi, F.; Combellas, C.; Pinson, J.; Podvorica, F. I., Electrografting of alkyl films at low driving force by diverting the reactivity of aryl radicals derived from diazonium salts. *Langmuir* **2014,** *30* (46), 13907-13.

Hetemi, D.; Medard, J.; Kanoufi, F.; Combellas, C.; Pinson, J.; Podvorica, F. I., Surface Modification of Polymers by Reaction of Alkyl Radicals. *Langmuir* **2016,** *32* (2), 512-8.

Holmes, D. R.; Bunn, C. W.; Smith, D. J., The crystal structure of polycaproamide: Nylon 6. *Journal of Polymer Science* **1955,** *17* (84), 159-177.

Hossain, M. Z.; Shimizu, N., In Situ Functionalization of Graphene with Reactive End Group through Amine Diazotization. *The Journal of Physical Chemistry C* **2017,** *121* (45), 25223-25228.

Hu, J.; Song, Y.; Zhang, C.; Huang, W.; Chen, A.; He, H.; Zhang, S.; Chen, Y.; Tu, C.; Liu, J.; Xuan, X.; Chang, Y.; Zheng, J.; Wu, J., Highly Aligned Electrospun Collagen/Polycaprolactone Surgical Sutures with Sustained Release of Growth Factors for Wound Regeneration. *ACS Applied Bio Materials* **2020,** *3* (2), 965-976.

Inai, N. H.; Lewandowska, A. E.; Ghita, O. R.; Eichhorn, S. J., Interfaces in polyethylene oxide modified cellulose nanocrystal - polyethylene matrix composites. *Composites Science and Technology* **2018,** *154*, 128-135.

International, A., *Atlas of Stress-strain Curves*. ASM International: 2002.

Isaac, B.; Taylor, R. M.; Reifsnider, K., Mechanical and Dielectric Properties of Aligned Electrospun Fibers. *Fibers* **2021,** *9* (1), 4.

Islam, M. S.; McCutcheon, J. R.; Rahaman, M. S., A high flux polyvinyl acetate-coated electrospun nylon 6/SiO2 composite microfiltration membrane for the separation of oil-in-water emulsion with improved antifouling performance. *Journal of Membrane Science* **2017,** *537*, 297-309.

Islam, S.; Hasan, M.; Ahmad, M. B., Chemical Modification and Properties of Cellulose-Based Polymer Composites. In *Lignocellulosic Polymer Composites*, 2014; pp 301-324.

Jackson, J. C.; Camargos, C. H. M.; Noronha, V. T.; Paula, A. J.; Rezende, C. A.; Faria, A. F., Sustainable Cellulose Nanocrystals for Improved Antimicrobial Properties of Thin Film Composite Membranes. *ACS Sustainable Chemistry & Engineering* **2021,** *9* (19), 6534-6540.

Jakob, M.; Mahendran, A. R.; Gindl-Altmutter, W.; Bliem, P.; Konnerth, J.; Müller, U.; Veigel, S., The strength and stiffness of oriented wood and cellulose-fibre materials: A review. *Progress in Materials Science* **2022,** *125*, 100916.

Jardin, J. M.; Zhang, Z.; Hu, G.; Tam, K. C.; Mekonnen, T. H., Reinforcement of rubber nanocomposite thin sheets by percolation of pristine cellulose nanocrystals. *International Journal of Biological Macromolecules* **2020,** *152*, 428-436.

Joshi, M. K.; Tiwari, A. P.; Maharjan, B.; Won, K. S.; Kim, H. J.; Park, C. H.; Kim, C. S., Cellulose reinforced nylon-6 nanofibrous membrane: Fabrication strategies, physicochemical characterizations, wicking properties and biomimetic mineralization. *Carbohydr Polym* **2016,** *147*, 104-113.

Junior de Menezes, A.; Siqueira, G.; Curvelo, A. A. S.; Dufresne, A., Extrusion and characterization of functionalized cellulose whiskers reinforced polyethylene nanocomposites. *Polymer* **2009,** *50* (19), 4552-4563.

Kalantari, M.; Du, R.; Ayranci, C.; Boluk, Y., Effects of interfacial interactions and interpenetrating brushes on the electrospinning of cellulose nanocrystals-polystyrene fibers. *J Colloid Interface Sci* **2018,** *528*, 419-430.

Kargarzadeh, H.; Mariano, M.; Huang, J.; Lin, N.; Ahmad, I.; Dufresne, A.; Thomas, S., Recent developments on nanocellulose reinforced polymer nanocomposites: A review. *Polymer* **2017,** *132*, 368-393.

Kariuki, J. K.; McDermott, M. T., Formation of Multilayers on Glassy Carbon Electrodes via the Reduction of Diazonium Salts. *Langmuir* **2001,** *17* (19), 5947-5951.

Khajavi, R.; Abbasipour, M., 5 - Controlling nanofiber morphology by the electrospinning process. In *Electrospun Nanofibers*, Afshari, M., Ed. Woodhead Publishing: 2017; pp 109-123.

Khattab, M. M.; Abdel-Hady, N. A.; Dahman, Y., 21 - Cellulose nanocomposites: Opportunities, challenges, and applications. In *Cellulose-Reinforced Nanofibre Composites*, Jawaid, M.; Boufi, S.; H.P.S, A. K., Eds. Woodhead Publishing: 2017; pp 483-516.

Khoshkava, V.; Kamal, M. R., Effect of Surface Energy on Dispersion and Mechanical Properties of Polymer/Nanocrystalline Cellulose Nanocomposites. *Biomacromolecules* **2013,** *14* (9), 3155-3163.

Kim, H. J.; Pant, H. R.; Amarjargal, A.; Kim, C. S., Incorporation of silver-loaded ZnO rods into electrospun nylon-6 spider-web-like nanofibrous mat using hydrothermal process. *Colloids and Surfaces A: Physicochemical and Engineering Aspects* **2013,** *434*, 49-55.

Kim, J. I.; Hwang, T. I.; Aguilar, L. E.; Park, C. H.; Kim, C. S., A Controlled Design of Aligned and Random Nanofibers for 3D Bi-functionalized Nerve Conduits Fabricated via a Novel Electrospinning Set-up. *Scientific Reports* **2016,** *6* (1), 23761.

Kimura, N.; Kim, B.-S.; Kim, I.-S., Effects of Fe2+ ions on morphologies, microstructures and mechanical properties of electrospun nylon-6 nanofibers. *Polymer International* **2014,** *63* (2), 266-272.

Kindt, S.; Wicht, K.; Heinrich, M. R., Thermally Induced Carbohydroxylation of Styrenes with Aryldiazonium Salts. *Angewandte Chemie International Edition* **2016,** *55* (30), 8744-8747.

Klata, E.; Borysiak, S.; Van de Velde, K.; Garbarczyk, J.; Krucinska, I., Crystallinity of polyamide-6 matrix in glass fibre/polyamide-6 composites manufactured from hybrid yarns. *Fibres & Textiles in Eastern Europe* **2004,** *12* (3), 64-69.

Knirsch, K. C.; Berner, N. C.; Nerl, H. C.; Cucinotta, C. S.; Gholamvand, Z.; McEvoy, N.; Wang, Z.; Abramovic, I.; Vecera, P.; Halik, M.; Sanvito, S.; Duesberg, G. S.; Nicolosi, V.; Hauke, F.; Hirsch, A.; Coleman, J. N.; Backes, C., Basal-Plane Functionalization of Chemically Exfoliated Molybdenum Disulfide by Diazonium Salts. *ACS Nano* **2015,** *9* (6), 6018-6030.

Ko, F. K.; Wan, Y., 4.2 Fundamentals of Process Modeling. In *Introduction to Nanofiber Materials*, Cambridge University Press.

Kojima, Y.; Usuki, A.; Kawasumi, M.; Okada, A.; Fukushima, Y.; Kurauchi, T.; Kamigaito, O., Mechanical properties of nylon 6-clay hybrid. *Journal of Materials Research* **1993,** *8* (5), 1185-1189.

Lagerwall, J. P. F.; Schütz, C.; Salajkova, M.; Noh, J.; Hyun Park, J.; Scalia, G.; Bergström, L., Cellulose nanocrystal-based materials: from liquid crystal self-assembly and glass formation to multifunctional thin films. *NPG Asia Materials* **2014,** *6* (1), e80-e80.

Laudenslager, M. J.; Sigmund, W. M., Electrospinning. In *Encyclopedia of Nanotechnology*, Bhushan, B., Ed. Springer Netherlands: Dordrecht, 2012; pp 769-775.

Laurentius, L.; Stoyanov, S. R.; Gusarov, S.; Kovalenko, A.; Du, R.; Lopinski, G. P.; McDermott, M. T., Diazonium-Derived Aryl Films on Gold Nanoparticles: Evidence for a Carbon–Gold Covalent Bond. *ACS Nano* **2011,** *5* (5), 4219-4227.

Le Gars, M.; Bras, J.; Salmi-Mani, H.; Ji, M.; Dragoe, D.; Faraj, H.; Domenek, S.; Belgacem, N.; Roger, P., Polymerization of glycidyl methacrylate from the surface of cellulose nanocrystals for the elaboration of PLA-based nanocomposites. *Carbohydrate Polymers* **2020,** *234*, 115899.

Le Gars, M.; Delvart, A.; Roger, P.; Belgacem, M. N.; Bras, J., Amidation of TEMPO-oxidized cellulose nanocrystals using aromatic aminated molecules. *Colloid and Polymer Science* **2020,** *298* (6), 603-617.

Le Gars, M.; Roger, P.; Belgacem, N.; Bras, J., Role of solvent exchange in dispersion of cellulose nanocrystals and their esterification using fatty acids as solvents. *Cellulose* **2020,** *27* (8), 4319-4336.

Lee, J.; Deng, Y., Increased mechanical properties of aligned and isotropic electrospun PVA nanofiber webs by cellulose nanowhisker reinforcement. *Macromolecular Research* **2012,** *20* (1), 76-83.

Lee, J. H.; Park, S. H.; Kim, S. H., Surface Alkylation of Cellulose Nanocrystals to Enhance Their Compatibility with Polylactide. *Polymers* **2020,** *12* (1), 178.

Lee, K.-H.; Kim, K.-W.; Pesapane, A.; Kim, H.-Y.; Rabolt, J. F., Polarized FT-IR Study of Macroscopically Oriented Electrospun Nylon-6 Nanofibers. *Macromolecules* **2008,** *41* (4), 1494-1498.

Lee, K.-Y.; Aitomäki, Y.; Berglund, L. A.; Oksman, K.; Bismarck, A., On the use of nanocellulose as reinforcement in polymer matrix composites. *Composites Science and Technology* **2014,** *105*, 15-27.

Lehr, J.; Williamson, B. E.; Downard, A. J., Spontaneous Grafting of Nitrophenyl Groups to Planar Glassy Carbon Substrates: Evidence for Two Mechanisms. *The Journal of Physical Chemistry C* **2011,** *115* (14), 6629-6634.

Leszczyńska, A.; Radzik, P.; Szefer, E.; Mičušík, M.; Omastová, M.; Pielichowski, K., Surface Modification of Cellulose Nanocrystals with Succinic Anhydride. *Polymers* **2019,** *11* (5), 866.

Li, B.; Pan, S.; Yuan, H.; Zhang, Y., Optical and mechanical anisotropies of aligned electrospun nanofibers reinforced transparent PMMA nanocomposites. *Composites Part A: Applied Science and Manufacturing* **2016,** *90*, 380-389.

Li, B.; Xu, W.; Kronlund, D.; Määttänen, A.; Liu, J.; Smått, J.-H.; Peltonen, J.; Willför, S.; Mu, X.; Xu, C., Cellulose nanocrystals prepared via formic acid hydrolysis followed by TEMPO-mediated oxidation. *Carbohydrate Polymers* **2015,** *133*, 605-612.

Li, D.; Tao, L.; Shen, Y.; Sun, B.; Xie, X.; Ke, Q.; Mo, X.; Deng, B., Fabrication of Multilayered Nanofiber Scaffolds with a Highly Aligned Nanofiber Yarn for Anisotropic Tissue Regeneration. *ACS Omega* **2020,** *5* (38), 24340-24350.

Li, L.; Bellan, L. M.; Craighead, H. G.; Frey, M. W., Formation and properties of nylon-6 and nylon-6/montmorillonite composite nanofibers. *Polymer* **2006,** *47* (17), 6208-6217.

Li, M.; Liu, X.; Liu, N.; Guo, Z.; Singh, P. K.; Fu, S., Effect of surface wettability on the antibacterial activity of nanocellulose-based material with quaternary ammonium groups. *Colloids and Surfaces A: Physicochemical and Engineering Aspects* **2018,** *554*, 122-128.

Li, W.; Zhao, X.; Huang, Z.; Liu, S., Nanocellulose fibrils isolated from BHKP using ultrasonication and their reinforcing properties in transparent poly (vinyl alcohol) films. *Journal of Polymer Research* **2013,** *20* (8), 210.

Li, Y.; Goddard, W. A., Nylon 6 Crystal Structures, Folds, and Lamellae from Theory. *Macromolecules* **2002,** *35* (22), 8440-8455.

Lin, N.; Dufresne, A., Surface chemistry, morphological analysis and properties of cellulose nanocrystals with gradiented sulfation degrees. *Nanoscale* **2014,** *6* (10), 5384-5393.

Liu, D.; Sui, G.; Dong, Y., 5 - Electrospun polymeric composite nanofibers with cellulose nanocrystals and their applications. In *Electrospun Polymers and Composites*, Dong, Y.; Baji, A.; Ramakrishna, S., Eds. Woodhead Publishing: 2021; pp 147-178.

Liu, J.; Zhai, H.; Sun, Y.; Wu, S.; Chen, S., Developing high strength poly(L-lactic acid) nanofiber yarns for biomedical textile materials: A comparative study of novel nanofiber yarns and traditional microfiber yarns. *Materials Letters* **2021,** *300*, 130229.

Liu, S.; Cheng, P.; Liu, W.; Zeng, J.-G., Ascorbic Acid-Initiated Tandem Radical Cyclization of N-Arylacrylamides to Give 3,3-Disubstituted Oxindoles. *Molecules (Basel, Switzerland)* **2015,** *20* (9), 15631-15642.

Liu, S.-d.; Li, D.-s.; Yang, Y.; Jiang, L., Fabrication, mechanical properties and failure mechanism of random and aligned nanofiber membrane with different parameters. *Nanotechnology Reviews* **2019,** *8* (1), 218-226.

Liu, Y.; Cui, L.; Guan, F.; Gao, Y.; Hedin, N. E.; Zhu, L.; Fong, H., Crystalline Morphology and Polymorphic Phase Transitions in Electrospun Nylon-6 Nanofibers. *Macromolecules* **2007,** *40* (17), 6283-6290.

Lu, Y.; Yu, G.; Wei, X.; Zhan, C.; Jeon, J.-W.; Wang, X.; Jeffryes, C.; Guo, Z.; Wei, S.; Wujcik, E. K., Fabric/multi-walled carbon nanotube sensor for portable on-site copper detection in water. *Advanced Composites and Hybrid Materials* **2019,** *2* (4), 711-719.

Ly, M.; Mekonnen, T. H., Cationic surfactant modified cellulose nanocrystals for corrosion protective nanocomposite surface coatings. *Journal of Industrial and Engineering Chemistry* **2020,** *83*, 409-420.

Mahmud, M. M.; Perveen, A.; Jahan, R. A.; Matin, M. A.; Wong, S. Y.; Li, X.; Arafat, M. T., Preparation of different polymorphs of cellulose from different acid hydrolysis medium. *International Journal of Biological Macromolecules* **2019,** *130*, 969-976.

Mahouche-Chergui, S.; Gam-Derouich, S.; Mangeney, C.; Chehimi, M. M., Aryl diazonium salts: a new class of coupling agents for bonding polymers, biomacromolecules and nanoparticles to surfaces. *Chem Soc Rev* **2011,** *40* (7), 4143-66.

Marcoux, P. R.; Hapiot, P.; Batail, P.; Pinson, J., Electrochemical functionalization of nanotube films: growth of aryl chains on single-walled carbon nanotubes. *New Journal of Chemistry* **2004,** *28* (2), 302-307.

Mariano, M.; Chirat, C.; El Kissi, N.; Dufresne, A., Impact of Cellulose Nanocrystal Aspect Ratio on Crystallization and Reinforcement of Poly(butylene adipate-co-terephthalate). *Journal of Polymer Science Part B-Polymer Physics* **2016,** *54* (22), 2284-2297.

Mariano, M.; El Kissi, N.; Dufresne, A., Cellulose nanocrystals and related nanocomposites: Review of some properties and challenges. *Journal of Polymer Science Part B: Polymer Physics* **2014,** *52* (12), 791-806.

Marshall, N.; Rodriguez, A.; Crittenden, S., Diazonium-functionalized thin films from the spontaneous reaction of p-phenylenebis(diazonium) salts. *RSC Advances* **2018,** *8* (12), 6690-6698.

Matsuo, T., 17 - Automotive applications. In *Polyesters and Polyamides*, Deopura, B. L.; Alagirusamy, R.; Joshi, M.; Gupta, B., Eds. Woodhead Publishing: 2008; pp 525-541.

Meree, C. E.; Schueneman, G. T.; Meredith, J. C.; Shofner, M. L., Rheological behavior of highly loaded cellulose nanocrystal/poly(vinyl alcohol) composite suspensions. *Cellulose* **2016,** *23* (5), 3001-3012.

Miao, C.; Hamad, W. Y., Alkenylation of cellulose nanocrystals (CNC) and their applications. *Polymer* **2016,** *101*, 338-346.

Millot, C.; Fillot, L.-A.; Lame, O.; Sotta, P.; Seguela, R., Assessment of polyamide-6 crystallinity by DSC. *Journal of Thermal Analysis and Calorimetry* **2015,** *122* (1), 307-314.

Moon, R. J.; Martini, A.; Nairn, J.; Simonsen, J.; Youngblood, J., Cellulose nanomaterials review: structure, properties and nanocomposites. *Chem Soc Rev* **2011,** *40* (7), 3941-94.

Nagalakshmaiah, M.; El Kissi, N.; Dufresne, A., Ionic Compatibilization of Cellulose Nanocrystals with Quaternary Ammonium Salt and Their Melt Extrusion with Polypropylene. *ACS Applied Materials & Interfaces* **2016,** *8* (13), 8755-8764.

Nasir, M.; Hashim, R.; Sulaiman, O.; Asim, M., 11 - Nanocellulose: Preparation methods and applications. In *Cellulose-Reinforced Nanofibre Composites*, Jawaid, M.; Boufi, S.; H.P.S, A. K., Eds. Woodhead Publishing: 2017; pp 261-276.

Natterodt, J. C.; Sapkota, J.; Foster, E. J.; Weder, C., Polymer Nanocomposites with Cellulose Nanocrystals Featuring Adaptive Surface Groups. *Biomacromolecules* **2017,** *18* (2), 517-525.

Ngo, T.; Danumah, C.; Ahvazi, B., Production of Cellulose Nanocrystals at InnoTech Alberta. 2018.

Nickerson, R. F.; Habrle, J. A., Cellulose Intercrystalline Structure. *Industrial & Engineering Chemistry* **1947,** *39* (11), 1507-1512.

Norrman, K.; Ghanbari-Siahkali, A.; Larsen, N. B., 6 Studies of spin-coated polymer films. *Annual Reports Section "C" (Physical Chemistry)* **2005,** *101* (0), 174-201.

Nunes, R. C. R., 13 - Rubber nanocomposites with nanocellulose. In *Progress in Rubber Nanocomposites*, Thomas, S.; Maria, H. J., Eds. Woodhead Publishing: 2017; pp 463-494.

Nuruddin, M.; Chowdhury, R. A.; Szeto, R.; Howarter, J. A.; Erk, K. A.; Szczepanski, C. R.; Youngblood, J. P., Structure–Property Relationship of Cellulose Nanocrystal–Polyvinyl Alcohol Thin Films for High Barrier Coating Applications. *ACS Applied Materials & Interfaces* **2021,** *13* (10), 12472-12482.

O'Neill, A.; Bishop, D.; Dalton, B.; Archer, E.; McIlhagger, A.; Dixon, D., Preparation and properties of polyamide 6 nanocomposites covalently linked with amide functional graphene oxide. *Journal of Thermoplastic Composite Materials* **2018,** *31* (2), 162-180.

Ogawa, Y., Electron microdiffraction reveals the nanoscale twist geometry of cellulose nanocrystals. *Nanoscale* **2019,** *11* (45), 21767-21774.

Oger, N.; d'Halluin, M.; Le Grognec, E.; Felpin, F.-X., Using Aryl Diazonium Salts in Palladium-Catalyzed Reactions under Safer Conditions. *Organic Process Research & Development* **2014,** *18* (12), 1786-1801.

Ogunsona, E. O.; Panchal, P.; Mekonnen, T. H., Surface grafting of acrylonitrile butadiene rubber onto cellulose nanocrystals for nanocomposite applications. *Composites Science and Technology* **2019,** *184*, 107884.

Olguín, C. F.; Agurto, N.; Silva, C. P.; Candia, C. P.; Santander-Nelli, M.; Oyarzo, J.; Gómez, A.; Silva, J. F.; Pavez, J., Tuning the Covering on Gold Surfaces by Grafting Amino-Aryl Films Functionalized with Fe(II) Phthalocyanine: Performance on the Electrocatalysis of Oxygen Reduction. *Molecules* **2021,** *26* (6), 1631.

Orellana, J. L.; Wichhart, D.; Kitchens, C. L., Mechanical and Optical Properties of Polylactic Acid Films Containing Surfactant-Modified Cellulose Nanocrystals. *Journal of Nanomaterials* **2018,** *2018*, 7124260.

Osorio, D. A.; Niinivaara, E.; Jankovic, N. C.; Demir, E. C.; Benkaddour, A.; Jarvis, V.; Ayranci, C.; McDermott, M. T.; de Lannoy, C.-F.; Cranston, E. D., Cellulose Nanocrystals Influence Polyamide 6 Crystal Structure, Spherulite Uniformity, and Mechanical Performance of Nanocomposite Films. *ACS Applied Polymer Materials* **2021,** *3* (9), 4673-4684.

Paci, M.; Filippi, S.; Magagnini, P., Nanostructure development in nylon 6-Cloisite® 30B composites. Effects of the preparation conditions. *European Polymer Journal* **2010,** *46* (5), 838-853.

Padalkar, S.; Capadona, J. R.; Rowan, S. J.; Weder, C.; Won, Y.-H.; Stanciu, L. A.; Moon, R. J., Natural Biopolymers: Novel Templates for the Synthesis of Nanostructures. *Langmuir* **2010,** *26* (11), 8497-8502.

Pagacz, J.; Raftopoulos, K. N.; Leszczyńska, A.; Pielichowski, K., Bio-polyamides based on renewable raw materials. *Journal of Thermal Analysis and Calorimetry* **2016,** *123* (2), 1225-1237.

Pan, L.; Duan, L.; Zheng, Z.; Hu, Y.; Aamir, A.; Bhuwan, S.; Tao, J.; Zhao, T.; Du, Z., Surface characteristics and adhesive strength to polyetheretherketone of titanium electrografted with aryl diazonium salt. *Materials & Design* **2016,** *95*, 555-562.

Paralikar, S. A.; Simonsen, J.; Lombardi, J., Poly(vinyl alcohol)/cellulose nanocrystal barrier membranes. *Journal of Membrane Science* **2008,** *320* (1), 248-258.

Parker, R. M.; Guidetti, G.; Williams, C. A.; Zhao, T.; Narkevicius, A.; Vignolini, S.; Frka-Petesic, B., The Self-Assembly of Cellulose Nanocrystals: Hierarchical Design of Visual Appearance. *Advanced Materials* **2018,** *30* (19), 1704477.

Pelipenko, J.; Kristl, J.; Janković, B.; Baumgartner, S.; Kocbek, P., The impact of relative humidity during electrospinning on the morphology and mechanical properties of nanofibers. *Int J Pharm* **2013,** *456* (1), 125-34.

Peng, J.; Walsh, P. J.; Sabo, R. C.; Turng, L.-S.; Clemons, C. M., Water-assisted compounding of cellulose nanocrystals into polyamide 6 for use as a nucleating agent for microcellular foaming. *Polymer* **2016,** *84*, 158-166.

Peng, J.; Walsh, P. J.; Sabo, R. C.; Turng, L. S.; Clemons, C. M., Water-assisted compounding of cellulose nanocrystals into polyamide 6 for use as a nucleating agent for microcellular foaming. *Polymer* **2016,** *84*, 158-166.

Peng, S.; Luo, Q.; Zhou, G.; Xu, X., Recent Advances on Cellulose Nanocrystals and Their Derivatives. *Polymers* **2021,** *13* (19), 3247.

Peng, S. X.; Shrestha, S.; Youngblood, J. P., Crystal structure transformation and induction of shear banding in Polyamide 11 by surface modified Cellulose Nanocrystals. *Polymer* **2017,** *114*, 88-102.

Peng, Y.; Via, B., The Effect of Cellulose Nanocrystal Suspension Treatment on Suspension Viscosity and Casted Film Property. *Polymers* **2021,** *13* (13), 2168.

Peng, Y. C.; Gardner, D. J.; Han, Y., Characterization of mechanical and morphological properties of cellulose reinforced polyamide 6 composites. *Cellulose* **2015,** *22* (5), 3199-3215.

Perween, S.; Khan, Z.; Singh, S.; Ranjan, A., PVA-PDMS-Stearic acid composite nanofibrous mats with improved mechanical behavior for selective filtering applications. *Scientific Reports* **2018,** *8* (1), 16038.

Pillay, S.; Vaidya, U. K.; Janowski, G. M., Effects of moisture and UV exposure on liquid molded carbon fabric reinforced nylon 6 composite laminates. *Composites Science and Technology* **2009,** *69* (6), 839-846.

Pinson, J.; Podvorica, F., Attachment of organic layers to conductive or semiconductive surfaces by reduction of diazonium salts. *Chemical Society Reviews* **2005,** *34* (5), 429-439.

Pinson, J.; Podvorica, F. I., Surface modification of materials: Electrografting of organic films. *Current Opinion in Electrochemistry* **2020,** *24*, 44-48.

Postek, M.; Vladár, A.; Dagata, J.; Farkas, N.; Ming, B.; Wagner, R.; Raman, A.; Moon, R.; Sabo, R.; Wegner, T.; Beecher, J., Development of the metrology and imaging of cellulose nanocrystals. *Measurement Science and Technology* **2010,** *22*, 024005.

Rahimi, S. K.; Otaigbe, J. U., The role of particle surface functionality and microstructure development in isothermal and non-isothermal crystallization behavior of polyamide 6/cellulose nanocrystals nanocomposites. *Polymer* **2016,** *107*, 316-331.

Rahimi, S. K.; Otaigbe, J. U., Polyamide 6 Nanocomposites Incorporating Cellulose Nanocrystals Prepared by In Situ Ring-Opening Polymerization: Viscoelasticity, Creep Behavior, and Melt Rheological Properties. *Polymer Engineering and Science* **2016,** *56* (9), 1045-1060.

Rahimi, S. K.; Otaigbe, J. U., The effects of the interface on microstructure and rheo-mechanical properties of polyamide 6/cellulose nanocrystal nanocomposites prepared by in-situ ring-opening polymerization and subsequent melt extrusion. *Polymer* **2017,** *127*, 269-285.

Reid, M. S.; Villalobos, M.; Cranston, E. D., Benchmarking Cellulose Nanocrystals: From the Laboratory to Industrial Production. *Langmuir* **2017,** *33* (7), 1583-1598.

Reimschuessel, H. K., Nylon 6. Chemistry and mechanisms. *Journal of Polymer Science: Macromolecular Reviews* **1977,** *12* (1), 65-139.

Reneker, D. H.; Yarin, A. L., Electrospinning jets and polymer nanofibers. *Polymer* **2008,** *49* (10), 2387-2425.

Ribeiro, A. S.; Costa, S. M.; Ferreira, D. P.; Calhelha, R. C.; Barros, L.; Stojković, D.; Soković, M.; Ferreira, I. C. F. R.; Fangueiro, R., Chitosan/nanocellulose electrospun fibers with enhanced antibacterial and antifungal activity for wound dressing applications. *Reactive and Functional Polymers* **2021,** *159*, 104808.

Robles, E.; Labidi, J.; Halász, K.; Csóka, L., 18 - Key issues in reinforcement involving nanocellulose. In *Cellulose-Reinforced Nanofibre Composites*, Jawaid, M.; Boufi, S.; H.P.S, A. K., Eds. Woodhead Publishing: 2017; pp 401-425.

Roy, D.; Kotula, A. P.; Natarajan, B.; Gilman, J. W.; Fox, D. M.; Migler, K. B., Effect of cellulose nanocrystals on crystallization kinetics of polycaprolactone as probed by Rheo-Raman. *Polymer* **2018,** *153*, 70-77.

Roy, D.; Semsarilar, M.; Guthrie, J. T.; Perrier, S., Cellulose modification by polymer grafting: a review. *Chemical Society Reviews* **2009,** *38* (7), 2046-2064.

Saha, S.; Hemraz, U. D.; Boluk, Y., The Effects of High Pressure and High Temperature in Semidilute Aqueous Cellulose Nanocrystal Suspensions. *Biomacromolecules* **2020,** *21* (2), 1031-1035.

Sahay, R.; Thavasi, V.; Ramakrishna, S., Design Modifications in Electrospinning Setup for Advanced Applications. *Journal of Nanomaterials* **2011,** *2011*, 317673.

Sandomierski, M.; Voelkel, A., Diazonium Modification of Inorganic and Organic Fillers for the Design of Robust Composites: A Review. *Journal of Inorganic and Organometallic Polymers and Materials* **2021,** *31* (1), 1-21.

Sastri, V. R., 7 - Engineering Thermoplastics: Acrylics, Polycarbonates, Polyurethanes, Polyacetals, Polyesters, and Polyamides. In *Plastics in Medical Devices (Second Edition)*, Sastri, V. R., Ed. William Andrew Publishing: Oxford, 2014; pp 121-172.

Shafizah, S.; Izwan, A. R. S.; Fatirah, F.; Hasraf, M. N. N., Review on cellulose nanocrystals (CNCs) as reinforced agent on electrospun nanofibers: mechanical and thermal properties. *IOP Conference Series: Materials Science and Engineering* **2018,** *440*, 012011.

Shah, R. K.; Paul, D. R., Nylon 6 nanocomposites prepared by a melt mixing masterbatch process. *Polymer* **2004,** *45* (9), 2991-3000.

Shakiba, M.; Rezvani Ghomi, E.; Khosravi, F.; Jouybar, S.; Bigham, A.; Zare, M.; Abdouss, M.; Moaref, R.; Ramakrishna, S., Nylon—A material introduction and overview for biomedical applications. *Polymers for Advanced Technologies* **2021,** *32* (9), 3368-3383.

Sheng, M.; Frurip, D.; Gorman, D., Reactive chemical hazards of diazonium salts. *Journal of Loss Prevention in the Process Industries* **2015,** *38*, 114-118.

Shewchuk, D. M.; McDermott, M. T., Comparison of Diazonium Salt Derived and Thiol Derived Nitrobenzene Layers on Gold. *Langmuir* **2009,** *25* (8), 4556-4563.

Shi, Z.; Li, S.; Li, M.; Gan, L.; Huang, J., Surface modification of cellulose nanocrystals towards new materials development. *Journal of Applied Polymer Science* **2021,** *138* (48), 51555.

Shojaeiarani, J.; Bajwa, D. S.; Stark, N. M., Spin-coating: A new approach for improving dispersion of cellulose nanocrystals and mechanical properties of poly (lactic acid) composites. *Carbohydr Polym* **2018,** *190*, 139-147.

Shojaeiarani, J.; Bajwa, D. S.; Stark, N. M.; Bajwa, S. G., Rheological properties of cellulose nanocrystals engineered polylactic acid nanocomposites. *Composites Part B: Engineering* **2019,** *161*, 483-489.

Singh, S.; Ramakrishna, S.; Berto, F., 3D Printing of polymer composites: A short review. *Material Design & Processing Communications* **2020,** *2* (2), e97.

Solak, A. O.; Eichorst, L. R.; Clark, W. J.; McCreery, R. L., Modified Carbon Surfaces as "Organic Electrodes" That Exhibit Conductance Switching. *Analytical Chemistry* **2003,** *75* (2), 296-305.

Song, W.; Liu, D.; Prempeh, N.; Song, R., Fiber Alignment and Liquid Crystal Orientation of Cellulose Nanocrystals in the Electrospun Nanofibrous Mats. *Biomacromolecules* **2017,** *18* (10), 3273-3279.

Sridhara, P. K.; Vilaseca, F., High Performance PA 6/Cellulose Nanocomposites in the Interest of Industrial Scale Melt Processing. *Polymers* **2021,** *13* (9), 1495.

Stephens, J. S.; Chase, D. B.; Rabolt, J. F., Effect of the Electrospinning Process on Polymer Crystallization Chain Conformation in Nylon-6 and Nylon-12. *Macromolecules* **2004,** *37* (3), 877-881.

Šturcová, A.; Davies, G. R.; Eichhorn, S. J., Elastic Modulus and Stress-Transfer Properties of Tunicate Cellulose Whiskers. *Biomacromolecules* **2005,** *6* (2), 1055-1061.

Su, J.; Calderón Gómez, J. C.; Grundmeier, G.; González Orive, A., Electrografting of 4-Nitrobenzenediazonium Salts on Al-7075 Alloy Surfaces—The Role of Intermetallic Particles. *Nanomaterials* **2021,** *11* (4), 894.

Sucharitpong, T.; Lam, N. T.; Sukyai, P., Production of Nylon-6/Cellulose Nanocrystal Composite Films Using Solvent Dissolution. *Sugar Tech* **2020,** *22* (2), 328-339.

Szabó, L.; Imanishi, S.; Kawashima, N.; Hoshino, R.; Takada, K.; Hirose, D.; Tsukegi, T.; Ninomiya, K.; Takahashi, K., Carbon fibre reinforced cellulose-based polymers: intensifying interfacial adhesion between the fibre and the matrix. *RSC Advances* **2018,** *8* (40), 22729-22736.

Tan, C.; Peng, J.; Lin, W.; Xing, Y.; Xu, K.; Wu, J.; Chen, M., Role of surface modification and mechanical orientation on property enhancement of cellulose nanocrystals/polymer nanocomposites. *European Polymer Journal* **2015,** *62*, 186-197.

Tan, C.; Peng, J.; Lin, W.; Xing, Y.; Xu, K.; Wu, J.; Chen, M., Role of surface modification and mechanical orientation on property enhancement of cellulose nanocrystals/polymer nanocomposites. *European Polymer Journal* **2015,** *62*, 186-197.

Tan, X.; Peng, Q.; Yang, K.; Yang, T.; Saskova, J.; Wiener, J.; Venkataraman, M.; Militky, J.; Xiong, W.; Xu, J., Preparation and Characterization of corn husk nanocellulose coating on electrospun polyamide 6. *Alexandria Engineering Journal* **2022,** *61* (6), 4529-4540.

Tang, J.; Sisler, J.; Grishkewich, N.; Tam, K. C., Functionalization of cellulose nanocrystals for advanced applications. *Journal of Colloid and Interface Science* **2017,** *494*, 397-409.

Tanpichai, S.; Oksman, K., Cross-linked nanocomposite hydrogels based on cellulose nanocrystals and PVA: Mechanical properties and creep recovery. *Composites Part A: Applied Science and Manufacturing* **2016,** *88*, 226-233.

Taylor, G., Electrically Driven Jets. *Proceedings of the Royal Society of London. Series A, Mathematical and Physical Sciences* **1969,** *313* (1515), 453-475.

Tian, C.; Fu, S.; Habibi, Y.; Lucia, L. A., Polymerization Topochemistry of Cellulose Nanocrystals: A Function of Surface Dehydration Control. *Langmuir* **2014,** *30* (48), 14670-14679.

Tian, D.; Wang, F.; Yang, Z.; Niu, X.; Wu, Q.; Sun, P., High-performance polyurethane nanocomposites based on UPy-modified cellulose nanocrystals. *Carbohydrate Polymers* **2019,** *219*, 191-200.

Tijing, L. D.; Woo, Y. C.; Yao, M.; Ren, J.; Shon, H. K., 1.16 Electrospinning for Membrane Fabrication: Strategies and Applications. In *Comprehensive Membrane Science and Engineering (Second Edition)*, Drioli, E.; Giorno, L.; Fontananova, E., Eds. Elsevier: Oxford, 2017; pp 418-444.

Titone, V.; Correnti, A.; La Mantia, F. P., Effect of Moisture Content on the Processing and Mechanical Properties of a Biodegradable Polyester. *Polymers* **2021,** *13* (10), 1616.

Tortorella, S.; Vetri Buratti, V.; Maturi, M.; Sambri, L.; Comes Franchini, M.; Locatelli, E., Surface-Modified Nanocellulose for Application in Biomedical Engineering and Nanomedicine: A Review. *Int J Nanomedicine* **2020,** *15*, 9909-9937.

Toupin, M.; Bélanger, D., Thermal Stability Study of Aryl Modified Carbon Black by in Situ Generated Diazonium Salt. *The Journal of Physical Chemistry C* **2007,** *111* (14), 5394-5401.

Tousignant, M. N.; Rice, N. A.; Peltekoff, A.; Sundaresan, C.; Miao, C.; Hamad, W. Y.; Lessard, B. H., Improving Thin-Film Properties of Poly(vinyl alcohol) by the Addition of Low-Weight Percentages of Cellulose Nanocrystals. *Langmuir* **2020,** *36* (13), 3550-3557.

Trache, D.; Tarchoun, A. F.; Derradji, M.; Hamidon, T. S.; Masruchin, N.; Brosse, N.; Hussin, M. H., Nanocellulose: From Fundamentals to Advanced Applications. *Frontiers in Chemistry* **2020,** *8* (392).

Tu, S.; Ren, X.; He, J.; Zhang, Z., Stress–strain curves of metallic materials and post-necking strain hardening characterization: A review. *Fatigue & Fracture of Engineering Materials & Structures* **2020,** *43* (1), 3-19.

Usov, I.; Nyström, G.; Adamcik, J.; Handschin, S.; Schütz, C.; Fall, A.; Bergström, L.; Mezzenga, R., Understanding nanocellulose chirality and structure–properties relationship at the single fibril level. *Nature Communications* **2015,** *6* (1), 7564.

Usuki, A., Nylon 6-clay Hybrid: From Invention to Practical Use. *R&D Review of Toyota CRDL* **2016,** *47* (1), 45-55.

Vallés, C.; Papageorgiou, D. G.; Lin, F.; Li, Z.; Spencer, B. F.; Young, R. J.; Kinloch, I. A., PMMA-grafted graphene nanoplatelets to reinforce the mechanical and thermal properties of PMMA composites. *Carbon* **2020,** *157*, 750-760.

Vanderfleet, O. M.; Cranston, E. D., Production routes to tailor the performance of cellulose nanocrystals. *Nature Reviews Materials* **2021,** *6* (2), 124-144.

Vanholme, R.; Demedts, B.; Morreel, K.; Ralph, J.; Boerjan, W., Lignin Biosynthesis and Structure. *Plant Physiology* **2010,** *153* (3), 895-905.

Vasanthan, N.; Salem, D. R., FTIR spectroscopic characterization of structural changes in polyamide-6 fibers during annealing and drawing. *Journal of Polymer Science Part B: Polymer Physics* **2001,** *39* (5), 536-547.

Venkatraman, P.; Trotto, E.; Burgoyne, I.; Foster, E. J., Premixed cellulose nanocrystal reinforcement of polyamide 6 for melt processing. *Polymer Composites* **2020,** *41* (10), 4353-4361.

Voronova, M.; Rubleva, N.; Kochkina, N.; Afineevskii, A.; Zakharov, A.; Surov, O., Preparation and Characterization of Polyvinylpyrrolidone/Cellulose Nanocrystals Composites. *Nanomaterials* **2018,** *8* (12), 1011.

Wang, L.; Gardner, D. J.; Wang, J.; Yang, Y.; Tekinalp, H. L.; Tajvidi, M.; Li, K.; Zhao, X.; Neivandt, D. J.; Han, Y.; Ozcan, S.; Anderson, J., Towards industrial-scale production of cellulose nanocomposites using melt processing: A critical review on structure-processing-property relationships. *Composites Part B: Engineering* **2020,** *201*, 108297.

Wang, W.-C.; Cheng, Y.-T.; Estroff, B., Electrostatic Self-Assembly of Composite Nanofiber Yarn. *Polymers* **2021,** *13* (1), 12.

Wang, Z.; Li, Q.; Chen, Z.; Liu, J.; Liu, T.; Li, H.; Zheng, S., Enhanced Comprehensive Properties of Nylon-6 Nanocomposites by Aniline-Modified Boron Nitride Nanosheets. *Industrial & Engineering Chemistry Research* **2018,** *57* (32), 11005-11013.

Wang, Z.; Li, Q.; Liu, J.; Li, H.; Zheng, S., Covalent Surface Functionalization of Boron Nitride Nanotubes Fabricated with Diazonium Salt. *Journal of Nanomaterials* **2018,** *2018*, 6717046.

Wendorff, J. H.; Agarwal, S.; Greiner, A.; Agarwal, S., *Electrospinning : Materials, Processing, and Applications*. John Wiley & Sons, Incorporated: Hoboken, GERMANY, 2012.

Wiedenhoeft, A.; Miller, R., 2 Structure and Function of Wood. *Handbook of Wood Chemistry and Wood Composites* **2005**.

Wohlhauser, S.; Delepierre, G.; Labet, M.; Morandi, G.; Thielemans, W.; Weder, C.; Zoppe, J. O., Grafting Polymers from Cellulose Nanocrystals: Synthesis, Properties, and Applications. *Macromolecules* **2018,** *51* (16), 6157-6189.

Wohlhauser, S.; Kuhnt, T.; Meesorn, W.; Montero de Espinosa, L.; Zoppe, J. O.; Weder, C., One-Component Nanocomposites Based on Polymer-Grafted Cellulose Nanocrystals. *Macromolecules* **2020,** *53* (3), 821-834.

Xue, J.; Wu, T.; Dai, Y.; Xia, Y., Electrospinning and Electrospun Nanofibers: Methods, Materials, and Applications. *Chemical Reviews* **2019,** *119* (8), 5298-5415.

Yan, J.; Qiang, L.; Gao, Y.; Cui, X.; Zhou, H.; Zhong, S.; Wang, Q.; Wang, H., Effect of fiber alignment in electrospun scaffolds on keratocytes and corneal epithelial cells behavior. *Journal of Biomedical Materials Research Part A* **2012,** *100A* (2), 527-535.

Yang, Y.; Jia, Z.; Liu, J.; Li, Q.; Hou, L.; Wang, L.; Guan, Z., Effect of electric field distribution uniformity on electrospinning. *Journal of Applied Physics* **2008,** *103* (10), 104307.

Yong, C.; Mei, C.; Guan, M.; Wu, Q.; Sun, X.; Xu, B.; Wang, K., Interfacial modification mechanism of nanocellulose as a compatibilizer for immiscible binary poly(vinyl alcohol)/poly(ethylene oxide) blends. **2018,** *135* (9), 45896.

Yousefian, H.; Rodrigue, D., Effect of nanocrystalline cellulose on morphological, thermal, and mechanical properties of Nylon 6 composites. *Polymer Composites* **2016,** *37* (5), 1473-1479.

Yousefian, H.; Rodrigue, D., Morphological, physical and mechanical properties of nanocrystalline cellulose filled Nylon 6 foams. *Journal of Cellular Plastics* **2017,** *53* (3), 253-271.

Yu, D. S.; Kuila, T.; Kim, N. H.; Lee, J. H., Enhanced properties of aryl diazonium salt-functionalized graphene/poly(vinyl alcohol) composites. *Chemical Engineering Journal* **2014,** *245*, 311-322.

Yu, S.; Oh, K. H.; Hwang, J. Y.; Hong, S. H., The effect of amino-silane coupling agents having different molecular structures on the mechanical properties of basalt fiber-reinforced polyamide 6,6 composites. *Composites Part B: Engineering* **2019,** *163*, 511-521.

Yuan, H.; Zhou, Q.; Zhang, Y., 6 - Improving fiber alignment during electrospinning. In *Electrospun Nanofibers*, Afshari, M., Ed. Woodhead Publishing: 2017; pp 125-147.

Zabegaeva, O. N.; Sapozhnikov, D. A.; Buzin, M. I.; Krestinin, A. V.; Kotelnikov, V. A.; Baiminov, B. A.; Afanasyev, E. S.; Pashunin, Y. M.; Vygodskii, Y. S., Nylon-6 and single-walled carbon nanotubes polyamide composites:Formulation and characterization. *High Performance Polymers* **2017,** *29* (4), 411-421.

Zargham, S.; Bazgir, S.; Tavakoli, A.; Rashidi, A. S.; Damerchely, R., The Effect of Flow Rate on Morphology and Deposition Area of Electrospun Nylon 6 Nanofiber. *Journal of Engineered Fibers and Fabrics* **2012,** *7* (4), 155892501200700414.

Zhang, Z.; Sèbe, G.; Hou, Y.; Wang, J.; Huang, J.; Zhou, G., Grafting polymers from cellulose nanocrystals via surface-initiated atom transfer radical polymerization. *Journal of Applied Polymer Science* **2021,** *138* (48), 51458.

Zhao, X.; Li, W.; Li, F.; Hou, Y.; Lu, T.; Pan, Y.; Li, J.; Xu, Y.; He, J., Wearable yarn supercapacitors coated with twisted PPy@GO nanosheets and PPy@PAN-GO nanofibres. *Journal of Materials Science* **2021,** *56* (32), 18147-18161.

Zheng, J.; Yan, X.; Li, M.-M.; Yu, G.-F.; Zhang, H.-D.; Pisula, W.; He, X.-X.; Duvail, J.-L.; Long, Y.-Z., Electrospun Aligned Fibrous Arrays and Twisted Ropes: Fabrication, Mechanical and Electrical Properties, and Application in Strain Sensors. *Nanoscale Research Letters* **2015,** *10* (1), 475.

Zhou, C.; Chu, R.; Wu, R.; Wu, Q., Electrospun Polyethylene Oxide/Cellulose Nanocrystal Composite Nanofibrous Mats with Homogeneous and Heterogeneous Microstructures. *Biomacromolecules* **2011,** *12* (7), 2617-2625.

Zhu, H.; Luo, W.; Ciesielski, P. N.; Fang, Z.; Zhu, J. Y.; Henriksson, G.; Himmel, M. E.; Hu, L., Wood-Derived Materials for Green Electronics, Biological Devices, and Energy Applications. *Chemical Reviews* **2016,** *116* (16), 9305-9374.

Zhu, R.; Yadama, V.; Liu, H.; Lin, R. J. T.; Harper, D. P., Fabrication and characterization of Nylon 6/cellulose nanofibrils melt-spun nanocomposite filaments. *Composites Part a-Applied Science and Manufacturing* **2017,** *97*, 111-119.